Université Paris Cité

Institut de Physique du Globe de Paris

École doctorale Sciences de la Terre et de l'environnement et physique de l'Univers - STEP'UP (ED 560)

Planétologie et Science Planétaire

Photometric modeling to characterize planetary surfaces in the solar domain

Par Dung Tri Nguyen

Dirigée par Stéphane Jacquemoud

Co-encadrée par Antoine Lucas

Présentée et soutenue le 11/12/2024

Devant un jury composé de :

Jean-Louis Roujean Directeur de recherche (CNRS)	Rapporteur
Mathieu Vincendon Maître de conférences (Université Paris-Saclay)	Rapporteur
Charles Bachmann Professeur (Rochester Institute of Technology)	Examinateur
Sonia Fornasier Professeur des universités (Université Paris Cité)	Examinatrice
Antoine Pommerol Maître de conférences (University of Bern)	Examinateur
Ewelina Rupnik Chargé de recherche (IGN)	Examinatrice
Sylvain Douté Directeur de recherche (CNRS)	Invité
Antoine Lucas Chargé de recherche (CNRS)	Invité

Acknowledgement

Verily, 'tis a marvel to reckon that thrice a year hath slipped by as the fleeting shadow of a sparrow upon the wall. What a toilsome voyage 't hath been, replete with trials and moments of wondrous delight. Methinks I have lent mine humble part to the advancement of science, for ever have I yearned to be a trailblazer of sorts. Forsooth, 'twas this longing that first led me to embark upon this grand PhD journey, and certes, I have found great joy in the days spent within the fair city of Paris, laboring at IPGP, journeying hither and yon, and drinking deep of all the world's marvels. My ken hath widened greatly, as the heavens stretch beyond the reach of mortal gaze. Now, anon, I stand yet again at the threshold of life's great forked path, where destiny waits with both eager promise and trembling uncertainty. Ere I tread this road anew, I would take a moment to muse upon the past and pour forth mine heartfelt gratitude to those kind souls who have stood steadfastly by my side throughout this odyssey.

Foremost, mine utmost gratitude turneth toward mine thesis masters, Prof. Stéphane Jacquemoud and Dr. Antoine Lucas. Oft did I find myself leaning upon the profound wisdom of Prof. Jacquemoud, whose mastery of photometry and modeling did illuminate mine path, and upon the learned hand of Dr. Lucas, whose deftness in many crafts, most notably photogrammetry, did provide succor in times of need. Their unwavering counsel and steadfast diligence have been to me a fount of great inspiration. Further, I must lay due stress upon the boundless aid rendered by Prof. Jacquemoud in grappling with that most wearisome trial, the bane of mine early days, aptly named "the ordeal of administrative paperwork". How I did falter and rail against its confounding labyrinth in mine first year, yet his patience and steadfastness proved a balm to mine troubled spirit.

Next, I would extend mine heartfelt thanks unto the noble STEP'UP Doctoral School at Université Paris Cité, whose generous patronage hath sustained mine PhD labors. This toil of mine was graciously upheld by the beneficence of CNES, as part of the ventures CAROLInA (Characterization of Multi-Scale Roughness using OpticaL ImAgery) and SURFACEs (Etude de la rugosité de surface par radiométrie multi-angulaire). Furthermore, let due homage be paid to Labex UnivEarth (ANR-10-LABX-0023 and ANR-18-IDEX-0001), whose support under the SOILSPECT project hath made this work possible. Their aid hath been a cornerstone of this endeavor, and for it, I am ever indebted.

Furthermore, I extend mine gratitude to the learned experts of the PSS team at IPGP : Prof. Cécile Ferrari and Dr. Sébastien Rodriguez, whose counsel hath oft been a beacon unto me, offering wisdom of great utility. Mine thanks also to Dr. Sylvain Douté of IPAG, who did instruct me in the art of fast Bayesian inversion, a keystone in the edifice of this project. To the Pleiades specialists of CNES - Dr. Sophie Coustance, Dr. Marc Sébastien, and Dr. Aimé Meygret — who furnished most excellent multiangular data, I offer my heartfelt appreciation. Likewise, I am grateful to the scholars of IGN — Dr. Ewelina Rupnik, Arthur Delorme, and Dr. Lulin Zhang — who lent their expertise in wielding the MicMac photogrammetry software. Further acknowledgment is owed to the esteemed DART team : Prof. Jean Philippe Gastellu-Etchegorry, Dr. Yingjie Wang, and Nguyen Quang Thang, who guided me in the craft of ray-tracing and the DART software. The Géotéca sages, Dr. Paul Passy and Brian Plaisant, also deserve mention for their aid in digitizing the Asal-Ghoubbet rift of Dr. Lorent Stieltjes. I render mine gratitude unto mine esteemed thesis committee, being Dr. Raphael Grandin, Dr. Frederic Schmidt, and Dr. Lucas Landier. Whenas tribulations and perplexities

did arise along the winding path of mine doctoral voyage, their most sagacious counsels did guide me aright, restoring mine steps unto the proper course. To those whose contributions graced this endeavor : Dr. Alice Dupiau, for her insights into photometric models ; Matthieu Gougeon, for his mastery of the MicMac software ; Vo Nhat Le, for the generation of Moon DEMs from astronaut images and the preparation of soil samples ; Erica Uccellatori, for her diligence in soil spectral measurement ; and Dr. Marouchka Froment, for her expertise in Bayesian inversion — I owe my deepest thanks. Lastly, I acknowledge the invaluable instruction derived from the works of Dr. Sébastien Labarre (Hapke model and roughness calculation), Dr. Jason Legendre-Champion (DART framework), and Mélanie Nguyen (goniometer measurement), whose writings have been mine ever-faithful guides.

Moreover, I would offer mine thanks to Taoufik Gabsi, an engineer at IPGP, whose skill and patience did aid me in overcoming sundry vexations of the computing kind. Likewise, Anne Legendre, a secretary of IPGP, hath mine gratitude for her assistance with the labyrinthine formalities tied to ventures beyond the halls of IPGP. To mine esteemed colleagues, who together did weave a tapestry of camaraderie and warmth, I extend mine deepest thanks : Yassine Boukhari, Corentin Feray, Dr. Mael Essayeh, Dr. Christos Ntinos, Xiang Zhang, Dr. Boris Maletckii, Dr. Nguyen Khanh Ninh, Gabrielle Chabaud, Sébastien Faes, Jin Shi, Wanbo Xiao, Dr. Jianhu He, Dr. Keisuke Onodera, Dr. Sreejaya Kizhaekke Pakkathillam, Dr. Josipa Majstorovic, and Dr. Zongbo Xu. Each hath played a part in creating an atmosphere most convivial and welcoming, for which I am ever grateful.

Finally, let mine heartfelt gratitude be extended unto Dr. Tong Si Son and Associate Professor Ngo Duc Thanh, whose kindly efforts in penning letters of recommendation did open the gateway to mine PhD journey. Likewise, I offer thanks to Dr. Dinh Thi Lan Anh and Pham Viet Dung, who have lent their aid not only in matters of mine work but also in the tribulations and joys of mine personal life. Many thanks I render unto mine cherished friends and beloved kin, dwelling both in the noble city of Paris and the treasured haven of Hanoi. Their steadfast love and fellowship have been a pillar of strength and joy in mine journey.

List of publications

(Under revision) **Nguyen D.T.**, Jacquemoud S., Lucas A., Douté S., Ferrari C., Coustance S., Marcq S. & Meygret A. (2024). Mapping the surface characteristics of the Asal-Ghoubbet rift by massive inversion of the Hapke model on Pleiades multiangular images. *Remote Sensing of Environment*.

(In preparation) Roque-Bernard A., **Nguyen D.T.**, Lucas A., Jacquemoud S. & Ferrari C. (2024), Photometric inversion of avalanches and ejecta on (4)Vesta : Insights into surface evolution and granular segregation. *Astronomy & Astrophysics*.

(Submitted on October 1, 2024) Zhang L., Rupnik E., **Nguyen T.D.**, Jacquemoud S. & Klinger Y. (2024). BRDF-NeRF : Neural radiance fields with optical satellite images and BRDF modelling. *International Journal of Applied Earth Observation and Geoinformation*. https://arxiv.org/abs/2409.12014

List of conferences

Jacquemoud S., **Nguyen D.T.**, Lucas A., Douté S., Ferrari C., Coustance S., Marcq S. & Meygret A. (2024). Photometric characterization of the Asal-Ghoubbet rift (Republic of Djibouti) by massive inversion of the Hapke model. *EGU General Assembly 2024*, Vienna, Austria, 14–19 April 2024, EGU24-16810. https://doi.org/10.5194/egusphere-egu24-16810.

Nguyen D.T., Jacquemoud S., Lucas A., Douté S., Ferrari C., Coustance S., Marcq S. & Meygret A. (2024). Unveiling the characteristics of the lunar surface by massive inversion of a photometric model. *55th Lunar and Planetary Science Conference*. The Woodlands, 11-15 March 2024 (LPI Contributions No. 30406). https://www.hou.usra.edu/meetings/lpsc2024/pdf/1998.pdf.

Nguyen D.T., Jacquemoud S., Lucas A., Douté S., Ferrari C., Coustance S., Marcq S. & Meygret A. (2024). Unveiling the characteristics of the lunar surface by massive inversion of the Hapke model, *EGU General Assembly 2024*, Vienna, Austria, 14–19 April 2024, EGU24-17062, https://doi.org/10.5194/egusphere-egu24-17062.

Nguyen D.T., Douté S., Jacquemoud S., Lucas A., Ferrari C., Coustance S., Marcq S. & Meygret A. (2023). Photometric characterization of planetary surfaces : Can surface roughness of the Moon be estimated by inversion of the Hapke model ? *Bulletin of the AAS*, 55(8). https://baas.aas.org/pub/2023n8i207p03.

Nguyen D.T., Jacquemoud S., Lucas A., Ferrari C., Coustance S., Marcq S., Meygret A. & Douté S. (2023). Photometric characterization of planetary surfaces : When the Earth meets the Moon. *54th Lunar and Planetary Science Conference 2023*, The Woodlands, 13-17 March 2023 (LPI Contrib. No. 2806). https://www.hou.usra.edu/meetings/lpsc2023/pdf/1239.pdf.

Résumé

Titre : Modélisation photométrique pour caractériser les surfaces planétaires dans le domaine solaire

Résumé :

Pour comprendre la formation et l'évolution des paysages ou élaborer des stratégies d'exploration des futures missions d'exploration planétaire, il est nécessaire de connaître les caractéristiques physiques des surfaces terrestres et planétaires. La photométrie est une des méthodes permettant d'étudier ces caractéristiques à distance, par l'intermédiaire de la fonction de distribution de la réflectance bidirectionnelle (BRDF). Il existe plusieurs modèles de BRDF, semi-empiriques ou physiques, capable de simuler la BRDF des surfaces naturelles. L'inversion de ces modèles, dont le modèle de Hapke est le plus répandu dans la communauté scientifique, a été largement utilisée au cours des dernières décennies pour révéler des propriétés physiques des surfaces complexes, notamment la rugosité de surface, la porosité, la taille et la forme des grains, la micro-texture, la composition minérale, etc. Cette méthode a cependant rarement été appliquée à grande échelle sur Terre en raison d'un certain nombre de difficultés. De plus, la validation du modèle est encore largement qualitative. Deux sites d'étude ont été retenus pour nos recherches : (1) le rift Asal-Ghoubbet (République de Djibouti), remarquable pour ses terrains arides, servant d'analogue potentiel aux surfaces extraterrestres ; (2) la face visible de la Lune, en particulier les sites d'atterrissage des missions Apollo. Ces sites sont d'un grand intérêt car ils offrent une grande variété de données orbitales et in situ : images satellites, photographies acquises à différentes échelles, échantillons de laboratoire. Une des originalités de ce travail de thèse est l'exploitation de l'imagerie Pléiades pour la Terre et la Lune, et l'inversion du modèle de Hapke sur la BRDF extraite de chaque pixel permettant de générer des cartes de paramètres du modèle (entre quatre et six) selon les zones étudiées. Nous avons cherché à déchiffrer la signification physique de chaque paramètre et tenté de les comparer avec des mesures de terrain. Les données de terrain comprennent des photographies multi-angulaires prises par drone ou à la main, pour créer des modèles numériques de terrain (MNT) à l'aide de la photogrammétrie, et des échantillons pour les mesures spectrales et l'identification des constituants chimiques. Enfin, la relation entre les propriétés physiques de la surface et sa BRDF a été investiguée grâce à l'utilisation du modèle de lancer de rayons DART-Lux.

Mots-clés : Modèle photométrique de Hapke ; Télédétection multiangulaire ; Photogrammétrie ; Modèle Numérique de Terrain ; Modèle de lancer de rayons DART ; imagerie Pléiades

Abstract

Title: Photometric modeling to characterize planetary surfaces in the solar domain

Abstract:

To understand the formation and evolution of landscapes, or to develop exploration strategies for future planetary exploration missions, we need to know the physical characteristics of terrestrial and planetary surfaces. Photometry is one method of studying these characteristics remotely, via the bidirectional reflectance distribution function (BRDF). There are several BRDF models, both semi-empirical and physical, capable of simulating the BRDF of natural surfaces. The inversion of these models, of which the Hapke model is the most widespread in the scientific community, has been widely used over the last few decades to reveals the physical properties of complex surface, including surface roughness, grain size and shape, micro-texture, mineral composition and so on. However, this method has rarely been applied on a large scale on Earth, due to a number of difficulties. Moreover, model validation is still largely qualitative. Two study sites have been selected for our research: (1) The Asal-Ghoubbet rift (Republic of Djibouti), remarkable for its arid terrain, serving as a potential analogue for extraterrestrial surfaces; (2) The near side of the Moon, in particular the landing sites of the Apollo missions. These sites are of great interest as they offer a wide variety of orbital and in situ data: satellite images, photos acquired at different scales, lab samples. One of the original features of this thesis work is the use of Pleiades imagery for the Earth and Moon, and the inversion of the Hapke model on the BRDF extracted from each pixel to generate maps of model parameters (between four and six) depending on the areas studied. We sought to decipher the physical meaning of each parameter and attempted to compare them with field measurements. Field data includes multi-angular photographs taken by drone or by hand, to create digital elevation models (DEM) using photogrammetry, and samples for spectral measurements and identification of chemical constituents. Finally, the relationship between the physical properties of the surface and its BRDF was investigated using the DART-Lux ray-tracing model.

Keywords: Hapke photometric model; Multiangular remote sensing; Photogrammetry; Digital Elevation Model; DART ray-tracing model; Pleiades imagery

Résumé étendu

L'étude des surfaces planétaires est cruciale en planétologie, car elle allie l'astronomie et les géosciences pour examiner les caractéristiques géologiques, géomorphologiques et atmosphériques des corps célestes. En analysant les caractéristiques des surfaces, telles que la composition minérale, la texture et la porosité, les chercheurs tentent de comprendre la formation et l'évolution des planètes, des lunes, des astéroïdes et des comètes, et d'en déduire si elles sont susceptibles d'abriter la vie. Les progrès de l'exploration spatiale ont permis d'enrichir nos connaissances grâce aux orbiteurs, aux rovers et à d'autres missions. Grâce aux données de télédétection, les scientifiques utilisent la photométrie et la radiométrie pour analyser l'interaction de la lumière avec les surfaces, caractérisée par la fonction de distribution de la réflectance bidirectionnelle (BRDF), qui varie en fonction des propriétés de la surface, telles que la rugosité, la taille des grains et la porosité.

Les modèles de transfert radiatif, représentation simplifiée de l'interaction entre la lumière et les surfaces ou objets naturels, sont un moyen efficace d'analyser la BRDF. Ils permettent de décomposer des structures complexes, de faire des ajustements et d'analyser le comportement d'un système. Dans ce travail, plutôt que de développer un nouveau modèle, j'ai utilisé des modèles existants et ai tenté de les valider en croisant les résultats avec la vérité terrain. Trois modèles sont associés à la photométrie : le modèle numérique de terrain (MNT), le modèle de transfert radiatif et le modèle de lancer de rayons. Les MNT fournissent une représentation tridimensionnelle d'un terrain, obtenue par des techniques de télédétection comme la photogrammétrie, le LiDAR ou l'InSAR Li et al. (2005). Les modèles de transfert radiatif simulent l'interaction entre la lumière et un milieu (surface, milieu semi-transparent). Dans ce travail, je me suis concentré sur le modèle de Hapke qui calcule la BRDF d'une surface dans une configuration de mesure donnée. La capacité de ce modèle à prédire et à décrire les mesures radiométriques a été validée par de nombreux travaux. Enfin, le modèle DART-Lux de lancer de rayons illustrera la dynamique de l'illumination au sein d'une scène et de ses composants.

Deux sites principaux ont été étudiés dans le cadre de ce travail de recherche :

- Le rift d'Asal-Ghoubbet (République de Djibouti), remarquable pour ses surfaces arides et variées, pouvant servir d'analogues aux surfaces extraterrestres.
- La face cachée de la Lune, en particulier les sites d'atterrissage des missions Apollo, pour lesquels nous disposons d'images satellites de acquises au sol. Ces sites revêtent une importance historique : ils ont fait l'objet de nombreuses expériences menées par les astronautes américains, notamment la collecte d'échantillons de sol. Ils font partie des très rares surfaces extraterrestres offrant des données expérimentales acquises au sol.

Pour ces deux sites, nous avons rassemblé un grand nombre de données multiscalaires comprenant des images satellites, des échantillons de roches et de sols et des images prises au sol et/ou par drone. L'exploitation d'imagesPléiades multi-angulaires acquises sur le rift d'Asal-Ghoubbet et la face visible de la Lune constitue une originalité de cette thèse. Le système Pléiades est constitué de deux satellites à très haute résolution, inaugurée fin 2011. Les caméras sont équipées d'un canal en mode panchromatique avec une distance d'échantillonnage au sol (GSD pour Ground Sample Distance) de 70 cm, et de quatre canaux en mode spectral avec une GSD de

2.8 m. Grâce à son agilité, des ensembles d'images stéréo/tri-stéréo peuvent être rapidement acquis, ce qui facilite la génération de MNT à haute résolution par photogrammétrie (Gleyzes et al., 2012). La polyvalence de Pléiades, en particulier sa capacité à observer les deux sites de recherche, est primordiale pour ce travail. Dans le rift d'Asal-Ghoubbet, nous avons au accès à une acquisition en mode vidéo de 21 images prises sous 21 angles de visée différents en seulement 4 minutes Labarre (2017). Ces images ont été corrigées des effets atmosphériques en décembre 2022 grâce au code de correction atmosphérique MAJA (Rouquié et al., 2017). Pour la Lune, un référentiel de plus de 1200 images couvrant des angles de phase compris entre 0° et 120° (au centre de la Lune) a été livré par le CNES. Les images terrestres ont une GSD de 2 m tandis que les images lunaires ont une GSD de 1500 m.

Un aspect innovant de ce travail est le développement d'une chaîne d'inversion massive du modèle de Hapke utilisant un algorithme d'inversion Bayésienne rapide (fBi). Cette chaîne de traitement inclut un prétraitement des images destiné à améliorer la précision géométrique, le processus d'inversion lui-même, l'évaluation de la qualité et l'interprétation des résultats. Nous avons testé les méthodes d'inversion Bayésienne de Monte Carlo et de fBi. Bien que les deux approches produisent des résultats similaires, l'inversion bayésienne rapide est jusqu'à cent fois plus rapide grâce à sa méthode d'échantillonnage plus efficace. Cette efficacité en fait de un outil prometteur pour les études photométriques à grande échelle. À notre connaissance, c'est la première fois qu'une telle inversion a été réalisée sur Terre. La production de données d'inversion à l'échelle d'une image entière a révélé des informations précieuses sur les paysages, notamment sur la façon dont les unités géologiques s'emboîtent les unes dans les autres. Elle a aussi permis de détecter de nouvelles caractéristiques de surface, qui pourraient sinon passer inaperçues dans une analyse locale. Son potentiel va au-delà du simple traitement des données et ouvre des perspectives pour le développement de méthodes innovantes d'analyse des données photométriques multi-angulaires.

Il reste cependant encore beaucoup à faire. A la fois sur le rift d'Asal-Ghoubbet et sur la Lune, l'inversion massive n'a été réalisée que sur la bande verte du satellite Pléiades, laissant les bandes rouge, bleue et proche infrarouge largement inexplorées par manque de temps. Le processus actuel requiert encore un travail important car chaque patch doit être analysé séquentiellement et manuellement. En outre, il y a une marge d'optimisation de certaines phases clés telles que l'extraction de la BRDF, la correction du terrain, la normalisation photométrique, le calcul de l'erreur quadratique moyenne (RMSE) ou la gestion de grandes matrices de configuration géométrique. Relever ces défis nous permettrait d'effectuer une inversion massive sur le rift d'Asal-Ghoubbet à la résolution originale de 2 m (au lieu de 10 m actuellement), ce qui améliorerait considérablement la précision et le niveau de détail de l'analyse. Les conditions sous-optimales des données restent un problème non résolu, empêchant l'obtention de meilleurs résultats d'inversion.

Grâce à fBi, nous avons considérablement accéléré le calcul et pu estimer les paramètres du modèle de Hapke sur une grande variété de terrains et à différentes échelles. Cela facilite les comparaisons croisées et améliore notre interprétation des paramètres en établissant des liens avec les mesures de terrain. Bien que l'albédo de diffusion simple (SSA) soit relativement facile à contraindre, il reste difficile à interpréter. Cela souligne la nécessité d'un développement méthodologique plus poussé ou d'approches alternatives pour combler le fossé entre les modèles théoriques et les observations. En outre, nous avons mis en évidence une relation entre l'albédo

de diffusion simple, l'angle de pente moyen calculé à partir des MNT millimétriques et la rugosité photométrique, qui donne un aperçu des propriétés de la surface. Pour les paramètres de la fonction de phase de Henyey-Greenstein, les caractéristiques des grains peuvent être déduites en utilisant le système d'interprétation décrit par McGuire and Hapke (1995), Souchon et al. (2011) et Pilorget et al. (2015), à l'aide du graphe b-c. Cependant, le potentiel du modèle de Hapke n'a pas été pleinement exploré dans ce travail. Bien que nous ayons estimé des paramètres liés à la porosité de surface et à l'opacité des grains (paramètres d'effet d'opposition), nous manquons de moyens expérimentaux pour mesurer et valider ces paramètres.

Grâce à la création d'une base de données préliminaire des paramètres du modèle de Hapke, nous supposons que chaque modèle de BRDF peut être associé de manière univoque à un terrain particulier, de la même manière que les mesures spectrales sont associées à la composition chimique. Dans notre cas, ces modèles de BRDF sont susceptibles de représenter un mélange de signatures essentiellement physiques, avec quelques contributions mineures de signatures chimiques. Ce nouveau concept ouvre une nouvelle voie de recherche visant à améliorer notre compréhension des surfaces planétaires par des méthodes photométriques. Les résultats futurs pourront être comparés et reliés à cette base de données, ce qui aidera à prédire les caractéristiques des surfaces planétaires.

Sur la base des travaux de Shepard et al. (2001), Bretar et al. (2013) et Labarre et al. (2019), nous avons développé un cadre d'étude de la rugosité des surfaces basé sur six paramètres de rugosité importants : l'angle de pente moyen, la hauteur quadratique moyenne, la longueur d'autocorrélation, le paramètre Z_S, la tortuosité et la dimension fractale. Chacun de ces paramètres saisit différents aspects de la rugosité, tels que la variation verticale et horizontale, la répétitivité de la surface et le comportement de mise à l'échelle. Ce cadre a été appliqué aux MNT du rift d'Asal-Ghoubbet, ainsi qu'aux MNT générés à partir des photographies du sol lunaire prises par les astronautes des missions Apollo et d'un MNT LROC du site d'atterrissage d'Apollo 17. Cette analyse est cruciale non seulement pour caractériser la surface, mais aussi pour valider la rugosité photométrique et les simulations de la BRDF à l'aide de méthodes de lancer de rayons. En outre, à l'instar de la base de données des paramètres du modèle de Hapke, cette étude génère une base de données des paramètres de rugosité correspondant à un seul type de surface. Cette base de données peut également servir de référence pour des futurs travaux, contribuant à la caractérisation des surfaces planétaires. Le rift Asal-Ghoubbet et la surface lunaire présentent une variété de types de terrain. Tout comme nous avons développé une base de données préliminaire des paramètres du modèle de Hapke, nous envisageons d'explorer des types de terrain encore plus variés, enrichissant ainsi la base de données des paramètres de rugosité établie. Il faudrait aussi étudier les paramètres de rugosité associés au modèle de Shkuratov, ainsi que ceux des modèles de diffusion utilisant des données radar et des modèles thermiques. L'étude de ces modèles pourrait offrir des perspectives nouvelles et améliorerait notre compréhension de la rugosité des surfaces.

La dernière contribution de cette thèse est la simulation de la BRDF à l'aide de MNT, de mesures spectrales et du modèle DART-Lux. Nous avons constaté que si les mesures spectrales affectent principalement l'intensité de la BRDF, elles ne modifient pas sa forme générale. La rugosité de surface, en revanche, affecte à la fois l'intensité et la forme de la BRDF dans le modèle de facettes lambertien appliqué à DART-Lux, alors qu'elle affecte principalement l'intensité dans

le modèle de Hapke. Un phénomène intéressant observé dans nos simulations, en particulier pour un angle d'incidence de 38°, est que l'effet d'opposition a tendance à se produire près de la direction d'incidence, mais exactement dans cette direction. Ces simulations ont permis de mieux comprendre l'effet de la rugosité sur la diffusion de la lumière par les surfaces naturelles. Les simulations futures pourraient tester d'autres angles d'incidence, effectuer des analyses de sensibilité du modèle de Hapke et inclure des effets atmosphériques pour affiner les résultats. En outre, des mesures au goniomètre n'ont été effectuées que sur trois des dix-neuf sites du rift d'Asal-Ghoubbet. Des mesures supplémentaires nous permettraient de simuler davantage de scénarios de BRDF. En outre, des MNT doivent encore être générés à partir des images des échantillons de sol prélevés. La production de MNT à l'échelle du micromètre à partir de ces images nous permettrait d'étudier plus en détail l'effet de la BRDF.

Contents

List of Figures

List of Tables

List of Acronyms

— **AMSA:** Anisotropic Multiple Scattering Approximation
— **ALSEP:** Apollo Lunar Surface Experiments Package
— **AOT:** Aerosol optical thickness
— **APERO:** Aérotriangulation Photogrammétrique Expérimentale Relativement Opérationnelle
— **ASP:** Ames Stereo Pipeline
— **ATCOR:** Atmospheric and Topographic Correction
— **BOA:** Bottom of atmosphere
— **BRDF:** Bidirectional reflectance distribution function
— **BRF:** Bidirectional reflectance factor
— **BSDF:** Bidirectional scattering distribution factor
— **CESBIO:** Centre d'Etudes Spatiales de la Biosphère
— **CNES:** Centre National d'Études Spatiales
— **CRISM:** Compact Reconnaissance Imaging Spectrometer for Mars
— **DART:** Discrete Anisotropic Radiative Transfer
— **DEM:** Digital elevation model
— **DNS:** Dynamic Nested Sampling
— **DTM:** Digital terrain model
— **ECMWF:** European Centre for Medium-Range Weather Forecasts
— **EM:** Expectation-Maximization
— **ENSG:** École nationale des sciences géographiques
— **EDRNAC:** Experiment Data Record Narrow Angle Camera
— **fBi:** Fast Bayesian inversion
— **FOV:** Field of view
— **GCP:** Ground control point
— **GDAL:** Geospatial Data Abstraction Library
— **GIS:** Geographic information system
— **GLLiM:** Gaussian Local Linearly Mapping
— **GPS:** Global Positioning System
— **GSD:** Ground sampling distance
— **GUI:** Graphical user interface
— **HMC:** Hemispherical-directional reflectance factor
— **HMC:** Hamiltonian Monte Carlo

— **HG:** Henyey-Greenstein
— **ICP:** Iterative Closest Point
— **IFOV:** Instantaneous field of view
— **IGN:** Institut national de l'information géographique et forestière
— **ILWIS:** Integrated Land and Water Information System
— **IMIS:** Incremental Mixture Importance Sampling
— **IMSA:** Isotropic Multiple Scattering Approximation
— **INRIA:** Institut national de recherche en sciences et technologies du numérique
— **IPGP:** Institut de Physique du Globe de Paris
— **IUWT:** Isotropic Undecimated Wavelet Transform
— **JAXA:** Japan Aerospace Exploration Agency
— **LOLA:** Lunar Orbiter Laser Altimeter
— **LRO:** Lunar Reconnaissance Orbiter
— **LROC:** Lunar Reconnaissance Orbiter Camera
— **LUT:** Look-up table
— **MAJA:** MACCS ATCOR Joint Algorithm
— **MAP:** Maximum a posteriori
— **MCMC:** Markov Chain Monte-Carlo
— **MDIS:** Mercury Dual Imaging System
— **MicMac:** Multi-Images Correspondances, Methods for Automatic Correlation
— **ML:** Maximum Likelihood
— **MLA:** Mercury Laser Altimeter
— **MOLA:** Mars Orbiter Laser Altimeter
— **MNT**: Modèle Numérique de Terrain (DEM in english)
— **MTPR:** Mean tie point residuals
— **NAC:** Narrow Angle Camera
— **NASA:** National Aeronautics and Space Administration
— **OMI:** Ozone Monitoring Instrument
— **OTB:** Orfeo ToolBox
— **PDF:** Probability distribution function
— **PASTIS:** Programme Autopano Sift pour les Tie-points dans les ImageS
— **RAMI:** RAdiation transfer Model Intercomparison
— **RDR:** Reduced Data Record
— **RMS:** Root-mean-square
— **RMSE:** Root-mean-square error
— **RMSH:** Root-mean-square height
— **RPV:** Rahman-Pinty-Verstraete
— **RTLS:** RossThick LiSparse
— **RTLSR:** RossThick-LiSparseReciprocal
— **RTLSRC:** RossThick-LiSparseReciprocalChen

— **RTLSRCS:** RossThick-LiSparseReciprocalChenSnow
— **RTM:** Radiative transfer model
— **SIFT:** Scale-Invariant Feature Transform
— **SLIM:** Smart Lander for Investigating Moon
— **SMAC:** Simplified Model for Atmospheric Correction
— **SMC:** Soil moisture content
— **SOS:** Successive Orders of Scattering
— **SRTM:** Shuttle Radar Topography Mission
— **SSA:** Single scattering albedo
— **SZA:** Sun zenith angle
— **TIR:** thermal infrared
— **TOA:** Top of atmosphere
— **USGS:** United States Geological Survey
— **UTM:** Universal Transverse Mercator
— **VIRTIS:** Visible and Infrared Thermal Imaging Spectrometer
— **VZA:** Viewing zenith angle
— **WAC:** Wide Angle Camera

General introduction

The study of planetary surfaces plays a crucial role in planetary science, which combines knowledge of Astronomy and the Geosciences. This exciting field studies the geological, atmospheric and geomorphological characteristics of celestial objects in our Solar system and beyond. Researchers attempt to decipher the enigmas of various celestial bodies, such as planets, moons, asteroids, and comets, by examining their surface characteristics (mineral composition, surface texture, porosity, etc.) and the forces that shape them. Observations of past climate markers and erosion help us to understand the genesis and transformation of soils and terrains. Thanks to recent advances in space exploration and remote sensing methods, our knowledge of planetary surfaces has taken a quantum leap forward. Missions involving orbiters, landers, rovers, and fly-bys have provided a wealth of information, enabling scientists to reconstruct the geological past of these celestial bodies and assess their potential for supporting life.

Following these advances, researchers are exploiting the available remote sensing data to find the best way of estimating surface characteristics. Their research focuses on photometry, the measurement of visible light and, by extension to other wavelength domains, on radiometry. More specifically, photometry examines how light is reflected by a surface or particle, depending on the measurement configuration, taking into account factors such as incidence, emergence, and phase angles. The angular variation of reflectance produces a pattern known as the Bidirectional Reflectance Distribution Function (BRDF). The BRDF (sr^{-1}) is the ratio of radiance ($W.m^{-2}sr^{-1}$) to irradiance ($W.m^{-2}$) in their respective directions. Just as different chemical compositions result in unique spectral responses, so different soil types can exhibit distinct BRDF patterns. These differences depend in part on the measurement configuration and the physical attributes of the surface, such as roughness, porosity, grain size and shape.

Physical models, which involves constructing a simplified representation of the interaction between light and natural objects, is an effective way of analyzing BRDF. They enable to break down complex structures, make adjustments and analyze the behavior of a system. This approach, which has been followed by researchers in IPGP's Planetology and Space Science team for the past fifteen years, provides the context of this thesis. Mélanie Arab-Sedze's PhD thesis (Arab-Sedze, 2013) on Reunion island showed that surface roughness decorrelates the radar signal. This subject subsequently became a focus of interest, as surface roughness also has an effect on reflectance in the solar domain. Taking advantage of the launch of the Pleiades 1B satellite on December 2, 2012, IPGP took advantage of the commissioning phase to ask CNES for video acquisition (spotlight mode acquisition) on the island. However, tropical storms and thick cloud cover prevented this acquisition. Dr. Rafael Grandin suggested that the Asal-Ghoubbet rift (Republic of Djibouti), where the climate is arid and cloud cover less significant, should be considered instead. Three years after

the Pleiades images were acquired, the team carried out two field experiments in April 2015 and February 2016, as part of Sébastien Labarre's PhD thesis (Labarre, 2017).

Due to time constrains, Sébastien Labarre was unable to generate all the digital elevation models used to determine surface roughness in the form of a statistical mean slope angle. Based on a few data points, it appears that the latter was poorly related to the photometric roughness obtained by inversion of the Hapke model. One hypothesis is that the lack of data could introduce a significant bias into the analysis. In addition, doubts is raised about the photometric roughness, which is not only affected by the actual surface roughness, but also by other surface attributes or model parameters. This observation is consistent with the parameter coupling reported by Shepard and Helfenstein (2007) and Helfenstein and Shepard (2011). Despite all these studies, the mysteries of surface roughness persist and no definitive conclusion has been found in the literature. To solve this conundrum, a new thesis project to study surface roughness using multiangular remote sensing data in the solar domain has been launched.

In this work, instead of developing a new model, I investigate a new use for existing models, integrate it into a research framework, and attempt to validate it by cross-examining results and ground truth. Figure 1 shows three models associated with photometry: the digital elevation model (DEM), the radiative transfer model and the ray tracing model. DEMs provide a three-dimensional representation of a terrain, obtained by remote sensing techniques such as photogrammetry, LiDAR or InSAR Li et al. (2005). Radiative transfer models simulate the interaction between light and a medium (surface, atmosphere). In our case, we focus on the Hapke model, which calculates the BRDF of a surface in any measurement configuration. Its ability to predict and describe radiometric measurements has been extensively tested. Finally, the DART-Lux ray tracing model will illustrate the dynamics of illumination within a scene and its components.

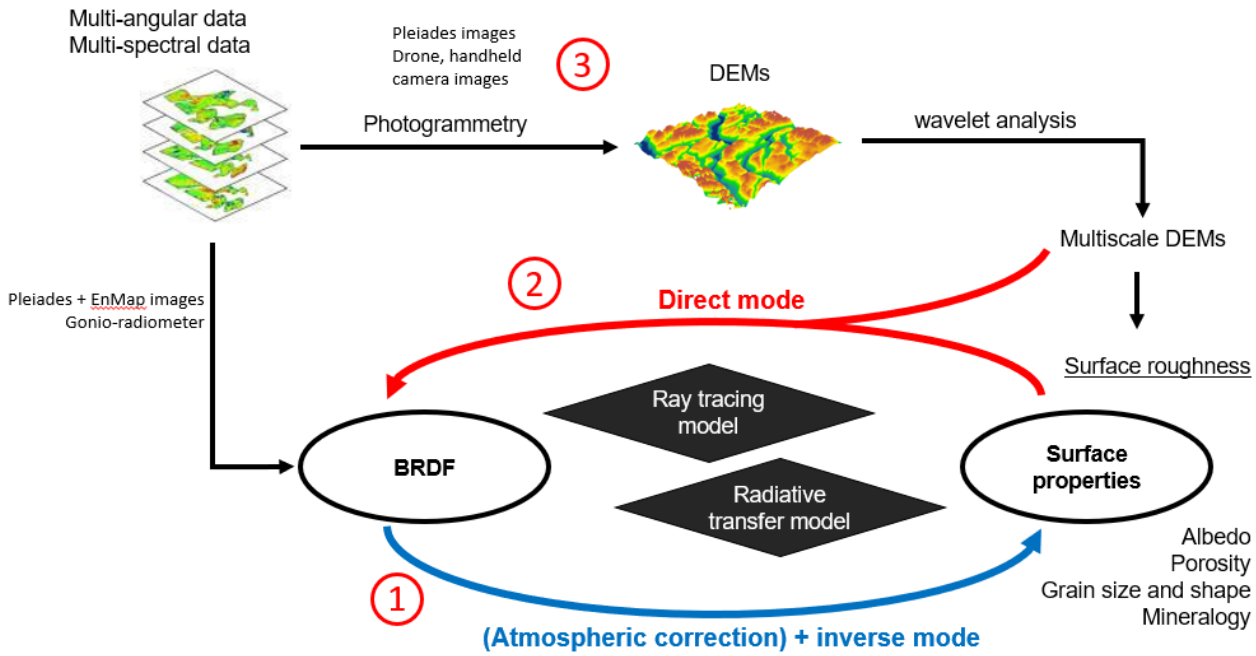

Figure 1 – The overall framework of the project.

The diagram in Figure 1 captures the essence of my work. In path (1), using multiangular Pleiades data (images taken from different viewing angles), I invert the Hapke model to estimate

its input parameters. Analysis of these parameter maps helps us to predict the physical and chemical characteristics of a surface (e.g., surface roughness, albedo, porosity, grain size and shape, mineralogy) in order to distinguish different soil types in a given area. If the planet has an atmosphere, atmospheric correction is required. In path (2), using the direct mode of the Hapke model, we use the physical characteristics of the surface to simulate its BRDF. Another task is to generate DEMs from multiangular images using photogrammetry (path 3). Wavelet analysis will be used to decompose the DEMs into different components, corresponding to different scales of surface roughness. This methodological approach paves the way for a comprehensive study of how multi-scale roughness influences the optical characteristics of a surface.

Two main sites were chosen for this research work:

- The Asal-Ghoubbet rift in the Republic of Djibouti, remarkable for its varied arid terrain, serving as a potential analog for extraterrestrial surfaces.
- The near side of the Moon, in particular the Apollo landing sites, which offer a unique blend of orbital and terrestrial imagery. These sites are of historical importance, as they provide the backdrop for many experiments carried out by American astronauts, including the collection of soil samples. These sites are among the few places outside the Earth that offer ground truth data.

The scope covered by this thesis not limited to surface roughness, but was considerably extended to include other surface physical properties, e.g., albedo and grain characteristics. This approach was chosen because of the knowledge of the interconnection between the Hapke model parameters. This makes sense, because the actual physical properties of a surface can influence each other. For example, surface compactness, unlike porosity, is often associated with very fine, homogeneous grains. We observed that tightly-packed soils of a similar type are naturally bright and smooth at different scales. Furthermore, as the performance of ray-tracing models has improved significantly in recent years, we can now study the relationship between BRDF and surface characteristics, to see the impact of changes from one to the other. Therefore, in addition to studying the relationships between parameters, we are also able to separate out the influence of individual soil characteristics.

To explain our work in more detail, we will first define photometry and the various photometric models (Chapter 1). Then, in Chapter 2, we will explain the various data and tools. They are used in different contexts and studies, so it is necessary to dedicate a separate section to them. Chapter 3 will be devoted to the processes surrounding the DEMs, which are essential for the study of surface roughness and BRDF simulation. The inversion of the Hapke model, detailed in Chapter 4, will give us an overview of the framework we have used to study the various photometric parameters. The massive inversion result and analysis will be presented in Chapter 5. Chapter 6 will focus on how to simulate BRDF using a ray-tracing model. In other words, chapter 4, 5 and 6 will enable us to explore the relationship between BRDF and surface properties in two directions. Finally, the conclusion will summarize the main points of our work, reflecting on its significance and offering final thoughts or recommendations for the future.

Chapter 1

Photometric models: significance and application

Introduction

In this chapter, we examine the fundamental concepts of photometry, exploring its principles and presenting several photometric models, and their applications in scientific research. Emphasis is placed on the Hapke model, which is the focus of our study. Its choice is mainly related to the physical meaning of its parameters. We present a detailed review of this model, recognizing that while only a subset of its parameters can be used in our context, a comprehensive understanding of the model as a whole is crucial. To this end, we explore all the parameters of the full version of the Hapke model, discussing not only the mathematical formulations, the conditions under which the model is applicable, but also the characteristic behaviors of these parameters. Key aspects covered include the coupling phenomenon, where several parameters interact in complex ways affecting the model outputs; model performance in scenarios involving wet soil, which can significantly influence reflectance properties due to moisture effects; and the sensitivity of model parameters.

1.1 Photometry

1.1.1 Background

Understanding the origin and evolution of land surfaces depends on our ability to accurately determine their characteristics, particularly their physical properties and mineralogical composition. Although in situ measurements provide highly accurate information, their limited availability forces us to rely on remote sensing data, mainly satellite imagery. The mineralogical composition of surfaces is generally extracted from hyperspectral data, using the specific spectral signatures of the minerals of which they are composed. Physical properties, on the other hand, are often deduced from the texture analysis of satellite images. This can reveal patterns, alignments and distributions of materials that indicate various surface-forming processes such as volcanic activity, sediment deposition or erosion. However, the effectiveness of texture analysis is intrinsically limited by the resolution of satellite sensors. The ground sampling distance (GSD) of most commercial

satellites is between 2 m and 5 m, down to 30 cm for very high-resolution sensors (Chouteau et al., 2022). While these sensors allow us to observe large-scale textural features, they do not capture details as small as grain size, which are often crucial to understanding surface characteristics.

This is why photometry has received so much attention in the field of Earth observation and planetary science. It offers a complementary method to above-mentioned techniques, and provides valuable information on the smallest scales of surface textures and properties. The bidirectional reflectance distribution function (BRDF) describes the scattering of a parallel light beam incident in one direction towards another direction in the hemisphere. It captures the intrinsic scattering properties of a surface, enabling other relevant quantities to be derived Nicodemus (1965); Schaepman-Strub et al. (2006). Reflectance variations are influenced by the physical and chemical properties of the reflective surface (roughness, porosity, grain size, shape and composition, mineralogy and opacity as a function of wavelength), which can form a unique pattern characterizing that surface.

Photometry has thus become the very foundation of this research. It is therefore imperative to distinguish between the different terms. From a certain point of view, it can be related to radiometry, since they both concern the study of the intensity of light scattered by a particle or reflected by a surface. However, whereas radiometry focuses on the variation of electromagnetic waves as a function of wavelength, photometry focuses more on variation as a function of lighting geometries (Domingue et al., 2016a). This is the definition we use in this thesis. In addition, there's another definition of photometry that we don't use, but that's worth knowing: brightness measurement. It takes into account the visible spectrum weighted by the eye's response, and uses units such as lumen, candela and lux (Ohno, 2000). Related to this, we must also distinguish photometry in planetary science and astronomy. Both applications of photometry focus on the study of light, but they differ fundamentally in their objectives and methodologies. In astronomy, photometry is used to measure the flux or intensity of light from celestial bodies such as stars, galaxies and other astronomical objects. The aim is to determine the luminosity of these objects, which can then be used to deduce various astrophysical properties such as size, temperature, distance and luminosity. Measurement angles are therefore not a determining factor for in astronomical photometry, unlike planetary science photometry.

Over the last few decades, photometry has been widely used in planetary science to analyze the surface materials of celestial bodies such as Mars (Cord et al., 2003; Fernando et al., 2013; Pilorget and Fernando, 2021), Mercury (Warell and Davidsson, 2010; Domingue et al., 2016a; Wohlfarth and Wöhler, 2022) and the Moon (Johnson et al., 2013; Sato et al., 2014; Nagori et al., 2023), as well as comets and asteroids (Spjuth et al., 2012; Ciarniello, M. et al., 2015; Fornasier et al., 2015). On Earth, it mainly applies to data acquired in the laboratory (Jacquemoud et al., 1992; Lucey, 1998; Helfenstein and Shepard, 2011; Souchon et al., 2011) or in the field (Pinty et al., 1989; Yang et al., 2011; Bachmann et al., 2017; Eon et al., 2018), much more rarely to satellite data (Wu et al., 2009; Labarre et al., 2019). Its application is mainly in the solar domain (see Appendix A), but it also extends to the far ultraviolet (Feaga et al., 2015; Gimar et al., 2022; Raut et al., 2018).

1.1.2 Photometric quantities

In a widely cited article, Nicodemus et al. (1977) gave a unified definition of reflectance in the broad sense and proposed a nomenclature to facilitate research work. Subsequently, the physics-based terminology was updated and adapted to the case of remote sensing by Martonchik et al. (2000). Most of the definitions of photometric quantities have been gathered in the work of Schaepman-Strub et al. (2006). Jeremy Tatum's online booklet [1] on planetary photometry is also a good summary. Therefore, we will only briefly mention some key points here, while advising readers wishing to delve deeper into the basics of photometry to consult these works.

Let's start with the components of the lighting geometries or, in other words, the geometric configuration of the acquisition. In Figure 2, i is the zenith (or incidence) angle of the illumination, ϕ_i the azimuth angle of the illumination, e is the zenith viewing (or emergence) angle and ϕ_e the azimuth viewing angle. The phase angle is the angle between the two directions. The geometric configuration is either the set (i, e, ϕ), with $\phi = |\phi_i - \phi_e|$ the absolute difference between the azimuth angles of incidence and emergence, or the set (i, e, g). The two sets are interchangeable using the formula:

$$\cos g = \cos i \times \cos e + \sin i \times \sin e \times \cos \phi \tag{1.1}$$

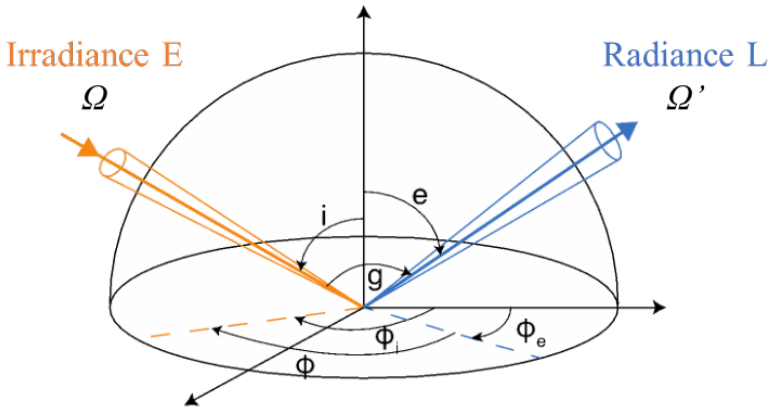

Figure 2 – Radiometric quantities in spherical coordinate (from Labarre (2017)).

Let's introduce a few reflectance-related quantities often used in photometry. First, let's consider an elementary surface uniformly illuminated in the direction Ω' and scattering light in the direction Ω' (Figure 2). We can then define irradiance $dE(i, \phi_i)[Wm^{-2}]$, the radiant flux received by a surface per unit area, and radiance $dL(i, \phi_i, e, \phi_e)[Wm^{-2}sr^{-1}]$, the radiant flux emitted, reflected or transmitted by a surface, per unit area and per unit solid angle.

The bidirectional reflectance distribution function (BRDF), expressed in $[sr^{-1}]$, describes the scattering of a parallel beam of incident light from one direction of the hemisphere into another direction of the hemisphere (Nicodemus et al., 1977). Expressed as the ratio of infinitesimal quantities, it cannot be measured directly. BRDF is controlled by various physical properties of the target surface, such as macroscopic roughness, grain size, porosity, etc. and the interaction between them, making it useful for surface characterization. In addition, it is also used for photometric correction of satellite images, to eliminate the effects of different observation

1. https://batch.libretexts.org/print/Letter/Finished/phys-7488/Full.pdf

geometries (Nagori et al., 2023). Its formula is associated with the radiance and irradiance presented above:

$$\text{BRDF} = \frac{dL(i, \phi_i, e, \phi_e)}{dE(i, \phi_i)} \tag{1.2}$$

BRDF is closely related to another radiometric quantity, the bidirectional reflectance r, also expressed in $[sr^{-1}]$, which is the ratio between the radiance reflected by the surface dL to the irradiance of the incident beam perpendicular to the direction of incidence $dF = dE/\cos i$. Bidirectional reflectance is commonly encountered in the formulation of radiative transfer models.

$$r(i, \phi_i, e, \phi_e) = \text{BRDF}(i, \phi_i, e, \phi_e) \times \cos i \tag{1.3}$$

As these two radiometric quantities cannot be measured directly, they must be determined indirectly using another radiometric quantity. One of these is the bidirectional reflectance factor (BRF, or reflectance factor REFF - according to Hapke (2012)). However, Schaepman-Strub et al. (2006), pointed out a complication: remote sensing measurements often do not align precisely with true bidirectional reflectance properties. Consequently, the data products derived from these measurements must be regarded as approximations to the true bidirectional reflectance of the surface. This discrepancy is mainly due to the instantaneous field of view (IFOV) of the instruments used in remote sensing. Unlike an ideal sensor, which would capture an infinitesimal differential solid angle, the IFOV of most remote sensing sensors is integrated over a relatively wide solid angle of view, affecting the accuracy of measured reflectance values. To overcome some of these problems, sensors need to be designed or configured to restrict the field of view considerably, often using specific optical or mechanical methods, thereby improving measurement quality. Figure 3 shows the measurable and conceptual photometric quantities involved in these processes.

Nevertheless, BRF can still be approximated. It is given by the ratio between the reflected radiation flux of the surface dA and the reflected radiation flux of an ideal, diffuse surface of the same dA under identical viewing geometry and illumination in a single direction. A Lambertian surface considered ideal reflects the same radiation in all directions, and its BRDF is $1/\pi$. Thus, the BRF [unitless] of any surface can be expressed as follows:

$$\text{BRF}(i, \phi_i, e, \phi_e) = \pi \times \text{BRDF}(i, \phi_i, e, \phi_e) \tag{1.4}$$

Spectralon® is commonly used as the ideal, diffuse surface: it's a polytetrafluoroethylene material reflecting 99.9% of light in the visible and near-infrared range, slightly less in the mid-infrared (Figure 4a). It can be machined into a wide variety of shapes for the construction of optical components such as calibration targets, integrating spheres and optical pump cavities for lasers (Georgiev and Butler, 2007). Infragold® is a plate made from a gold-copper alloy that reflects 95% of light between 2 and 20 μm (Figure 4b). These two reference panels are quasi-Lambertian. The most ideal measurement case is that of a dark, clean room with a laser source and detector, i.e., a goniometer in a controlled environment. In this case, the measurement cone has a very small surface area, and the scattering of incoming and outgoing light is minimal. As a result, we are close to a BRF measurement, as the light rays are almost parallel and directional. Essentially, two

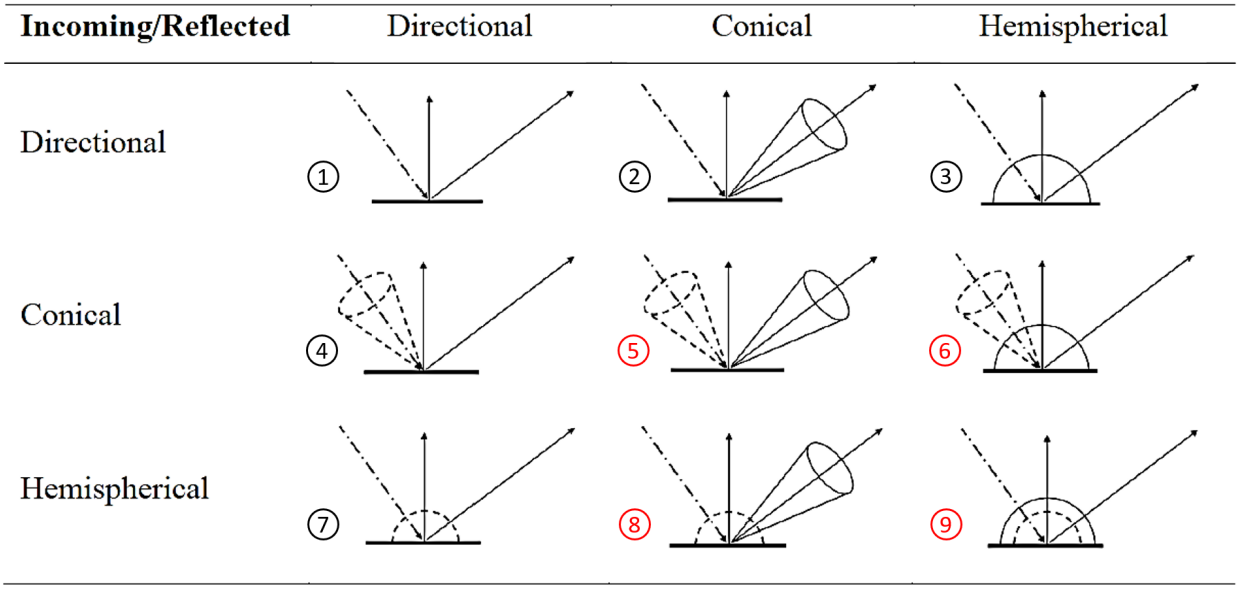

Figure 3 – Relationship between incoming and reflected radiant energy, with the incoming (dashed line) and reflected radiation (solid line) (Wang, 2022). The terminology used to describe reflectance quantities can be found in the works of Nicodemus et al. (1977); Schaepman-Strub et al. (2006). The red circles and numbers correspond to measurable quantities (cases 5, 6, 8, 9), the others (cases 1–4, 7) to conceptual quantities.

measurements are needed to determine the BRF, which is the ratio of the incoming energy to the sensor with the sample and with the Spectralon®.

(a) (b)

Figure 4 – a) Spectralon® and b) Infragold® panels (Labsphere Inc.).

For practical applications beyond the laboratory, most satellite, airborne and field instrument measurement configurations correspond to hemispherical and conical configuration. This captures both the direct and diffuse components contributing to the irradiance field, a critical aspect when deriving various quantities of surface reflectance from raw measurements. These measurements require sophisticated processing to accurately determine the radiance observed at the surface. Several atmospheric correction algorithms have been developed specifically for airborne or spaceborne sensor data. They take into account all atmospheric contributions, which are deciphered from the radiance at the sensor to determine the so-called “surface reflectances”.

For example, the ATCOR (Atmospheric and Topographic Correction) processing chain effectively adjusts sensor-level radiance for path radiance and the adjacency effect (Richter and Schläpfer, 2002). However, it does not correct for hemispheric irradiance, resulting in so-called hemispheric and directional reflectance factor (HDRF) data.

In order to refine these HDRFs, various modeling approaches have been used to eliminate the effects of diffuse illumination, as shown by Lyapustin and Privette (1999); Martonchik (1994); Martonchik et al. (1998). These methods provide data on the bidirectional reflectance factor (BRF). Research by Schaepman-Strub et al. (2006) demonstrates a strong correlation between HDRF and BRF ($r^2 > 0.98$) in most spectral bands of NASA's Multi-angle Imaging Spectro-Radiometer (MISR) sensor and for different viewing angles of all scenes. In our research, the ATCOR system used on Pleiades data is integrated in MAJA, an advanced atmospheric correction framework. On the basis of this information, the Pleiades HDRF data can be considered to be equal to BRF. The integration of MAJA forms a crucial part of our processing pipeline for the Pleiades dataset, which will be detailed in Chapter 2.

In this study, we carefully differentiate between the terms "BRDF", "BRF" and "reflectance factor" (r) in order to clarify the scope and application of each in the context of light scattering and surface characteristic analysis. BRDF is mainly used to discuss the theoretical link between light-scattering behaviors and surface properties. BRF, on the other hand, is used specifically in measurement-related contexts, since all measurable photometric quantities are automatically converted to BRF in practical applications. The reflectance factor is used when addressing the concepts of radiative transfer models, which is a standard term found in various scientific studies (Hapke, 1986; Rahman et al., 1993; Wanner et al., 1995; Roujean et al., 1997).

1.2 Photometric models applied to bare soil

1.2.1 Parametric models

a) Rahman-Pinty-Verstraete (RPV) model

The Rahman-Pinty-Verstraete (RPV) model (Rahman et al., 1993) is a parametric model representing surface anisotropy. The BRDF is decomposed into the amplitude $\rho_0(\lambda)$, which depends on the wavelength and an associated angular field describing the anisotropic behavior of the surface under study. It is the product of three distinct functions: the modified Minnaert function $M(i, e, k)$, the Henyey-Greenstein function $F_{HG}(g, \Theta)$, and the backscattering (hot spot) function $H(\rho_C, G)$, which take into account both the illumination direction and the observation direction. Thus, the RPV model describes the BRDF of a surface as follows:

$$\text{BRDF}(i, e, \phi) = \rho_0 \times M(i, e, k) \times F_{HG}(g, \Theta) \times H(\rho_C, G) \tag{1.5}$$

The modified Minnaert function (Minnaert, 1941) is written as:

$$M(i, e, k) = \frac{\cos^{k-1}(i) \cos^{k-1}(e)}{(\cos i + \cos e)^{1-k}} = (\cos i \cos e(\cos i + \cos e))^{k-1} \tag{1.6}$$

This function controls the shape of the BRF field: bowl-shaped when $k < 1$, bell-shaped when $k > 1$ and 1 for the quasi-Lambertian surface. The Henyey-Greenstein function (Henyey and Greenstein, 1940) describes the relative amount of light scattered in different directions:

$$F_{HG}(g, \Theta) = \frac{1 - \Theta^2}{(1 + 2\Theta \cos g + \Theta^2)^{3/2}} \tag{1.7}$$

with Θ a parameter that controls the amount of light scattered in the backward direction ($0 \leq \Theta \leq 1$) or in the forward direction ($-1 \leq \Theta \leq 0$). There are two versions of the hot-spot function. The one taken from the original article by Rahman et al. (1993) was used in the work of Koukal et al. (2014):

$$H(\rho_0, \rho_C, G) = 1 + \frac{1 - \rho_0}{\rho_C + G} \tag{1.8}$$

A more recent and widespread on is used by Roosjen et al. (2015), as well as by the RAMI (RAdiation transfer Model Intercomparison) initiative [2] and CESBIO-DART team [3]:

$$H(\rho_C, G) = 1 + \frac{1 - \rho_C}{1 + G} \tag{1.9}$$

with the geometrical factor $G = \sqrt{\tan^2 i + \tan^2 e - 2 \tan i \tan e \cos \phi}$. This second version has been extensively tested, and we have found that it adapts very well to our data, whereas the first version has not been sufficiently tested. The parameters are detailed in Table 1.1:

Symbol	Range	Parameter	Description
ρ_0	[0,1]	Amplitude parameter	Intensity of reflectance
k	[0,2]	Anisotropy parameter	Shape of the scattering lobe: $k < 0$ for the bowl shape and $k > 1$ for the bell shape
Θ	[-1,1]	Backscattering parameter	Degree of forward ($0 \leq 1$) and backward scattering ($-1 \leq 0$)
ρ_C	[0,2]	Hotspot parameter	Hotspot effect

Table 1.1 – Description of RPV model parameters (Koukal et al., 2014; Roosjen et al., 2015)

The RPV model has mainly been used for research on vegetation, aerosols and land use classification (Koukal et al., 2014). Its application to bare soil remains very rare. (Roosjen et al., 2015) studied the effects of soil water content on reflectance anisotropy using laboratory goniometer measurements and RPV model inversions. The Discrete Anisotropic Radiative Transfer (DART) software, which we will describe in Chapter 6, uses this model (Gastellu-Etchegorry et al., 2017) and effectively simulates the radiation budget and remote sensing acquisitions of urban and natural landscapes.

2. https://rami-benchmark.jrc.ec.europa.eu/_www/definition.php
3. https://dart.omp.eu/Public/documentation/contenu/documentation/DART_User_Manual.pdf

b) Ross-Thick Li-Sparse (RTLS) model

The RossThick-LiSparse model (RTLS) (Wanner et al., 1995; Roujean et al., 1997) is a parametric model that represents the anisotropy of surfaces, in particular the dense vegetation layer. BRDF is decomposed into three additive terms: isotropic diffusion f_{iso}, volumetric scattering $f_{vol}K_{vol}(i,e,g)$ and a term accounting for shading effects $f_{geo}K_{geo}(i,e,g)$. Thus, the RTLS model describe the surface BRDF as follows:

$$BRDF(i,e,\phi) = f_{iso} + f_{vol}K_{vol}(i,e,\phi) + f_{geo}K_{geo}(i,e,\phi) \tag{1.10}$$

The kernel describing volume diffusion is based on the theory of radiative transfer in plant canopies as illustrated by Ross (2012):

$$K_{vol}(i,e,g) = \frac{\left(\frac{\pi}{2} - g\right)\cos g + \sin g}{\cos i + \cos e} - \frac{\pi}{4} \tag{1.11}$$

with g the phase angle. The kernel, which takes into account shading effects, is based on geometric optics. Consider the intermediate variables:

$$i' = \tan^{-1}\left(\frac{b}{r}\tan i\right) \tag{1.12}$$

$$e' = \tan^{-1}\left(\frac{b}{r}\tan e\right) \tag{1.13}$$

$$\cos g' = \cos i' \cos e' + \sin i' \sin e' \cos\phi \tag{1.14}$$

$$D = \sqrt{\tan^2 i' + \tan^2 e' - 2\tan i' \tan e' \cos\phi} \tag{1.15}$$

$$\cos t = \frac{b}{h}\frac{\sqrt{D^2\left(\tan i', \tan e', \sin\phi\right)}}{\frac{1}{\cos i'} + \frac{1}{\cos e'}} \tag{1.16}$$

In the case of vegetation, the parameters b/r and b/h are the form factors of tree crowns. The LiSparse kernel (Eq. 1.40), derived from Wanner et al. (1995), was developed to model the bidirectional reflectance of vegetation canopies made up of spatially discrete surface objects, such as tree crowns, which cast shadows on the background. For the LiSparse kernel, a sparse set of such objects is assumed.

$$K_{geo}(i,e,g) = O(i',e',t) - \frac{1}{\cos i'} - \frac{1}{\cos e'} + \frac{1+\cos g'}{2\cos e'} \tag{1.17}$$

with $O(i',e',t) = \frac{1}{\pi}(t - \sin t\cos t)\left(\frac{1}{\cos i'} + \frac{1}{\cos e'}\right)$. The RTLS model normally comprises three parameters: f_{iso} (contribution from isotropic diffusion), f_{vol} and f_{geo} which serve as weighting factors for the kernels K_{vol} and K_{geo} which describe volume diffusion (i.e., layered canopy diffusion) and geometric diffusion (i.e., shadow effects), respectively (Koukal et al., 2014). A five-parameter version is also available, with b/r and b/h in addition to those mentioned above.

For the vegetation study, these parameters are fixed ($h/b = 2$ and $b/r = 1$) in line with the MODIS operational processing configuration (Wanner et al., 1997; Koukal et al., 2014). However, when applied to bare soils, our results show that adopting the five-parameter RTLS model significantly improves the fit, compared with the three-parameter version. In this case, both parameters describe soil grains instead of tree crowns, but this conjecture has not been proven. In addition, the RTLS model is known to underestimate reflectance close to the hot spot direction (Lucht et al., 2000; Jiao et al., 2016). Jiao et al. (2016) have developed a method that improves the ability of this model to simulate the magnitude and width of the hotspot effect. It corrects the volumetric diffusion component of the model using an exponential approximation of a physical hotspot kernel, which recreates the magnitude and width of the hotspot using two free parameters (C1 and C2, respectively). The RossThick kernel (K_{vol}) is then replaced by the RossThickChen kernel (K_{RTC}):

$$K_{RTC} = \frac{\left(\frac{\pi}{2} - g\right)\cos g + \sin g}{\cos i + \cos e} \times \left(1 + C_1 e^{-\frac{g}{2}}\right) - \frac{\pi}{2} \tag{1.18}$$

C_1 is related to the magnitude of the hot spot peak, while C_2 defines the half-width of the hot spot, the ratio between canopy height and leaf size (in radian unit).

Table 1.2 gives a full description of the model parameters.

Symbol	Range	Description
f_{iso}	[0,1]	Isotropic scattering contribution
f_{vol}	[0,2]	Volume scattering contribution
f_{geo}	[0,1]	Geometric scattering contribution
h/b	[1,4]	(Vegetation) height of crown center to vertical crown radius ratio
b/r	[1,4]	(Vegetation) vertical to horizontal crown radius ratio
C_1	[0,1]	Magnitude of the hotspot peak
C_2	[0,15]°	Half width of the hotspot peak

Table 1.2 – Description of RTLS model parameters (Koukal et al., 2014; Jiao et al., 2016).

The RTLS model has proved accurate in recreating many types of natural surface, from highly anisotropic snow-covered terrain (Lyapustin et al., 2010) to backscattering surfaces such as those found in vegetation (Schaaf et al., 2002). However, its application to bare soil remains a novelty. An exhaustive literature search showed that only Ceamanos et al. (2013) used the RTLS model to extract the reflectance of Mars' surface from CRISM observations.

1.2.2 Radiative transfer models

Empirical models do not attempt to explain the physical parameters, but provide a mathematical description of the patterns observed in the BRDF. Semi-empirical models are based on the simplified physical principles of geometrical optics and radiative transfer theory.

a) Geometric models

The models in this section were not used in our study. However, they form the basis of the following models or provide a new perspective.

Cierniewski (1987) has designed a mathematical model examining the impact of soil surface roughness on visible and near-infrared reflectance. It is based on the assumption that the reflectance of anisotropic rough surfaces is strongly correlated with the area of shaded soil fragments and therefore depends on soil roughness, illumination and observation geometry. A rough soil surface is simulated using spheres of equal size arranged so that their centers form a square grid on a freely inclined plane. This model converts the bare soil reflectance data obtained for smooth samples into data relating to any natural rough surface states under unlimited illumination, defined by solar altitude, slope angle and orientation of the ground surface to the sun. The main elements of the model are:

- Shadowing coefficient: expresses the proportion of shadowed areas in a given soil surface area, influencing soil reflectance.
- Roughness factor: is defined as the ratio of the surface area of soil aggregates and clods to the total soil surface, it impacts the shadowing coefficient.

Sadeghi et al. (2018) used an analytical radiative transfer model to explore how soil particle size affects soil reflectance. They assumed that soil particles have a narrow size distribution, which allows an average particle size to be assumed. The model divides soil reflectance into surface reflectance and volume reflectance:

- Surface reflectance: is calculated using a modified Stokes radiative transfer model, considering reflections and transmissions through soil particles.
- Volume reflectance: is derived from a beam-tracing model, which takes into account light scattered by particles below the surface.

b) The Shkuratov model

The Skuratov model is a family of empirical models in which the dependence of reflectance on phase angle is explicitly decoupled from the dependence on incidence and emission angles, and thus from topography Kaasalainen and Torppa (2001); Shkuratov et al. (2011); Schr oder et al. (2013). It is also known to use a new set of geometrical configuration (α, β, γ), which are the phase angle, the photometric latitude and longitude. These sets are related to the previously defined set (i, e, ϕ) and to each other as follows:

$$\cos i = \cos\beta \cos(\alpha - \gamma) \tag{1.19}$$

$$\cos e = \cos\beta \cos\gamma \tag{1.20}$$

$$\cos\phi = \frac{\cos\alpha - \cos i \cos e}{\sin i \sin e} \tag{1.21}$$

and conversely,

$$\cos\alpha = \cos i \cos e + \sin i \sin e \cos\phi \tag{1.22}$$

$$\cos\beta = \sqrt{\frac{(\sin(i+e))^2 - (\cos(\varphi/2))^2 \sin 2e \sin 2i}{(\sin(i+e))^2 - (\cos(\phi/2))^2 \sin 2e \sin 2i + (\sin e)^2 (\sin i)^2 (\sin\phi)^2}} \tag{1.23}$$

$$\cos\gamma = \frac{\cos e}{\cos\beta} \tag{1.24}$$

Here we summarize the theory proposed by Shkuratov et al. (2011). The model is written as the product of two terms, the phase function and the disk function: $r_F = A_{eq}(\alpha) D(\mu_0, \mu, \alpha) = A_N f(\alpha) D(\mu_0, \mu, \alpha)$. The equigonal albedo A_{eq} describes the phase dependence of brightness and provides information on the complexity of the light-scattering surface structure. The disk function D describes how reflectance varies on the planetary disk at constant phase angle. Let's take a closer look at these two terms.

Disk function

We consider two well-known disk functions, each normalized at $i = e = \alpha = 0$.

• The parameter-free version of the Akimov function is theoretically derived for an extremely rough, slightly randomly undulating surface:

$$D(\alpha, \beta, \gamma) = \cos\frac{\alpha}{2} \cos\left(\frac{\pi}{\pi - \alpha}\left(\gamma - \frac{\alpha}{2}\right)\right) \frac{(\cos\beta)^{\alpha(\pi-\alpha)}}{\cos\gamma} \tag{1.25}$$

The analysis of light scattering by complex structures leads to the notion of equifinality of a scattering law (Shoshany, 1991), when several structures result in the same scattering law. Subsequently, the Akimov disk function can be rigorously derived not only for totally rough surfaces (Akimov, 1975, 1988; Shkuratov et al., 1994), but also for fractal-like surfaces with the same Gaussian local slopes statistics at each hierarchical roughness level (Shkuratov et al., 2003).

• A semi-empirical version of the Akimov disk function has been developed for the Moon:

$$D(\alpha, \beta, \gamma) = \cos\frac{\alpha}{2} \cos\left(\frac{\pi}{\pi - \alpha}\left(\gamma - \frac{\alpha}{2}\right)\right) \frac{(\cos\beta)^{\eta\alpha(\pi-\alpha)}}{\cos\gamma} \tag{1.26}$$

With the exception of the parameter η, Equation 1.27 is identical to Equation 1.27. It measures the deviation from the pure fractal surface with an infinite number of hierarchical levels.

Phase function in a wide range of phase angles

The equigonal albedo A_{eq} depends only on the phase angle and is directly related to the phase function $A_{eq} = A_N f(\alpha)$. A_N is the normal albedo, and $f(\alpha)$ is the phase function normalized to unity at $\alpha = 0^\circ$. We consider two possible expressions for $f(\alpha)$.

• The empirical formula suggested by Akimov (1988):

$$f(\alpha) = \frac{e^{-\mu_1\alpha} + m_0 e^{-\mu_2\alpha}}{1 + m_0} \tag{1.27}$$

which contains three parameters: μ_1 the parameter associated with surface roughness, m_0 and μ_2 the amplitude and width of the opposition peak, respectively. Determination of these two parameters requires measurements at phase angles of less than 10°.

• Velikodsky et al. (2011) have proposed a more precise expression for the approximation of the phase function of the airless body:

$$A_{eq}(\alpha) = A_N(A_1 e^{-\mu_1 \alpha} + A_2 e^{-\mu_2 \alpha} + A_3 e^{-\mu_3 \alpha}), \quad A_1 + A_2 + A_3 = 1 \tag{1.28}$$

The first term (A_1, μ_1), which has a maximum exponent value, describes the components of the shadowed and unshadowed opposition peaks. The former may be due to the effect of fractality (Shkuratov and Helfenstein, 2001), and the latter to coherent backscatter enhancement (Shkuratov, 1988; Hapke, 2002) and/or lensing effect (Shkuratov, 1983; Trowbridge, 1984). The second term (A_2, μ_2) corresponds to the single particle scattering and the shadow hiding effect in the regolith. It also depends on the albedo due to incoherent multiple scattering between regolith particles (Hapke et al., 1998). The third term (A_3, μ_3) describes the shadow hiding effect on the lunar surface topography (Hapke et al., 1998) and the exponent has a minimum value.

Final expression of the photometric model

The photometric model we are considering is written as follows:

$$A(\alpha, \beta, \gamma, \lambda) = A_n \frac{e^{-\mu_1 \alpha} + m_0 e^{-\mu_2 \alpha}}{1 + m_0} \cos\frac{\alpha}{2} \cos\left(\frac{\pi}{\pi - \alpha}\left(\gamma - \frac{\alpha}{2}\right)\right) \frac{(\cos\beta)^{\eta\alpha(\pi-\alpha)}}{\cos\gamma} \tag{1.29}$$

this equation involves five parameters: $A_n = A_n(\lambda) = A_{eq}(0, \lambda)$ the normal albedo, $m_0 = m_0(\lambda)$, $\mu_2 = \mu_2(\lambda)$, the parameters of the opposition effect, $\mu_1 = \mu_1(\lambda)$ the parameter related to surface roughness, and $\eta = \eta(\lambda)$ which measures the deviation from a pure fractal surface. It should be noted that the constraint of this model requires a wide range of phase angles. In keeping with the tradition, parameter information will also be presented in Table 1.3.

Symbol	Description
A_n	Normal albedo
m_0 and μ_2	Opposition effect parameters
μ_1	Surface roughness parameter
η	Deviation from a pure fractal surface

Table 1.3 – Shkuratov model parameters (Shkuratov et al., 2011).

Unlike the parameters of the previous models, there is no effective range for the parameters, as they have not been found in the literature. On the other hand, if the measurements do not include very small phase angles, we can consider the simplified version:

$$A(\alpha, \beta, \gamma, \lambda) = A_n e^{-\mu_1 \alpha} \cos\frac{\alpha}{2} \cos\left(\frac{\pi}{\pi - \alpha}\left(\gamma - \frac{\alpha}{2}\right)\right) \frac{(\cos\beta)^{\eta\alpha(\pi-\alpha)}}{\cos\gamma} \tag{1.30}$$

It reduces the number of parameters to three: A_n, μ_1 and η. Note that Shkuratov proposes an expression for the normal albedo when the optical and microphysical properties of the medium

are known, i.e., Shkuratov's particle model. Note also that the reflection coefficient can be obtained by dividing Equation 1.31 by $\cos i$:

$$r = \frac{A(\alpha, \beta, \gamma, \lambda)}{\cos i} = \frac{A(\alpha, \beta, \gamma, \lambda)}{\cos \beta \cos(\alpha - \gamma)} \tag{1.31}$$

This is one of several versions of the Shkuratov models (Shkuratov et al., 2011) that interest us because of the presence of a surface roughness parameter. In the context of planetary science photometry, we have also observed the widespread use of the Kaasalainen-Shkuratov model. Although it contains the two principal components, there are different versions of the phase and disk functions. Users can test and interchange them to best describe the BRDF pattern of the planetary surface (Domingue et al., 2016a; Filacchione et al., 2022). Overall, the Shkuratov model and its variants are mainly used for the lunar surface and the surface of small bodies such as comets and asteroids.

d) Monte Carlo models

Monte Carlo simulation is a computational algorithm that uses repeated random sampling to determine the probability of occurrence of a set of outcomes. It is one of the algorithms used in ray tracing, which is developed in Chapter 6. Here we present several works using this technique. Egan and Hilgeman (1978) present a six-flux Monte Carlo model to analyze the reflectance of particle surfaces, taking into account both scattering and absorption effects. Cooper and Smith (1985) proposes a model to assess the effects of macroscopic soil surface irregularities on spectral reflectance. The Monte Carlo approach is applied to track the paths of photons as they interact with an undulating ground surface, taking into account the following key points:

- The soil surface is defined as a periodic function with known variations in height and angle (Figure 5).
- Photons are incident on the soil surface at specified zenith angles, and their paths are tracked until they escape. The model increments counters based on the escape angles of photons.
- Scattering is assumed to be Lambertian, with photons scattered in directions determined by the surface orientation. The model calculates interactions until changes between successive photon packets are minimal.

Parviainen and Muinonen (2009) investigate the effects of volume and surface shadowing in particulate porous media with macro-scale surface roughness using Monte Carlo ray tracing. The bidirectional reflection of these media over the hemisphere is investigated, focusing on fluctuations in reflection caused by both volume shading, due to porosity, and rough surface shading, due to larger surface irregularities (Figure 6).

Lucas et al. (2022) focus on porosity, a feature common to a variety of materials, both natural (e.g., soil, rock) and artificial (e.g., ceramics). These porous structures exist at different scales, from nanometers to millimeters, and affect the appearance of the material, which is particularly relevant in contexts such as computer graphics and remote sensing. They therefore present a numerical analysis of models of porous materials that focuses on the appearance of such materials under the influence of their microscopic structure. At the center of this research is the simulation of the

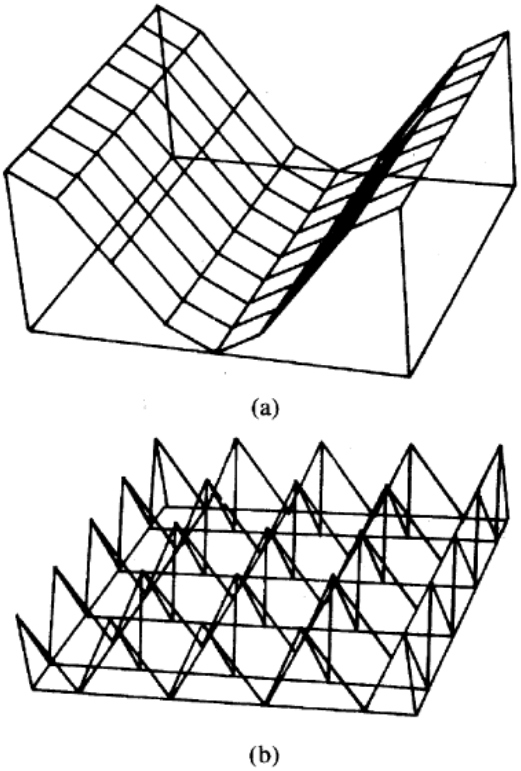

Figure 5 – (a) Simulated "row" periodic surface represented by a cosine height function. (b) Simulated "clump" periodic soil surface represented by a cosine height function varying in x and y directions (Cooper and Smith, 1985).

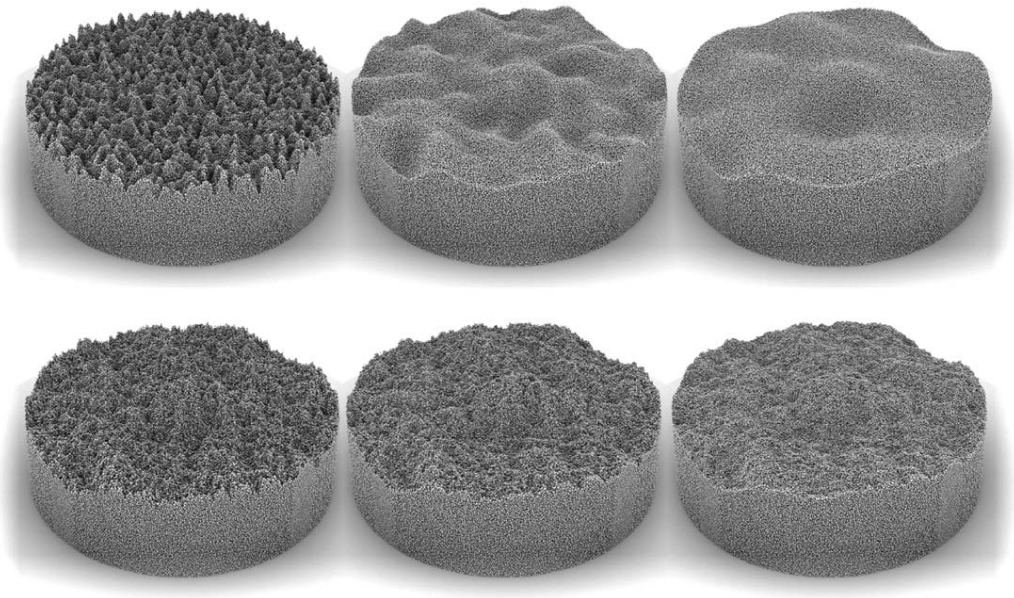

Figure 6 – Media realisations with 4×10^6 particles, with fixed packing volume density. The top row shows the roughness created from Gaussian correlation statistics with increasing correlation length (from left to right). The bottom row shows the roughness from fractional Brownian motion statistics with increasing Hurst exponent (from left to right) (after Parviainen and Muinonen (2009)).

BRDF of materials with different porosity (Figure 7). Simulations are performed by tracing light paths through microscopic structures of opaque spherical aggregates.

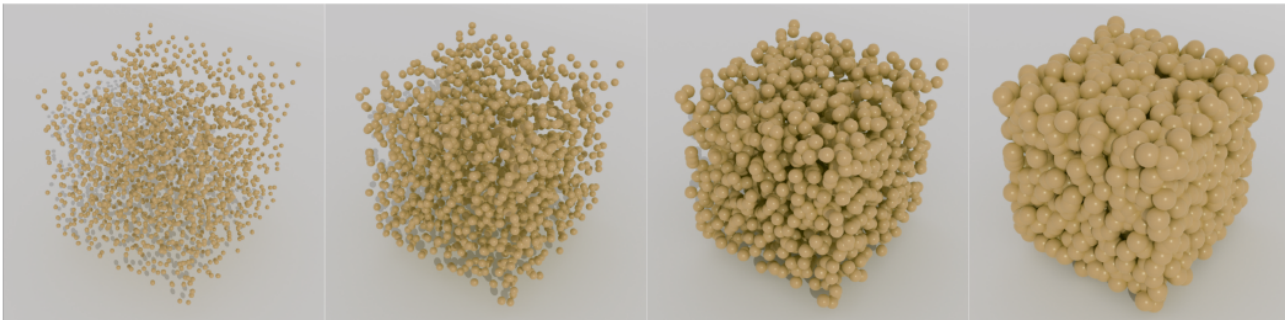

Figure 7 – Visualization of porous material structures. These structures are composed of clusters of mono-dispersed spheres with varying porosity values Lucas et al. (2022).

1.3 The Hapke photometric model

1.3.1 Introduction

The Hapke model aims to solve, using analytical expressions, the radiative transfer equation for a semi-infinite medium composed of irregular, randomly oriented particles whose size is large compared to the wavelength. This model is at the center of our research work for several reasons. First, its ability to predict and/or describe radiometric measurements has been extensively studied. The model can be used in two ways: in direct mode and in inverse mode. In direct mode, the reflectance of a surface with known properties is calculated by assigning values to each of the model's input parameters, and can then be compared to the measured reflectance. In this way, the physical accuracy and absolute precision of the model can be verified. In the inverse mode, an optimization algorithm attempts to minimize a merit function, defined as the difference between measured and modeled reflectance values, by changing the input parameters. Second, since the model contains parameters with a physical implementation, it is validated by comparing the retrieved parameter values with the measured values (Hapke, 2012). Here, we focus on the inverse mode, using multi-angular remote sensing data. We aim to accurately predict the BRDF of a surface from a limited number of measurement configurations and to estimate the value of model parameters to infer the physical and chemical properties of a bare soil.

1.3.2 Decomposition of the Hapke model

The Hapke model is based on the Lommel-Seelinger law, which approximates the scattering properties of dark particulate surfaces such as lunar regolith (Hapke and van Hoen, 1963). The bidirectional reflectance is given by Equation 1.32.

$$r_{LS} = K_{LS} \frac{\cos(i)}{\cos(i) + \cos(e)} p(g) \tag{1.32}$$

where K_{LS} is a constant and $p(g)$ is the phase function. The Hapke model introduces the parameter ω as the single scattering albedo. In its most popular version, $p(g)$ is represented by the two-parameter Henyey-Greenstein phase function. The model may also include some additional terms: the porosity function K, the Shadow Hiding Opposition Effect (B_{SHOE}) and Coherent Backscatter Opposition Effect (B_{CBOE}), and the shadowing function S. This results in the general formula of

Equation 1.34 (Hapke, 2012).

$$r(i,e,g) = K\frac{\omega}{4\pi}\frac{\mu_{0e}}{\mu_{0e}+\mu_e}[p(g)B_{SHOE}(g) + H(\frac{\mu_{0e}}{K})H(\frac{\mu_0}{K}) - 1]B_{CBOE}(g)S(i,e,g) \tag{1.33}$$

with μ_{0e} and μ_e the modified cosines of incidence and emergence angles (also called cosines of the effective angle, to account for the effect of roughness). The term $H(x)H(y) - 1$ represents the Isotropic Multiple Scattering Approximation (IMSA), with H the Ambartsumian–Chandrasekhar function that accounts for the bidirectional reflectance of a semi-infinite medium of isotropic scatterers (Hapke, 2002) (Equation 1.34):

$$H\left(x\right) = \left[1 - wx\left(r_0 + \frac{1-2r_0x}{2}\ ln\frac{1+x}{x}\right)\right]^{-1} \tag{1.34}$$

with

$$r_0 = \frac{1\ -\ \sqrt{1-w}}{1+\sqrt{1-w}} \tag{1.35}$$

Another option is to replace it with the modified IMSA called Anisotropic Multiple Scattering Approximation (AMSA), which is more accurate but imposes more computational constraints (Hapke, 2012). As a result, this version of the model is less popular. Although the AMSA model was later developed to improve performance, it is still debatable which approach is more appropriate for soils. In practice, we rarely see the full implementation of Equation 1.33. According to Nagori et al. (2023), the accurate determination of photometric parameters is very difficult and most cases impractical. This is due to the mathematical coupling of parameters in model inversion as well as the limited availability of phase angle ranges in data sets. Therefore, depending on data conditions and available computing power, some factors can be omitted by setting them to either zero or unity. The details of the various terms and parameters are presented in the following chapters.

a) Single scattering albedo (SSA)

The single scattering albedo ω [unitless] is the probability that a photon incident on a particulate medium will be scattered rather than absorbed (Hapke, 2012). $\omega \in [0, 1]$ and is written as follows:

$$\omega = \frac{S}{E} = \frac{S}{S+A} \tag{1.36}$$

where S, A and E are the volume scattering, absorption and extinction coefficients [m^{-1}]. The SSA does not depend on the measurement conditions, but only on the optical behavior of the particles (Domingue et al., 2016a; Zhou et al., 2021). It can be determined either by inversion of the Hapke model or by an analytical formula based on the optical properties of the soil grains (Hapke et al., 1998; Pilorget et al., 2016).

What controls the SSA? According to Hapke et al. (1998), the influencing soil properties are the chemical composition of the particles, which determines the absorption coefficient, and the microstructure of the particles (grain size and shape). Shepard and Helfenstein (2007) state that it could be related to soil compaction, which is assessed by soil density. It has also been reported

that ω decreases with increasing absorption coefficient and particle size (Fernando et al., 2016; Gao et al., 2021; Sheng et al., 2024). The single scattering albedo of soils composed of fine grains tends to be higher than that of soils composed of large grains (Johnson et al., 2013).

In terms of application, SSA allows differentiation of constituents in a powder intimate mixture by identifying their chemical and physical properties (Cord et al., 2005). Thus, it can be applied to spectral decomposition and content extraction of mixed powders (Zhou et al., 2021). Moreover, it is the best constrained parameter (Johnson et al., 2013) and the least affected by the choice of other model parameters (Shepard and Helfenstein, 2007).

Since SSA has a physical meaning, it is inevitably intertwined with other model parameters is inevitable, so that their variation is likely to affect its value. For example, Shepard and Helfenstein (2007) suggest that surface roughness and porosity are negatively correlated with SSA, which determines the overall intensity of the BRDF curve.

b) Phase function

The phase function of a particle is the probability that a photon incident in one direction will be scattered in another direction, forming a phase angle g with the direction of incidence (Sharma, 2015). It varies with the wavelength and the physical properties of the particle. It depends on the absorption of the particle and how the light interacts with external and internal structures (Sato et al., 2014; Pilorget et al., 2016). These authors report that the phase function, SSA and the macroscopic roughness are wavelength dependent.

One of the most commonly used phase functions in radiometry is the Henyey-Greenstein (HG) function. It has a single parameter ξ and is generally applied to data with a limited number of measurements or to models with many poorly constrained parameters.

$$p(\xi, g) = \frac{1 - \xi^2}{(1 + 2\xi \cos g + \xi^2)^{3/2}} \tag{1.37}$$

The one-parameter HG phase function varies from completely forward scattering ($\xi = 1$) to completely backscattering ($\xi = -1$) to isotropic scattering ($\xi = 0$) (Golish et al., 2021). The azimuth has a strong effect on ξ: the closer it is to the principal plane, the better the estimate (Schmidt and Fernando, 2015).

The two-parameter HG phase function is also widely used. It has two parameters, b and c_{og}, which are related to ξ by the formula $\xi = -bc_{og}$.

$$p(b, c_{og}, g) = \frac{1 + c_{og}}{2} \frac{1 - b^2}{(1 - 2b \cos g + b^2)^{3/2}} + \frac{1 - c_{og}}{2} \frac{1 - b^2}{(1 + 2b \cos g + b^2)^{3/2}} \tag{1.38}$$

The parameter b controls the asymmetry of the scattering. A value close to 0 indicates isotropic scattering, while a value close to 1 indicates the propagation of the scattered light along a preferential direction. The parameter c_{og} controls the distribution of the scattered light. A value of c_{og} greater than 0 indicates predominant backscattering, while a negative value indicates predominant forward scattering (Hapke, 2012). Apart from Equation 1.38, some authors (Souchon et al., 2013; Schmidt and Fernando, 2015; Pilorget et al., 2016) prefer to use another version of the

two-parameter HG phase function:

$$p(b,c,g) = (1-c)\frac{1-b^2}{(1+2b\cos g+b^2)^{3/2}} + c\frac{1-b^2}{(1-2b\cos g+b^2)^{3/2}} \tag{1.39}$$

The value interpretation for b remains the same, while $c = (1+c_{og})/2$. As a result, a value greater than 0.5 indicates predominant backscattering and vice versa. Otherwise, c is reported to be wavelength dependent (Grumpe et al., 2014). Plotting c (or c_{og}) as a function of b results in a “hockey-stick diagram” or a "b-c plot" (Figure 8) that identifies the soil grain type based on the location of the soil sample on the graph (McGuire and Hapke, 1995; Souchon et al., 2013): grain shape, opaqueness, micro-roughness and porosity. Sheng et al. (2024) found a positive logarithmic correlation between b, c and the grain size (limited to 800-1500 nm). Hapke (2012) proposed an empirical relationship linking b and c_{og}:

$$c_{og} = \left(\frac{0.05}{b-0.15}\right)^{\frac{3}{4}} - 1 \tag{1.40}$$

Both parameters have been derived for a variety of planetary surfaces (Ciarniello, M. et al., 2015; Li et al., 2019; Belgacem et al., 2021; Hess et al., 2021).

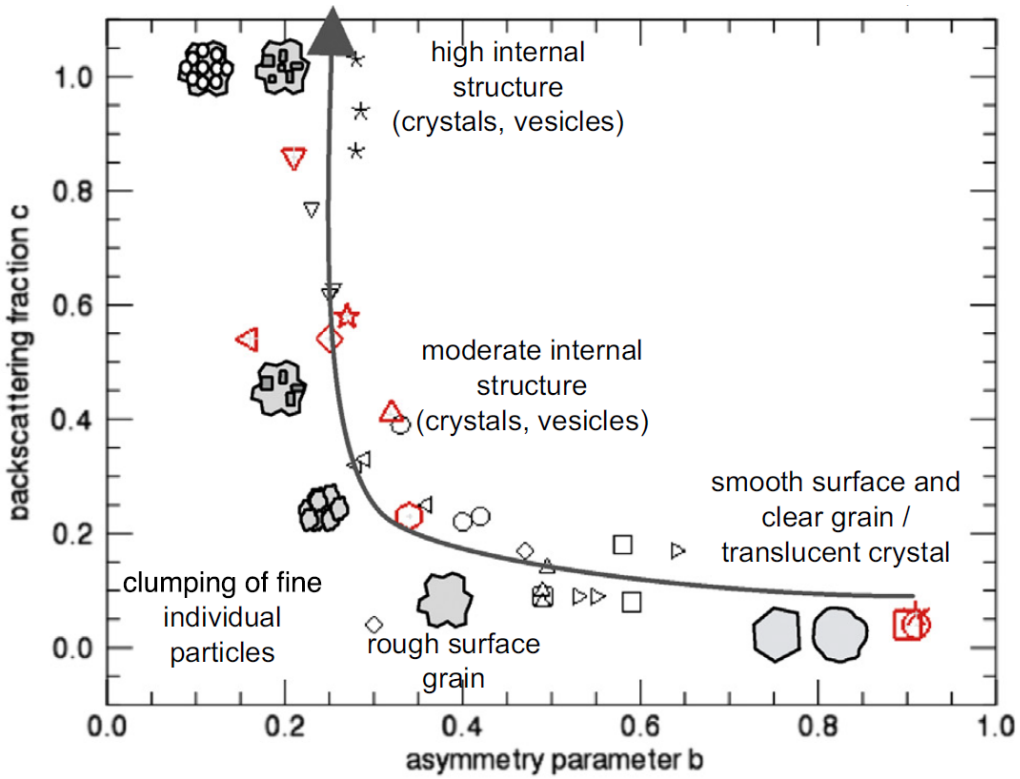

Figure 8 – Hockey-stick diagram (Fernando et al. (2016), adapted from McGuire and Hapke (1995); Souchon et al. (2011).

In addition to these two phase functions, some people use a three-parameter HG phase function:

$$p(b,c_{og},g) = \frac{1+c_{og}}{2}\frac{1-b_1^2}{(1-2b_1\cos g+b_1^2)^{3/2}} + \frac{1-c_{og}}{2}\frac{1-b_2^2}{(1+2b_2\cos g+b_2^2)^{3/2}} \tag{1.41}$$

In this expression, the first term describes the backward lobe and the second the forward

lobe; the relative strengths of the lobes are determined by c_{og}, and their shapes by b, or b_1 and b_2. The parameters c_{og}, b_1 and b_2 are related to ξ by the formula $\xi = -\frac{1+c_{og}}{2}b_1 + \frac{1-c}{2}b_2$ (Hapke, 2012). Nevertheless, although this phase function is the most accurate, the improvement is marginal and not sufficient to justify a third parameter (Hartman and Domingue, 1998). For this reason, it remains unpopular and features in two works of Spjuth et al. (2012); Jost et al. (2013) out of hundreds of research papers using the Hapke model. Another phase function based on second-order Legendre polynomials has been proposed in the literature (Pinty et al., 1989; Jacquemoud et al., 1992; Wu et al., 2009; Domingue et al., 2016a; Zhou et al., 2021):

$$p(b', c', g) = 1 + b' \cos g + c'(3\cos^2 g - 1)/2 \tag{1.42}$$

However, their physical interpretation is either ambiguous or non-existent.

c) Opposition effect

The opposition effect (also known as opposition surge) refers to a sharp increase in the intensity of light scattered by a surface close to the zero-phase angle around the camera shadow. It is observed on soils and vegetation of the Earth, and on most bodies in the Solar System (Figure 9). It can be explained by two mechanisms (Hapke, 1986): Shadow hiding and Coherent backscattering opposition effect (SHOE). Shadow hiding is expected to occur in absorbing media, where multiple scattering plays a less significant role compared to highly reflective materials, such as aluminum oxide particles. In contrast, coherent backscattering becomes more important in such reflective materials, as it enhances the backscattering effect due to the constructive interference of light rays following reciprocal paths (Kar et al., 2016).

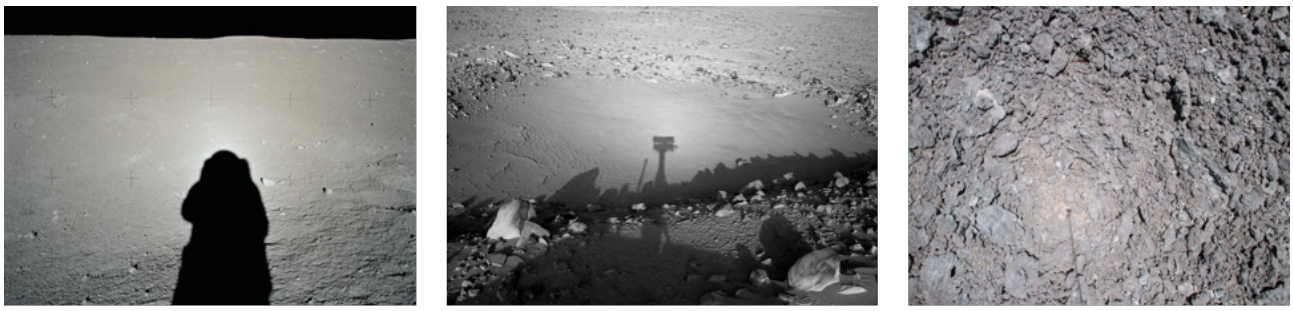

Figure 9 – Opposition effect on various planetary surfaces. a) Apollo 11 landing site on the Moon (image AS11-40-5882 [4]); b) Spirit rover on Mars [5]; c) Asal-Ghoubbet rift (Republic of Djibouti).

- **Shadow Hiding Opposition Effect (SHOE)**

Large shadows are generally observed on rough surfaces at high phase angles. When switching to low phase angles, the hidden slope and the bottom of the relief are revealed, resulting in increased radiance in the direction of the sensor (Figure 10). This phenomenon, known as Shadow Hiding Opposition Effect (SHOE), is considered the main factor contributing to the opposition peak for phase angles below 20°.

5. https://www.nasa.gov/history/alsj/a11/images11.html
5. http://pancam.sese.asu.edu/pancam_instrument/images/Hollow.jpg

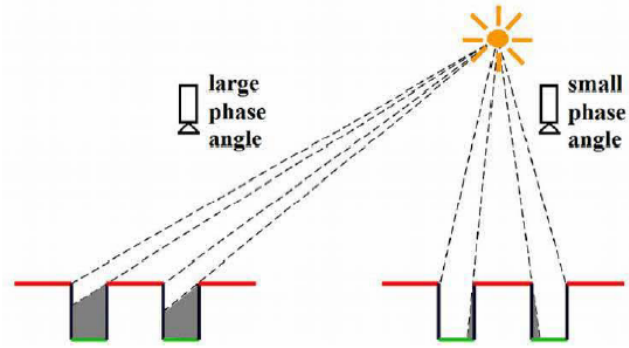

Figure 10 – Schematic representation of the Shadow Hiding Opposition Effect (Wöhler, 2011).

In Equation 1.43, B_{SHOE} which controls the opposition effect depends on two parameters, the width of the opposition peak h_S and its amplitude B_{S0}.

$$B_{SHOE}(g) = 1 + B_{S0}B_S(g) \tag{1.43}$$

$$B_S(g) = \left(1 + \frac{1}{h_S}\tan\frac{g}{2}\right)^{-1} \tag{1.44}$$

According to Hapke (2012), h_S is proportional to the product of the porosity factor K and the filling factor ϕ_f.

$$h_S = \epsilon K(\phi_f)\phi_f \tag{1.45}$$

with ϵ a proportionality constant that depends on grain shape and size distribution. h_S lies in the range $[0, +\infty)$. If the particles are larger than the wavelength and have a narrow size distribution, ϵ is equal to $3/8$. However, according to Bachmann et al. (2017); Eon et al. (2018), ϵ is equal to $(3/8)^{(3/2)}$. The higher h_S, the more compact the surface (Belgacem et al., 2021); conversely, the lower h_S, the more porous the surface, with a less uniform grain size distribution (Johnson et al., 2013). The grain size distribution, which can be derived from h_S, provides information on the ratio between the largest and smallest grain in the regolith, but not the actual size (Tatsumi et al., 2018). Gunderson et al. (2007) reported that the opposition effect broadens with wavelength. Therefore, in the context of SHOE theory, the surface appears to be less porous at longer wavelengths. In contrast, Shkuratov et al. (2007) who carried out laboratory measurements on various soil samples, found no spectral variation in the width of the opposition effect.

It has been shown that the magnitude of the opposition effect B_{S0} is linked to the opacity of the particles (Hapke, 2012) but also to their composition and microstructure (Helfenstein et al., 1997). In theory, a value of 1 means that particles are opaque and all light is scattered (Johnson et al., 2013); a value of 0 means semi-transparent particles and a porous medium. For example, opaque particles with iron inclusions cast shadows and produce high values of B_{S0}, while transparent particles allow light to penetrate the medium and produce low values of B_{S0}. Therefore, low values of B_{S0} are expected to be associated with large values of c (Shepard and Helfenstein, 2007).

h_S and B_{S0} are higher for dry soil, indicating a wider and stronger opposition effect (also called opposition surge). Jost et al. (2013) indicated that both were linked to soil compaction. Studying the

opposition effect is often presented as the best way to determine the state of surface compaction or bulk porosity (Shepard and Helfenstein, 2007). However, in practice, it is very difficult to acquire low phase angle radiometric measurements in the laboratory or in the field, as the sensor shadow obscures the surface. Therefore, in the absence of such measurements, there is no way to constrain h_S and B_{S0}, and the expressions for B_{SHOE} are therefore fixed at unity (Domingue et al., 2016a). Fernando et al. (2013) then reported that there was no change in the determination of the other parameters (ω, b, c, and $\overline{\theta}$).

- **Coherent Backscattering Opposition Effect (CBOE)**

Incident radiation can undergo multiple scattering in the particulate medium before exiting. When a ray follows one path, another part of the wavefront may follow the same path in the medium, but in the opposite direction (Figure 11), resulting in an increase in brightness due to the reflected light combining coherently with the emitted light. This is called the Coherent Backscattering Opposition Effect (CBOE).

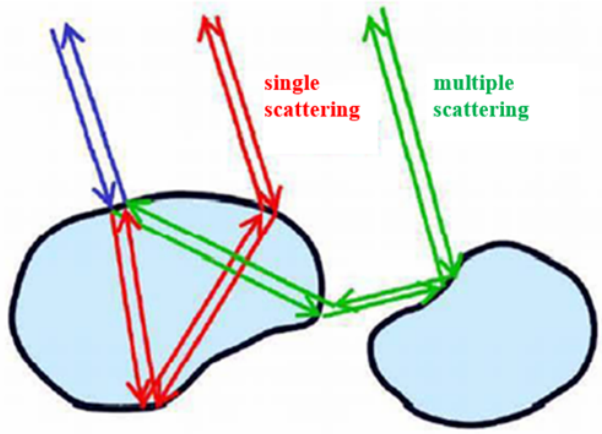

Figure 11 – Schematic representation of the Coherent Backscattering Opposition Effect (Wöhler, 2011).

This phenomenon is often neglected because SHOE dominates for phase angles above 3° and CBOE only has a significant effect for very small phase angles below 3° (Helfenstein et al., 1997; Hapke, 2012). Consequently, the term B_{CBOE} is often omitted in the absence of measurements for such low phase angles. B_{CBOE} is also a function of the width h_c and amplitude B_{C0} of the opposition peak contributing to the CBOE.

$$B_{CBOE}(g) = 1 + B_{C0}B_C(g) \tag{1.46}$$

The expression for $B_C\,(g)$, which contains h_c, is complex and will not be detailed here. We'll just mention that h_c is wavelength dependent and the mean free path of photons in the scattering volume (Hapke, 2012). Indeed, we have found no article giving physical meaning to B_{C0}. Parameter degeneracy can also occur when inverting the Hapke model on data acquired at phase angles below 5°. This is because the model parameters are not independent and interactions can occur (Fernando et al., 2016).

When implementing the two opposition effect terms, it is difficult to distinguish between CBOE and SHOE by model inversion (Hapke, 2012). Setting B_{CBOE} to unity does not completely

eliminate the effects of CBOE. Therefore, the SHOE parameters are a mixture of the two types of backscattering (Sato et al., 2014). Hapke (2002) suggested to use circularly polarized observations to constrain the opposition effect, but this has not been studied in depth. Some authors have used a single set of parameters B_0 and h for both opposition effects (Gunderson et al., 2007; Sato et al., 2014), with B_0 eventually exceeding unity to account for the CBOE. Several studies include these parameters to match the solar phase curve of dark bodies with strong opposition effect, although they are not physical (Simonelli et al., 1999).

d) Shadowing function and roughness parameter

A natural rough surface is made up of randomly oriented facets that cast shadows when illuminated. There are two types of shadow: tilted and projected. The first phenomenon occurs when the angle between the normal vector of some facets and the direction of the incident light is greater than 90°, so they are not illumined. The second occurs when the facets other than those of interest are in the path of illumination and block the incident radiation. The reflectance must therefore be corrected for this roughness-induced shading phenomenon.

According to Hapke (2012), the bidirectional reflectance of a rough surface is the product of the reflectance of the macroscopically smooth surface, at an effective angle of incidence and an effective angle of emergence, and the shadowing function. To use this function, several assumptions have to be made: (1) the size of the facets is large compared to the wavelength, so that the laws of geometrical optics apply; (2) the facets are described by a two-dimensional slope distribution function $a(\vartheta, \varphi)$, where ϑ is the angle between the normal to the facet and the vertical, called the slope angle, and ξ is the azimuth angle of the facet normal; (3) the slope distribution function $a(\vartheta, \varphi)$ is isotropic, i.e., independent of the azimuth of the facet normal φ, so it is reduced to $a(\vartheta)$; (4) the roughness is characterized by the mean slope angle of the facets $\overline{\theta_M}$, which is assumed to be small; and (5) multiple scattering between facets is negligible. The full formula for the shadowing function is complex and involves a large number of intermediate functions, so it will not be presented here. Instead, it can be found in Hapke (1984) or Shiltz and Bachmann (2023).

The shadowing function S includes the photometric roughness parameter $\overline{\theta}$, defined as the mean slope angle integrated over all scales from grain size to local topography. The lower limit depends on the physics of radiative transfer, but is typically several times the mean interparticles distance, which is on the order of 100 to 1000 μm. Meanwhile, the upper limit is determined by the field of view of the detector, which determines the ground sample distance (GSD) on the surface: in astronomy, it is typically a few decimeters to a few kilometers (Hapke, 2012). The length scale and physical meaning of this parameter remains ambiguous (Shiltz and Bachmann, 2023), and a number of authors have attempted to clarify this issue. Shepard and Helfenstein (2007) explored this issue further and showed that the millimeter scale is the only one with any significant roughness. Belgacem et al. (2021) showed that the roughness parameter corresponds to the smallest scale that can produce shadows. Fernando et al. (2013) added that it is mainly related to microstructure. Another paper identified this parameter as a measure of the shading produced by the particles Pilorget et al. (2016), which would depend not only on the distribution of the facets, but also on their transparency and scattering behavior. And since $\overline{\theta}$ is related to the surface morphology, it does not depend on the wavelength, unlike the other parameters (Protopapa et al., 2020). Finally, (Shiltz and Bachmann, 2023) pointed out a flaw in the interpretation of the Hapke

roughness parameter in previous works when comparing it with that measured in the field, and proposed an alternative roughness correction factor.

When inverting the Hapke model, it is not possible to constrain the roughness parameter from the disk-integrated phase function over a small range of phase angles (Helfenstein and Veverka, 1989). The effects of SSA and $\overline{\theta}$ on soil reflectance can only be separated with photometric data acquired at phase angles above 50° (Fernando et al., 2015). Fernando et al. (2013) report that observations ranging from small phase angles to phase angles above 90° are required to accurately determine photometric roughness. The angle of incidence has a significant effect on the surface roughness estimate: the larger it is, the better the estimate of $\overline{\theta}$. Therefore, sampling at high incidence angles is strongly recommended for laboratory, airborne or spaceborne observations (Schmidt and Fernando, 2015). For laboratory and planetary observations not too close to the limb or terminator, roughness can be assumed to be unimportant, so $\overline{\theta}$ can be set to zero (Hapke, 2012).

The full formulation for the shadowing function is presented. It should be noted that this function is the most complicated part of the Hapke model. Its uses will increase the calculation time considerably. Firstly, it requires the use of the cosines of the effective angle, which appears in the Lommel-Seelinger and Ambartsumian–Chandrasekhar functions, replacing the traditional cosines of the incidence and emergence angles. However, these cosines do not exist in the shadowing function. The formulae for them are Equations 1.47 and 1.48:

$$\mu_{0e} = \begin{cases} \chi(\overline{\theta})[\cos i + \sin i \tan\overline{\theta}\frac{\cos\phi E_2(\overline{\theta},e)+\sin^2(\phi/2)E_2(\overline{\theta},i)}{2-E_1(\overline{\theta},e)-(\phi/\pi)E_1(\overline{\theta},i)}] & \text{when } i < e \\ \chi(\overline{\theta})[\cos i + \sin i \tan\overline{\theta}\frac{E_2(\overline{\theta},i)-\sin^2(\phi/2)E_2(\overline{\theta},e)}{2-E_1(\overline{\theta},i)-(\phi/\pi)E_1(\overline{\theta},e)}] & \text{when } i \geq e \end{cases} \tag{1.47}$$

$$\mu_{0e} = \begin{cases} \chi(\overline{\theta})[\cos e + \sin e \tan\overline{\theta}\frac{E_2(\overline{\theta},e)+\sin^2(\phi/2)E_2(\overline{\theta},i)}{2-E_1(\overline{\theta},e)-(\phi/\pi)E_1(\overline{\theta},i)}] & \text{when } i < e \\ \chi(\overline{\theta})[\cos e + \sin e \tan\overline{\theta}\frac{\cos\phi E_2(\overline{\theta},i)-\sin^2(\phi/2)E_2(\overline{\theta},e)}{2-E_1(\overline{\theta},i)-(\phi/\pi)E_1(\overline{\theta},e)}] & \text{when } i \geq e \end{cases} \tag{1.48}$$

with the associating terms:

$$\chi\left(\overline{\theta}\right) = \frac{1}{\sqrt{1+\pi\tan^2\overline{\theta}}} \tag{1.49}$$

$$E_1\left(\overline{\theta},x\right) = \exp\left(-\frac{2}{\pi}\cot\overline{\theta}\cot x\right) \tag{1.50}$$

$$E_2\left(\overline{\theta},x\right) = \exp\left(-\frac{1}{\pi}\cot^2\overline{\theta}\cot^2 x\right) \tag{1.51}$$

Now we will move on to the shadowing function:

$$S(i,e,\phi,\overline{\theta}) = \begin{cases} \frac{\mu_e}{\eta(e)}\frac{\mu_0}{\eta(i)}\frac{\chi(\overline{\theta})}{1-f(\phi)+f(\phi)\chi(\overline{\theta})[\mu_0/\eta(i)]} & \text{when } i < e \\ \frac{\mu_e}{\eta(e)}\frac{\mu_0}{\eta(i)}\frac{\chi(\overline{\theta})}{1-f(\phi)+f(\phi)\chi(\overline{\theta})[\mu_0/\eta(e)]} & \text{when } i \geq e \end{cases} \tag{1.52}$$

with $\mu_0 = \cos i$, $\mu = \cos e$ and several associated terms:

$$\eta(x) = \chi\left(\overline{\theta}\right)\left[\cos x + \sin x \tan\overline{\theta}\frac{E_2\left(x,\overline{\theta}\right)}{2 - E_1\left(x,\overline{\theta}\right)}\right] \tag{1.53}$$

$$f(\phi) = \exp\left(-2\tan\frac{\phi}{2}\right) \tag{1.54}$$

e) Porosity

The reflectance of a particulate medium with a grain size larger than the wavelength also depends on the porosity of the soil, i.e., the voids between the particles (Hapke, 2008). For this reason, a porosity correction factor K, which depends on the filling factor ϕ_f (the amount of regolith volume filled by material) or equivalently on the porosity P ($\phi_f = 1 - P$), has been added to the model. The porosity can either be obtained by the inversion of the Hapke model or an independent formula (Kar et al. (2021)). The relationship between the porosity correction factor and the filling factor is shown in Equation 1.16.

$$K = \frac{-\ln(1 - 1.209\phi_f^{2/3})}{1.209\phi_f^{2/3}} \tag{1.55}$$

Physically, both K and h_S should depend on the surface porosity and should therefore be related. From Helfenstein and Shepard (2011) and Buratti et al. (2022), we have:

$$K = 1.069 + 2.019h_S + 0.577h_S^2 + 0.062h_S^3 \tag{1.56}$$

Regarding the effect of this component on the BRDF curve, most models predict that for a single material, reflectance increases as density increases (or porosity decreases). This is an explicit result of the Hapke model, which predicts an increase in reflectance with increasing filling factor for all albedos except the highest ($\omega > 0.99$). This has been consistently observed in the laboratory, whether the increase in density is due to a decrease in particle size or to an increase in material packing density (Bachmann et al., 2014). However, Hapke (2012) found out that this is only true for homogeneous soil samples with $\phi_f = \frac{\pi}{6}/(1 + \frac{\lambda}{D})^3$, where λ is the wavelength and D is the grain size or diameter. The reflectance decreases when the sample is pressed to a fill factor above this threshold. This was confirmed by a series of experiments with different sand samples (Bachmann et al., 2014). In addition, particulate soils with different porosities produce different opposition effects. The larger the filling factor, the narrower the peak (Ciarniello et al., 2014).

Initial results showed that porosity had a weaker effect on bright surfaces than on dark surfaces (Hapke, 2008). Helfenstein and Shepard (2011) added that porosity and possibly surface roughness could be retrieved on low to moderate albedo surfaces, but not on high albedo surfaces. By measuring different samples, Kar et al. (2016) confirmed that porosity has little effect on the reflectance of a high albedo surface with particle sizes comparable to the wavelength. On the other hand, the porosity factor was only useful for medium to high albedo soils, otherwise its effect cannot be decoupled from SSA, so it can be omitted (Ciarniello et al., 2017; Li et al., 2019). In addition, Sato et al. (2014) argued that accurate determination of the filling factor is only possible when observations are made at high emission angles for highly reflective materials.

The filling factor ϕ_f is influenced by soil density, grain size, and roughness (Eon et al., 2018). Its interactions with other parameters such as porosity have been documented by Fornasier et al. (2015). It is indeed involved in the opposition effect and multiple scattering formulae, which affects the SSA.

1.3.3 Hapke model parameters summary

The full description of the Hapke model parameters is listed in Table 1.4. In our work, considering the data condition (Chapter 2), we mainly use either the 4 or 6-parameter Hapke model, both containing ω, $\overline{\theta}$, b and c. Specifically in the 6-parameter model, we use the parameters h and B_0, which include the width and amplitude of the opposition effect, but mostly the SHOE. They take the range [0,1].

1.3.4 Other characteristics of the Hapke model

With regard to wet soil

All the points we have mentioned refer to the application of the Hapke model to dry soil and regolith. On the other hand, the interaction between wet soil and incident light proved to be very different. Nevertheless, attempts have been made to quantify to which parameters the Hapke model is most sensitive. The most important factor would be SSA, as it is closely related to the intensity of outgoing light. It is the most closely correlated with soil moisture content (SMC) of all parameters, and decreases as SMC increases, as the darkening effect becomes more apparent (Zhang et al., 2020; Gao et al., 2021). The main reason for this is that changing the medium surrounding the particles from air to water reduces their relative refractive index and thus increases the average degree of forwardness of scattering as determined by the asymmetry parameter. As a result, incident photons have to scatter more times before re-emerging from the medium and are therefore more likely to be absorbed (Twomey et al., 1986).

In addition to the pronounced effect on SSA, the porosity would increase and the shape of the phase function would change significantly, favoring forward rather than backward scattering (Gunderson et al., 2007). Pommerol et al. (2013) agreed with this observation, stating that the introduction of liquid water, even in relatively small amounts, results in the disappearance of the backscattering peak and the appearance of a forward-scattering peak whose intensity increases with the amount of water introduced. In addition, specular reflections only appear when water is present in sufficient quantities to form to form a film on the surface of the sample. If there is enough water to form a thick and flat film, the specular peak is very narrow. If the amount of water is less, the liquid film will conform to the topography of the underlying grains, resulting in a very broad specular peak. To better characterize the wet soil in both backward and forward scattering, some authors (Sun et al., 2016; Gao et al., 2021; Ding et al., 2022) have used the SOILSPECT model (Jacquemoud et al., 1992), which is a variant of the Hapke model with a different phase function: the sum of two Legendre polynomials with four parameters.

Sensitivity analysis

Sensitivity analysis is a estimate of how the output and the target variables are affected by changes in other input variables. For a complex model with interdependent parameters such as the Hapke model, we can see the need to carry out this type of analysis. Thanks to Labarre et al. (2017), we can confirm what we have mentioned and notice some salient features of the model. In their implementation of the Hapke model, h_S and B_0 are generally attributed to the opposition effect; h_S is closely linked to P by Equation 1.14, so their contribution will be rather similar and h_S is omitted from the global sensitivity analysis.

Based on Figure 12, SSA and photometric roughness contribute the most to the global sensitivity analysis, indicating that they are the two most influential input parameters of the Hapke model over a wide range of phase angles. The contribution of the other parameters to the BRDF is less than 10% or limited to small phase angles (±30°) (Labarre et al., 2017). The contribution of θ is more pronounced at phase angles > 30°, while b and c become more prominent at phase angles < 30°. The contribution of the porosity P is almost the same everywhere and the contribution of B_0 is almost non-existent. We can also see the influence of each parameter on the other. At a glance, it is easy to see that the interaction between ω, b and c is significant at low phase angles and ω, θ at higher phase angles.

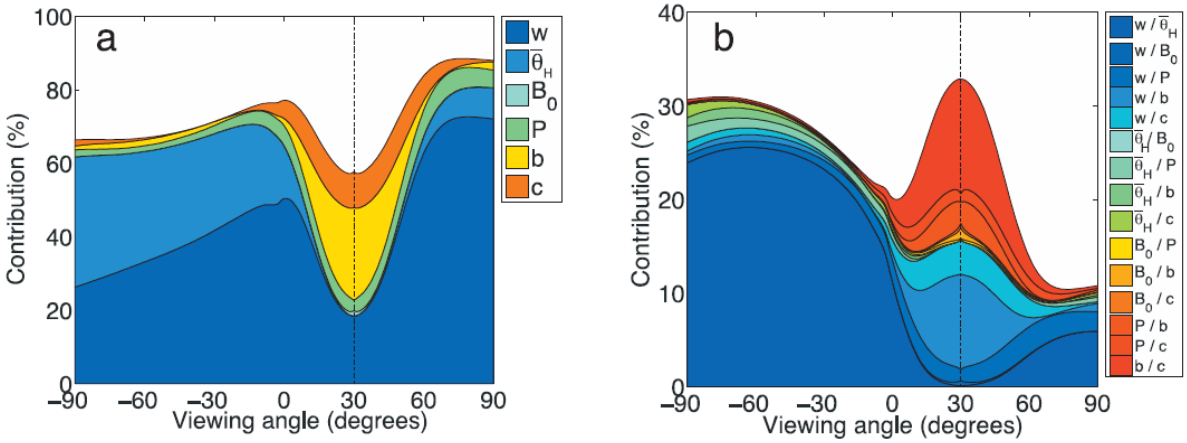

Figure 12 – Sensitivity analysis of the Hapke model in the principal plane. (a): contribution of the parameters; (b): contribution of the interactions. The dashed line represents the direction of the incident light (Labarre et al., 2017).

1.3.5 Key points

In summary, there are a number of important points to be made about the Hapke model:

- For observational data, the phase angles should have some values above 90° and also cover a wide range. The difference between the lowest and the highest value should be about 50° or more. These factors are needed to better constrain the model parameters (Fernando et al., 2016).
- The azimuthal plane is important for constraining the photometric parameters: the closer it is to the principal plane, the better the results. A deviation of only 30° leads to a significant increase in uncertainty (Schmidt and Fernando, 2015). For a limited number of directions,

using the principal plane with a high angle of incidence is considered the best solution. What's more, five directions is the minimum number of angular configurations in the principal plane to obtain well-constrained photometric parameters. Schmidt and Bourguignon (2019).

- Most of the parameters, with the exception of the roughness parameter, are likely to be wavelength dependent, so that the single-particle phase function has wider lobes at longer wavelengths and favors backscattering (Gunderson et al., 2007).
- The interdependence of the model parameters has been critically examined (Helfenstein and Veverka, 1989), leading us to study this effect on different samples.
- The two-parameter HG phase function is widely used because it contains physical parameters and describes the data with good accuracy (Johnson et al., 2013).

Conclusion

Throughout this chapter, we have provided an overview of photometry, focusing on its fundamental concepts, particularly in the context of planetary surfaces. Emphasis has been placed on the need for a precise understanding and differentiation of the various radiometric quantities to ensure their appropriate use in specific analytical scenarios. This precision is essential for accurate photometric analysis.

We have reviewed several photometric models, with particular emphasis on the Hapke model, which is notable for its ability to simulate the BRDF of soil and other particulate surfaces. Despite its strengths, it is recognized for its complexity and the need to carefully consider several factors, including the geometric configurations of observations and the coupling effect of model parameters.

The information in this chapter is essential for the following chapters, where the choice of data and analysis methods will be strongly influenced by the principles and ideas discussed here. By establishing a solid understanding of photometric principles and models, we set the stage for more advanced applications and analyses, ensuring that the reader is well equipped to meet the challenges of photometric data interpretation in planetary science and beyond. This foundation not only facilitates a deeper understanding of the theoretical underpinnings of photometry, but also prepares the reader for the practical applications and challenges of their future studies.

Symbol	Range	Parameter	Description	Physical implication
ω	[0,1]	Single scattering albedo	The ratio of the amount of light at a given wavelength scattered by a representative incremental volume of a medium to the combined amount of light scattered from and absorbed by it	Particle composition, size and microstructure
$\overline{\theta}$	[0°,60°]	Photometric roughness	Mean slope angle, averaged over a size range limited at the upper end by the angular resolution of the detector and at the lower end by radiative scattering	Typically roughness at microscale (100 - 1000 μm)
b	[0,1]	Asymmetry parameter of the HG phase function	Anisotropy of the scattering (b < 0.5 broad / b $\geq$ 0.5 narrow scattering lobe)	Particle shape, composition and internal structure
c	[0,1]	Backscattering parameter of the HG phase function	Main scattering direction (c < 0.5 forward scattering / c $\geq$ 0.5 backward scattering)	Particle shape, composition and internal structure
h_S	[0,+∞]	Width of the opposition effect (SHOE)	Width of the reflectance surge at low phase angle (3-20°), mainly due to the shadow-hiding	Grain size distribution and filling factor, surface compactness
B_{S0}	[0,1]	Amplitude of the opposition effect (SHOE)	Amplitude of the reflectance surge at low phase angle (3-20°), mainly due to the shadow-hiding	Particle composition, surface opaqueness
h_C		Width of the opposition effect (CBOE)	Width of the reflectance surge at very low phase angle (<3°), mainly due to the coherent backscattering	
B_{C0}		Amplitude of the opposition effect (CBOE)	Amplitude of the reflectance surge at very low phase angle (<3°), mainly due to the coherent backscattering	
K		Porosity factor		

Table 1.4 – Description of the Hapke model parameters (Hapke, 2012).

Chapter 2

Data and tools

Introduction

In this chapter we examine the targets of our study: the Asal-Ghoubbet Rift on Earth and the near side of the Moon. While the initial motivations for selecting these sites were briefly outlined in the Introduction, here we delve into a more detailed exploration of their specific characteristics and the strategic rationale behind their selection for this research. We begin by presenting the available data for these sites, describing how it was collected, the conditions under which it was obtained, and its current state.

Our data sets can be divided into two main groups:

• Global scale data, which includes two sets of multi-angular Pleiades images. One set covers the entire Asal-Ghoubbet trench and the other the near side of the Moon. These datasets allow the mapping of surface physical properties via massive inversion of the Hapke model.

• Local scale field data, also divided into two groups. The first group consists of ground imagery and soil samples from nineteen study sites within the Asal-Ghoubbet rift. These include images taken by drones and handheld cameras to generate millimetre-scale Digital Elevation Models (DEMs), as well as soil and rock samples collected in the field. The second group consists of ground photographs of the Moon taken by astronauts during the Apollo missions, also used to generate millimeter-scale DEMs.

Finally, we discuss the preprocessing steps required to convert the raw data into a format suitable for analysis. This includes procedures such as calibration and alignment of images acquired from different sources or scales.

2.1 The regions of interest

2.1.1 The Asal-Ghoubbet rift (Republic of Djibouti)

The Asal-Ghoubbet rift, located in the Republic of Djibouti, is a remarkable geophysical feature extending 30 kilometers from Ghoubbet Bay to Lake Asal (Figure 13). This rift is bounded by two sequences of overlapping normal faults and exhibits significant vertical relief with depths ranging

from 300 to 800 meters. The escarpments along these faults are markedly subvertical, rising up to 150 meters. The structural dimensions of the rift vary along its entire length; the narrowest section is 2 to 3 kilometers wide, while the wider segments at either end reach widths of 8 to 10 kilometers. This variability in width may be indicative of the dynamic tectonic forces at work beneath the surface. According to Manighetti et al. (1998), the formation of the Asal-Ghoubbet rift began about 1 million years ago. This geological evolution has been marked by significant tectonic and volcanic activity, mainly concentrated along the rift axis. Evidence of this active geological history includes basaltic lava flows and weathered paleosols dated between 8,000 and 6,000 years ago, suggesting recent and ongoing transformations (Stein et al., 1991). A notable geological feature in the rift is the large, highly faulted Fieale volcano, located in the south-eastern half of the inner rift floor. It illustrates the complex interplay between volcanic activity and tectonic deformation (Stieltjes, 1980; Stein et al., 1991). In addition, contemporary volcanism occurs to the northwest of Fieale, characterized by an "axial" volcanic ridge that extends for several kilometers along the inner floor. Ardoukôba volcano, located at the north-western end, experienced its last volcanic event in 1978 (Pinzuti et al., 2013). This continuous volcanic activity within the rift not only underlines its dynamic nature, but also contributes to its geological complexity.

The rift has been a focal point for detailed scientific investigation due to its complex and diverse geological features, which extend over approximately 100 km^2. This interest is well documented in numerous studies and surveys, including geodetic, topographic, and geological assessments (Stieltjes, 1973, 1980; Pinzuti et al., 2013; Smittarello et al., 2016). The rift's remarkable radiometric diversity is characterized by striking contrasts, from the bright white saline deposits to the deep black of recent basaltic lava flows, providing a unique spectrum of natural colors and textures for analysis. The rift's landscape is also varied, with rough, coarse lava flows interspersed with smooth, flat sedimentary basins, all cut by sharp, near-vertical fault lines. These diverse topographic features provide a rich tapestry for geological and geophysical studies. The region's hot, semi-arid climate further enhances its suitability for remote sensing studies. The low soil moisture and sparse vegetation typical of the area mean that the photometric signals received from satellite sensors are predominantly from the soil itself, with very little interference from vegetation or water. This makes the rift an exceptional natural laboratory for studying the physical properties of natural soils using remote sensing techniques. In summary, the Asal-Ghoubbet rift region was strategically chosen because of its unique geographical and environmental characteristics, which include a wide range of bare soil landscapes.

2.1.2 The near side of the Moon

The Moon is the most studied extraterrestrial body for a simple reason: it is the closest celestial body to Earth. In a few words, almost the entire Moon is covered by a rubble pile of charcoal-gray, powdery dust and rocky debris known as lunar regolith. Due to the sparse atmosphere, a steady rain of asteroids, meteoroids, and comets constantly strikes the surface, grinding it into fragments ranging from huge boulders to fine powder over billions of years. The lunar surface consists of bright, heavily cratered highlands and smooth, dark lowland maria (plural form of mare - a large, dark basaltic plain formed by lava filling ancient impact basins), which are most prominent on the near side. The highlands, saturated with large craters due to their greater age compared to the maria, dominate both the lunar far side and most of the near side. The highlands predominantly

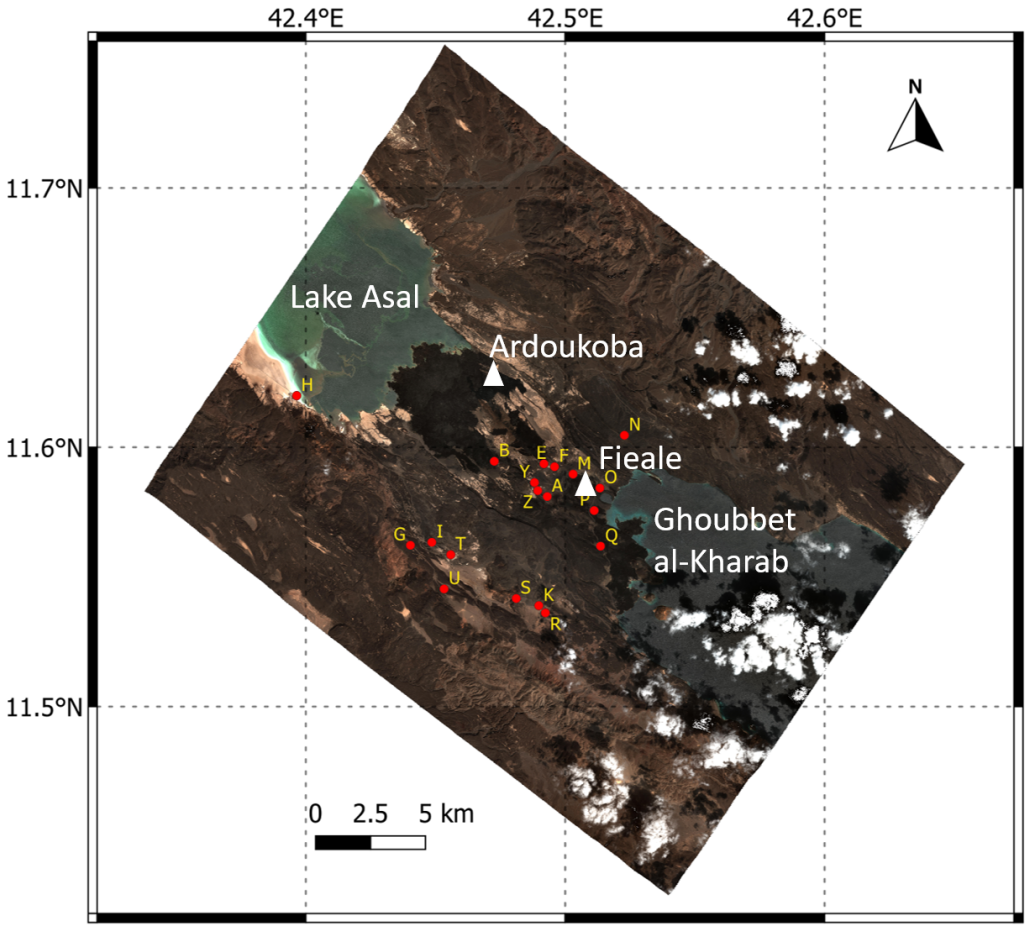

Figure 13 – Asal-Ghoubbet rift (Republic of Djibouti) (11.43˚-11.74˚N, 42.34˚-42.65˚E): a) Pleiades composite image acquired with a solar zenith angle of 37.8˚, a viewing zenith angle of 24˚, and a relative azimuth angle of 152.8˚. The ground sampling distance (GSD) is 2 m. Red dots indicate study sites (Figure 25).

expose highly anorthositic rocks, while the maria are characterized by basaltic lava flows that erupted about 0.5 billion years after major impact events (Crawford et al., 2014). Lunar rocks fall into four categories: (1) basaltic volcanic rocks, (2) pristine rocks found mainly in the lunar highlands, (3) breccias, and (4) lunar soil (Taylor et al., 1991). The most abundant constituents of most lunar rocks, accounting for over 90% by volume, are silicates such as pyroxene, plagioclase feldspar, olivine, potassium feldspar, and silica (Papike et al., 1991). Oxide minerals are next in abundance, particularly in some mare basalts. Ilmenite is the most abundant oxide mineral on the Moon, and its presence is directly related to the bulk composition of the magma from which it crystallized: the higher the TiO_2 content, the higher the ilmenite content in lunar rocks (Campbell et al., 1978). Native iron, a rare element on Earth, is common in lunar rocks (Reid et al., 1970).

Some information on the lunar geological timescale is needed to familiarize ourselves with the geological units, which is necessary for future interpretation. Let's start with the oldest period, the Nectarian (3.92 Ga), which covers all the events that occurred between the formation of the Nectaris and Imbrium impact basins. 12 multi-ring impact basins are recognized in the Nectarian period, including the Serenitatis and Crisium basins (Mare Serenitatis and Mare Crisium). The Imbrium owes its name to the Imbrium Basin, which is thought to have formed at 3.85 Ga, when large basalts filled basins and craters. Finally, the Eratosthenian period (3.16 Ga) is the second

most recent period, named after the Eratosthenian crater and characterized by young craters with an attenuated ray system and small-scale basalts filling basins and craters (Wilhelms et al., 1987). During this period the lunar surface was covered with freshly excavated material, which is generally light in color and darkens over time due to space weathering processes. On this basis, the highlands are an exhumed terrain, higher in elevation and also lighter in color due to the weathering process that stripped away the older layers. As for the maria, it is most likely a mixture of native materials darkened by time and ancient materials from the highlands.

The near side of the Moon is the lunar hemisphere that always faces the Earth, as opposed to the far side. Only one side of the Moon is visible from the Earth because the Moon rotates on its axis at the same speed as the Earth, a situation known as tidal locking. This is also where most lunar missions have taken place. In the 20th century, the first recorded lunar mission was that of the American Pioneer 0 spacecraft, which was launched in 1958. A year later, the USSR successfully launched the Luna-2 spacecraft, which place an impactor on the lunar surface. It wasn't until 1969, 10 years later, that a man was sent to the surface of the Moon on the Apollo 11 mission. The Apollo program was the American manned spaceflight program led by the National Aeronautics and Space Administration (NASA), which successfully prepared and landed the first men on the Moon between 1968 and 1972.

In addition to the Apollo program, several lunar exploration missions have been launched since 1959, notably by Europe (SMART-1), the US (Apollo series, LRO, LCROSS), India (Chandrayaan-1, Chandrayaan-2), Japan (Kaguya), the Soviet Union (Luna series) and China (Chang'E series). Recently, there has been a renewed interest in the Moon. During this thesis (2021-2024), Artemis I, launched on November 16, 2022, was the first integrated flight test of NASA's deep space exploration systems, in preparation for Artemis II (scheduled for September 2025), the first manned flight test of the Space Launch System and Orion spacecraft around the Moon. Artemis III will then send the first humans to explore the region near the south pole, and Artemis IV should inaugurate the first permanent lunar station [1]. In addition, the Chandrayaan-3 mission was launched on July 14, 2023, and its lander landed successfully in a region near the lunar south pole on August 23, 2023. The Smart Lander for Investigating Moon (SLIM) of Japan Aerospace Exploration Agency (JAXA) landed intact on January 19, 2024. Finally, Chang'E 6 (launched on May 3, 2024, returned on June 25, 2024) is also an honorable mention, but it focuses on the far side of the Moon, outside the scope for this thesis.

In summary, the Moon provides a unique reservoir of data that is highly conducive to the type of study we are undertaking. In addition to satellite data, ground data collected by astronauts during lunar landings and by lunar rovers provide invaluable insights into the lunar surface. These ground images provide a detailed local context that complements the wider coverage offered by satellite imagery, and are considered the ground truth for the validation of our scientific results. What's more, interest in the Moon continues unabated, with new missions planned and new data to be supplied.

1. https://www.nasa.gov/humans-in-space/artemis/

2.2 Global scale data: Multiangular Pleiades images

Pleiades is a high-resolution optical imaging constellation being launched by the Centre National d'Études Spatiales (CNES) in late 2011 and 2012. It consists of two satellites and provides daily coverage of any location on Earth. The two satellites have a panchromatic channel with a ground space distance (GSD) of 0.5 m and four spectral bands (visible and near-infrared) with a GSD of 2 m (Figure 14). The image quality (absolute calibration) was reported to be 4%. Furthermore, thanks to the platform's great agility, images can be acquired at different viewing angles ranging from nadir to ±47° (Gleyzes et al., 2012) or even ±55° for our data set. The acquisition of stereo pairs, or even triplets, facilitates the construction of metric DEMs using photogrammetry.

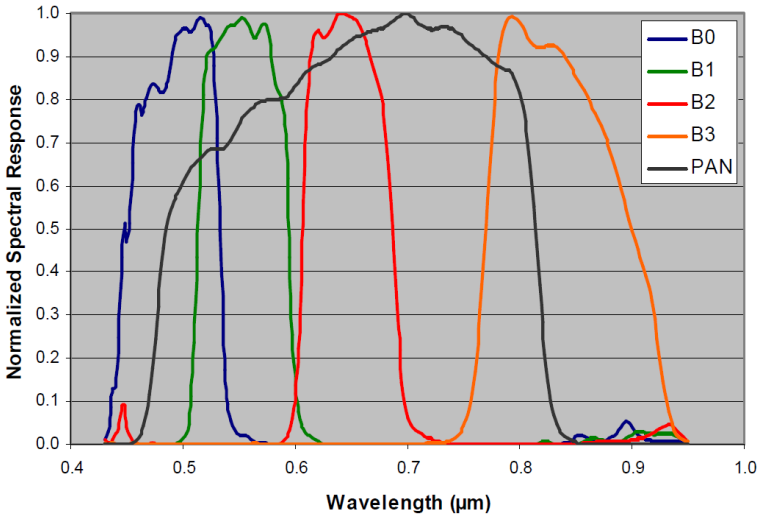

Figure 14 – The Pleiades spectral bands (Lachérade et al., 2012).

The satellites' sensors can also take images of the Moon for calibration purposes. According to Lacherade et al. (2014), the spatial resolution is about 1500 m for the four spectral bands, so an image of the Moon consists of nearly 27 million pixels, leading to very high accuracy in deriving the lunar irradiance measured by the sensor and integrated on the lunar disk.

2.2.1 Asal-Ghoubbet rift

a) Sensor geometry

An acquisition mode called VIDEO was programmed by CNES over the Asal-Ghoubbet rift on January 26, 2013, enabling 21 images to be taken from different angles during the four-minute satellite flight over (Figure 15 and Table 2.1). The variation of the solar zenith angle is marginal (0.6°), in contrast to the variation of the viewing zenith angle, which varies between 10° and 55° in the backward and forward directions. The phase angle varies between 35° and 90°. The importance of phase angle in BRDF analysis is well documented by Fernando et al. (2016) and Schmidt and Fernando (2015). Values above 90° and ranges above 50° are required to constrain the Hapke model. The phase angle is between 30° and 90°, which is important for the choice of estimated Hapke model parameters and the quality of the inversion results.

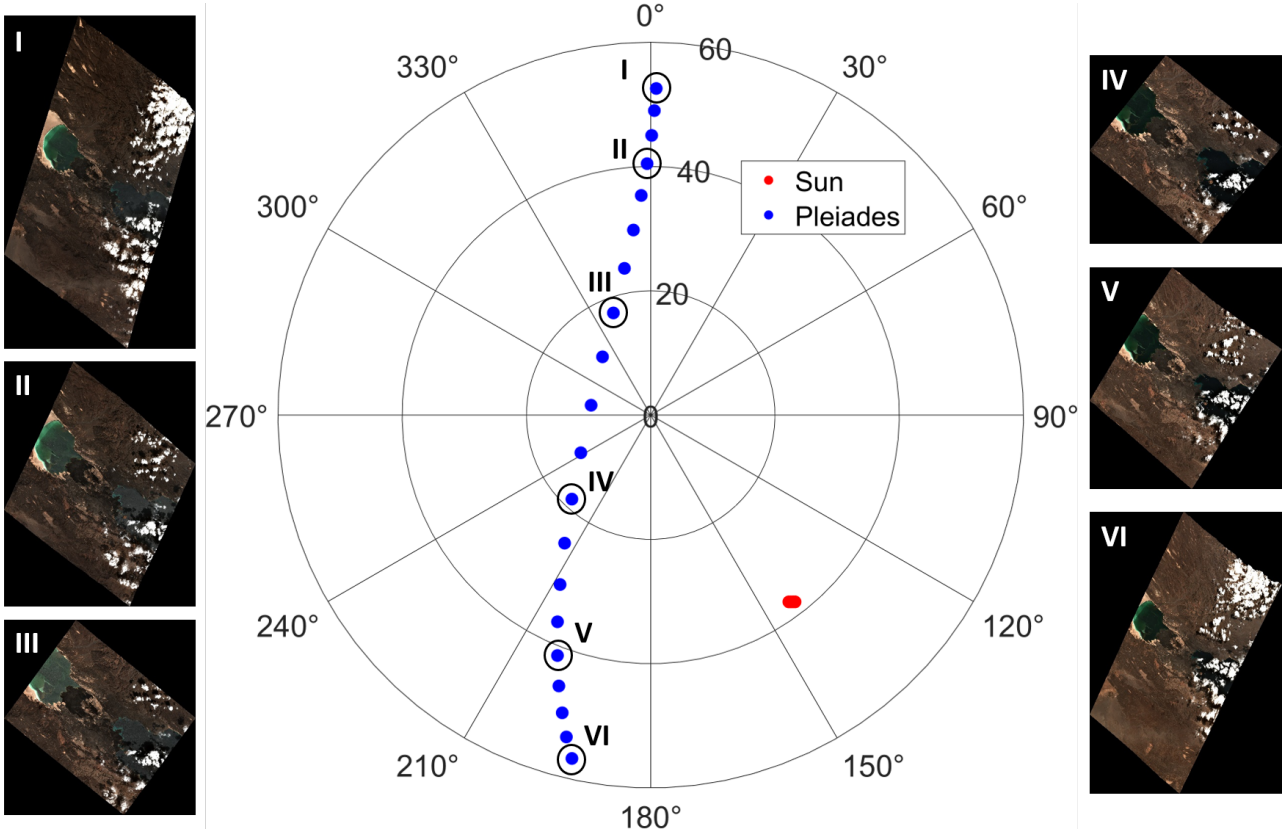

Figure 15 – Polar plot showing the geometric configuration of the Pleiades acquisition: Sun directions (red dots) and viewing directions (blue dots). The radial distance of the points indicates the zenith angle while the azimuth is measured from the reference direction of the geographic north. Roman numerals link the Pleiades images to the imaging configuration.

b) Atmospheric corrections

The pre-processing of the Pleiades images includes atmospheric corrections carried out by the Physics for Optical Remote Sensing Measurement Service at CNES. They were performed using MAJA (MACCS ATCOR Joint Algorithm) (Hagolle et al., 2015; Rouquié et al., 2017), a sophisticated multi-mission atmospheric correction processor designed to process time series of high-resolution images, such as the Sentinel-2 images. Some of the formulas and parameters used in the atmospheric correction are described in detail here:

- The surface pressure P [hPa] was calculated for each pixel from its elevation, obtained from the Shuttle Radar Topography Mission (SRTM). The barometric formula is as follows:

$$P = \rho_0 (1 - \frac{LZ}{T_0})^{\frac{g_0 M}{R_0 L}} \tag{2.1}$$

  with the sea level standard atmospheric pressure $\rho_0 = 1013.25$ hPa, the temperature lapse rate $L = 0.0065$ K/m, the altitude Z in meter, the sea level standard temperature $T_0 = 288.15$ K, the earth-surface gravitational acceleration $g_0 = 9.80665 m/s^2$, the molar mass of dry air $M = 0.0289644 kg/mol$ and finally the universal gas constant $R_0 = 0.0289644 kg/mol$.
- Water vapor content:
  - We used the specific humidity data from ERA5, the latest climate reanalysis from the

	Name	SZA (°)	VZA (°)	Phase angle (°)
1	IMG_PHR1B_MS_001_20130126_074920_406	37.97	55.73	87.3
2	IMG_PHR1B_MS_001_20130126_074932_156	37.97	52.56	84.38
3	IMG_PHR1B_MS_001_20130126_074956_156	37.98	45	77.64
4	IMG_PHR1B_MS_001_20130126_075020_906	37.83	35.37	69.32
5	IMG_PHR1B_MS_001_20130126_075045_406	37.82	23.99	59.99
6	IMG_PHR1B_MS_001_20130126_075110_656	37.68	12.17	49.84
7	IMG_PHR1B_MS_001_20130126_075136_531	37.67	12.78	41.3
8	IMG_PHR1B_MS_001_20130126_075202_031	37.53	24.83	36.47
9	IMG_PHR1B_MS_001_20130126_075227_406	37.53	36.48	35.63
10	IMG_PHR1B_MS_002_20130126_075252_531	37.52	46.02	36.99
11	IMG_PHR1B_MS_002_20130126_075317_156	37.38	53.54	38.9
12	IMG_PHR1B_MS_002_20130126_074944_156	37.97	49	81.18
13	IMG_PHR1B_MS_002_20130126_075008_531	37.82	40.45	73.65
14	IMG_PHR1B_MS_002_20130126_075033_156	37.82	29.9	64.8
15	IMG_PHR1B_MS_002_20130126_075058_531	37.83	17.5	54.74
16	IMG_PHR1B_MS_002_20130126_075123_656	37.67	9.73	45.15
17	IMG_PHR1B_MS_002_20130126_075149_281	37.68	18.54	38.45
18	IMG_PHR1B_MS_002_20130126_075214_781	37.53	30.92	35.62
19	IMG_PHR1B_MS_002_20130126_075239_906	37.53	41.49	36.11
20	IMG_PHR1B_MS_002_20130126_075304_781	37.38	49.98	37.77
21	IMG_PHR1B_MS_002_20130126_075329_281	37.38	56.69	39.97

Table 2.1 – List of Pleiades images in the Asal-Ghoubbet rift with the geometric configuration. The values are slightly different from those of Labarre (2017) due to the recalculation by CNES.

European Centre for Medium-Range Weather Forecasts (ECMWF), which is defined at different altitudes [2].

- The specific humidity data treatment involves:
  - Reading the two ERA5 files around the acquisition date
  - Temporal interpolation
  - Spatial interpolation at each point of the Pleiades image
  - The amount of water vapor W $[g/cm^2]$contained between two pressure levels is then calculated for each pixel:

$$W(\mathbf{p}) = \frac{\mathbf{S}(\mathbf{p})[P(\mathbf{p}) - P(\mathbf{p}+1)]}{\mathbf{g}} \tag{2.2}$$

    where $\mathbf{S}$ is the specific humidity in g/cm^2, P is the atmospheric pressure [hPa], $\mathbf{g}$ is the earth-surface gravitational acceleration and $\mathbf{p}$ is the pressure level.
  - Total water vapor will be the sum of all pressure levels up to surface pressure at pixel level.
- The water vapor values are calculated for each pixel and can be found in the supplied product file. The value read must be divided by a quantization value of 200 to obtain

2. https://cds.climate.copernicus.eu/cdsapp#!/dataset/reanalysis-era5-pressure-levels?tab=form

the AOT.

- Aerosol optical thickness at 550 nm:
  - AOT is retrieved from CAMS global reanalysis data (EAC4) [3]
  - We read the two CAMS files that frame the acquisition date. A temporal interpolation is performed, followed by a spatial interpolation at each point of the Pleiades image.
  - The average AOT value used to process the series is 0.19.
  - The AOT values used for each pixel can be found in the supplied product file. It must be divided by a quantization value of 200 to obtain the AOT.
- Column ozone content: We used the value of 244 DU, obtained from the OMI (Ozone Monitoring Instrument) spectrophotometer on board the Aura satellite.
- Aerosol model was used in accordance with Rouquié et al. (2017)

Concerning the atmospheric correction software used, once the atmospheric composition has been determined, the surface reflectances are determined in the same way as in the MAJA software used by THEIA (land surface data and services hub of the IR Data Terra) to process Sentinel-2 products:

- Gas absorption correction using the Simplified Model for Atmospheric Correction (SMAC) radiative transfer software
- Correction for aerosol absorption and scattering and molecular scattering using lookup tables (LUT) precomputed with the Successive Orders of Scattering (SOS) radiative transfer code. The solar and satellite viewing angles used correspond to those at the center of the image
- Correction for adjacency effect, an undesirable addition to the signal due to the scattering of the atmosphere and the neighboring objects.
- Terrain correction has not been applied at this stage

With regard to the cloud removal tool within the the MAJA software, cloud masks were determined based on several set of criteria:

- Spectral criteria to mask dense clouds
- Multi-temporal criteria
- Criteria on a cirrus band, located at 1.38 μm in a deep water vapor absorption band. In this band we can only see high altitude targets such as cirrus because the signal coming from the low level surface is completely absorbed by the water vapor [4].

According to these criteria, Sentinel-2 and VENμS data are suitable for applying the cloud removal tool. On the other hand, Pleiades does not acquire multi-temporal image series and does not have a cirrus band. Therefore, despite the presence of some clouds in the Pleiades images (Figures 13 and 15), we did not generate a cloud mask. The effect of clouds, mainly low clouds, and cast shadows was minimized by filtering out pixels with significant residuals after inversion of the Hapke model on Pleiades images. These pixels were easily identified and excluded from the estimated parameter maps (Chapter 5).

3. https://ads.atmosphere.copernicus.eu/cdsapp#!/dataset/cams-global-reanalysis-eac4?tab=form
4. https://labo.obs-mip.fr/multitemp/4109/, https://zenodo.org/records/1209633

c) Data structure

There are 21 folders, each containing five `.TIF` images acquired in the same geometric configuration: four corresponding to the multispectral channels (blue, green, red and near infrared) and one to the panchromatic channel. In addition, each folder contains an RGB composite image in `.JPG` format for overview purposes. Some of these composite images are shown in Figures 13 and 15.

2.2.2 On the Moon

a) Sensor geometry and data status

We received a list of over 1,200 images taken at different times, under different lighting conditions and at different phase angles relative to the Moon's center (Figure 16). This file contains the satellite coordinates in Cartesian coordinates (with the center of the Moon at the origin), the latitude and longitude of the Sun and satellite in selenographic coordinates (Figure 17), the phase angle at the origin and the date of acquisition.

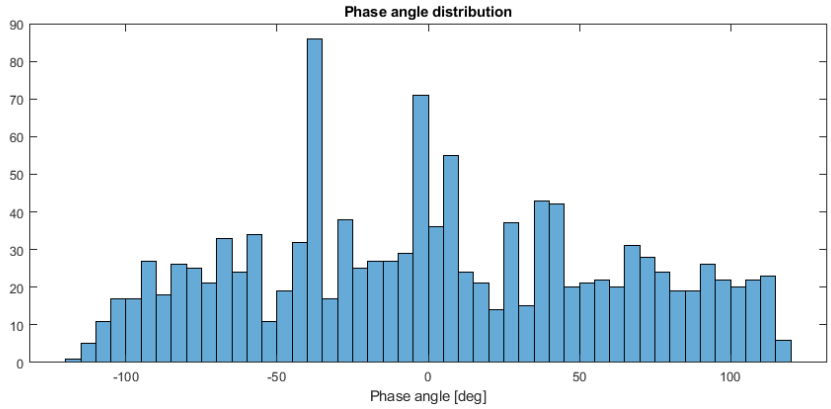

Figure 16 – Phase angle distribution of Pleiades images available on the Moon on request.

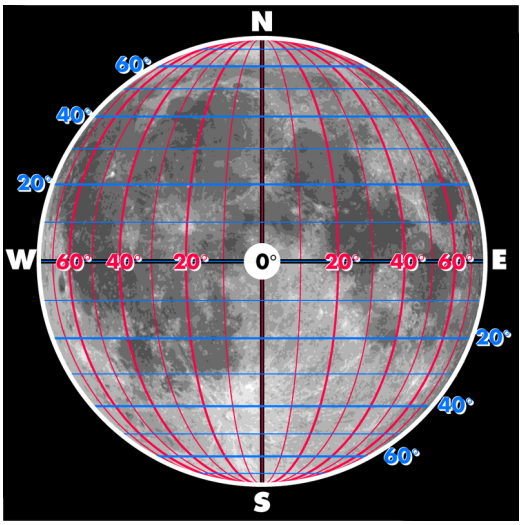

Figure 17 – Selenographic coordinate system at the near side of the Moon [5].

5. https://commons.wikimedia.org/wiki/File:Moon-map.png

Figure 18a shows the dynamic range of positions of the Sun and the Pleiades satellite relative to the center of the Moon. This configuration is essential for understanding the interaction between the Sun, Earth, Moon and Pleiades satellite, shown in Figure 18b. Due to synchronous tidal locking, which results in the same side of the Moon always facing the Earth, the Moon experiences regular cycles of sunrise and sunset similar to those of the Earth, which means that the Sun can appear at any longitude relative to the Moon. However, the latitudinal motion recorded in our dataset shows that the Sun's position varies in a much narrower range, between [-1.5, 1.5]°. This constraint is due to the large distance between the Sun and the Moon and the small inclination of the Moon's orbit around the Earth relative to the Earth's orbit around the Sun (±5° [6]). On the other hand, the variation of Pleiades in selenographic longitude and latitude is limited to a maximum of 8.5°. This limitation is due to several factors: the tidal locking of the Moon, the sun-synchronous orbit of the satellite, which is perpendicular to the line connecting the Earth to the Sun, and the inclination of the Moon's orbit relative to the Earth's orbit. These factors combine to limit the range of positions observable from the satellite and influence the way Pleiades captures images of the Moon. As a result, we predict a wide range of incidence angles, but a limited range of emergence angles.

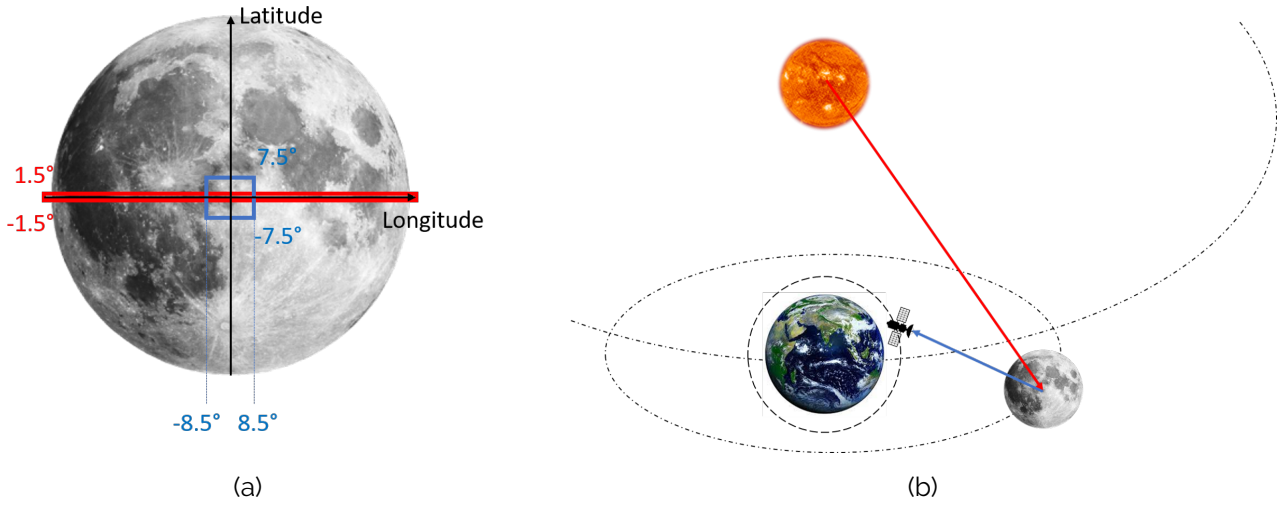

Figure 18 – a) The selenographic coordinates of the Sun and Pleiades; b) Demonstration of the dynamics between the Moon, Sun, Earth and the Pleiades satellite (not to scale).

To effectively use the Hapke model to analyze photometric data, it is essential to transform the raw latitude and longitude coordinates of the Sun and satellite into a unified geometric configuration that the model can process (i, e, g). The haversine formula is suitable for this purpose, as it determines the great-circle distance between two points on a sphere given their longitudes and latitudes (Brummelen, 2013). Important for navigation, this formula is a special case of a more general formula of spherical trigonometry, the haversine law, which relates the sides and angles of spherical triangles. Alternatively, we can calculate the angle between two points on the sphere (as known as the bearing). The general formula is:

$$hav(\theta) = \sin^2\left(\frac{\theta}{2}\right) = hav(\varphi_2 - \varphi_1) + \cos\varphi_1 \cos\varphi_2 hav(\lambda_2 - \lambda_1) \tag{2.3}$$

where φ_1, φ_2 are the latitudes of point 1 and point 2, λ_1, λ_2 are the longitudes of point 1 and point 2. We can easily see that the Sun zenith angle (i) is the bearing between the Sun and the point of

6. https://science.nasa.gov/moon/moon-phases/

interest on the Moon. Therefore, without using the haversine symbol, we have:

$$\sin^2\left(\frac{i}{2}\right) = \sin^2\left(\frac{\varphi_{Sun} - \varphi_p}{2}\right) + \cos\varphi_{Sun}\cos\varphi_p \sin^2\left(\frac{\lambda_{Sun} - \lambda_p}{2}\right) \tag{2.4}$$

where φ_{Sun}, φ_p are the latitude of the Sun and a given point on the Moon's surface, λ_{Sun}, λ_p are the longitude of the Sun and that point. Hence,

$$i = 2\arcsin\left(\sqrt{\sin^2\left(\frac{\varphi_{Sun} - \varphi_p}{2}\right) + \cos\varphi_{Sun}\cos\varphi_p \sin^2\left(\frac{\lambda_{Sun} - \lambda_p}{2}\right)}\right) \tag{2.5}$$

Similarly, the viewing zenith angle is the bearing between the satellite and the point of interest.

$$e = 2\arcsin\left(\sqrt{\sin^2\left(\frac{\varphi_{sat} - \varphi_p}{2}\right) + \cos\varphi_{sat}\cos\varphi_p \sin^2\left(\frac{\lambda_{sat} - \lambda_p}{2}\right)}\right) \tag{2.6}$$

where φ_{sat} and λ_{sat} are the latitude and longitude of the satellite. Next, the phase angle (g) is the bearing between the Sun and the satellite:

$$g = 2\arcsin\left(\sqrt{\sin^2\left(\frac{\varphi_{Sun} - \varphi_{sat}}{2}\right) + \cos\varphi_{Sun}\cos\varphi_{sat} \sin^2\left(\frac{\lambda_{Sun} - \lambda_{sat}}{2}\right)}\right) \tag{2.7}$$

Then calculating the azimuth difference (ϕ) becomes straightforward using the spherical cosine law:

$$\phi = \arccos\left(\frac{\cos g - \cos i \cos e}{\sin i \sin e}\right) \text{ with } i \neq 0, e \neq 0 \tag{2.8}$$

If either the Sun or the satellite is at nadir ($i = 0$ or $e = 0$), ϕ is set to be zero. Then, as we wanted the selected images to be regularly spaced in terms of phase angle on either side of positive or negative longitude (Figure 17), we need to assign $g \in \mathbb{Z}$ instead of $g \in \mathbb{N}$ as the result of Equation 2.6. So we set $g < 0$ when $\lambda_{Sun} < \lambda_{sat}$ for visualization and data selection purposes.

We had to carefully select an image for the inversion from over 1,200 images. To do this, we defined a number of phase angle intervals and then chose an image whose phase angle was within each interval, preferably in the middle of the interval in question. Initially, 20 images were chosen because this number is close to the number of Pleiades images in the Asal-Ghoubbet rift. We received the first series on February 3, 2023, with only 18 of the 20 images. For the two remaining images with very high phase angles (103° and 110°), the CNES geometric refinement tool didn't work because the high phase angle introduces large spatial distortions, so the directories for these images are empty. In addition, we noticed artifacts at the boundary between illuminated and unilluminated areas of the Moon (and not at the boundary between the Moon and space), where the solar zenith angle reaches 90°. The transition over $i = 90°$ is not very smooth due to the lunar elevation. So the radiance values (measured by the satellite) don't exactly match the calculated sun zenith angle (which also varies within a pixel). When calculating reflectance, the calibration tool, a small radiance value ends up being divided by an amount that approaches zero, so that the parts at the poles and at the boundary between lit and unlit areas in the full Moon images

appear abnormally bright. These areas with high sun zenith angle (above 70˚) inevitably have to be removed during the inversion process.

Later on, we gained an insight into the three image calibration processes: geometric refinement, projection and co-registration. As far as geometric refinement is concerned, each satellite has different devices to determine its position and attitude (GPS, gyroscopes, inertial wheels...). For a high-resolution system such as Pleiades, these data are not sufficient to restore the line of sight with the required accuracy (1 μrad at 10kHz). In addition, Pleiades is designed to operate only during the day, and some modeling of the geometric behavior has been done only for daytime acquisitions. This does not apply to the lunar images taken at night. Geometric refinement is the process of restoring all the geometric parameters (position, attitude, mechanical deformations between all the elements of the satellite...) in order to obtain the correct line of sight performance. This is usually done by comparing the acquired data with a reference image in the set. Specifically for the Moon acquisition, the data provider uses a Pleiades image where identifiable common points between different images (called tie points, usually recognizable impact craters) have been marked and relates the line/column position in the image to its position on the Moon (e.g., selenographic latitude/longitude). They correlate each image with this reference image to propagate these tie points to each image, and then, some numerical optimization allows us to retrieve all the necessary geometric parameters.

Next, in terms of projection, once the geometric refinement is done, we can accurately (1̃ pixel precision for the Moon) calculate the line of sight of each pixel. The projection phase consists of intersecting each line of sight with the surface (this includes the respective lunar satellite distance, librations, etc.), relating each pixel to a given point on the surface, and then resampling the data. For the specific -103˚ and -110˚ phase angle images mentioned earlier, the correlation with the reference image did not work because they look too different. Without geometric refinement, all the lines of sight are way off and it is impossible to create a projected image that looks like the Moon. However, we can still solve this by generating different reference images, which would work. It should also be noted that with these phase angles, the solar illumination at the Apollo landing sites could be quite low, probably half of them were not illuminated at all, and the radiometric quality could be limited.

For the co-registration, the projected Pleiades image was compared to high resolution Kaguya data (< 0.05˚ in latitude/longitude) using SIFT. CNES also notes that the registration between the Pleiades products is within one stereographic pixel (4.5 km). In January 2024, CNES identified an error in the generation of the previously provided images. The geometric refinement had been calculated but not applied before projection into selenographic coordinates. CNES has reprocessed the images and checked the correlation with the LOLA albedo product. For lunar phases within [-90˚,90˚], the average shift in line/column is about 1 pixel (in selenographic coordinates). For higher phases, the geometric refinement is not good, but the shift is reasonable for some products, so the images could be used. The results are better near the center of the Moon, but at the lunar limb, the shift between the images increases and can reach several pixels. A total of 25 images (Table 2.2) are provided at the end.

Based on Table 2.2, we can see that the variation of the viewing zenith angle (VZA or e) is insignificant (4˚-11˚), compared to the sun zenith angle (SZA or i) (0-120˚). Therefore, the SZA variation is the main factor leading to a wide range of phase angles. The variation of VZA is mainly

	Name	SZA (°)	VZA (°)	Phase angle (°)
1	IMGPHR_PHR1A_L1_20120420_IPU_20120420_0893-002_V1	112.35	10.39	119.36
2	IMGPHR_PHR1A_L1_20120614_IPU_20120614_9366-002_V1	107.29	6.20	111.52
3	IMGPHR_PHR1B_L1_20130107_IPU_20130107_0565-006_V1	105.81	7.53	98.99
4	IMGPHR_PHR1B_L1_20130107_IPU_20130107_1733-004_V1	118.22	6.01	112.67
5	IMGPHR_PHR1B_L1_20130207_IPU_20130207_5327-004_V1	121.24	3.96	118.95
6	IMGPHR_PHR1B_L1_20130304_IPU_20130304_0554-002_V1	65.41	1.69	66.98
7	IMGPHR_PHR1B_L1_20130308_IPU_20130308_2341-002_V1	102.71	5.01	102.38
8	IMGPHR_PHR1B_L1_20130328_IPU_20130328_7989-004_V1	20.30	8.49	26.19
9	IMGPHR_PHR1B_L1_20130328_IPU_20130328_8470-002_V1	12.81	8.00	18.57
10	IMGPHR_PHR1B_L1_20130402_IPU_20130402_4772-004_V1	1.48	6.88	6.98
11	IMGPHR_PHR1B_L1_20130502_IPU_20130502_7577-004_V1	45.39	4.75	48.61
12	IMGPHR_PHR1B_L1_20130503_IPU_20130503_0324-002_V1	53.56	6.79	57.61
13	IMGPHR_PHR1B_L1_20130522_IPU_20130522_6176-004_V1	104.98	9.32	110.74
14	IMGPHR_PHR1B_L1_20130522_IPU_20130522_6260-002_V1	97.43	9.81	103.86
15	IMGPHR_PHR1B_L1_20130522_IPU_20130522_6913-004_V1	90.71	10.14	97.53
16	IMGPHR_PHR1B_L1_20130522_IPU_20130522_7021-004_V1	83.17	10.36	90.51
17	IMGPHR_PHR1B_L1_20130523_IPU_20130523_8975-004_V1	75.63	10.40	83.27
18	IMGPHR_PHR1B_L1_20130523_IPU_20130523_9051-004_V1	68.08	10.26	75.86
19	IMGPHR_PHR1B_L1_20130530_IPU_20130530_1523-004_V1	14.54	4.22	15.17
20	IMGPHR_PHR1B_L1_20130530_IPU_20130530_1661-002_V1	20.41	4.95	22.14
21	IMGPHR_PHR1B_L1_20130530_IPU_20130530_1788-002_V1	27.09	6.09	29.96
22	IMGPHR_PHR1B_L1_20130531_IPU_20130531_4776-002_V1	32.93	7.02	36.74
23	IMGPHR_PHR1B_L1_20130531_IPU_20130531_5123-004_V1	47.94	9.12	53.62
24	IMGPHR_PHR1B_L1_20130531_IPU_20130531_5429-002_V1	64.62	10.39	71.62
25	IMGPHR_PHR1B_L1_20131014_IPU_20131014_7668-002_V1	70.30	7.40	68.62

Table 2.2 – List of provided Pleiades Moon images, with the geometric configuration at the Moon center.

due to the orbit of the Pleiades satellite around the Earth. The angular separation of the satellite orbit is proportional to the arctangent of the ratio between orbit radius of the satellite and the Earth-Moon distance. Since the former is insignificant compared to the latter, this angular separation is small, resulting in the small maximum VZA (below 9° - Figure 18). Meanwhile, technically the SZA can now take any value between -180° and 180°. However, the visible part of the Moon appears to be small in images with an center SZA of 90° or more. As a result, there is less illumination, fewer identifiable tie-points, and a lower quality calibration. This is the reason for the abnormally high BRF on the limb pixels, at the transition between the sky and the Moon, corresponding to high SZA (Figure 19). For safe use, we normally only take measurements between 0 and 70° in the local SZA for the inversion.

b) Data structure

We observe a wide range of phase angles (7°-120°) in Table 2.2. As there are data points with a phase angle below 20°, it is possible to use the 6-parameter Hapke model. For each image

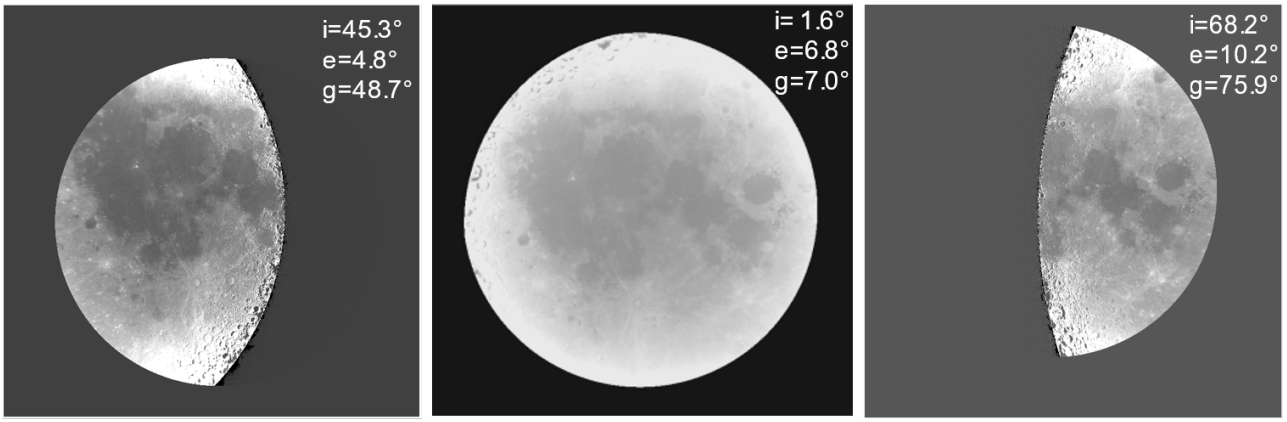

Figure 19 – Examples of Pleiades images of the Moon in stereographic projection. The outer part of the Moon is abnormally bright.

folder we have four images corresponding to the four Pleiades channels. All images capture the near side of the Moon, with GSD ≈ 1500 m. In addition, the geometry is also included. However, instead of a single configuration set for each image, we received maps of SZA, VZA, SAA (Sun azimuth angle) and VAA (viewing azimuth angle) for each channel, which is superfluous as they are the same between channels. The provision of geometric configuration maps is one of the key differences compared to the Asal-Ghoubbet rift Pleiades images. It is essential for the terrain correction, as the Moon curvature is significant for images that capture the entire surface.

2.3 Global scale data: Other Moon-orbiting satellites

Most of the lunar data is available on two websites: (1) The Lunar Orbital Data Explorer [7] provides search, browse and download tools for the Planetary Data System (PDS) science data archives from a number of spacecrafts and observatories. The website is hosted by the PDS Geosciences Node at Washington University in St. Louis. It contains raw and calibrated data sets from LRO, Chandrayaan-1, Clementine, Gravity Recovery and Interior Laboratory, Lunar Prospector, Lunar Orbiter, and Arecibo Observatory/National Radio Astronomy Observatory. Although limited to the Moon, they provide a wide range of data that can be crucial in extending the acquisition methods. (2) Astropedia [8] is a planetary data and cartography catalogue hosted by the Astrogeology Science Center of the United States Geological Survey (USGS). Compared to the previous website, it covers all the planets of the Solar System, in addition to the Moon and several other small bodies such as Ceres, Vesta, and Pluto. As for the Moon, it includes LRO, Clementine, KAGUYA, Apollo and Lunar Orbiter data (Nguyen, 2019).

In our case, we used the Lunar LRO LOLA Global DEM [9], with GSD ≈ 118 m, to perform the terrain correction (Section 4.2.1). In terms of elevation accuracy, LiDAR (from LOLA) provides more accurate elevation data than photogrammetry (from LROC imagery [10]) because it measures distances to objects using laser pulses, providing 3D point clouds with high accuracy. In photogrammetry, distance measurement depends on several factors, potentially increasing the

7. https://ode.rsl.wustl.edu/moon/
8. https://astrogeology.usgs.gov/search?target=&system=&p=1&accscope=&searchBar=
9. https://astrogeology.usgs.gov/search/map/moon_lro_lola_dem_118m
10. https://astrogeology.usgs.gov/search/map/moon_lroc_wac_dtm_gld100_118m

risk of errors. Therefore, the Lunar Kaguya TC Global DEM [11] was used to assess the alignment of the Pleiades images on the Moon.

2.4 Local scale field data

2.4.1 Asal-Ghoubbet rift

Field data were meticulously collected in the Asal-Ghoubbet rift in February 2016 as part of the CAROLInA (Characterization of multi-scAle Roughness using OpticaL ImAgery) project funded by CNES. Partly presented in Labarre et al. (2019), they focus on 19 specific sites of interest across the rift, each ranging in size from 400 m^2 to 600 m^2 (Figures 13 and 20). Originally, there were 23 sites, but four of them (sites C, D, V and X) do not have enough suitable images to construct DEMs. The physical and chemical properties of these sites are fully described in Table 2.3. They are located in four different areas: i) near Lake Asal (site H), ii) along the western flank of the rift, which shows great variability in terms of geological terrains, soil types and erosion patterns (sites G, I, K, S, T and U), iii) on the eastern flank north of Ghoubbet al-Kharab (site N), and iv) around the central Fieale volcano, where volcanic deposits and structures predominate (sites A, B, E, F, M, O, P, Q, Y, Z). The vast area of basaltic flow between the lowest elevations on DEM. However, no field data could be collected in this area due to the difficulty of accessing this terrain.

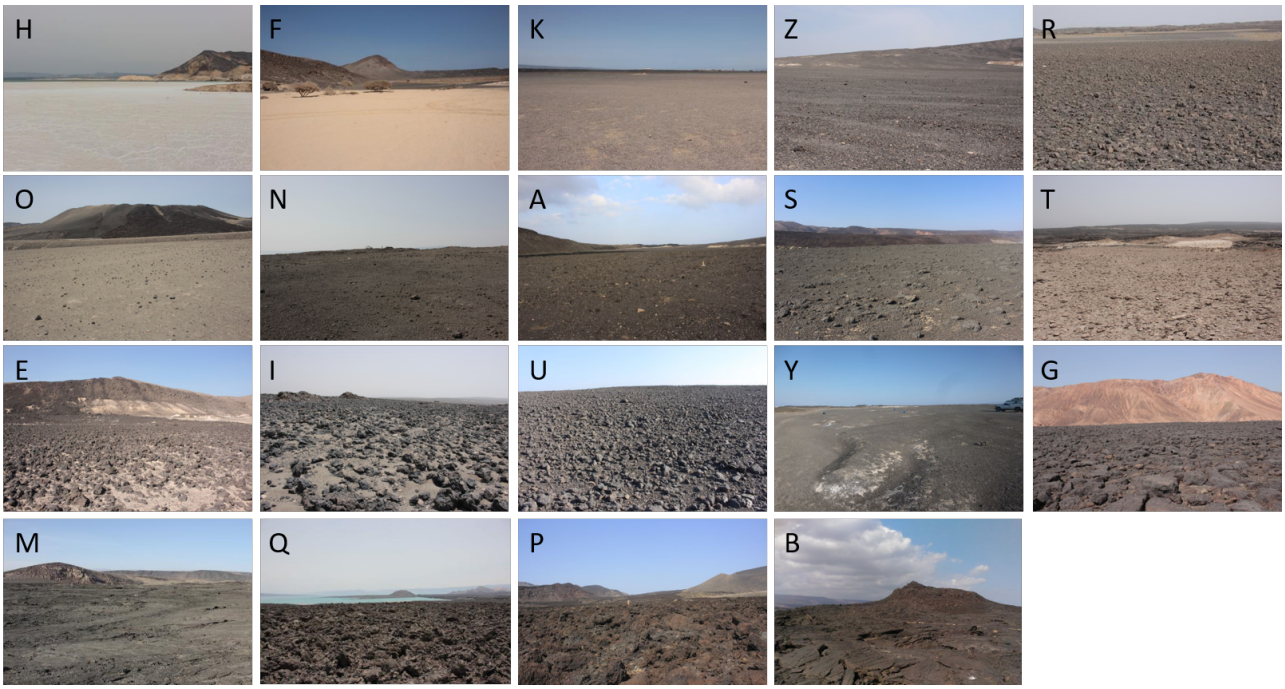

Figure 20 – The nineteen sites of the Asal-Ghoubbet rift, in ascending order of surface roughness (from top left to bottom right).

- *Ground images*

Photographs were used to generate high-resolution DEMs. They were taken by drone and by hand along a transect or within a circle. This has made it possible to obtain DEMs at different resolutions, opening up the possibility of studying the multi-scale roughness of the sites. Drone

11. https://astrogeology.usgs.gov/search/map/moon_selene_kaguya_tc_global_orthomosaic_474m

Site	Latitude N	Longitude E	Description	Mineral composition
A	11.581021	42.493072	Lapilli deposits	Anorthite, Diopside, Hématite, Smectite
B	11.594598	42.472655	Ropy pahoehoe lava	/
E	11.593649	42.491789	Centimetric lava blocks on lacustrine deposits	Anorthite, Quartz, Calcite, Augite, Albite, Amphibole, Palygorskite, Talc, Smectite
F	11.592512	42.495872	Clay deposits	Calcite, Quartz, Albite, Zeolithe, Palygorskite, Smectite, Talc
G	11.562228	42.440316	Decimetric porous lava blocks	/
H	11.619922	42.396506	Salt bank	Halite, Gypsum
I	11.563368	42.448571	Decimetric lava blocks on lacustrine deposits	/
K	11.538943	42.489818	Sand, fluvial deposit	Diopside, Anorthite, Smectite
M	11.589644	42.503011	Fissured lava crust	Diopside, Anorthite, Chlorite, Smectite, Palygorskite
N	11.604637	42.522814	Fractured ancient (aphyric) lava	Diopside, Anorthite, Amphibole, Chlorite, Smectite
O	11.584279	42.513356	Fluvial deposit	Anorthite, Diopside, Smectite
P	11.575606	42.511158	A'a lava	/
Q	11.561884	42.513632	Slab-like basalt porphyry lava	Diopside, Smectite
R	11.536166	42.492341	Coarse lapilli on lacustrine deposits	Bytownite, Anorthite, Vermiculite, Palygorskite
S	11.541699	42.481100	Altered aphyric lava	/
T	11.558583	42.455869	Pulverulent limestone, rich in mollusc shells	Calcite, Muscovite, Quartz, Palygorskite, Smectite
U	11.545372	42.453302	Small alkaline basalt blocks	/
Y	11.586405	42.488147	Remodeled hyaloclastic deposits	Anorthite, Diopside, Smectite, Mg-rich Calcite, Halite, Palygorskite
Z	11.583280	42.489402	Reshaped hyaloclastic deposits	/

Table 2.3 – Geographical coordinates, geological description and mineral composition of 19 sites.

photography is particularly effective for surveying large areas on a scale ranging from a few millimeters to a few centimeters. Photos taken by hand produce sub-millimeter DEMs that allow the study of surface texture and microforms. Transects are obtained by walking along parallel lines in a study site, while circles involve taking photos from several positions around a central point. Ground control points (GCP) that are easily identifiable on the images were placed on the ground during acquisition to correct distortions in the DEMs and improve their accuracy. As previously mentioned, all the DEMs were generated using MicMac.

• *Soil samples*

Soil samples were collected, during the aforementioned mission in 2016, from the various sites and were available in rock, gravel or powder form (Figure 21).

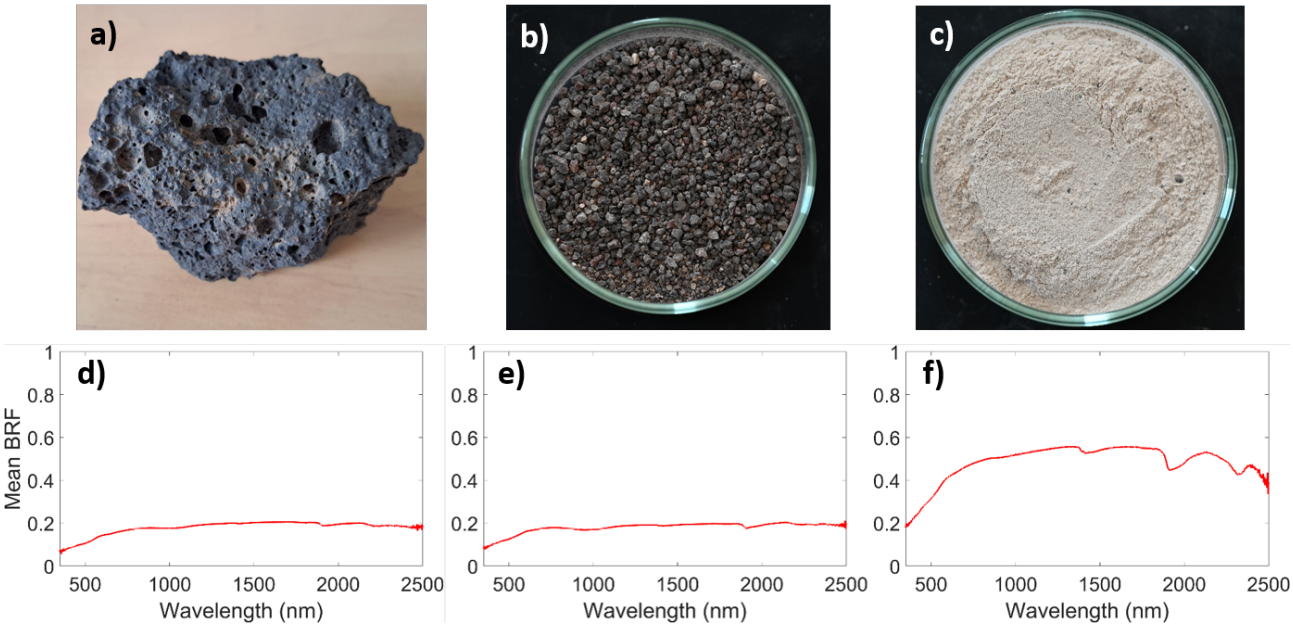

Figure 21 – Field samples of a) rock (site G), b) lapilli (site A), and c) powder (site T). More details are given in Appendix A.

• *BRF measurement of soil samples with goniometer*

From May 31 to June 4, 2021, Mélanie Nguyen, Alice Dupiau and Stéphane Jacquemoud (IPGP) carried out reflectance factor measurements on various soil samples using the SHINE (SpectropHotometer with variable INcidence and Emergence) spectrogonio radiometer of the Institut de Planétologie et d'Astrophysique de Grenoble (IPAG). These sample measurements were used to test the Bayesian inversion using MCMC and the fast Bayesian inversion. SHINE is a high-performance optical instrument, unique in Europe, designed to measure the spectral and directional reflectance of small soil samples in the solar and short-wave infrared domains. The soils must be placed in stainless steel Petri dishes and sieved beforehand, as most are agglomerated into compact lumps. As mentioned above, calibration was carried out using a Spectralon or a an Infragold reference panel (Section 1.1.2). Among 13 samples examined, three are dry samples from the Asal-Ghoubbet rift, namely Djibouti site F, site R and site T (Appendix B). The incident angles are 0°, 30° or 60°, the emergent angles vary in the range [0,70]°. Most measurements are made in the principal plane, where the incident, emergent and normal directions remain in the same plane. As a result, the azimuth difference ϕ tends to be either 0° or 180°, with only a few measurements (no more than 5) taking values in the range [0,90]° (Nguyen, 2021).

• *Spectral measurement of soil samples with FieldSpec© 3 ASD spectroradiometer*

Soil reflectance spectra were measured in the lab between 400 nm and 2500 nm using the ASD FieldSpec© 3 spectroradiometer. The light source was an ASD lamp inclined at 15˚ to the vertical. The pistol grip, equipped with a 8˚ field-of-view, was positioned 24 cm from the samples to take measurements at nadir. Soils samples were rotated 90˚ between each series of 10 acquisitions. The 40 spectra obtained were then averaged to reduce the influence of surface heterogeneities,

and the final reflectance spectrum resampled to 1 nm spectral sampling interval. These spectra may differ slightly from those obtained in the field, as the surface features of the samples at the time of collection are not perfectly preserved. However, this does not significantly change their representativeness. These reflectance spectra are shown in Appendix B and are used to investigate correlations with the SSA determined by inversion of the Hapke model.

- *Mineral composition*

X-ray diffraction analyses of soil and rock samples were carried out at the Institut de Minéralogie, de Physique des Matériaux et de Cosmochimie (Paris, France) to determine their chemical composition, essential information for the interpretation of SSA and phase function parameters estimated by inversion of the Hapke model. The identified constituents of the samples are listed in Appendix B and serve as a reference for the interpretation of the inversion results.

2.4.2 The Moon

The photographs are from the Apollo Lunar Surface Journal [12], a record of the lunar surface operations carried out by the dozen astronauts who landed on the Moon between 1969 and 1972. In this thesis, we will focus on the Apollo 17 mission, which is considered the richest in terms of the amount of samples collected and also the detailed information on lunar rocks gathered by astronaut Harrison Schmitt, the first geologist to go to the Moon. According to Haase et al. (2019), astronauts Eugene Cernan and Harrison Schmitt took 2218 photographs of the lunar surface during the Apollo 17 mission, using the 70 mm Hasselblad camera, with an average pixel size of 22 μm.

2.5 Data preprocessing

2.5.1 Reprojection (Pleiades Moon data)

Originally, the Pleiades data on the Moon came in a special projection called stereographic projection, unlike the rest of the data set, which came in an equidistant cylindrical projection. In mathematics, a stereographic projection is a perspective projection of the sphere, with the point of perspective on the surface of the sphere at a point exactly opposite the point of tangency for the plane (Figure 22). Using the selenographic coordinate system, the coordinate (0,0) is at the center point at the bottom, and the near side of the Moon can be represented by the lower hemisphere. We can therefore produce the Moon image by projecting the features of the lower hemisphere onto the plane, following the projection ray coming from the other pole, passing through the equator and stopping at the tangent plane. In the equidistant cylindrical projection, however, the meridians and parallels are equally spaced lines that form a Cartesian grid. Each rectangular grid cell has the same size, shape and area only in the projected space. Despite the induced distortion, this projection is easy to handle and is commonly used in the NASA-distributed data. In our case, we see its use in the Kaguya global lunar image and the global LOLA DTM.

To convert from a stereographic projection to an equidistant cylindrical projection, we use the function `gdalwarp` of GDAL. The full command is as follows:

12. https://www.nasa.gov/history/alsj/

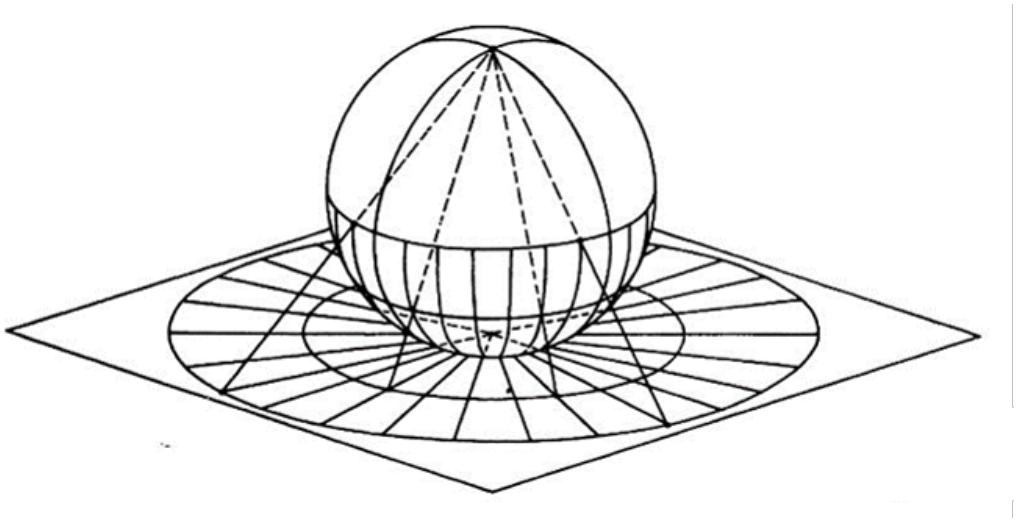

Figure 22 – The relationship between spherical coordinates and stereographic projection (Apostol, 1973).

```
gdalwarp -s_srs <proj1> -t_srs <proj2> -r near -of GTiff <input_dir>
<output_dir>
```

where `<proj1>` and `<proj2>` are:

```
+proj=stere +lat_0=0 +lon_0=0 +ellps=sphere +R=1737500 +units=m
```

and

```
+proj=eqc +lat_ts=0 +lat_0=0 +lon_0=0 +x_0=0 +y_0=0 +a=1737400 +b=1737400
+units=m +no_defs
```

where `<input_dir>` and `<output_dir>` are the input and output directories of the raster. The number 1737500 m represents the radius of the Moon as supplied by CNES. It differs from 1737400 m, which is widely used in the data distributed by NASA. This applies to both the images and the geometric configuration maps.

2.5.2 Image co-registration

- *Asal-Ghoubbet rift*

Precise alignment of the images is essential in this work because BRDF must be extracted on the same pixels. As the ortho-images supplied by CNES could not be fully superposed, we undertook an additional coregistration step. We first applied the Scale-Invariant Feature Transform (SIFT) algorithm (Lowe, 1999) in Orfeo ToolBox (Grizonnet et al., 2017) to identify the tie points between the master image, the one with the smallest phase angle and therefore assumed to be the least distorted, and the other images. We then calculated the average distance between the match points and applied a uniform adjustment to align all the images with the reference position of the master image. The average distance measured between the master image and the others is, for 16 images out of 21, less than or equal to five pixels, representing a ground distance of 10 m. It should be noted, however, that this approach mainly corrects translational misalignments but not other distortions.

• *The Moon*

Comparing the Pleiades images to the Kaguya global image of the Moon, the alignment is acceptable, so co-registration was unnecessary.

2.5.3 Image resampling

• *Asal-Ghoubbet rift*

As the common area for all the images covers 26.7 km × 20.3 km, over a hundred million pixels would have to be processed at a spatial resolution of 2 m. The computation time for such a large amount of data would be prohibitive, on the order of several months on a PC. We have therefore reduced the resolution of the images by a factor of five (GSD = 10 m). However, the original resolution (GSD = 2 m) was retained for the experimental sites, which cover 20 m × 20 m or 20 m × 30 m and correspond to only a few hundred pixels. The Pleiades DEM (GSD = 4.5 m) is downsampled accordingly. We used bilinear resampling, a simple algorithm with a low computational cost that works well with a continuous surface.

• *The Moon*

The GSD of the Pleiades images is 1500 m, while the GSD of the LOLA DTM is 118 m. We therefore need to reduce the DEM sampling so that the GSD is similar, in order to facilitate processing between the different data. Again, we used bilinear resampling.

Conclusion

This section concludes with a presentation of the regions of interest, the Asal-Ghoubbet rift and the near side of the Moon, and the strategic reasons for their selection. With its varied types of terrain and minimal disturbance from wildlife or human activity, the Asal-Ghoubbet rift provides an excellent terrestrial analogue for planetary environments. Conversely, the near side of the Moon was chosen because of the wealth of satellite and terrestrial data available, making it a rich resource for scientific investigation. Comparing these different data sets offers a unique possibility to gain a better understanding of the processes at work on planetary surfaces.

We also discussed the types and scales of data we use, detailing how each dataset is acquired, its characteristics and the preprocessing steps required to make it suitable for analysis. Among the different types of data, the Pleiades multi-angular images of the Asal-Ghoubbet rift and the Moon stand out. These images benefit from the satellite's high-resolution sensor and flexible pointing capability, allowing us to obtain detailed photometric data from multiple angles, which is essential for advanced photometric analysis. By integrating all these data sources and applying rigorous data processing techniques, we can study and compare the geological features of the Earth and Moon. This lays the groundwork for the inversion and analysis chapters to follow, and also highlights the innovative approach of our research in harnessing detailed planetary data for wider scientific discovery.

Chapter 3

Digital elevation model generation and surface roughness study

Introduction

This chapter described the generation of digital elevation models (DEM) using the datasets discussed previously. We begin with an introduction to photogrammetry, a widely-used technique for DEM generation. We will use MicMac, a powerful open source software known for its accessibility, its ability to handle large datasets and produce high quality elevation models. We will examine the specific configurations and parameters within MicMac that are optimized for our data to ensure that the resulting DEMs are both accurate and aligned with our research objectives. Once the DEMs have been generated, we will carry out thorough post-processing to improve and validate their quality.

We will then focus our analysis on surface roughness, a critical surface property introduced earlier in the thesis. The elevation data obtained from the DEMs provide the necessary metrics to quantify and evaluate it. To capture the multiscale nature of surface roughness, we use wavelet decomposition as an effective technique for detailed analysis.

At the end of this chapter, we will show the roughness calculation on the DEMs (in the AG rift and on the Moon) and their roughness components obtained by wavelet decomposition. We will then attempt to analyze the terrain characteristics using a number of roughness parameters.

3.1 General concepts of photogrammetry

Stereo-photogrammetry allows the 3D structure of an object or scene to be reconstructed from photographs taken from different angles. This technique is used in a wide range of applications including topographic mapping, architecture, engineering, cultural heritage, and geology. The reason for its widespread use is simple: the rapid development of of low-cost, high-quality cameras, together with increases in computation speed and accuracy over the last two decades, and active research in photogrammetry and computer vision, have made this technique affordable (Bretar et al., 2013).

The way this works is similar to human vision: our eyes register two slightly offset images of a given object, then our brain processes the images to visualize them in three dimensions in our mind. The details of each step will be discussed later, but in summary, the common points in each image, called tie points, are identified; then a line of sight (a ray) is constructed from the camera position to each point; finally, the intersection of these lines determines the three-dimensional location of the point (Figure 23).

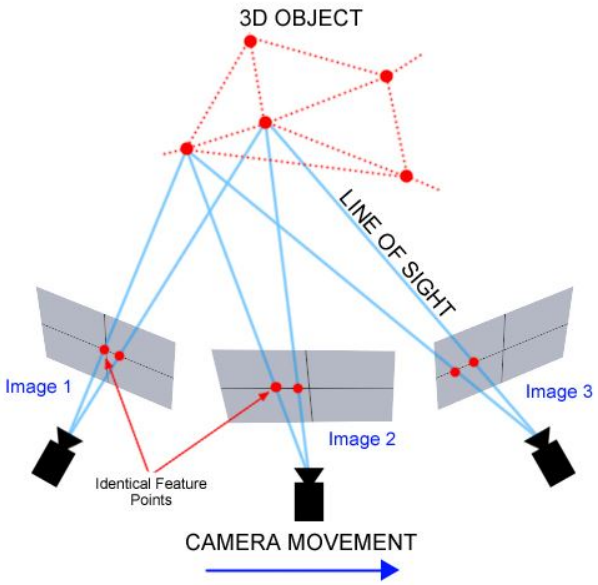

Figure 23 – Easy representation of the 3D configuration during the photogrammetry process [1].

The procedure begins with the identification of tie points between images, followed by orientation calculations, including interior, relative, and absolute orientations, as shown in Table 3.1. Image correlation is then performed, leading to the final step of triangulation. This is the process of combining overlapping photographs taken from different angles to determine the 3D position of each point, ultimately creating a surface model. Each of these stages plays a crucial role in determining the overall quality of the final output. The result of triangulation is a point cloud, which can then be projected to create a DEM. This process generally requires images of the region of interest from different viewing angles with a high degree of overlap, as well as accurate camera model and orientation data.

Scientists have several photogrammetry softwares available to them, including commercial, free and open source options. Each offers unique features to suit different research needs, preferences, and budgets. SOCET SET, Agisoft Metashape or Pix4D are leading commercial sofwares, widely recognized for their robust processing capabilities, extensive support and advanced features that facilitate detailed and accurate photogrammetric analysis. On the other hand, the availability of free and open source software offers alternatives that are beneficial for academic and low-budget projects. Notable examples include IGN's MicMac, Nasa's Ames Stereo Pipeline (ASP), COLMAP and VisualSFM.

1. https://thehaskinssociety.wildapricot.org/photogrammetry

Orientation	**Interior**	**Relative**	**Absolute**
Connection	Between the pixel (camera) and the image coordinate system	Between the relative position and attitude of two images	Between image coordinate to the object space coordinate system (terrain)
Input	— Digital image — Camera type and extra information on lens distortion, pixel size of the digital images — Image coordinates of the fiducial marks	— Images — Results of interior orientation	— Images — Externally-provided control information (ground control points are one of them)
Output	— Pixel coordinates of each fiducial — Parameters of the chosen transformation from pixel to image space	— Three-dimensional arbitrary coordinates of the conjugate features	— Absolute position and attitude of camera positions — Three-dimensional coordinates of the conjugate features

Table 3.1 – Discerning the three major orientations (Heipke, 1997; Linder, 2009).

3.2 The MicMac sofware

3.2.1 Overview

MicMac was developed by IGN (Institut national de l'information géographique et forestière) and ENSG (École nationale des sciences géographiques) with contributions from IPGP (Pierrot-Deseilligny and Clery, 2011; Pierrot-Deseilligny and Paparoditis, 2012; Bretar et al., 2013). We have chosen it for several reasons:

• It is easily accessible because it is free and open source, and runs on a variety of operating systems: Gnu/Linux, Windows and Mac.

• It can be operated either via a graphical user interface or via command lines, making it a great tool for testing and studying digital photogrammetry, while still being able to use modifications made by professionals.

• It is highly adaptable to terrestrial, aerial and even satellite imagery. It also provides tools for geo-referencing finished products in a predefined coordinate system (local, global or absolute).

• It has the ability to process massive datasets (which is also possible with ASP).

• Thanks to the privileged relationship between IPGP and the MicMac development team, our expertise of the behavior, abilities and limitations of the code is important.

MicMac has been used for various types of 3D reconstruction and is applicable to a wide range of fields: forestry (Lisein et al., 2014), heritage (Pinte et al., 2015), archaeology (Mouget and Lucet, 2014), tectonics (Rosu et al., 2015). In addition to the advantages mentioned above, MicMac has its own limitations: its learning curve is steep, it's not optimized and it's not very user-friendly.

MicMac was used by Labarre (2017); Rupnik et al. (2018) to reconstruct a 4.5 m resolution DEM of the Asal-Ghoubbet rift from Pleiades images (Figure 24). In addition to this regional scale DEM, 17 millimeter-scale DEMs were derived from drone surveys, and a further 5 submillimeter-scale DEMs were derived using a handheld camera Labarre (2017).

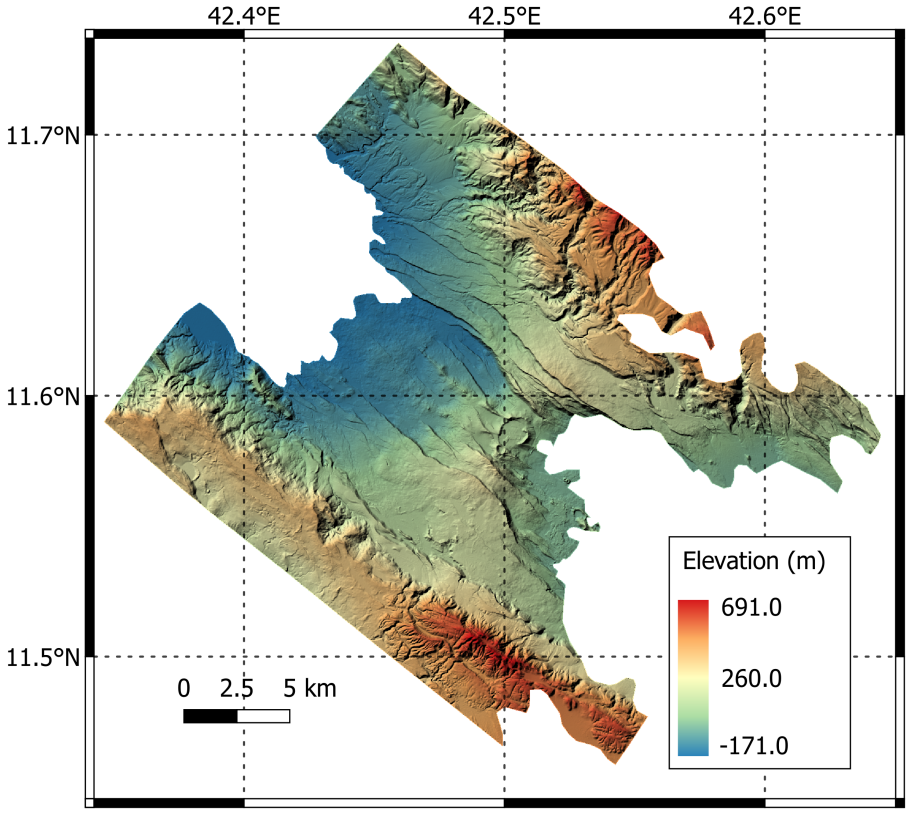

Figure 24 – DEM generated from Pleiades images (Labarre, 2017; Rupnik et al., 2018).

3.2.2 Structure and tools

a) Structure

The MicMac pipeline consists of a sequence of complex steps, each of which consists of smaller, integrated tools. Here is a breakdown of the four main steps in the pipeline, with the name of the corresponding tool:

- **PASTIS** (Programme Autopano Sift pour les Tie-points dans les ImageS) is essentially an interface to the well-known Sift++ distribution (Vedaldi, 2007) of the SIFT (Scale-Invariant Feature Transform) algorithm (Lowe, 2004).

Site	Drone DTM	Profile DTM	Circle DTM	ASD	Diffractogram
A	4.0		0.6		
B	3.5				
E	3.2				
F	3.0		0.6		
G	3.2				
H	3.0				
I	3.2		0.6		
K	3.0				
M	2.8	0.8			
N	1.3				
O	8.0		0.6		
P	3.2		0.6		
Q	2.8	0.9	0.6		
R	3.2	0.9	0.6		
S	3.2	1.0	0.6		
T	2.8	0.7	0.6		
U	2.5	0.5	0.6		
Y	3.5		0.6		
Z	2.5				

Figure 25 – Progress of data generation and collection, combining the work of this thesis (blue boxes) and that of Labarre (2017) (green boxes). Empty boxes indicate no data, while red boxes represent damaged/incomplete data. The values are the DEM resolution in millimeter. The last two columns indicate the sites for which reflectance spectra and mineralogical composition were measured in the laboratory (Chapter 2).

PASTIS is an integral component of the photogrammetry toolkit, specifically designed to automate the critical process of identifying tie points between multiple images. This automation is essential for establishing relative orientations between images, which is a fundamental step in constructing accurate 3D models and maps from 2D images. Its effectiveness is largely due to the resilience of the algorithm to changes in scale, rotation and noise, making it particularly suitable for processing images acquired under different environmental and operational conditions. Despite these strengths, the PASTIS SIFT algorithm is not without its challenges: (1) Diachronism sensitivity: The algorithm can be sensitive to changes between images over time, such as variations in lighting conditions, environmental changes, and the dynamic movement of shadows. These factors can lead to inconsistent and unreliable tie points, as the algorithm may fail to correctly match points that do not appear identical due to these temporal variations. (2) Difficulty with strong affine

transformations: PASTIS may have difficulty matching images that have undergone significant affine transformations—changes that include rotation, scaling, translation, and shearing, especially when the images are taken from very different perspectives or angles (Le Bris and Paparoditis, 2010).

- **APERO** (Aérotriangulation Photogrammétrique Expérimentale Relativement Opérationnelle) plays a critical role in the photogrammetry workflow by using the tie points identified by PASTIS and any other relevant measurements to accurately determine the orientation of images. Its main task is to calculate both the external orientation, which refers to the position and angle of the camera relative to the photographed object, and the internal orientation, which deals with the optical characteristics of the camera itself. It operates through a two-block system that addresses both the initial orientation solution and its optimization.

    - **Initial Solution Calculation**: The first block of APERO uses a rigorous approach centered on geometric constraint equations that adhere to the coplanarity principle: For two photographs, the two conjugate rays defined on each object point must be coplanar. The corresponding mathematical condition, known as the coplanarity equation, implies that the two camera stations, the two image points, and the object point are in the same epipolar plane (Figure 26). The process starts by identifying a "parent" image, which is typically the image with the most overlap with other images in the dataset. The choice of the parent image is strategic, as it acts as an anchor for the alignment of all other images. Subsequent images are oriented relative to this parent image. This orientation involves the computation of essential matrices that are fundamental in describing the geometric transformations, such as rotation and translation, required to align each new image with the reference. The priority for processing images is determined by the number of tie points and their spatial distribution across the images. Images with a higher number of tie points and a well-distributed set of points are generally processed earlier, as they provide more robust data for accurate alignment.
    - **Bundle Adjustment Module**: The second block of APERO includes a bundle adjustment module, a technique described by Triggs et al. (2000), which refines the initial solution by minimizing a cost function using a least squares method. This minimization is achieved by linearizing the equations to simplify the computations. The position of each corresponding point is determined by the intersection of the lines of sight (or beams) from all the images in which the point is visible. This intersection is computed in the ground reference frame, integrating both the internal orientation parameters of each sensor and the relative orientations from the initial setup. Each 3D point determined from the lines of sight is then reprojected back into the individual images. During reprojection, the image position of the 3D point is predicted based on the refined camera parameters and compared with its actual position in the image. The differences between these projected and actual positions are the reprojection errors, which are critical metrics in the optimization process. These errors are quantified for each point in each image, providing a comprehensive set of discrepancies. The sum of all reprojection errors forms a cost function, which is then minimized using a least squares method. This statistical approach is ideal for dealing with the potentially large

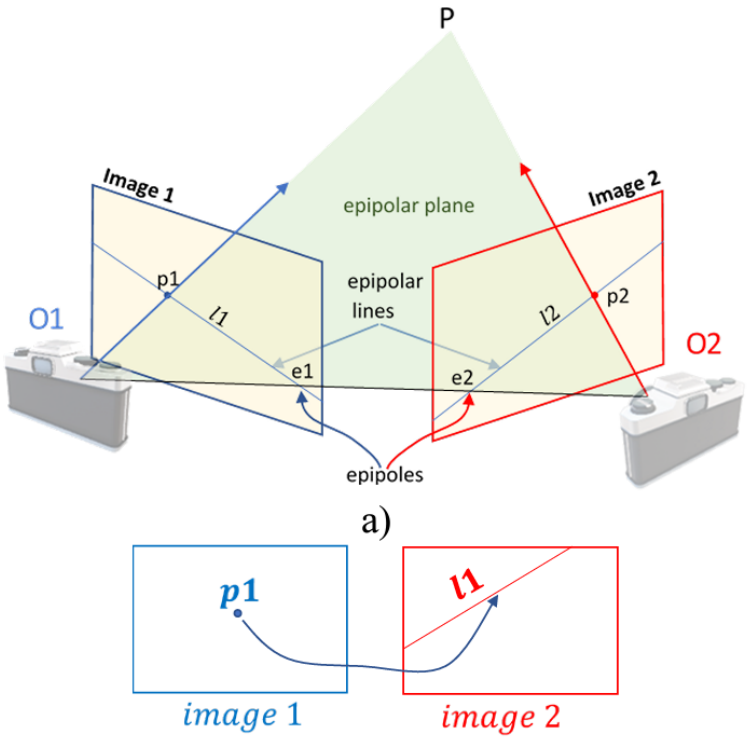

a)

Figure 26 – Basic principle of 3D point reconstruction from images – geometry of coplanarity. An object is captured in at least two different photographs and the corresponding image point coordinates of p_1 and p_2 are measured. With additional camera orientation information for O_1 and O_2, the corresponding 3D point P can be calculated by forward intersection (Fritsch et al., 2020; Alsadik and Abdulateef, 2022).

number of variables and observations and aims to find the parameter set that best fits all the observed data Pierrot-Deseilligny and Paparoditis (2012). The iterative optimization adjusts the orientation parameters incrementally until the reprojection errors are minimum, indicating that the positions and orientations of the cameras and the scene geometry have been optimally determined.

- **MICMAC** (Multi-Images Correspondances) is based on the orientations refined by APERO, which performs a dense matching of correctly oriented images. It calculates dense correlations and obtains topographic information on each point of the surface, based on the correlation method in epipolar geometry. The solution to this problem, as described by Roy and Cox (1998), has the disadvantage of being very demanding in terms of computational time and memory. Pierrot-Deseilligny and Paparoditis (2012) proposed a multi-resolution approach by defining an image pyramid of resolution 2^K with $K \in \{1, ..., N\}$. This technique limits the possible solutions at each step, which greatly reduces the computation time. This tool works using one of the two correlation strategies:

  - **Terrain geometry** (Paparoditis et al., 2000) is an approach particularly suited to images taken from high altitudes, such as from aircraft or satellites. This method focuses on creating a single, comprehensive depth map that encompasses the entire area covered by the image. For each object point in the terrain, the elevation is determined by simultaneously matching all images in which it is visible. Users can adjust various parameters to improve the matching, such as the size of the correlation window, which

affects the precision and the scale of the matching, and a regularization parameter, which helps to deal with real surface discontinuities, and thus noise in the final product.

- **Image geometry** (Pénard et al., 2006), on the other hand, is better suited to shorter range or lower elevation imagery, such as that taken during in situ measurements. It is particularly useful when dealing with complex objects or terrain that do not lend themselves well to a simple depth map, and are better represented as a point cloud. The depth for each image point is calculated by intersecting the ray from that point with the ray from the pixel that has the highest correlation coefficient on a corresponding "child" image. This calculation is made along the epipolar line. This method generates as many depth maps as there are images. The generated depth maps are then merged and converted into a geometric terrain model.

- **PORTO** uses rectified images, optionally processed by MicMac, to stitch together a global orthophoto. This involves aligning the images not only spatially, but also in terms of lighting and color, to ensure a seamless, large-scale representation of the area.

b) End-user tools

This section briefly introduces some of the main tools used to create DEMs. They are presented in the order of the complete MicMac photogrammetric procedure, from start to finish. However, in some specific situations, which will be presented later, certain steps may be skipped.

• **Tapioca**: a PASTIS interface for the calculation of tie points (points in common between images).

• **Tapas**: a simplified APERO interface dealing with relative orientations.

• **AperiCloud** generates a point cloud from the tie points calculated by `Tapioca` in the orientation calculated by `Tapas`. It allows to visualize the position of the shots as well as the estimated relative position of the surface points. The generated point cloud is in `.ply` format and can be visualized using MeshLab or CloudCompare. This tool is usually used immediately after `Tapas` to check if there are any anomalies during the initial stages of the procedure.

• **SaisieAppuisInit** generates an interface to manually locate the GCPs on the images. Based on our experience, we only need to define their location on a few instead of all images, and MicMac will automatically find the location of that GCP in the rest of the images.

• **GCPBascule** allows to transform a purely relative orientation (as computed with `Tapas`) into an absolute one, as soon as there are at least three GCPs whose projection is known in at least two images. To ensure uniformity of coordinates in all three spatial directions, absolute orientation is calculated in the Universal Transverse Mercator (UTM) system.

• **Campari** performs Bundle Block Adjustment, refining the orientation using the observations provided by the tie points and ground control points. It is similar to `Tapas`, which allows the observations to be used either as control points (influencing the adjustment) or as verification points (not influencing the adjustment). Verification points are used to ensure the quality of the results by comparing their position before and after refinement with their actual position on the

ground. Their distribution on the image should be dispersed, especially in areas without GCPs.

- **Malt / C3DC / PIMs**:

The `Malt` tool is a simplified interface to the MICMAC matching tool that allows the reconstruction of a depth map suitable for terrain geometry. Meanwhile, the `C3DC` tool calls Malt in image geometry. There is another tool called `PIMs`, which stands for *Per Image Matchings*. This tool calculates a depth for each image. These depth maps are then georeferenced and merged into a single digital surface model covering the entire area, with the tool `PIMs2Mnt`.

3.3 DEM generation

3.3.1 Asal-Ghoubbet rift

The difference between the methods could be attributed to the presence or absence of GCPs. In the case of photogrammetry with drone photography, it generally follows the steps that was introduced by Labarre (2017) (Figure 27a). On the other hand, the absence of GCPs in the case of handheld camera photography leads us to carry out the procedure in a slightly different way (Figure 27b). The main differences are the absolute orientation and the post-processing steps consisting of alignment and scaling.

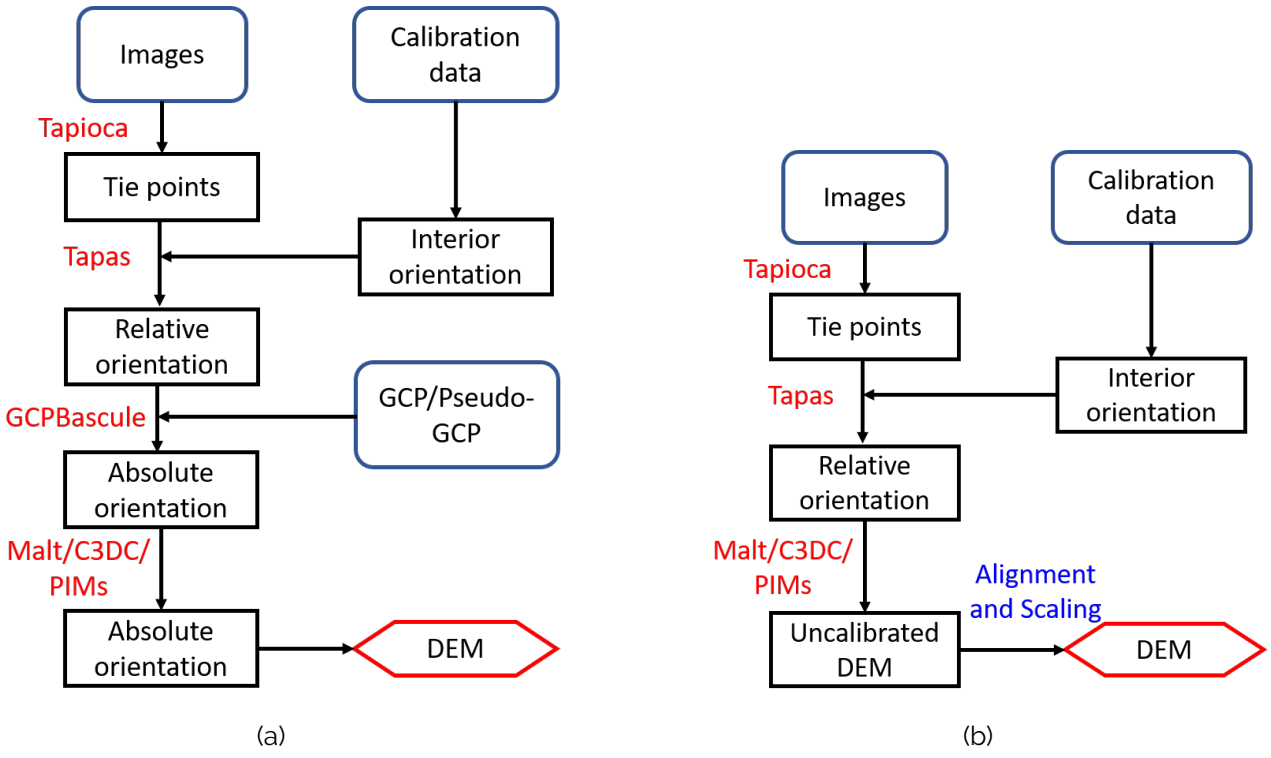

Figure 27 – Diagrams illustrating the MicMac software processing chain. The blue boxes represent input data, the black boxes the processing stages, the red text the different MicMac tools for each step and the blue text the external processing. There are two scenarios: a) The presence of GCPs or user-defined coordinates (pseudo-GCP) Labarre (2017); b) The absence of GCPs.

In the case of circle photography (DEM generation using handheld photography taken around a circle, introduced in Section 2.4.1), a common feature between the images is a block of wood, which is used to create pseudo-GCPs (Figure 28a). Unlike normal GCPs, their coordinates are not

established using a GPS sensor, but rather on the basis of the user's knowledge of the element in the scene. The resulting DEM is therefore not georeferenced. Knowing the exact size of this wooden block ($16 \times 16 \times 2.7$ cm), we defined the top surface of the block as a plane parallel to the xy plane with a constant height of 2.7 cm. Its center point is at $(x, y, z) = (0, 0, 2.7)$ cm. In Figure 28a, wa have generally defined three points on the block as inputs to the `SaisieAppuisInit` tool. Then, G1=(0,0,2.7), G2=(-11,31, 11,31, 2.7) and G3=(11,31, 11,31, 2.7) (all in centimeter) are obvious results of the Pythagorean theorem. Thanks to the pseudo-GCPs, the rest of the procedure would be similar to Figure 27a.

In the case of the profile photographs, we applied the same procedure as for the circle one on some sites. On other sites, however, we were unable to do this because (i) the wooden block only appears towards the end of one side, making correlation on the other side unreliable, or (ii) there are no wooden blocks or other identifiable objects in the images. In situation (ii), we didn't specify the GCPs and went straight from relative orientation (`Tapas`) to DEM generation (Figure 27b). Subsequently, if the profile photographs fell within the coverage area of the drone DEM, we tried to find areas of overlap between these two datasets and then reconfigured the geometry of the small profile DEM to fit within the larger drone DEM. This procedure will be explained in Section 3.4.

Once the size of an object in a scene is known, we can choose to use the diagram in Figure 27b instead of Figure 27b. Having obtained a DEM of arbitrary scale (where its components still maintain proportional relationships), the first step is to transform the DEM into a point cloud. We then calculate the scaling factor between the size of the known object in the DEM and its actual size. This scaling factor is then applied to the entire point cloud, and finally the rescaled point cloud is projected to create a new, accurately scaled DEM. This whole process is called "recalibration" and is a key part of DEM post-processing.

3.3.2 The Moon

For the ground images taken by the Apollo Lunar Surface Journal, we used the same scheme as shown in Figure 27a. As these are ground-based images without GCPs, we again need to define pseudo-GCP. For example, in figure 28a we found the size of the astronaut's boot. Using this information, we defined the coordinates of several points on the footprint.

Instead of footprints, the known object may be a gnomon, a tool that provides a physical reference to facilitate the measurement of angles and distances in surveyed environments. It typically consists of a stadia rod, mounted on a gimbal inside a tripod. By casting a shadow, the gnomon provides a visible marker of the angle of the sun in relation to the lunar surface. This shadow is used to determine the position of the Sun in the sky, which can be correlated with the time and position of the Moon. The length of the rod and the painted scale provide a reference for estimating the size of nearby objects. In Figure 30, we can see this in the point cloud.

2. https://airandspace.si.edu/collection-objects/boot-left-lunar-overshoe-cernan-apollo-17-flown/nasm_A19740133005
3. https://www.lpi.usra.edu/science/kring/lunar_exploration/geologicTools.pdf

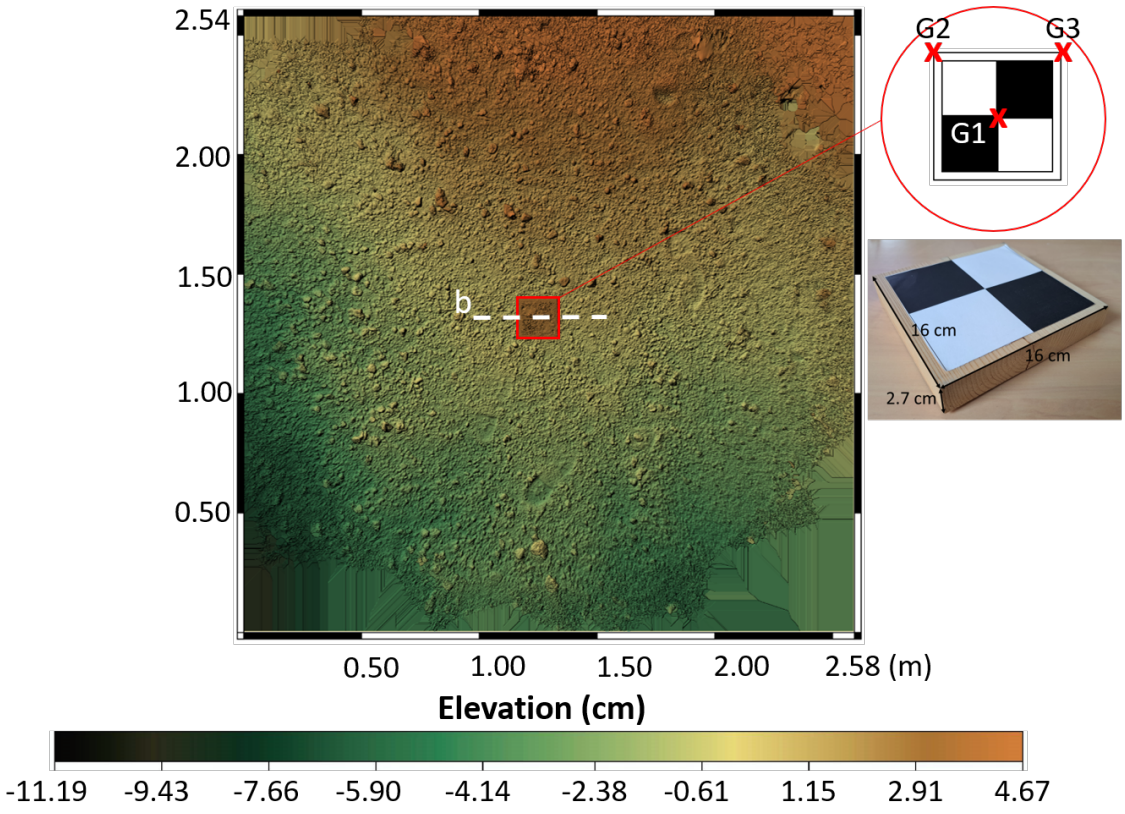

(a)

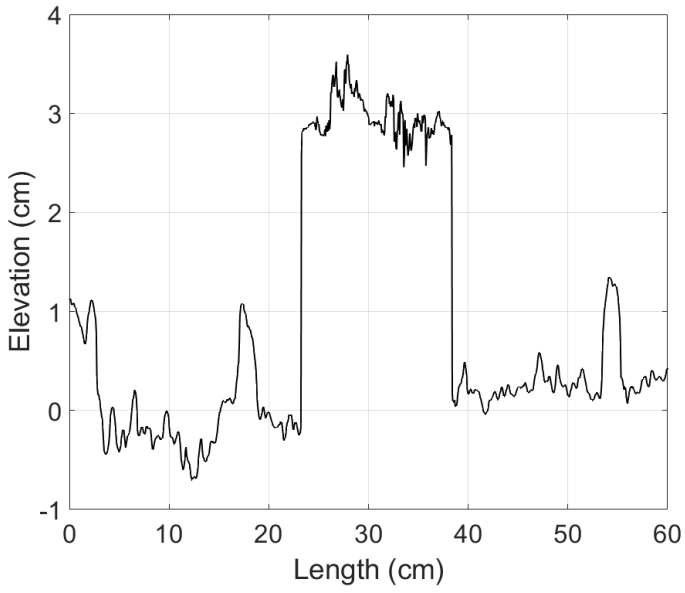

(b)

Figure 28 – a) Circle DEM of site A, showing the wood block and the pseudo-GCP identification (red x symbol), which plays an important role in the DEM generation. The white dashed line in the center of the DEM is the extent of the elevation profile plotted in graph (b).

3.4 DEM alignment

The need to align DEMs arises when we have two types of DEMs: one is georeferenced and the other has an arbitrary scaling, a consequence of the scheme in Figure 27b. Before aligning two DEMs (or rather two point clouds), we should find the tie points using the

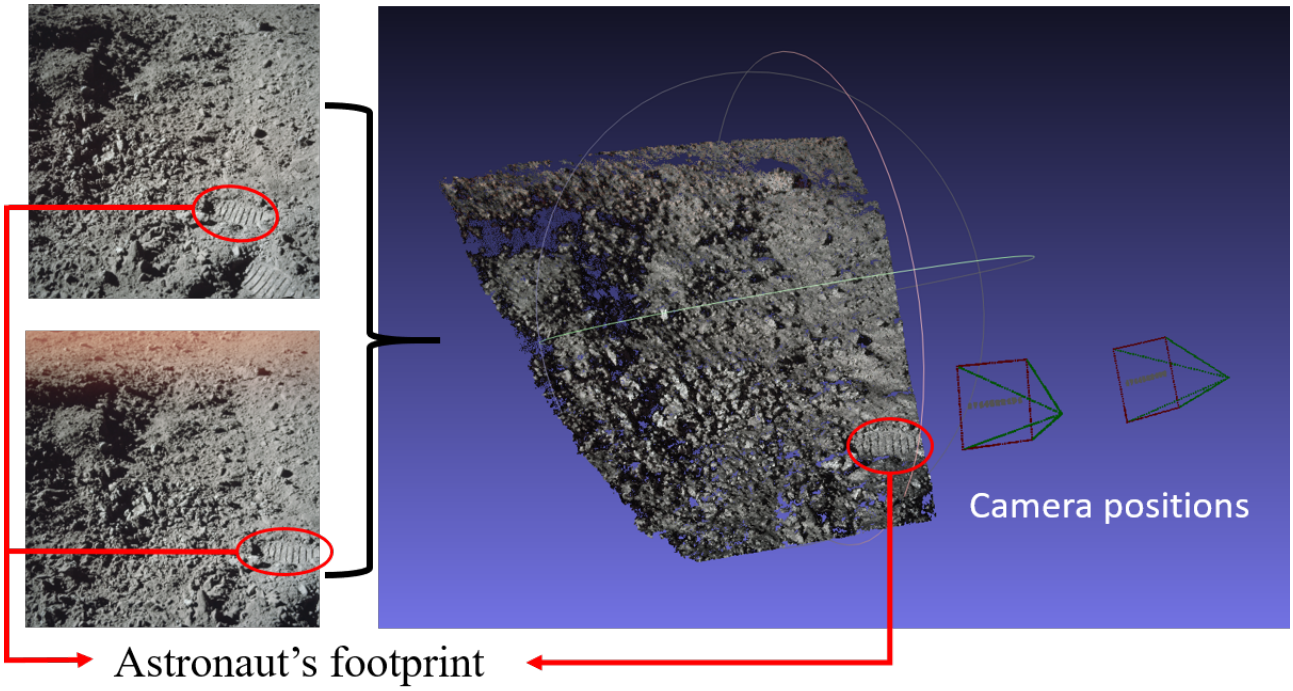

Figure 29 – Dense point cloud of the near-ALSEP site (Apollo 17) generated by MicMac (with C3DC), visualized using Meshlab Nguyen (2019). The two pyramids on the right side of the image indicate the 3D position and orientation of the camera with respect to the captured terrain. The red circle indicates the location of the astronaut's footprint (33×17.8 cm^2).

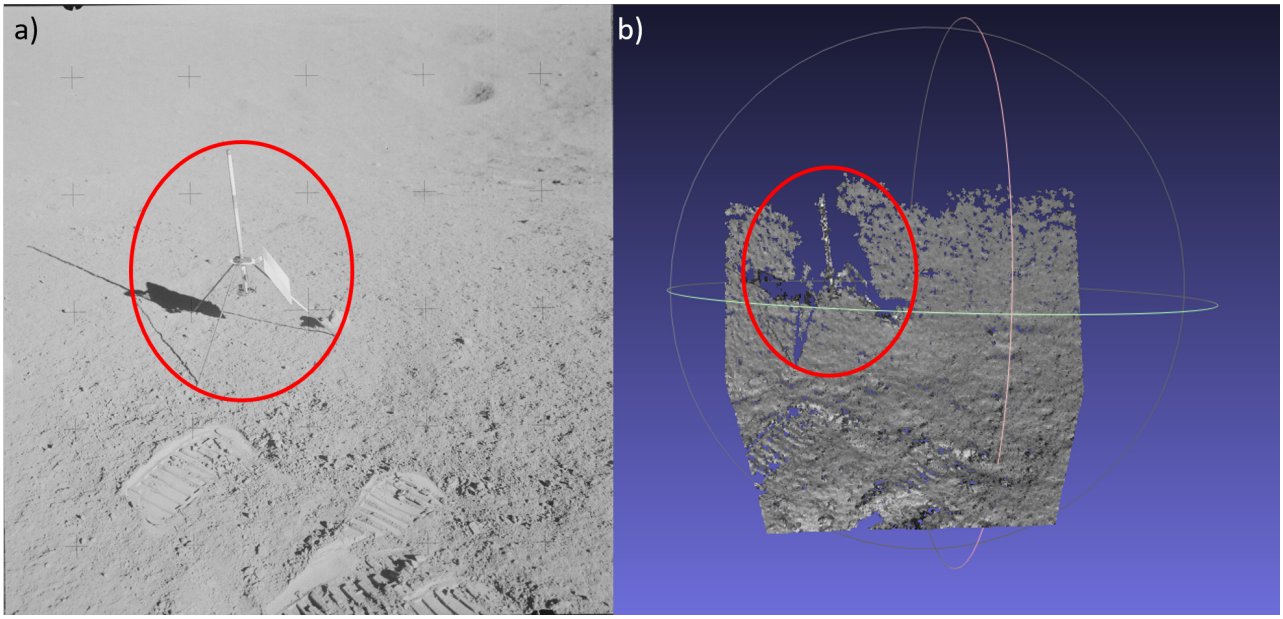

Figure 30 – a) Image AS14-68-9410 used to create the DEM and b) Dense point cloud of site A in Apollo 14 landing site generated by MicMac (with C3DC), visualized using Meshlab Vo (2023). In the red circle is a gnomon of known size (62 cm when deployed [3]).

`HomologousPointsExtraction` tool from Orfeo ToolBox (OTB), which uses the same SIFT algorithm implemented in MicMac. The input data are simply the two DEMs (downsampled if necessary). The main output is a text file listing the tie points in four columns: the xy coordinates of the points in the first DEM and the xy coordinates of the corresponding points in the second DEM. Next, we need to bring the two DEMs into the center of the Cartesian coordinate system using a simple

translation. Naturally, the coordinates of the tie points are also shifted.

Two methods are used in the alignment process: the Helmert transformation and the iterative closest point (ICP). The Helmert transformation is used to roughly move two DEMs closer together, although it does not guarantee high accuracy. The ICP is used as a refinement step when the DEMs are already close together. When they are far apart, it is common to use both methods in sequence. However, neither the Helmert transformation nor the ICP are suitable for aligning surfaces with non-rigid deformation (e.g., facial structures that deform beyond translation, rotation, and scaling) (Li et al., 2022). Fortunately, this does not apply to our data. It is also important to note that aligning DEMs using these methods allows them to be indirectly georeferenced.

3.4.1 Helmert transformation

The Helmert transformation Arfken et al. (2012) is a geometric transformation method in three-dimensional space. It is often used in geodesy to create datum transformations. It can be expressed as:

$$X_B = C + \mu R X_A \tag{3.1}$$

with the transformed vector $X_B = \begin{bmatrix} x_B \\ y_B \\ z_B \end{bmatrix}$, the initial vector $X_A = \begin{bmatrix} x_A \\ y_A \\ z_A \end{bmatrix}$, the translation vector $C = \begin{bmatrix} C_x \\ C_y \\ C_z \end{bmatrix}$, containing the three translations along the coordinate axes, μ the scale factor, R_X, R_Y and R_Z the rotation matrices:

$$R_X = \begin{bmatrix} 1 & 0 & 0 \\ 0 & \cos(\alpha_x) & \sin(\alpha_x) \\ 0 & -\sin(\alpha_x) & \cos(\alpha_x) \end{bmatrix}, R_Y = \begin{bmatrix} \cos(\alpha_y) & 0 & -\sin(\alpha_y) \\ 0 & 1 & 0 \\ \sin(\alpha_y) & 0 & \cos(\alpha_y) \end{bmatrix}, R_Z = \begin{bmatrix} \cos(\alpha_z) & \sin(\alpha_z) & 0 \\ -\sin(\alpha_z) & \cos(\alpha_z) & 0 \\ 0 & 0 & 1 \end{bmatrix} \tag{3.2}$$

with $\alpha_x, \alpha_y, \alpha_z$ the rotation angles around the x-, y-, and z-axes counterclockwise. Then,

$$R = R_x.R_y.R_z \tag{3.3}$$

This equation has seven parameters ($C_x, C_y, C_z, \mu, \alpha_x, \alpha_y, \alpha_z$). Therefore, at least seven tie points are required to use this method. In MATLAB, we first converted the DEM to be aligned into point clouds, defined the Helmert transformation function, and then used the Nelder-Mead (simplex) method to find the most likely set of Helmert parameters. We then simply applied the transformation to the remaining points, projected it and created a new DEM.

3.4.2 Iterative Closest Point

The Iterative Closest Point (ICP) algorithm is designed to minimize the difference between two sets of points. Typically, it iteratively minimizes the mean square distance between corresponding points, which requires an initial estimate of the alignment, and then converges on a local minimum. Note that ICP is only effective when the two DEMs are already partially aligned (possibly by a Helmert transformation), allowing the algorithm to focus on fine-tuning the remaining misalignment. This method was first introduced by Besl and McKay (1992). Since ICP operates on point clouds, it is necessary to either use the original point clouds generated by MicMac or to convert the two DEMs to point cloud formats prior to alignment. The algorithm can be found in MATLAB (Wilm, 2024) or in Python using the verb|Open3D| library. For a more detailed view, variants of the ICP algorithm can be broken down into five consecutive steps (Correll et al., 2022):

- Selection of points in meshes or point clouds
- Matching these points to the samples in the other mesh/point cloud

We can use SIFT, which matches points based on their visual appearance. As with SIFT feature sorting, the search for the closest matching point can be accelerated by representing the point cloud in a k-d tree, a space partitioning data structure for organizing points in a k-dimensional space.

- Weighting the corresponding pair

Since some pairs match better than others, intelligent weighting could significantly improve the quality of the resulting transformation. One approach is to give more weight to points that are close together. Another approach is to take into account the color of the point or to use the distance of their SIFT features (giving more weight to pairs with a small distance than to pairs with a large distance). Finally, the expected noise can be used to weight the pairs.

- Rejection of certain pairs that are considered to be outliers

One of the main problems with ICP is the presence of outliers due to sensor noise or simply incomplete overlap between two successive distance images. A preferred approach to dealing with this problem is to reject pairs where one of the points lies on a boundary of the point cloud, as these points are likely to correspond to points in non-overlapping regions. Depending on the underlying data, it may be also useful to reject pairs that are too far apart. This is a threshold-based equivalent of the distance-based weighting described above.

- Assignment of an error metric on the basis of the point pairs and minimization of the error metric

Once the points have been selected and matched, the pairs weighted and rejected, the correspondence between two point clouds needs to be expressed in terms of an appropriate error measure, which is then minimized. A simple approach is to consider the sum of the squared distances between each pair. This formulation can often be solved analytically. Let $A = a1, ..., an$, $B = b1, ..., bn$ be point clouds in R^n. The goal is now to find a vector $t \in R^n$ that minimizes the error function $\Phi(A + t, B)$. An error function for the squared distance is then given by Equation 3.4.

$$\Phi(A+t,B)=\frac{1}{n}\sum_{a\in A}\|a+t-N_B(a+t)\|^2 \tag{3.4}$$

$N_B(a+t)$ is a function that returns the nearest neighbor of a translated by b in B. One of the main problems is that the actual value of t affects the matching result. What appears to be a good match often turns out not to be the final match. A simple numerical approach to this problem is to find t iteratively. First, $t=0$ and nearest neighbors/pairs are determined. We can now calculate a δt that optimizes the least-square problem based on this matching, using any solver available for the optimization problem. We can then shift all the points in A by δt and start again by calculating new pairings and deriving a new δt. This process is repeated until the cost function reaches a local minimum.

Although it is possible to use ICP for registration, this technique has a major drawback: the original algorithm does not include a scaling factor. There is an improved version of ICP in the literature called SICP (Du et al., 2010) which takes this into account, but we have not tested it.

3.5 Result of DEM generation

3.5.1 Asal-Ghoubbet rift

Figure 25 lists all the DEMs generated in the Asal-Ghoubbet rift. As already mentioned in Section 3.2.1, most of the drone and profile DEMs generated by Labarre (2017) in the frame of his PhD thesis have a millimeter scale. In this thesis, I have generated the remaining ones. The profile DEMs of sites M and U could not be produced in 2017 because there was no way of relating them to terrain coordinates. I performed additional DEM alignment. The most notable contribution of my work is the generation of the circle DEMs. In the end, I completed the dataset by generating 2 additional millimeter-scale DEMs and 12 submillimeter-scale DEMs, making a total of 36 DEMs. The three high-resolution DEMs produced at site T using the three acquisition methods are shown in Figure 31.

3.5.2 The Moon

In 2019, Nguyen (2019) produced a 1.95 mm pixel DEM using a stereo pair taken at the Apollo Lunar Surface Experiments Package (ALSEP) site during the Apollo 17 mission (Figure 32a). From April to July 2023, Vo Nhat Le collected all the lunar ground images from all the Apollo missions that can be used to construct DEMs (Vo, 2023). She was able to produce a total of 29 DEMs (1 from Apollo 11, 3 from Apollo 12, 4 from Apollo 14, 8 from Apollo 15, 7 from Apollo 16, 6 from Apollo 17) using MicMac and the framework introduced in section 3.5.2. The new DEMs have a pixel size of 1.15 mm. In addition, the Yutu-2 rover (Chang'E 4) Panoramic Camera DEM (pixel size = 5 mm) was provided by Guo et al. (2021) (Figure 32b).

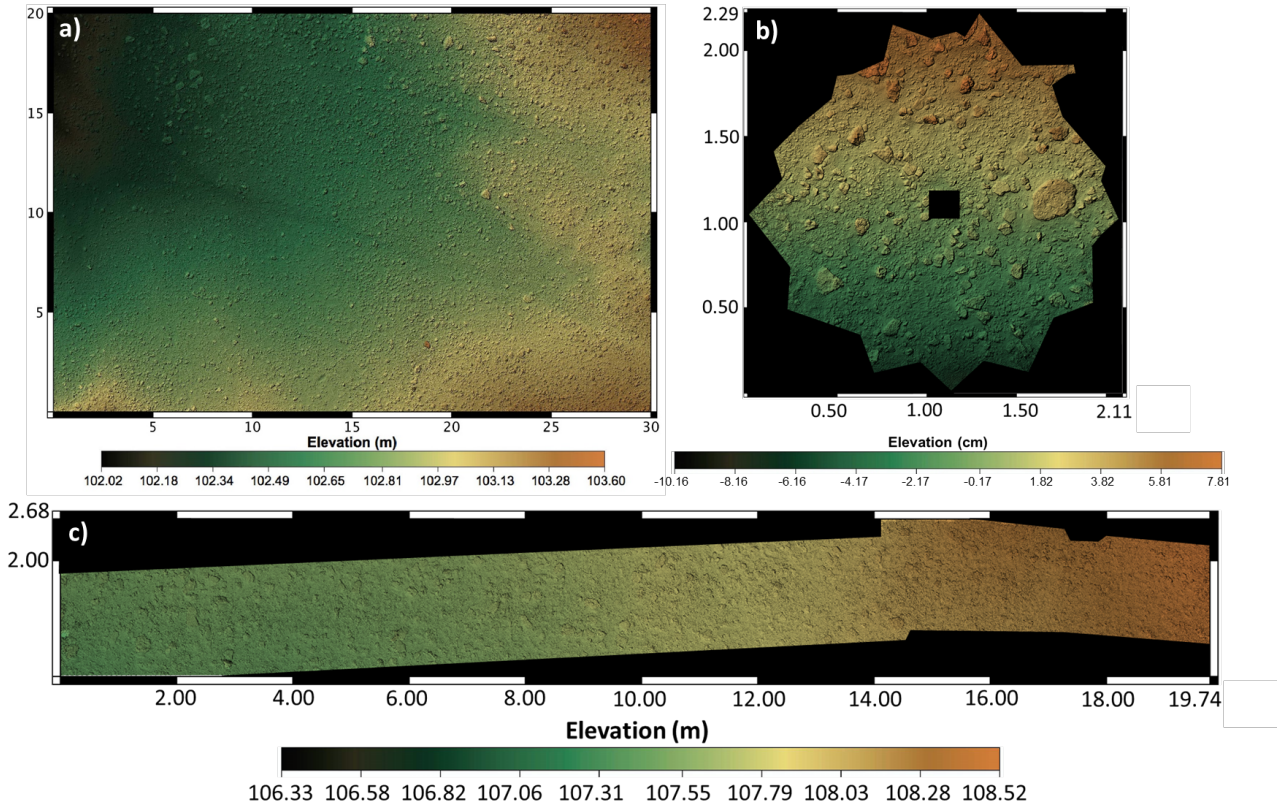

Figure 31 – Digital elevation models of site T, reconstructed from a) drone photography; b) hand-collected photographs within a circle; c) hand-collected photographs along a transect. Distances on the x and y axes are given in meters.

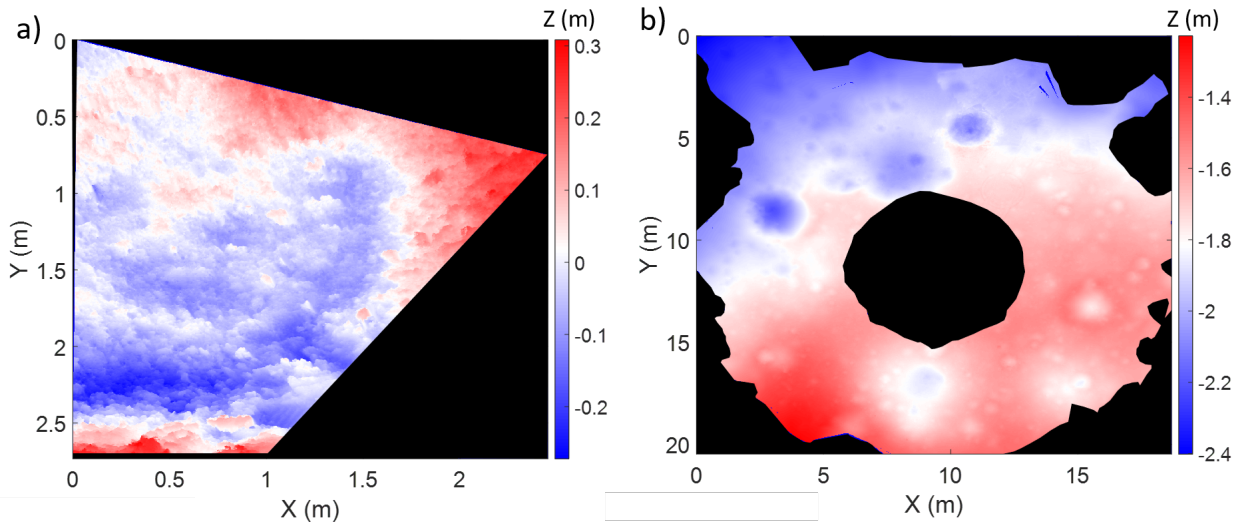

Figure 32 – Some lunar ground DEMs: a) Apollo 17 ALSEP site (pixel size = 1.95 mm) (Nguyen, 2019); b) Proximity of Chang'E 4 landing region (pixel size = 5 mm) (Guo et al., 2021).

3.6 Quality Assessment

According to Labarre (2017), the orientation quality can be estimated by the mean residuals of the tie points (MTPR) (expressed in pixels) and the residual distance between the estimated coordinates of the GCPs in the images and their actual coordinates measured in the field by the Global Positioning System (GPS). The MTPR corresponds to the mean square error between

the initial position of the tie points in the images and their reprojection from the 3D coordinate estimated by the compensation. A perfect orientation, where the image rays intersect at a single point, gives $MTPR = 0$. In practice we find that 0.5 < MTPR < 1 gives excellent results and MTPR ≈ 1 indicates good orientation. If MTPR < 1.5, orientation is considered fair or poor, usually due to insufficient overlap between images or poor internal calibration. This parameter is an estimate of the relative quality of the orientation. Meanwhile, residual distances are mainly used to verify the information provided by the mean residuals of the attachment points. Labarre (2017) assessed the quality of 12 drone DEMs in the Asal-Ghoubbet rift (sites A, B, E, F, H, I, M, Q, R, S, T, Y) and observed that the orientation is satisfactory in most cases. The other results (sites G, K, N, P, U) are presented in Table 3.2 and their quality is also satisfactory. The only exception is site O, whose MTPR is > 1.5. Unfortunately, although the DEM of site K exists in the archives, we have lost the results of the intermediate steps used for the quality assessment. Overall, this estimation method seems to be limited to DEMs obtained from data containing true GCPs.

Site	MTPR (pixel) (drone)	Residual distance (m) (drone)					STD (cm) (circle)
A	1.14	0.0028	0.0050	0.0051	0.0040	0.0038	0.5203
B	1.33	/	0.0012	0.0007	0.0011	0.0027	/
E	1.28	0.0024	0.0010	0.0019	0.0020	0.0019	/
F	1.17	0.0013	0.0008	0.0012	0.0010	0.0010	0.2023
G	1.39	0.0041	0.0105	0.0137	0.0053	0.0023	/
H	1.04	0.0012	0.0007	0.0007	0.0006	0.0012	/
I	1.02	0.0043	0.0042	0.0065	0.0028	0.0041	0.1317
K	/	/	/	/	/	/	/
M	1.24	0.0017	0.0008	0.0016	/	0.0029	/
N	1.08	0.0396	0.0178	0.004	0.0116	0.0033	/
O	1.84	0.0094	0.0167	0.0200	0.0174	0.0053	0.4198
P	1.02	0.0064	0.0065	0.0070	0.0088	0.0023	0.1089
Q	1.33	0.0043	0.0044	0.0050	0.0043	0.0013	0.5416
R	1.12	0.0016	0.0019	0.0023	0.0012	0.0009	0.0836
S	1.01	0.0010	0.0006	0.0008	0.0014	0.0017	0.1617
T	1.08	0.0008	0.0015	0.0023	0.0008	0.0007	0.1350
U	1.19	0.0090	0.0040	0.0059	0.0084	0.0023	0.3583
Y	1.02	0.0008	0.0009	0.0010	0.0010	0.0017	0.1526

Table 3.2 – Quality estimation of drone DEMs for relative orientation (MTPR) and absolute orientation (residual distance from GCPs), each containing 5 GCPs and of circle DEM for STD of wooden block surface elevation for 18 sites.

For the DEMs generated from pseudo-GCPs, or those with no GCP at all, we need to find an alternative method. In these cases, the only known and verifiable object is the wooden block, so we can only partially assess the DEM quality by looking at the height statistics of this object (Figure 28). The remaining areas outside the block have no measurements and are therefore not verifiable. In Table 3.2, the results seem to be acceptable as the SD is less than 6 mm in the DEMs covering 2.5×2.5 m.

In another specific case, where the DEMs are created without the presence of GCPs, they are

to be aligned and scaled with another DEM that encompasses them. Therefore, the quality of the DEM in question will largely depend on this larger DEM (drone DEM) and the goodness of fit. To estimate the latter, we estimate the RMSE. The only case where the DEM alignment is applicable is the profile DEM of site U. However, the RMSE is quite large: about 0.3 m. This proves that the DEM construction is much better in case we have GCPs. For the other profile DEMs, according to Labarre (2017), the relative orientations for sites M, Q, S and T give MTPR of 0.41, 0.38, 0.33 and 0.47 pixels, which is a very good result and much better than the drone DEM construction. We were able to find the profile DEM of site S in the archive, which gives an MTPR of 1.5, which is marginally acceptable according to the predefined standard. Otherwise, there are sites where profile DEMs of arbitrary scale exist (sites G and I), but no object of recognisable size and the SIFT algorithm could not detect enough tie points, so they are generally on hold. These are marked as red boxes in Figure 25, along with the unprocessable data (the images have little overlap and a low degree of consistency).

3.7 Surface roughness

3.7.1 Overview

The DEMs were used to calculate surface roughness, which is a soil property that controls the movement of surface materials and gravity-induced processes. For example, it can impede or redirect the flow of water, snow, sand and debris. At the same time, rough surfaces change in response to surface movement. Surface roughness can effectively reflect terrain characteristics and the degree of erosion (García Moreno et al., 2008; Grohmann et al., 2011; Wu et al., 2018; Brožová et al., 2021). Therefore, a surface roughness map can increase the reliability of flow simulations, improve our understanding of the formation and modification process, the stratigraphic age and the properties of the materials making up the surface (Cai and Fa, 2020; Brožová et al., 2021). It also influences the distribution of incident radiation and, indirectly, soil moisture, temperature and aeration. Finally, it imposes technical constraints on future exploration of the Solar System, such as the safe landing and circulation of rovers. In summary, surface roughness is essential in micrometeorology, agriculture, hydrology, volcanology, natural hazard mitigation and planetary science (Bretar et al., 2013).

3.7.2 Definition

Intuitively, roughness is the degree of irregularity of a surface. In order to quantify this property, it is necessary to review the many definitions of roughness. According to Shepard et al. (2001), it is a topographical expression of a surface on a horizontal scale. Grohmann et al. (2011) and Trevisani et al. (2023) equate it with texture, microrelief or microtopography. Furthermore, Wu et al. (2018) states that surface roughness is the degree of deviation between an actual surface and an ideal surface (the geoid) in the vertical direction, also a generic term referring to various aspects and scales of the spatial variability structure of surface morphology. For Trevisani et al. (2023), it is a general concept covering several aspects of the spatial variability of surface structure, which can be characterized at different scales and metrics. The term has been used in various works to represent an essential property of a surface that is both the result of and a factor influencing

natural processes. However, there seems to be a lack of common understanding of roughness, and it is difficult to harmonize the concept between different disciplines. As Smith (2014), this lack of consensus stems from terminological confusion, a large number of roughness parameters and the scale dependence of roughness (intuitively perceptible in Figure 33).

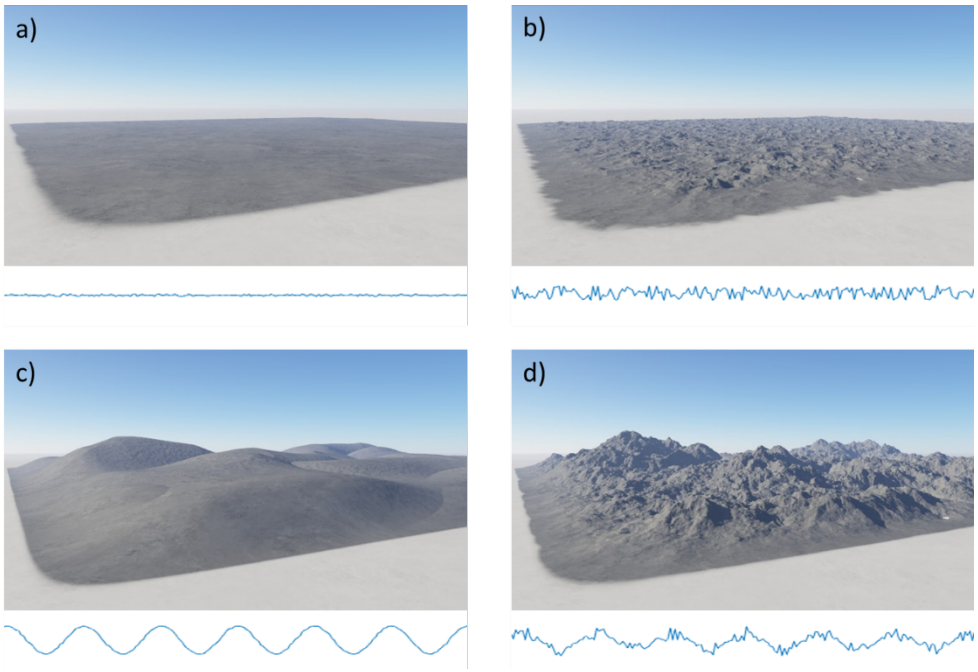

Figure 33 – Intuitive perception of roughness: a) Flat at all scales; b-c) Rough at small scale, smooth at large scale and vice versa; d) Rough at all scales [4]

We adopt here the definition of Smith (2014) and Trevisani et al. (2023): surface roughness is a multiscale property that characterizes topographic variability within scale windows with a definitive set of roughness parameters. This definition would suit our purposes: either to map roughness as a variable, or to use roughness to interpret and distinguish the underlying geological processes that shape surfaces over a wide range of temporal and spatial scales. Topographic variability encompasses the millimeter and submillimeter scales (the domain of photometric roughness, slightly larger than the grains that make up the surface) and all scales up to the kilometer scale, corresponding to the major phenomena that affect the entire planetary object. Each window corresponds to a scale and is bounded at the bottom by the measurement scale (the size of the pixel or an element in the available data) and at the top by the user-defined partition scale, which is less than or equal to the available elevation profile or DEM. It would be difficult to choose a single parameter to describe the surface roughness, as it might reveal incomplete information. Therefore, we need to choose representative parameters that reflect certain aspects of roughness and that are not too similar to each other. The choice is explained in detail in the following sections.

3.7.3 Previous work on roughness retrieval

a) Method oriented

In this section, we will look at surface roughness studies according to instruments, techniques, models and software. As an overview, roughness measurement techniques are generally based

4. https://planetside.co.uk/wiki/index.php/Heightfield_Generate

on laser scanning systems, radar or stereo images acquired by a spacecraft, drone or handheld camera (Rosenburg et al., 2011; Pommerol et al., 2013; Kreslavsky et al., 2013). The laser scanning system is a technique for accurately measuring terrain height, which is used to calculate surface roughness. In addition, stereo-photogrammetry has proven its ability to extract digital terrain models (DTMs) with sub-millimeter accuracy (Bretar et al., 2013). It can also be estimated by inversion of a photometric model. The roughness parameter of the Hapke model (Hapke, 2008) is defined as the mean slope angle at all scales. However, it has been shown that the photometric response of a surface is mainly determined by submillimeter or millimeter scales Labarre et al. (2017). Radar and thermal models have also been used to indirectly assess surface roughness (Fa et al., 2011; Bandfield et al., 2015). Another lesser known method based on shadow analysis, which only requires photography at a solar zenith angle of around 45°, has also been investigated. However, it only works on bright, uniformly colored surfaces García Moreno et al. (2008).

The high-resolution digital terrain models (DTMs) produced by the Lunar Reconnaissance Orbiter Camera's (LROC) narrow-angle cameras (NAC) allow the roughness of the lunar surface to be studied at the meter scale. In addition, the panoramic camera on board the Yutu-2 rover collected millimeter-resolution stereoscopic images of the Chang'e-4 landing zone. These images served as the basis for 5 mm/pixel resolution DTMs generated by photogrammetry and photoclinometry, an essential tool for assessing surface roughness at the millimeter or decimeter scale (Guo et al., 2021). Bland et al. (2021) used SOCET SET software on Galileo images to derive DTMs and determine roughness by extracting elevation profiles on Europa, a satellite of Jupiter. MESSENGER's Mercury Dual Imaging System (MDIS) images were analyzed using Ames Stereo Pipeline (ASP) as part of Barker et al. (2022)'s work.

Roughness information is also essential for interpreting anomalous radar signals and reducing ambiguity in water ice detection, as it significantly affects the intensity and polarization of radiation scattered by regolith surfaces (Cai and Fa, 2020). On the Moon, it has mainly been estimated from the Mini-RF radar instrument on board the Lunar Reconnaissance Orbiter (LRO) and Chandrayaan-1 (Fa et al., 2011). In addition, Magellan synthetic aperture radar observations on Venus (Ganesh et al., 2022), Cassini RADAR on Titan, a satellite of Saturn (Bonnefoy et al., 2022), Mars Reconnaissance Orbiter Shallow Radar (SHARAD) on Mars (Grima et al., 2022) have been used to derive roughness.

Thermal emission from the lunar surface is also well known to be affected by surface roughness. Using a thermal model with a roughness parameter and thermal infrared (TIR) measurements from the Diviner (aboard the LRO), Bandfield et al. (2015) showed that the Moon could be strongly anisothermal due to surface roughness. This model was also applied to Visible and Infrared Thermal Imaging Spectrometer (VIRTIS) data from comet 67P/Churyumov–Gerasimenko, which was studied during the Rosetta mission (Marshall et al., 2018).

b) Application oriented

On Earth, significant research has been devoted to roughness estimation in a wide range of applications. For example, surface roughness has been used to detect landslides (Van Den Eeckhaut et al., 2012), to study wind patterns and pollutant dispersion (Macdonald et al., 1998), to estimate soil infiltration rates (Moore and Singer, 1990), and to study sediment transport and the interaction of acoustic waves with the seafloor (Lyons et al., 2002). As a result, surface roughness

research has largely contributed to Earth sciences. Many of these examples are discussed in Smith (2014).

As far as planetary science is concerned, we have observed its application on several telluric bodies such as the Moon, Mars, Mercury, Venus, some asteroids and comets. For example, analysis of Lunar Orbiter Laser Altimeter (LOLA) data on the Moon shows that roughness at the meter scale and above contains information about space weathering, micrometeorite bombardment and regolith gardening Helfenstein and Shepard (1999). In addition, Kreslavsky and Head III (2000) has shown that surface roughness at the kilometer scale and above reflects geological events such as large impact craters and volcanic eruptions. In contrast, roughness at the hectometer scale depends mainly on small impact craters, regolith accumulation and modification processes. Older geological units, such as pond flows or high plateaus, are generally rougher on a large scale, while more recent impact craters are rougher than older ones (Rosenburg et al., 2011; Kreslavsky et al., 2013). Similar methods have been applied to the Mars Orbiter Laser Altimeter (MOLA) (Kreslavsky and Head III, 2000) and the Mercury Laser Altimeter (MLA) (Pommerol et al., 2013; Barker et al., 2022).

3.7.4 Roughness parameters

An attempt has been made to review all the roughness parameters used in Earth and planetary science. Shepard et al. (2001) describes the most commonly used parameters: Root-mean-square (RMS) height, RMS or Allan deviation, RMS slope, autocorrelation length, effective slope, median and absolute slope, power spectrum (given by the magnitude of the Fourier transform of the profile). Kreslavsky and Head III (2000) use the median absolute value of the differential slope at a given baseline length, while Kreslavsky et al. (2013) use the interquartile range of the profile curvature at three baselines as a measure of topographic roughness. Grohmann et al. (2011) use the area ratio, vector dispersion, standard deviation of elevation, residual topography, slope, and profile curvature for their analysis. They also mention other methods: Fourier analysis, geostatistics, fractal dimension, and entropy. Following their work, Brožová et al. (2021) added some algorithms (vector ruggedness measure, terrain ruggedness index) that were implemented in GRASS GIS. In addition, we can mention the use of local elevation range, direction cosine eigenvalue, 2D semivariogram, Fourier and wavelet transform, among others, in the work of Wu et al. (2018).

As discussed in Smith (2014), there is an overabundance of roughness parameters. Similar issues of parameter redundancy and lack of normalization have been raised, but these are at odds with the need to capture diverse aspects of surface shape. Our view is that roughness should be characterized by a set of parameters rather than a single one. Based on the type of data to be fed into the algorithm, Grohmann et al. (2011) divided the parameters into two groups: profile-based parameters (1D data) and array-based parameters (2D data). In addition, Smith (2014) grouped the parameters based on some specific aspects of roughness. There are four groups in total: amplitude (focusing only on the elevation component, e.g., elevation probability distribution statistics), spacing (focusing only on the horizontal scale of surface deviations, e.g., feature length, feature spacing), hybrid (combining the previous two, e.g., slope parameters, tortuosity), and multiscale parameters (e.g., geostatistics, fractal dimension).

a) Data preprocessing

The input to the roughness calculation is either an elevation profile or a DEM. In either case, we need to perform several preprocessing steps to minimize the error and bias.

• **Filtering no-value pixels**: In the case of an elevation profile, we simply delete those pixels and reassemble the rest. However, this is not possible with 2D data. In this case, as long as the percentage of those pixels is insignificant, we can interpolate using either a nearest neighbor or a bilinear scheme (to preserve the range of values). If the percentage is significant, we have no choice but to crop and take the usable part, or abandon the faulty DEM.

• **Detrending**: is a crucial process in surface roughness analysis, particularly when the aim is to isolate and study small scale features without the confounding influence of larger scale variations. According to Shepard et al. (2001), a common method of detrending involves subtracting the line of best fit from the elevation data. This approach effectively removes the influence of local slope variations and allows the study of microrelief around a newly established horizontal reference level. The result is a dataset with zero mean height, which simplifies further analysis of small-scale roughness by standardizing the baseline of the elevation profile. Similarly, for a DEM, we fit a plane using the MATLAB function `fit` with the "poly11" option, which means that we fit all DEM points to the formula $z = p00 + p10 \times x + p01 \times y$, where (x,y,z) are the 3D coordinates and $(p00, p10, p01)$ are the three coefficients of the two-variable first-order equation. We then subtract the planar fit from the original DEM and obtain the result shown in Figure 34a. We can see that the variation in elevation has been significantly reduced and is centered around zero. Note that we have chosen "poly11" to eliminate the effect of the slope, which is greater than the DEM. If a user wanted to eliminate the effect of the slope being less than the DEM, they could increase the number of polynomials, for example "poly22".

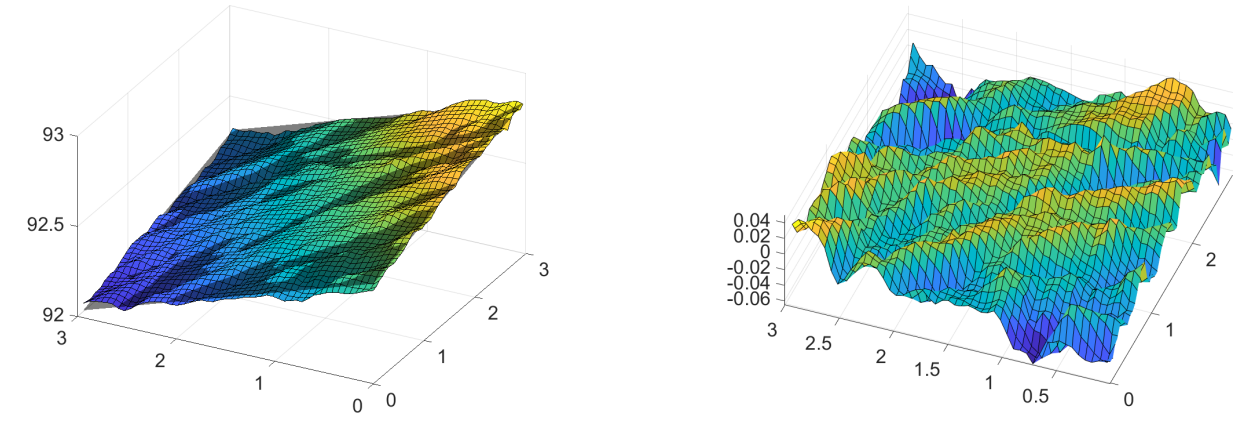

(a) (b)

Figure 34 – Drone DEM of site A (Asal-Ghoubbet rift) a) before and b) after detrending. In (a), the colored mesh is the DEM and the black mesh is the planar fit. The unit of the axes is meters.

Another approach is to decompose the terrain profile into several components of different energy or frequency. Techniques such as wavelet or Fourier analysis are used to achieve this decomposition. By identifying and omitting the components corresponding to the local slope, researchers can remove the influence of large-scale roughness. This method is favored for its ability to decompose the data into fundamental frequency components, each representing different

scales of roughness (Bretar et al., 2013; Smith, 2014; Rosenburg et al., 2011; Grima et al., 2022). This method is explained in more detail in Section 3.8.

• **Filtering outliers**: is another important step after detrending. It has to be done manually by looking at the elevation data, defining a probable range and dropping the rest.

b) Choice of roughness parameters

A rough surface can be considered as a random (or stochastic), stationary and ergodic phenomenon. Statistics are, therefore, often used to study and model the roughness of a surface. The latter is described by a function $z = f(x, y)$, where x and y are the Cartesian coordinates of the points in the horizontal plane, taken as reference, and z is the height with respect to this plane. For a linear profile, we consider $z = f(x)$. We use various parameters that are described by Shepard et al. (2001). In addition, in order to prioritize flexibility, the study focused on the profile-based algorithm.

Mean slope angle ($\overline{\theta_M}$)

It can be considered as a hybrid profile-based parameter as it takes into account both amplitude and spacing. It can be written as:

$$\overline{\theta_M} = arctan\frac{z}{x} \tag{3.5}$$

with z the elevation at location x. The greater the mean slope angle, the greater the roughness of the surface. In the literature, we have only come across the use of this specific parameter in the study by Hapke (1984); Labarre et al. (2019), which uses the same dataset. Instead of the mean slope angle, other authors have used similar metrics: the RMS slope (Shepard et al., 2001; Bandfield et al., 2015; Bland et al., 2021), the standard deviation of the slope (Grohmann et al., 2011; Brožová et al., 2021), or the median differential slope (Rosenburg et al., 2011; Pommerol et al., 2013; Kreslavsky and Head III, 2000). They are similar to the mean slope angle, based on slope statistics and the implication of higher roughness as the value increases. Although the mean slope angle is rarely used, it has a greater influence on the photometric roughness obtained by model inversion (Chapters 4 and 5).

Root-mean-square height (RMSH) (ξ')

Reported as the most common and easiest parameter to obtain, we have seen its use in many works (Bretar et al., 2013; Fa et al., 2011; Wu et al., 2018; Cai and Fa, 2020; Guo et al., 2021). The higher the RMSH, the greater the vertical variations of the surface, therefore the surface is considered to be rougher. However, this parameter only focuses on the amplitude, not the horizontal structures, and thus incompletely characterizes the surface roughness (Bretar et al., 2013). Technically, it can be applied to both 1D and 2D data. According to Shepard et al. (2001), RMSH can be written as:

$$\xi' = \sqrt{\frac{1}{N}\sum_{i=1}^{N}(z(x_i) - \bar{z})^2} \tag{3.6}$$

with N the number of sample points, $z(x_i)$ the surface height at location x_i, and $\bar{z}$ the mean profile elevation over all x_i.

Autocorrelation length (L_C)

This is another hybrid profile-based parameter. To account for the relationship between the height of two points on a profile, separated by a distance δ, we defined the autocorrelation function or normalized autocovariance function $\rho_N(\delta)$. It is the ratio of the covariance of the profile with the lagged version of δ to its variance ξ^2, and can be seen as the correlation of the profile with respect to a lagged version of δ:

$$\rho_N(\delta) = \frac{1}{\xi^2}\frac{1}{N}\sum_{i=1}^{N_\delta}(z_{i+\delta} - \bar{z})(z_i - \bar{z}) = \frac{1}{\xi^2}\frac{1}{N}\sum_{i=1}^{N_\delta}(z_{i+\delta}z_i) \tag{3.7}$$

with ξ the standard deviation of the elevation, N_δ the number of pairs of points separated by distance δ, z_i the elevation at point i, and $z_{i+\delta}$ the elevation at point $i+\delta$ of the profile. To perform this calculation, we start from a zero distance to a distance equal to one-third of the profile. The autocorrelation function lies between -1 and +1 (perfect correlation). The maximum value is reached when $\delta = 0$, when the two series overlap perfectly. $\rho_N(\delta)$ decreases progressively as δ increases because the sections of the profile are less and less correlated (Figure 35). At low roughness, the autocorrelation function can be modeled by an exponential function:

$$\rho_N(\delta) = e^{\frac{\delta}{L_C}} \tag{3.8}$$

For high roughness, it can be represented by a Gaussian function (Blaes and Defourny, 2008).

$$\rho_N(\delta) = e^{-\frac{\delta^2}{L_C}} \tag{3.9}$$

The autocorrelation length L_C is defined as the minimum distance between two points for which the autocorrelation function is $e^{-1} \sim 0.3679$. Beyond this distance, the correlation is no longer significantly different from zero. This roughness parameter provides a horizontal description of the surface roughness of the soil (spatial wavelength).

$$L_C = \rho_N^{-1}\left(e^{-1}\right) \tag{3.10}$$

In contrast to the standard deviation of the height, as the correlation length increases, the horizontal variations of the surface become smaller, and the surface is considered to be less rough. These functions are often used in the microwave domain to model the scattering of electromagnetic radiation from natural surfaces (Fa et al., 2011).

Z_S parameter

Zribi (2003)noted that most studies involving the radar backscattering coefficient to estimate surface roughness using the correlation length resulted in significant errors. In order to account for both the degree of irregularity and the horizontal variations of the surface, they combined the effects of two parameters (RMSH ξ auto-correlation length L_C) in a new index Z_S. It can be considered as a hybrid parameter that works for profile-based data.

$$Z_S = \frac{\xi'^2}{L_C} \tag{3.11}$$

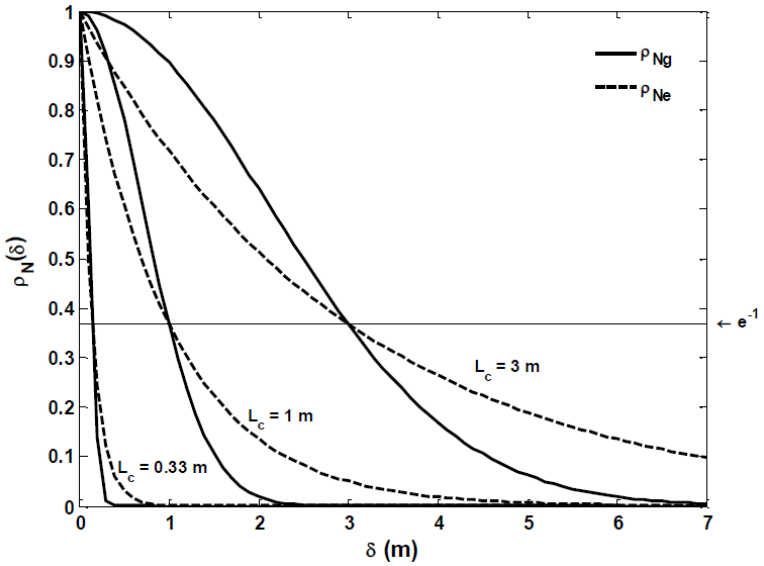

Figure 35 – Example of Gaussian and exponential autocorrelation function (ρ_{Ng} and ρ_{Ne}) for different values of L_C Arab-Sedze (2013).

A smooth surface has a low Z_S value due to a low RMSH and a high autocorrelation length, and vice versa. This parameter seems appropriate for studying the surface scattering of a radar wave. Its use has been observed in the work of Bretar et al. (2013).

Tortuosity τ

The tortuosity index is another parameter that takes into account the horizontal and vertical scales of roughness (Bertuzzi et al., 1990), so it would be appropriate to classify it as a hybrid parameter for 1D data. It is defined as the ratio between the length of the profile L and the length of its projection L_0.

$$\tau = \frac{L}{L_0} \tag{3.12}$$

As these variations increase, the path along the profile increases and so does the tortuosity. A rough surface will therefore have higher tortuosity values than a smooth surface.

Fractal dimension (D)

Other parameters, such as the fractal dimension, can be used to characterize the roughness of a surface. This parameter measures the degree of irregularity of the surface according to the scale of measurement. There needs to be a more rigorous and formal definition of fractals. A fractal can be defined as an irregular object whose structures repeat at all scales of observation, but which cannot be described by Euclidean geometry because of its infinite detail. A fractal structure has properties of self-similarity and scale-invariance. The most classic example is the coastline of a country, which increases in length as the scale of measurement decreases. This approach has often been used to describe surface roughness (Pachepsky et al., 1997; Shepard et al., 2001; Vidal Vázquez et al., 2005; Pardo-Igúzquiza and Dowd, 2022). Several methods have been proposed to characterize the fractal dimension of a linear profile (semivariogram, box-counting, power spectrum, etc.). Here we present the roughness-length method described by Malinverno (1990) and commonly used (Vidal Vázquez et al., 2005; Bretar et al., 2013). The determination of the

fractal dimension is based on the estimation of a power law involving the mean standard deviation of the RMS ($RMS\,(\Delta)$) (or Allan variance) calculated for different length scales Δ:

$$RMS\,(\Delta) = \frac{1}{n_\Delta} \sum_{i=1}^{n_\Delta} \sqrt{\frac{1}{m_i - 2} \sum_{j \in \Delta_i} (z_j - \bar{z}_j)^2} \tag{3.13}$$

with n_Δ the total number of windows of length Δ, m_i the number of points within the window Δ_i, z_j the elevation at point j in the profile, and $\bar{z}_j$ the average elevation corresponding to Δ_i. The standard deviations are then calculated for each subset. Shepard et al. (2001) suggest limiting the first value of Δ to 20% of the total profile length. Its length decreases by a factor of 0.9 between two calculations, until an interval containing at least 10 measurement points is obtained. For a self-affined (or fractal) surface, a scale increment of a factor Δ in the horizontal direction results in a scale change Δ^H in the vertical direction.

$$RMS\,(\Delta) = A\Delta^H \tag{3.14}$$

with A a constant and H a scale parameter called the "Hurst coefficient" or "Hurst exponent". This parameter quantifies the rate of change of roughness with scale. If $\log(RMS\,(\Delta))$ is plotted against $\log(\Delta)$, the points are aligned and the Hurst exponent is determined as the slope of the regression curve ($0 \leq H \leq 1$). By definition, the fractal dimension D is equal to $2 - H$ for a linear profile ($1 \leq D \leq 2$). A high value of D (low H) means that the surface appears smooth as the resolution increases. It can be also considered rough at fine scales. Conversely, a low D (high H) value indicates that the roughness is stable over many measurement scales. Finally, when $D = 1$ ($H = 1$), the surface is considered to be auto-similar and the roughness is statistically constant regardless of scale.

Most terrestrial surfaces do not behave perfectly fractal over all horizontal scale ranges, sometimes resulting in significant changes in the slope of the semivariograms. The power law fit to calculate H is then performed over two or more different scale ranges, the separation of which corresponds to a transition in the processes that formed the surface (Figure 36). Fractal analysis has become a popular quantitative method for characterizing both the rate of change of roughness with spatial scale and the amplitude of roughness (Helfenstein and Shepard, 1999). While the fractal dimension is widely used in radar backscatter models (Shepard et al., 2001), it also finds applications in radiometric models of BRDF in the solar domain (Drossart, 1993; Efford, 1993).

The use of the fractal dimension or Hurst exponent is ubiquitous, as it already incorporates the inherent multiscale nature of surface roughness (Bretar et al., 2013; Labarre et al., 2017; Gerekos et al., 2021; Trevisani et al., 2023). On the Moon, scale-dependent roughness characteristics have been described quantitatively by the Hurst exponent (Helfenstein and Shepard, 1999; Shepard et al., 2001). At hectometer to kilometer scales, the Hurst exponents of the highlands are significantly larger than those of the maria (Rosenburg et al., 2011), while at meter to hectometer scales, the Hurst exponent distributions of the maria and highlands overlap (Cai and Fa, 2020).

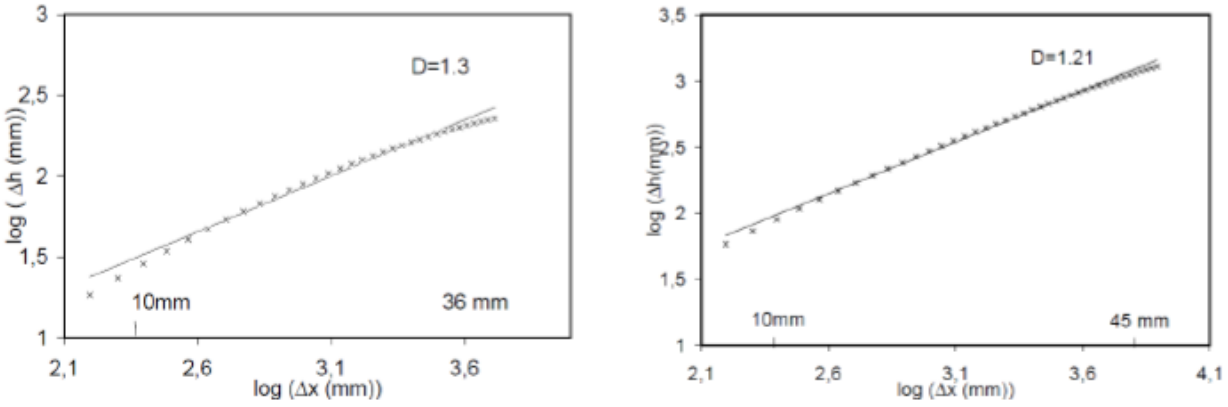

Figure 36 – Fractal dimension determination for moderately rough soil (left) and ploughed, gravelly soil (right). The Δh represents the change in elevation for each scale Δx (Zribi, 1995).

c) Roughness calculation

To calculate the mean slope angle, Labarre (2017) converted the DEMs into randomly oriented facets generated from a regular grid and then repeated the whole process a few times to find the average result. This method guarantees the statistical aspect of the result, but the creation of randomly generated facets was considered too computationally intensive and time consuming to process. In contrast, we drew horizontal and vertical line profiles and determined the mean slope angle and other roughness parameters for each profile to form the statistical distributions. The advantage of this method is that it requires less computational resources than the facet method, while giving a good estimate of roughness if the number of profiles is sufficient, with the results of the two methods being proportional. Figure 37 confirms this, with the exception of site A, which acts as an outlier due to the recent refinement of the DEM, which is more accurate than before.

3.8 DEM decomposition by wavelet transform

3.8.1 Overview

We have defined surface roughness as a physical quantity that is strongly dependent on scale. The description of a surface is obviously concerned with the variation of roughness with scale, so we are looking for a way to separate the roughness components within a DEM for deeper study, hence DEM decomposition.

DEM is essentially an image containing the elevation data and can be compared to a 2D signal. Decomposing a 2D signal is a ubiquitous task that has been performed over the last two centuries. The most widely used technique is the Fourier transform. However, it has limitations, particularly in extracting the temporal and spatial location of frequency features, and the appearance of an artifact near discontinuities in a function, known as the Gibbs phenomenon (Gibbs, 1899). The wavelet transform represents a significant evolution of the Fourier transform and its variants. By definition, it decomposes a signal into a set of basis functions consisting of contractions, expansions and translations of a wavelet, a function that integrates to zero and has finite energy (Daubechies, 1990). Wavelets are used in a family obtained by shifting and dilating the graph of a mother wavelet

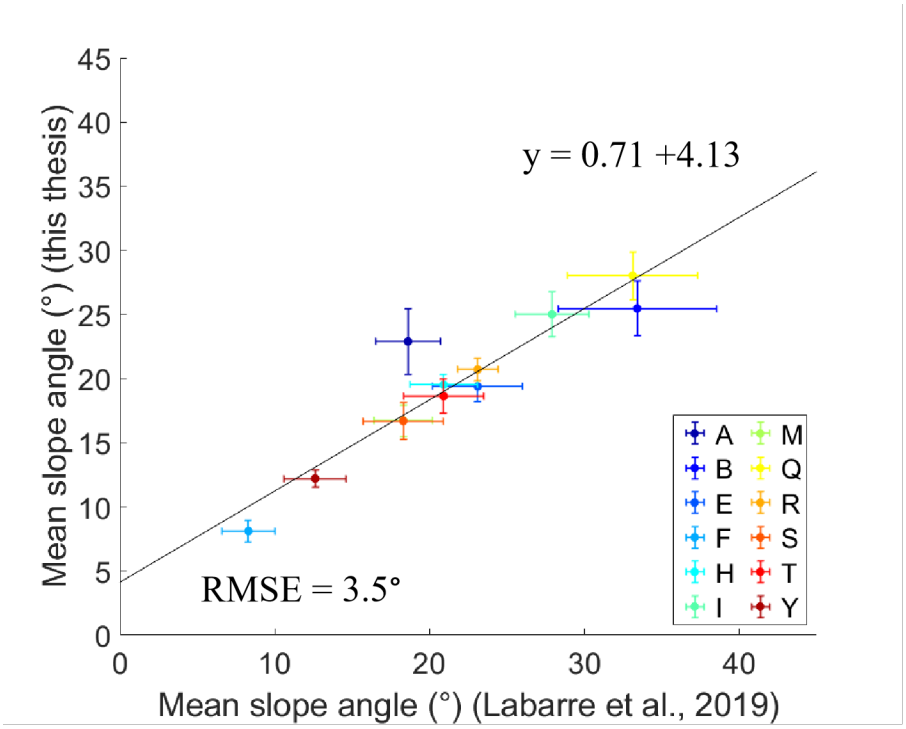

Figure 37 – Comparison between the average slope angle of Labarre et al. (2019) and this thesis. The legend illustrates calculations from drone DEMs of the respective AG rift sites. The black line is the first-order fit of the data points.

to analyze signals. The wavelet transform allows a more flexible and detailed analysis of signals, especially transient signals, by adjusting the window size for different frequency components within a signal. The detailed comparison between the two techniques has been shown in the work of Labarre (2017), which shows that the wavelet transform is more suitable for DEM analysis.

3.8.2 Isotropic Undecimated Wavelet Transform (IUWT)

For our purposes, we used an improved version of the wavelet transform called the Isotropic Undecimated Wavelet Transform (IUWT). Popular in astronomy, it decomposes an image into a set of coefficient representing different scales. This multi-scale representation is well suited for detecting isotropic features commonly found in astronomical data, such as stars, galaxies, and galaxy clusters (Starck and Murtagh, 2006). It has been used by Labarre et al. (2017, 2019).

The IUWT offers unique advantages for processing discrete data and preserving resolution in the study of fine-scale surface features. It can be compared to the Discrete Wavelet Transform (DWT), which allows the creation of an orthogonal family of wavelets to provide a robust and complete representation of functions or signals. However, standard DWT generally involves downsampling, which reduces the resolution of the approximate and detail coefficients at each level of decomposition. While this process is computationally efficient, it can remove information critical to the analysis of fine detail, such as millimeter and sub-millimeter DEM features. In contrast, the undecimated wavelet transform (UWT) used by the IUWT does not incorporate downsampling. This means that the approximate and detail coefficients at each level retain the same length as the original signal, preserving all data points and avoiding any loss of information due to downsampling. With IUWT, the low pass and high pass filter coefficients are upsampled at each decomposition

level. This process ensures that the resolution of the coefficients decreases as the level increases (by a factor of 2). Another feature of the IUWT is its tendency to detect isotropic rather than directional structures. This feature is particularly useful for general DEM studies, where the interest is often in identifying and analyzing features that have no preferred orientation.

A wavelet transform produces a series of transformations of an image, providing a resolution-related set of "views" of the image. As explained by Starck et al. (2007), IUWT is based on the "À Trous" algorithm (meaning "with holes", so called because of the interlaced convolution used in successive stages) (Holschneider et al., 1989; Shensa, 1992). We consider sampled data $\{c_0(k)\}$, defined as the scalar product at pixels k of the function $f(x)$ with a scaling function $s(x)$ corresponding to a low-pass filter:

$$c_0(k) = \langle f(x), s(x-k) \rangle \tag{3.15}$$

The scaling function is chosen so that the dilation equation is satisfied and is expressed as follows:

$$\frac{1}{2} s\left(\frac{x}{2}\right) = \sum_k h(k) s(x-k) \tag{3.16}$$

where h is a discrete low-pass filter associated with the scaling function s. This means that a low-pass filtering of the image is, by definition, closely linked to another resolution level of the image. The smoothed data $c_j(k)$ at a given resolution j and at a position k is the scalar product:

$$c_j(k) = \frac{1}{2^j} \langle f(x), s\left(\frac{x-k}{2^j}\right) \rangle \tag{3.17}$$

This is therefore obtained by the convolution:

$$c_j(k) = \sum_l h(l) c_{j-1}(k + 2^{j-1} l) \tag{3.18}$$

The difference signal w_j between two successive resolutions is:

$$w_j(k) = c_{j-1}(k) - c_j(k) \tag{3.19}$$

or:

$$w_j(k) = \frac{1}{2^j} \langle f(x), \psi\left(\frac{x-k}{2^j}\right) \rangle \tag{3.20}$$

Here, the wavelet function ψ is defined by:

$$\frac{1}{2} \psi\left(\frac{x}{2}\right) = s(x) - \frac{1}{2} s\left(\frac{x}{2}\right) \tag{3.21}$$

For the scaling function, $s(x)$, the B-spline of degree 3 was used in our calculations. We have derived a simple algorithm in order to compute the associated wavelet transform:

• We initialize j to 0 and start with the data $c_j(k)$.

• We increment j and perform a discrete convolution of the data $c_{j-1}(k)$ using the filter h. The distance between the central pixel and the neighbouring pixel is 2^{j-1}.

• After this smoothing, we obtain the discrete wavelet transform from the difference $c_{j-1}(k) - c_j(k)$.

• If j is less than the number of resolutions p that we want to calculate, then go on to step 2.

• The set $\mathcal{W} = \{w_1, ..., w_\mathrm{p}, c_\mathrm{p}\}$ represents the wavelet transform of the data.

A series expansion of the original signal, c_0, in terms of the wavelet coefficients is now given as follows. The final smoothed array $c_\mathrm{p}(x)$ is added to all the differences w_j:

$$c_0(k) = c_p(k) + \sum_{j=1}^{p} w_j(k) \tag{3.22}$$

This equation provides a reconstruction formula for the original signal. At each scale j, we get a set $\{w_j\}$. This has the same number of pixels as the input signal. Using the B3 spline, the filter h is $\left(\frac{1}{16} \quad \frac{1}{4} \quad \frac{3}{8} \quad \frac{1}{4} \quad \frac{1}{16}\right)$. When extended to two-dimensional space:

$$h = \begin{pmatrix} \frac{1}{256} & \frac{1}{64} & \frac{3}{128} & \frac{1}{64} & \frac{1}{256} \\ \frac{1}{64} & \frac{1}{16} & \frac{3}{32} & \frac{1}{16} & \frac{1}{64} \\ \frac{3}{128} & \frac{3}{32} & \frac{9}{64} & \frac{3}{32} & \frac{3}{128} \\ \frac{1}{64} & \frac{1}{16} & \frac{3}{32} & \frac{1}{16} & \frac{1}{64} \\ \frac{1}{256} & \frac{1}{64} & \frac{3}{128} & \frac{1}{64} & \frac{1}{256} \end{pmatrix} \tag{3.23}$$

For ease of calculation, a simplification of this wavelet is to assume separability in the 2-dimensional case. In the case of the B3 spline, this leads to a row-by-row convolution with one-dimensional h, followed by column-by-column convolution.

3.8.3 Framework

We use the IUWT algorithm from `https://github.com/andferrari/IUWT.jl`, which is created by André Ferrari. It was originally written in the `julia` programming language, so we took the extra step of converting it to the MATLAB language for convenience. Following the work of Labarre (2017), the DEMs are decomposed into 8 levels (Figure 38).

To study the gradual change in certain roughness parameters as a function of scale, we keep these 8 levels and apply the calculation. If we go up one level, the scale is twice as large as the previous one. However, when it comes to simulating BRDF using a ray-tracing model, it's difficult to handle 8 additional DEMs on top of the original. We therefore decided to follow Labarre (2017) and combine these levels to produce 3 types of DEM: (1) the "roughness" DEM contains the lowest decomposition levels (1, 2 and 3). This version focuses on surface features at submillimeter, millimeter and centimeter scales; (2) the "waviness" DEM is the combination of levels 4, 5 and 6. These are shown in Figure 39. It is sensitive to features at centimeter and decimeter scales; (3) the "form" DEM focuses on topographic features at decimeter and meter scales, combining levels 7 and 8.

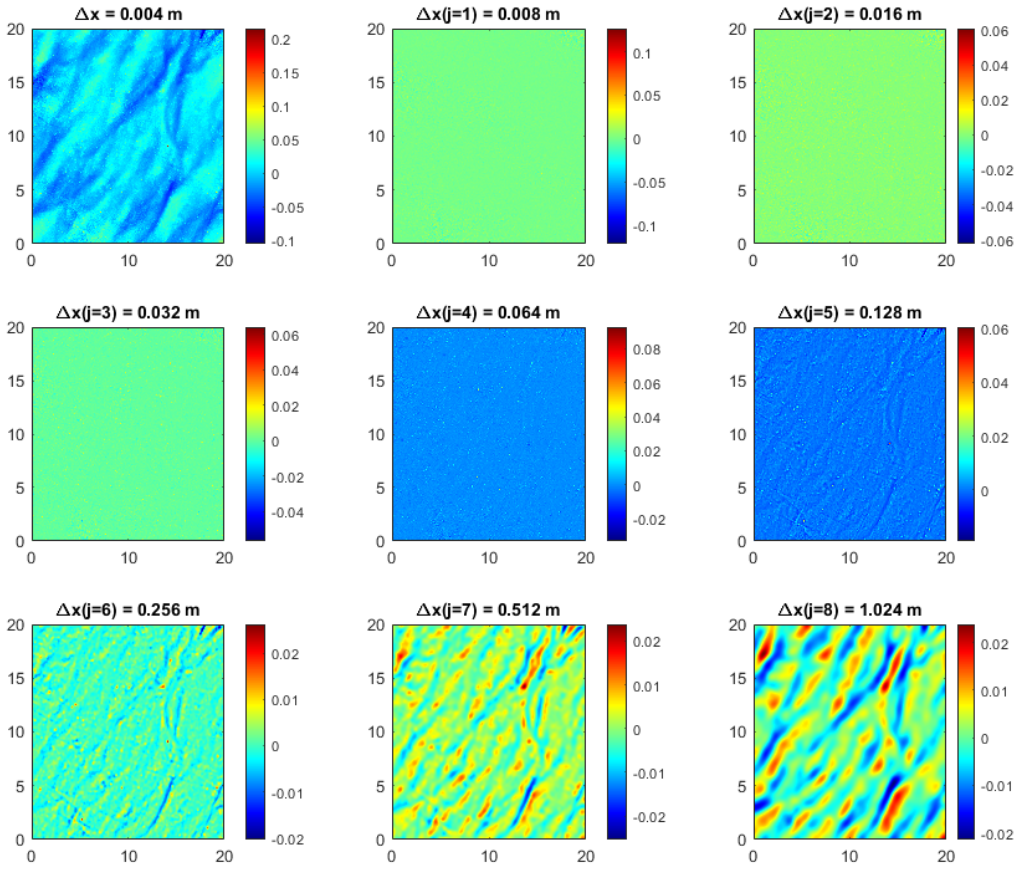

Figure 38 – The original DEM (upper left corner) of site A in the Asal-Ghoubbet rift (constructed from drone photographs) and its 8-level wavelet decomposition, using the IUWT algorithm. The axes and the spatial scale Δx are in meter, j is the scale number.

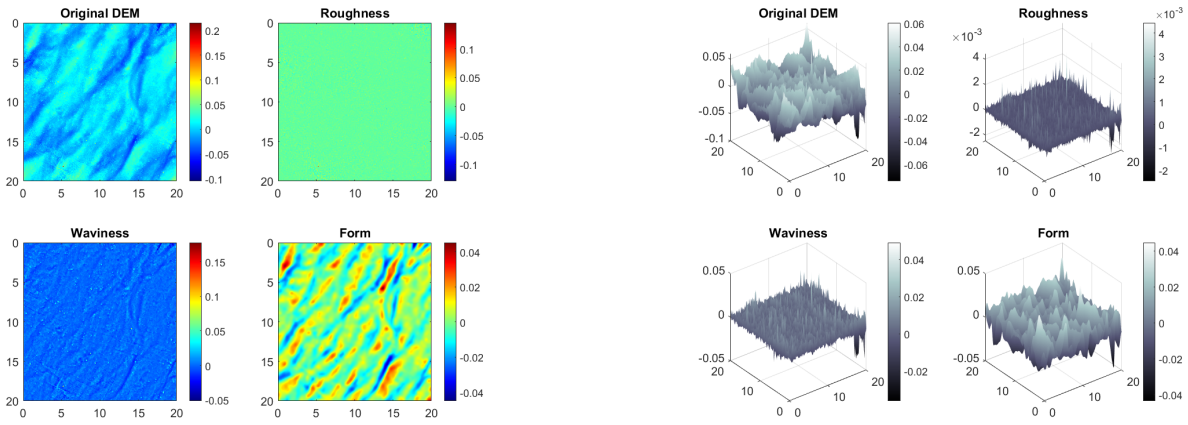

(a) (b)

Figure 39 – The original DEM of site A in the Asal-Ghoubbet rift (constructed from drone photographs) and three wavelet components: "roughness", "waviness", "form", presented in a) two dimensions and b) three dimensions. The axes are in meters.

3.9 Results of roughness calculation

3.9.1 Asal-Ghoubbet rift

a) Between DEMs of different sites

The results of the roughness calculation with drone DEMs are presented in Table 3.3, which contains the mean values and standard deviation. A similar calculation has also been carried out in the case of DEMs from handheld photographs and those from wavelet transform. In another form of representation, Figure 40 shows the results obtained with drone DEMs as well as other types. In this section, we will present our observation of Figure 40 and compare it with what we see in the field (Figure 41).

Site	$\overline{\theta_M}$	(°) RMSH (cm)	L_C (cm)	$Z_S(\times 10^{-3})$	τ	D
A	22.91 ± 2.57	1.47 ± 0.26	76.24 ± 16.06	0.31 ± 0.14	1.19 ± 0.06	1.7 ± 0.04
B	25.47 ± 2.12	16.66 ± 5.68	129.71 ± 38.18	23.9 ± 14.2	1.39 ± 0.14	1.34 ± 0.06
E	19.39 ± 1.15	2.51 ± 0.96	83.36 ± 61.48	1.18 ± 0.82	1.15 ± 0.03	1.52 ± 0.04
F	8.12 ± 0.83	0.72 ± 0.28	45.36 ± 20.09	0.12 ± 0.06	1.02 ± 0	1.52 ± 0.05
G	25.11 ± 2.09	4.31 ± 0.67	19.5 ± 13.81	11.25 ± 3.01	1.34 ± 0.07	1.37 ± 0.05
H	19.52 ± 0.81	0.48 ± 0.04	5.87 ± 2.78	0.47 ± 0.16	1.11 ± 0.01	1.75 ± 0.02
I	25.02 ± 1.77	3.01 ± 0.76	153.25 ± 83.72	0.94 ± 1.06	1.27 ± 0.05	1.57 ± 0.02
K	8.64 ± 1.22	0.92 ± 0.26	103.32 ± 29.14	0.1 ± 0.06	1.02 ± 0.01	1.62 ± 0.07
M	16.74 ± 1.23	5.95 ± 1.32	115.26 ± 48.01	3.32 ± 1.02	1.11 ± 0.03	1.35 ± 0.04
N	23.88 ± 1.28	1.38 ± 0.37	93.8 ± 42.68	0.25 ± 0.15	1.29 ± 0.03	1.68 ± 0.04
O	8.61 ± 1.45	1.32 ± 0.34	110.8 ± 33.48	0.17 ± 0.08	1.02 ± 0.01	1.58 ± 0.04
P	25.82 ± 0.61	13.27 ± 2.77	77.87 ± 62.42	30.08 ± 16.82	1.64 ± 0.08	1.36 ± 0.05
Q	28.04 ± 1.87	7.33 ± 1.62	125.4 ± 43.84	4.83 ± 2.33	1.38 ± 0.15	1.48 ± 0.03
R	20.72 ± 0.89	1.26 ± 0.3	26.08 ± 31.79	1.18 ± 0.74	1.15 ± 0.01	1.61 ± 0.04
S	16.7 ± 1.45	1.49 ± 0.41	48.78 ± 40.07	0.76 ± 0.55	1.09 ± 0.02	1.53 ± 0.07
T	18.64 ± 1.31	2.38 ± 0.84	129.18 ± 77.73	0.76 ± 1.01	1.12 ± 0.02	1.54 ± 0.06
U	28.32 ± 1.61	3.09 ± 0.31	17.29 ± 12.75	6.98 ± 2.4	1.39 ± 0.06	1.5 ± 0.04
Y	12.21 ± 0.66	3.52 ± 2.03	131.25 ± 43.21	1.25 ± 1.08	1.04 ± 0.01	1.51 ± 0.11
Z	19.66 ± 1.4	1.24 ± 0.27	73.69 ± 20.4	0.22 ± 0.07	1.12 ± 0.02	1.65 ± 0.03

Table 3.3 – Roughness calculation result of the DEMs generated from drone photographs in the Asal-Ghoubbet rift. The roughness parameters are: mean slope angle ($\overline{\theta_M}$), root-mean-square height (RMSH), autocorrelation length (L_C), Z_S, tortuosity (τ) and fractal dimension (D).

The mean slope angle in Figure 40 gives us the progression from sand, silt (sites F, O, K, Y) (8°-13°) to smooth lava and slab structure (sites S, M, T) (13°-19°), to a mixture of sand, gravel and centimeter-sized pebbles (sites E, H, Z, R, A, N) (19°-24°), and finally to the rough basalt blocks and decimeter-sized rocks (sites I, G, B, P, Q, U) (24°-29°) (Figure 41). Site S is an exception because it's technically a mixed terrain, with a sandy field and very few rocks in between, so its roughness is on the lower side. We also observe that, except for a few sites with high roughness (sites P, Q, U), the mean slope angle of the circle and profile DEMs do not agree well with the mean slope angles

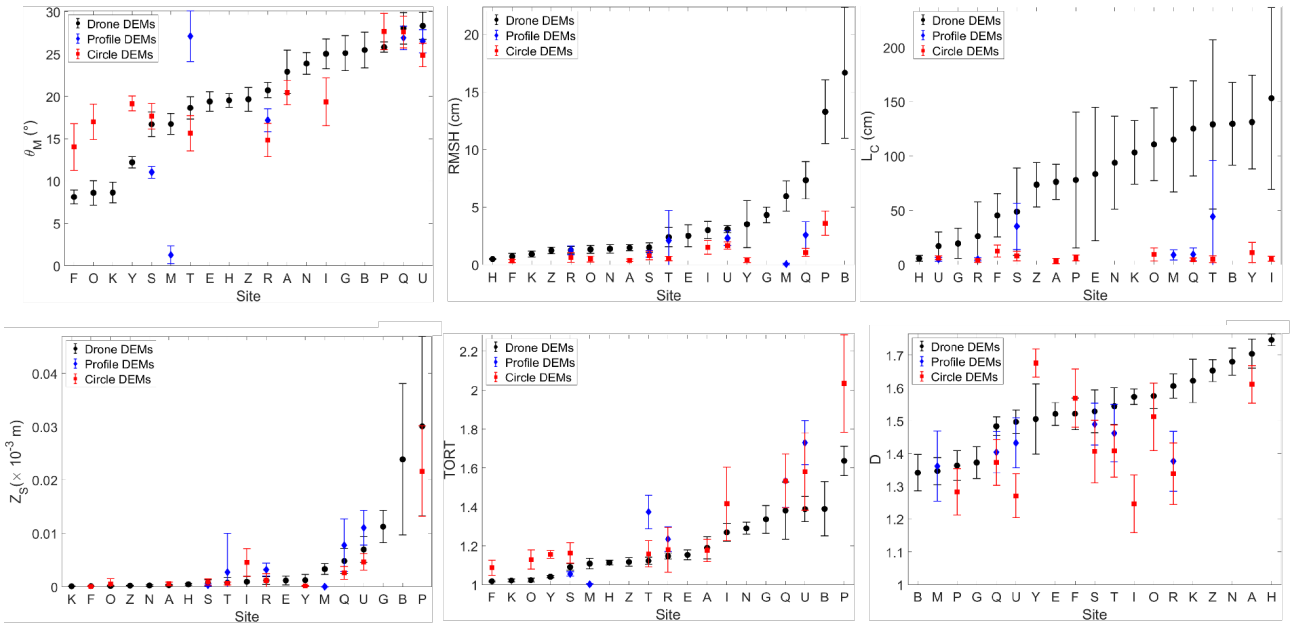

Figure 40 – Roughness calculation over 19 sites of the Asal-Ghoubbet rift, using DEMs created from drone and handheld photography (profile and circle mode). In each graph, the sites are ranked on the x-axis in order of increasing value of the corresponding drone DEM roughness parameter.

of the drone DEMs. This observation highlights either the locality of roughness features or the difference in roughness at the sub-millimeter scale compared to the millimeter scale.

In terms of RMSH from the drone DEMs, it makes sense that sites H, F, K have the lowest roughness as they are grainy, flat fields. On the contrary, sites M, Q, P, B have the highest roughness, corresponding to the rocky or undulating lava fields. Other sites generally contain gravel or a mixture of rock and sand. Regarding the results from the profile and circular DEMs, the RMSH seems to be very low and does not vary significantly (less than 4 cm).

Compared to the previous two parameters, the autocorrelation length L_C seems less intuitive. The results suggest that locations B, Y, I have the lowest roughness while locations H, U, G have the highest. Slab-like or slightly undulating structures are considered smooth, while sites with a variety of different structures (sand, pebbles, rocks) are considered rough. The results of the other DEM types have low L_C, with the exception of sites T and S.

If we look at the other roughness parameters, most of the Z_S values are low ($< 10^{-5}$ m). The exceptions are points G, B, P, where we can confirm the high roughness. For the tortuosity parameter, the graph is similar to that of the mean slope angle in terms of roughness order. Interestingly, for Z_S and τ, the profile and circle DEM results agree with the drone DEM results.

This is not the case for the fractal dimension. What's more, the amplitude order is completely different from previous graphs, which makes sense since it is the only multiscale parameter. Remember that the higher the D, the faster the surface smoothens as the resolution increases. In other words, it would be rough at the fine scale and smooth at the large scale. According to Figure 40, sites K, Z, N, A, H seem to fit this description, as they show a gravel-like structure, coarse at the millimeter and sub-millimeter scales. With its micrometer grain size, site F is considered intermediate in terms of fractal dimension. The roughness of sites B, M, P (lava fields) should be

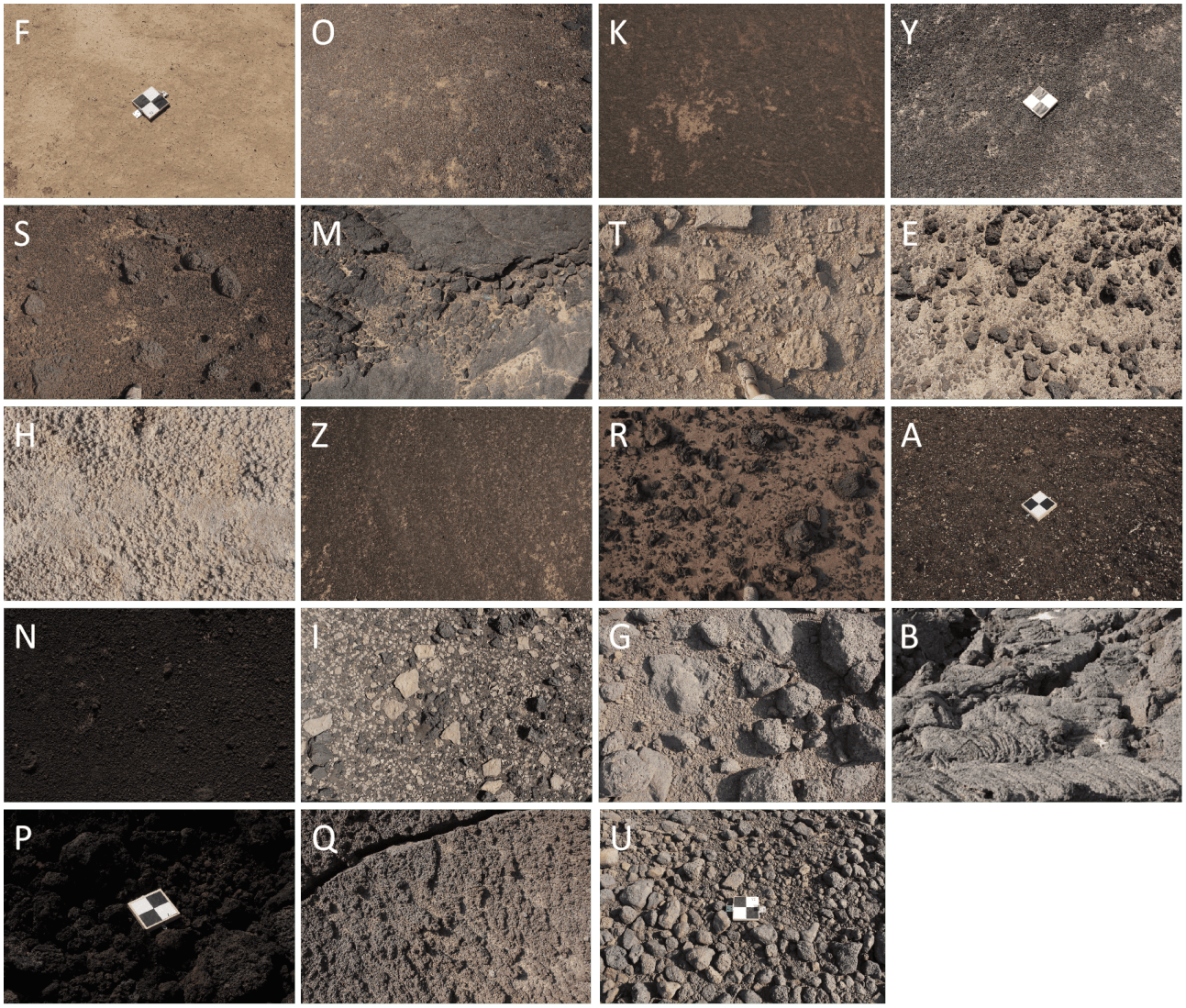

Figure 41 – Close-up images of Asal-Ghoubbet rift sites, arranged in ascending order of average slope angle (Figure 40). Most of the photos were taken at man-height (1.8 m) and at an angle <30˚ to nadir. The exceptions are site B, where the image was taken almost horizontally with the ground, and site P, where the camera was held closer to the ground (with the wooden block for scale).

consistent at different scales. We will test this hypothesis in the next section.

b) Between DEM roughness components

In this section, instead of presenting our observations for each parameter, we will only discuss the difference between the roughness calculation results of the original DEMs and their roughness components. In addition to interpreting the fractal dimension result from the previous section, we also try to find notable trends.

When moving from small to large scale (roughness, waviness to shape), $\overline{\theta_M}$, L_C, Z_S, tortuosity and fractal dimension generally decrease while RMSH increases (Figures 42, 43 and 44) for a very simple reason: RMSH does not take horizontal resolution/step size into account and only includes vertical measurements in the formulation. The rate of change of the height is not as important as that of the horizontal resolution. As $\overline{\theta_M}$, RMSH, Z_S and τ become more important with higher roughness, we will examine them together. Sites F, K and O systematically have the

lowest roughness and sites Q, B and P the highest for all three levels of roughness. It seems that for sites with extremely rough lava fields (B and P), the roughness remains stable at different scales, as shown by the value of the fractal dimension in the previous section. In contrast, sites that are consistently smooth (F, O, K) do not have a relatively low D. Site H is a curious case, as its roughness ranking decreases progressively with scale, which is consistent with its fractal dimension value. In the L_C plots, site N (fractured lava) always has the lowest value, while site O (fluvial deposit) always has the highest. In the fractal dimension plots, site O tends to be one of the lowest. These observations can be interpreted as the effect of homogeneity: site N is the least homogeneous, while site O is the most homogeneous at different scales.

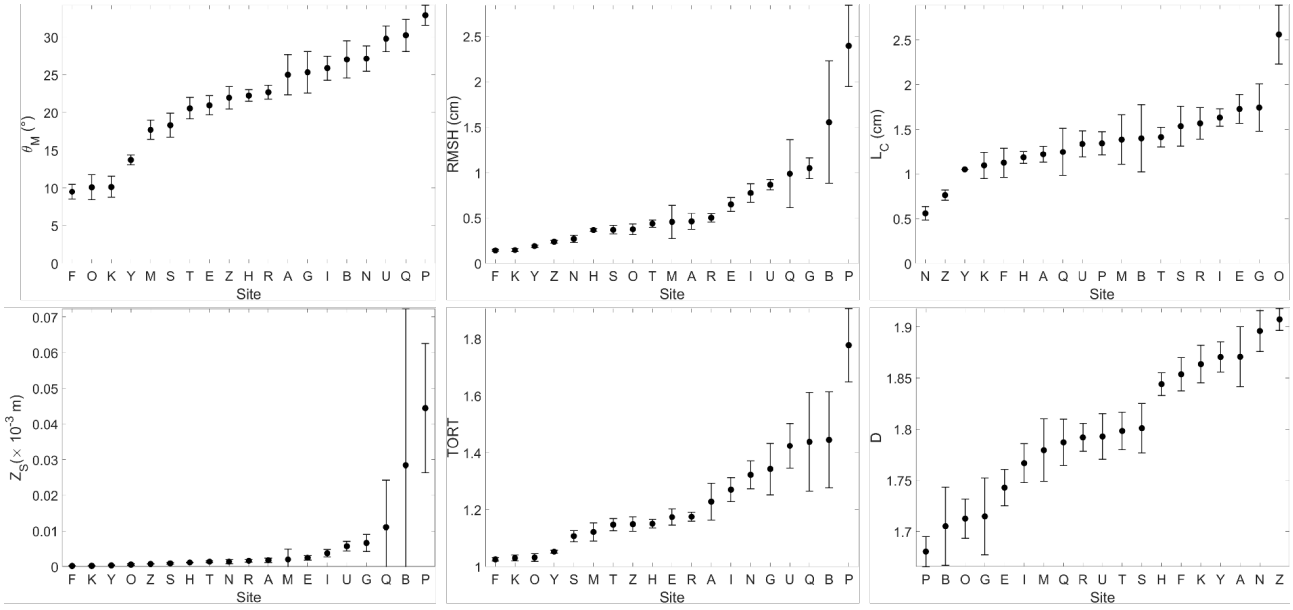

Figure 42 – Roughness calculation over "roughness" components of 19 drone DEMs in the Asal-Ghoubbet rift. In each graph, sites are ranked on the x-axis in order of increasing value of the respective roughness parameter.

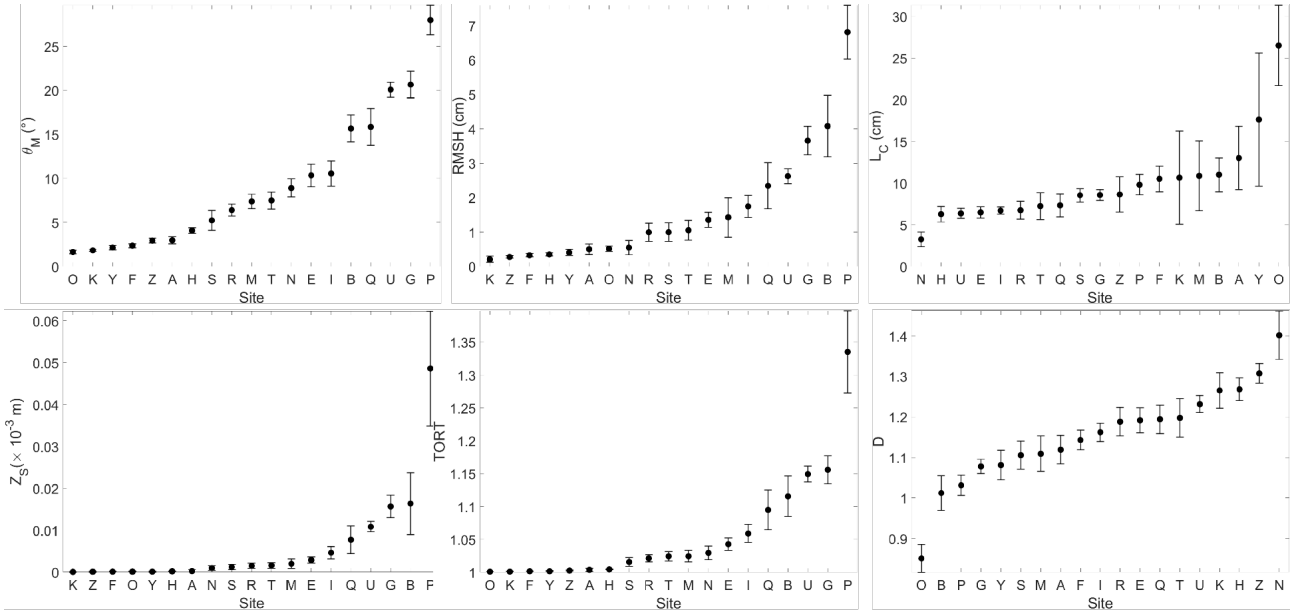

Figure 43 – Roughness calculation over "waviness" components of 19 drone DEMs in the Asal-Ghoubbet rift. In each graph, sites are ranked on the x-axis in order of increasing value of the respective roughness parameter.

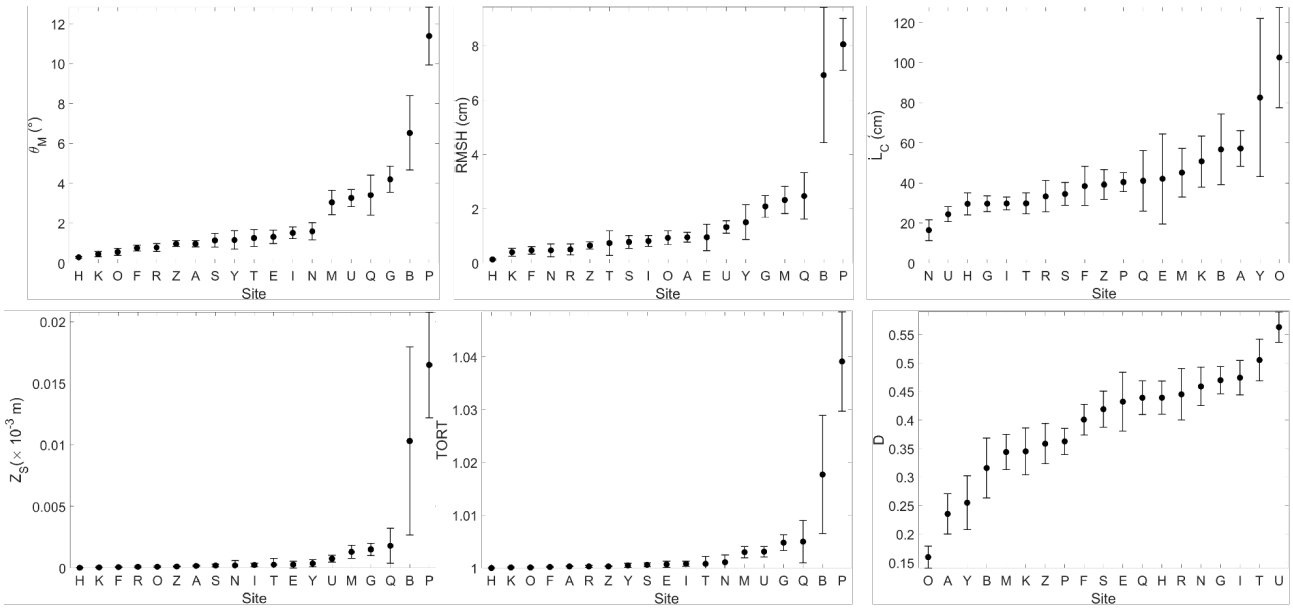

Figure 44 – Roughness calculation over "form" components of 19 drone DEMs in the Asal-Ghoubbet rift. In each graph, sites are ranked on the x-axis in order of increasing value of the respective roughness parameter.

3.9.2 The Moon

a) Roughness calculation at meter scale (Apollo 17 landing site)

Continuing the work of Nguyen (2019), we have improved the roughness calculation code and applied it to the four geological units within the Apollo 17 landing site. The data we used is the altimetry from LOLA and the LROC DEM produced by (Haase et al., 2019).

To facilitate interpretation of the results, we provide the following contextual information about the Apollo 17 landing site. It is located in the Taurus-Littrow Valley, a predominantly mountainous region at the junction of Mare Serenitatis and Mare Tranquillitatis. Upland material dominates the area, forming a series of rugged massifs near the center of the map, with more subdued terrain extending eastwards. The upland units are probably composed of breccias generated by the Serenitatis impact, as well as pre-existing breccias displaced by this event. In addition, younger ejecta from the Crisium and Imbrium impacts may be present, although they are indistinguishable. To the west and southwest, typical lunar maria materials, almost certainly basalt, infiltrate and envelop the highland terrain. A particularly interesting unit in the western region consists of a relatively young and unusually dark material covering both terra and maria. It covers a wide range of terrain in the western part of the map and is interpreted as pyroclastic volcanic deposits. The Apollo 17 landing site is located on this dark deposit covering the terra material in a bay surrounded by mountain ranges (Scott et al., 1972). The extent of the Apollo 17 mission and the geological unit (Scott et al., 1972) are shown in Figure 45.

• **Massif**: is characterized by bright, massive formations with smooth, steep, curvilinear to straight scarps adjacent to re-entrant features along the outer ring of the Serenitatis basin. These formations are mainly composed of breccia layers that were largely ejected from the Serenitatis basin and later exposed by faulting and uplift during and after the basin formation. The upward changes in morphology are partly indicative of the influence of lunar erosional processes on

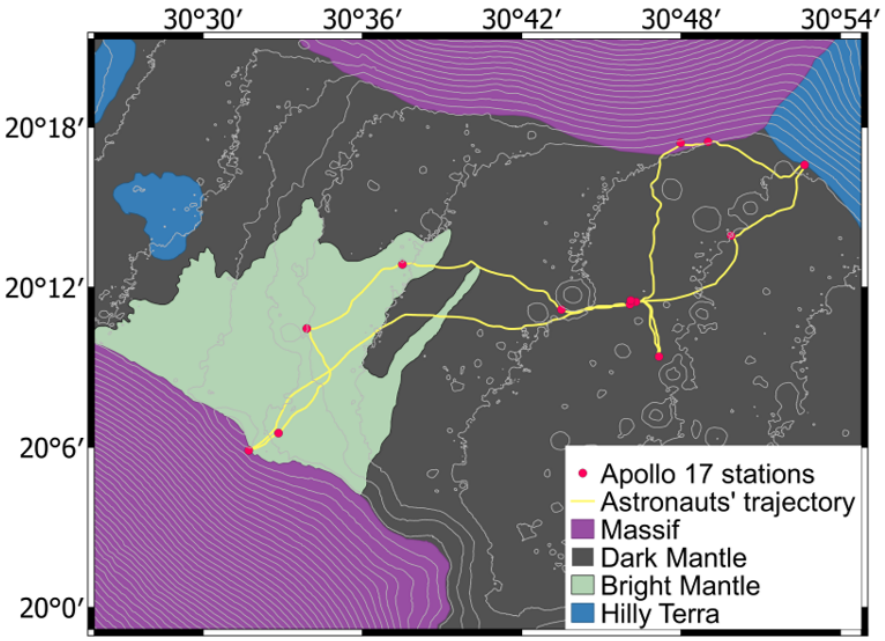

Figure 45 – Geologic map (Scott et al., 1972) integrated with Apollo 17 EVA trajectory (Haase et al., 2019).

fractures and joint systems. In addition, the presence of curvilinear scarps and dome-shaped summits in certain massifs may indicate a volcanic origin.

• **Bright Mantle**: is characterized by a bright to moderately bright, irregularly shaped patch at the base of the massif, southwest of the landing site. At a scale of 200 meters, the surface is bumpy to slightly striated, becoming smoother at larger scales. The area was probably formed by an avalanche and debris flow from the steep face of the massif. This movement of material may have been triggered by ejecta from a large, relatively young crater colliding with the slope of the massif, with secondary ejecta from the crater mixing with material from the massif. Variations in contact characteristics and albedo indicate that the bright material may be both older and younger than parts of the dark mantle. The superimposed dark craters may be of volcanic origin or formed by impact, with the dark rims probably exhumed from beneath the bright mantle.

• **Dark Mantle**: is characterized by a fine, smooth texture with a very low albedo, covering parts of the pond, plains and high plateaus, with the darkest regions found in low lying areas. The distribution of size and frequency of superimposed craters, ranging from 20 to 100 m in diameter, gives an insight into the geological history of the region. The area is mainly composed of pyroclastic volcanic material, probably erupted from numerous small vents located between the Littrow and Vitruvius craters, some of which are over 40 m in diameter.

• **Hilly Terra**: is composed of smooth, shiny to moderately shiny materials that form rounded hills up to 5 km in diameter, with moderate to high relief. These hills occur both individually and in clusters, some with central clefts that partially divide them. The deposits are composed of breccias intercalated with blankets of ejecta from various lunar basins and large craters. It is likely that ejecta from the Serenitatis basin make up the majority of these deposits. The formation of the hills and cracks is mainly attributed to structural changes in the ejecta blankets over time, although some may have been formed by agglomerated ejecta.

We now turn to the results of the roughness calculation (Figure 46). As usual, we have applied 6

roughness parameters to each geological unit. At first glance, the LROC and LOLA data are largely in agreement and show similar trends. According to the plots of $\overline{\theta_M}$, RMSH, Z_S and τ, the Massif and Hilly Terra are similar in terms of roughness and are also the least rough, which is consistent with the information above. This is followed by the Shiny Mantle and the Dark Mantle, which are the roughest, which can be explained by the presence of meter-scale craters. We also observe that the upland units (Massif and Hilly Terra) generally have a low standard deviation compared to the other two mantle units. Next, the L_C parameter shows that the dark mantle is the roughest, while Hilly Terra is the smoothest. In terms of fractal dimension, the Dark Mantle is likely to be rough at different scales, while the highland units are likely to be smooth at higher scales, in agreement with Scott et al. (1972).

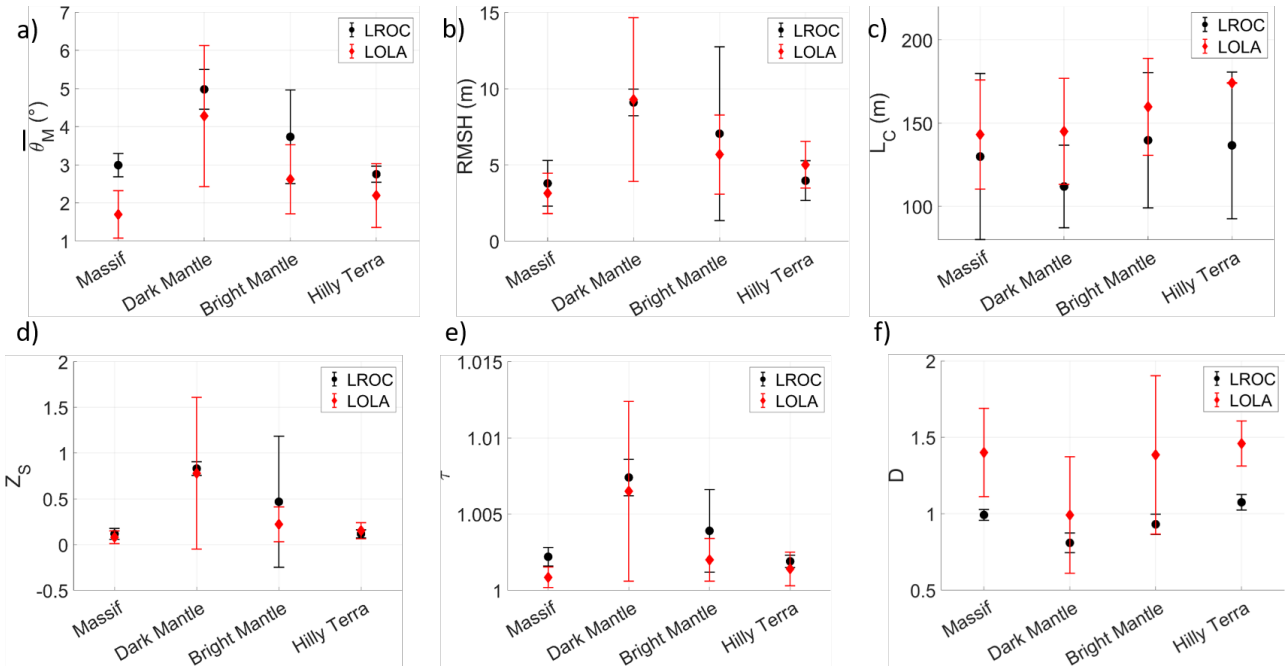

Figure 46 – Roughness calculation DEM generated using photogrammetry on LROC images (Haase et al., 2019) and LOLA measurements.

b) Roughness calculation at millimeter scale (Apollo landing sites)

According to (Vo, 2023), the DEMs mentioned in Section 3.5.2 were subjected to roughness calculation, using the 6 parameters mentioned above. The final results are shown in Figure 47.

At first glance, it is difficult to find a general description of a particular unit, as each unit contains sites that vary so much in roughness. However, let us examine each parameter and compare it with the results in the Asal-Ghoubbet rift.

Most sites have RMSH values that do not exceed 5 cm, which is also true for the Asal-Ghoubbet rift sites. The only two sites that stand out are Apollo 14's G station (7.9 cm) and Apollo 11's Little West Crater (18.2 cm). The former is comparable to site Q (mixture of sand and decimeter-scale rocks), while the latter is higher than any RMSH value in the Asal-Ghoubbet rift, and slightly higher than site B (very rough lava field). Since there is no correspondence between these sites (see Figure 48a and b), it is likely that there was a problem with the DEMs. We will track these two sites in the remaining plots in Figure 47.

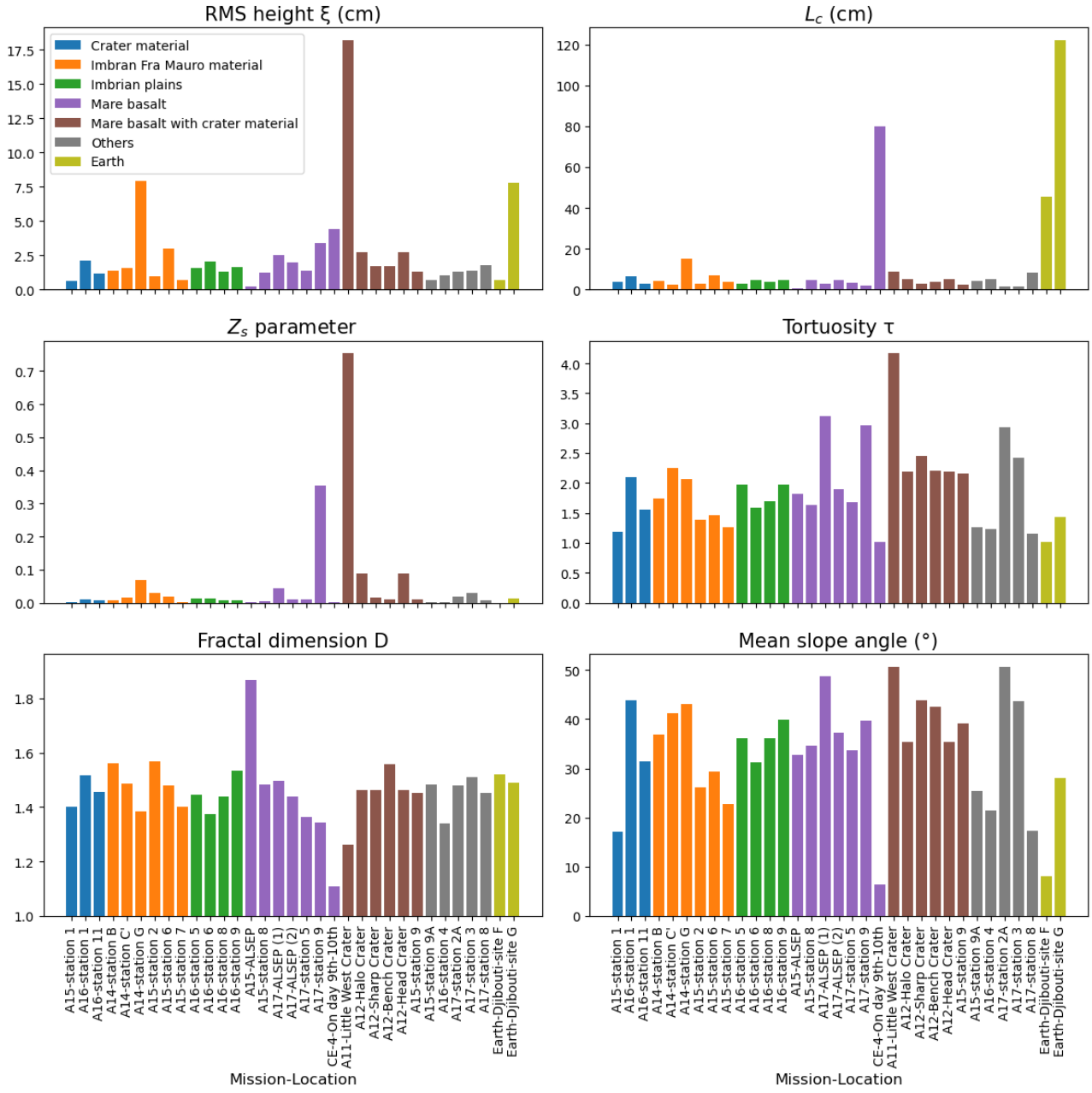

Figure 47 – Roughness calculation of DEMs constructed from lunar surface photographs (Vo, 2023). The DEMs are grouped according to geological units. The graph also includes site F and G of the Asal-Ghoubbet rift (flat and rough terrains) for reference.

On the graph of L_C most of the values are below 10 cm. The only site in the AG trench that has this type of value is site H (flat salt field), which is consistent with our knowledge of the lunar surface. The high value associated with Chang'E 4 DEM is ≈80 cm, comparable to sites A (gravel field), E and T (centimeter/decimeter rock-sand mixture) of the Asal-Ghoubbet rift. According to the ground images in the article by Guo et al. (2021), the Chang'E 4 DEM site is flat at meter scale (with several craters about 2 m in diameter, as seen in Figure 32b) and decimeter scale, but rough at millimeter to centimeter scale. Despite this, it is still considered "smoother" than other sites. This is further evidence that L_C cannot simply be rated as higher for smoother terrain.

In the case of Z_S, we are interested in 2 sites that have some values that are conspicuously larger than any values in the AG rift. One is Apollo 17 Station 9, which is a mixture of rock and regolith (Figure 48c). So the high value might make sense in this case, being representative of high

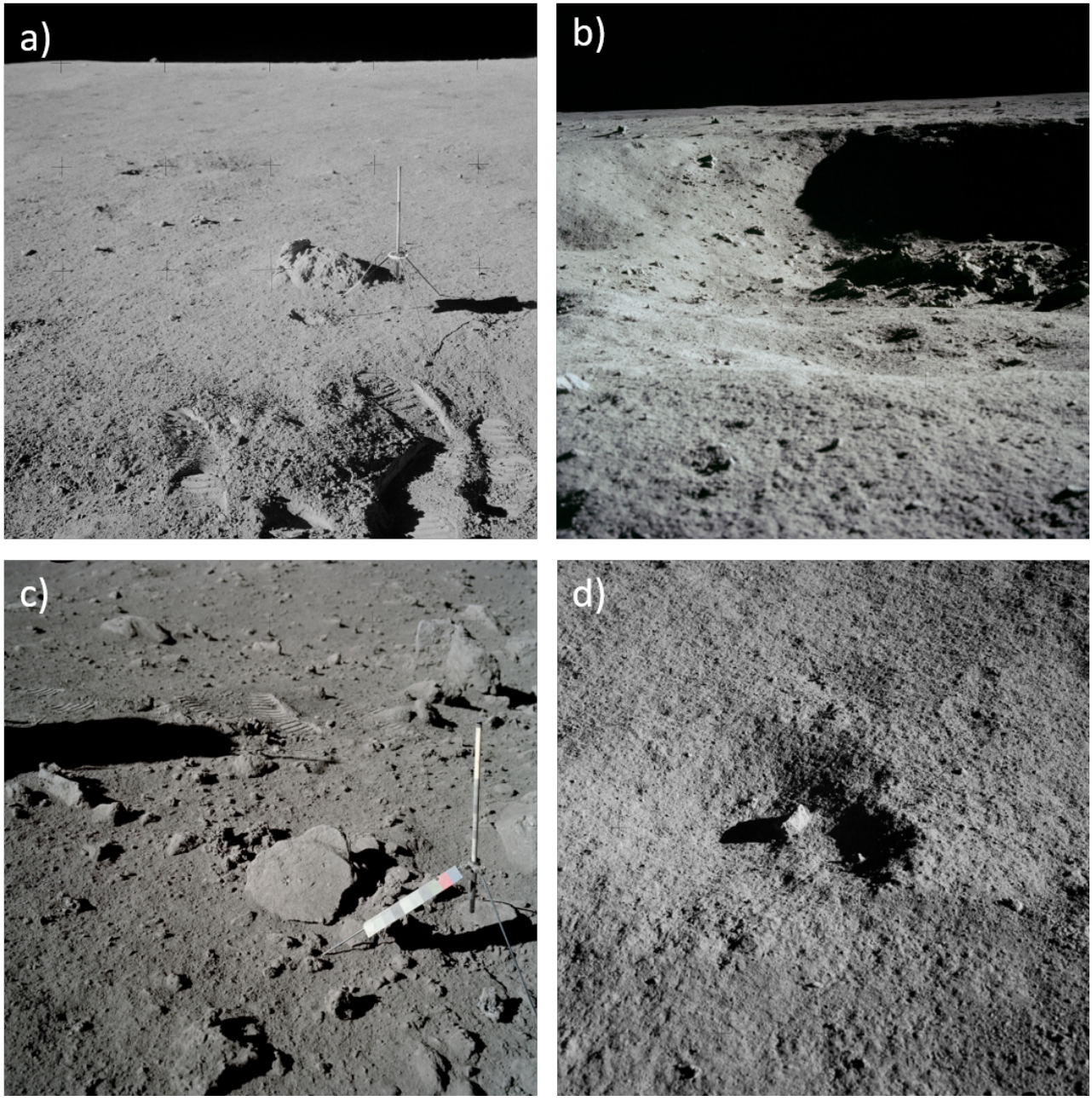

Figure 48 – Ground images taken by the astronauts on several Apollo missions: a) Station G from Apollo 14; b) Little West crater from Apollo 11; c) Station 9 from Apollo 17; c) ALSEP from Apollo 15.

roughness. The other is the small west crater of Apollo 11, about which we have already expressed our suspicions.

As for tortuosity, most of the results are between 1 and 2.5, corresponding to most sites in the AG rift, except for site P (rough lava field). On the lower side we have the value of Chang'E 4 DEM ($\tau = 1.017$), similar to sites F, K and O of the AG rift, which also have the lowest roughness. On the higher side we have Apollo 17's ALSEP (1) and Station 9, and Apollo 11's small west crater.

The value of the fractal dimension is usually in the range [1.3, 1.6], which is also true for most of the sites in the AG rift. The lowest value is the Chang'E 3 DEM ($D = 1.11$), which is lower than all the values we found in the AG rift. The highest value is 1.87, which belongs to the Apollo 15 ALSEP (Figure 48d). This value in turn is higher than all the values we found in the Asal-Ghoubbet rift.

The mean slope angle range between 17° and 45°. The lowest value is Chang'E 4 (6.47°), which

is smaller than site F (8.12°). The highest values are A17 ALSEP (2) (48.67°) and Little West Crater of Apollo 11 (50.62°), much higher than any Asal-Ghoubbet rift site (maximum is 28.32°).

In summary, most values are within the expected range that we have seen on Earth. The anomalous roughness values in the west crater of Apollo 11 could be due to errors in DEM generation and need to be checked. Another calculation that needs to be checked concerns the Chang'E 4 DEM, which has terrain similar to other sites, yet has extremely low roughness values for several parameters (tortuosity, fractal dimension and mean slope angle), while we have no reasonable explanation.

Conclusion

We have demonstrated the framework used to produce DEMs using photogrammetry and MicMac. In some situations, the lack of GCPs makes the process much more complicated and requires additional post-processing steps. Even then, success is not guaranteed. Fortunately, in most cases we have ready-to-use DEMs of acceptable quality. These will be important for roughness analysis and BRDF simulation using the ray-tracing model.

In the study of surface roughness, we conducted a comprehensive literature review and identified the most important and widely accepted roughness parameters. Based on this, we developed a new framework for roughness calculation and applied it to DEMs generated from drone and handheld photography, together with their wavelet decomposition components. The results provide detailed insights into the characteristics of each roughness parameter and offer a deeper understanding of the different aspects of terrain roughness. Mean slope angle balances both horizontal (scale) and vertical (height) components, while RMSH focuses exclusively on height variation. The autocorrelation length highlights the repetitiveness of surface features at certain scales, and the Z_S parameter emphasizes changes in elevation, making it useful for detecting significant roughness features. Tortuosity works in a similar way to mean slope angle, judging by its results. Finally, the fractal dimension provides an insight into how roughness changes at different scales, which can be further verified by analyzing the roughness parameters of the DEM components.

Given the variety of terrain types within the Asal-Ghoubbet Rift, roughness calculation combined with wavelet decomposition provides a valuable reference database that allows us to characterize planetary surfaces through numerical analysis, rather than relying solely on visual inspection. We have demonstrated this approach by comparing it with calculations carried out on the Moon, and have found several correlations. The results of this analysis will serve as a priori knowledge, laying the groundwork for the study of photometric roughness in Chapters 4 and 5.

Chapter 4

Inversion of the Hapke model

Introduction

In this chapter, we will list the inversion techniques commonly found in the literature, discuss about their advantages and disadvantages, and describe a preferred method that is used in this work: the fast Bayesian inversion. At the end of the chapter, we evaluate its performance by performing some tests and comparing it with the well-known standard Bayesian inversion method that uses Markov chain Monte-Carlo sampling.

4.1 Model inversion methods

4.1.1 Deterministic optimization methods

Deterministic methods are those that produce a single, consistent result as long as the initial sample (the user-defined initial values of the parameters) remains the same between different runs. They are often fast (in a matter of seconds), but tend to produce a solution based on a local rather than a global minimum. The merit function, called the chi-square function, which corresponds to the sum of squares of the distances between the measurements and the model in the observation space, is key to the inversion process. A minimization algorithm tries to find a combination of parameters that will produce the smallest value of the chi-square function. However, there is a risk of finding a local minimum, which means that another combination of parameters may produce an even smaller chi-square value. There are ways to get around this drawback: (1) to run the inversion several times with different initial guesses, which may be represented as a grid within the parameter space, or (2) to choose the initial guess close to the solution (Gimar et al., 2022). Here we present two commonly used deterministic methods applied to the Hapke model.

Levenberg-Marquardt

This method combines the gradient descent algorithm and the Gauss-Newton algorithm for solving nonlinear least squares problems. The gradient descent algorithm is used when we are far from the solution. The search follows the direction of steepest descent, which is the opposite of the gradient vector. This allows a fast convergence to the solution. Its implementation is quite

simple, but it is not very accurate, especially when the gradients are small. The Gauss-Newton algorithm is used when we are close to the solution (Marquardt, 1963). The Levenberg-Marquardt method is implemented in MATLAB with the function `lsqnonlin`. This method has been used by Schröder et al. (2017); Protopapa et al. (2020); Gimar et al. (2022).

Nelder-Mead (simplex) method

Unlike the previous method, the simplex method requires only the values of the function to be minimized and not its partial derivatives. It requires a large number of calls to the merit function, but is generally considered to be robust. It is based on geometrical principles: The parameter space of dimension p is explored by a family of points called a simplex, which is a geometric figure made up of $p+1$ points (vertices). Depending on the value of the merit function at each vertex, the algorithm modifies the simplex by one of three operations: reflection, expansion and contraction (Nelder and Mead, 1965). It is implemented in MATLAB with the function `fminsearch`. If we want to restrict each parameter to a given interval, we can use the function `fminsearchbnd` (D'Errico, 2024). This method has been used by Masoumzadeh et al. (2015); Bachmann et al. (2017); Eon et al. (2020).

4.1.2 Stochastic optimization

Successful retrieval of Hapke model parameters is closely related to the choice of model inversion technique, due to the non-linear nature of the model, which can lead to multiple solutions. To this end, we used Bayesian inversion, which is based on Bayes' conditional probability theorem and the principle of updated knowledge. It offers two main advantages over deterministic methods: i) a greater chance of bypassing local minima due to its probabilistic rather than deterministic nature, ii) better control of possible multiple solutions and their uncertainty.

The theory can be found following Aster et al. (2013), where we need to determine a posteriori $P(m|d)$, the conditional distribution of the model parameters given the observation (Equation 4.1).

$$P(m|D) = \frac{P(m)P(D|m)}{P(D)} \tag{4.1}$$

where D is the collected data or measurements and m is the hypothesis about a set of parameters (a sample candidate). The probability of having m before considering the data is described by $P(m)$, called the a priori. It should reflect our preconceptions about the parameters, e.g. the bounds, the favorable value ranges. In many cases, the probability distribution function (PDF) of the a priori is assumed to be uniform due to the lack of prior knowledge about the parameters. Next, $P(D|m)$ is the probability of obtaining the data D given the hypothesis of the parameter set m. In other words, it indicates the compatibility of the evidence, the observation, with the given hypothesis, calculated from the PDF of the measurement errors. On the denominator, $P(D)$ is known as the evidence or marginal likelihood for our model, integrated over all possible parameter values m (Equation 4.2). In other words, it is understood the likelihood of the evidence under any circumstances.

$$P(D) = \int P\left(D|m\right)\ P\left(m\right)\ dm \tag{4.2}$$

According to Aster et al. (2013), $P(D)$ is simply regarded as a normalizing constant of $P(m|D)$, so that its integral in the model space is one. In some cases, it is not necessary to know the normalizing constant, for example to compare two parameter hypotheses m_1 and m_2 within the same model (Equation 4.3).

$$\frac{P\left(m_1|D\right)}{P\left(m_2|D\right)} = \frac{P\left(m_1\right)P\left(D|m_1\right)}{P\left(m_2\right)P\left(D|m_2\right)} \tag{4.3}$$

The Bayesian method has several advantages over deterministic methods. Its implementation leads to a greater probability of bypassing local minima due to its probabilistic rather than deterministic nature, and to better control of the result and the uncertainty. Indeed, the Bayesian method provides the PDF not only of the observation space, but also of the parameter space (Fernando et al., 2016). As can be seen, not all parameters take the form of a normal distribution, since there are special cases where a parameter has a uniform PDF, which means that it does not affect the result. In another special case, there may be a multimodal distribution, and whether or not the result is valid depends very much on the final analysis.

Markov chain Monte-Carlo

For numerical implementation, Bayesian inversion typically uses Markov chain Monte Carlo (MCMC), a class of algorithms for systematic random sampling from high-dimensional probability distributions. As the name suggests, it is a combination of two sampling methods. Like Monte Carlo sampling, MCMC draws random samples from the distribution. It also draws samples, the next of which depends on the previous one, in the same way as a Markov chain. This allows the algorithms to focus on the quantity approximated from the distribution, even with a large number of random variables. Its process can be briefly explained Calvetti and Somersalo (2007):

(1) Start with the point of your choice x_0 belonging to R^n (an initial set of values for n parameters).

(2) Draw a random vector $\omega_1 \sim \mathcal{N}(0, I)$ and define $x_1 = x_0 + \gamma\omega_1$, with γ the step size (the largest step a parameter can take), known as the learning rate.

(3) Repeat the process: set $x_{k+1} = x_k + \gamma\omega_{k+1}$, $\omega_{k+1} \sim \mathcal{N}(0, I)$

The choice of step size can be tricky: a small value makes the iteration result more often accepted, but may make the speed of convergence unacceptable. Conversely, a large value shortens the time required to reach the high probability region, but makes it more difficult to obtain the best solution. Therefore, a balance is found when the step size is set either heuristically or adaptively.

Metropolis-Hastings sampling

Among the MCMC methods, the Metropolis algorithm is the simplest to implement and the most widely used. In general, it uses a random walk to propose possible samples from an arbitrary target PDF (the posterior PDF), and then probabilistically chooses to accept or reject each candidate sample based on its probability in the target PDF (Lapotre et al., 2017). The key component of this method is the acceptance rate α, which determines the acceptance/rejection of candidates.

$$\alpha = \frac{P(m_c)\,P(D|m_c)}{P(m)\,P(D|m)} \text{ with } 0 < \alpha \leq 1 \tag{4.4}$$

In the context of Equation 4.4, m and m_c are the previous and newly proposed parameter hypotheses. At first glance, this equation is similar to Equation 4.3, and the acceptance ratio simply capitalizes on the comparison between two posterior probabilities. For uninformative prior distributions, α simply corresponds to the likelihood ratio (Aster et al., 2013). A further simplification occurs when the noises affecting the data are independent and normally distributed with standard deviation σ, so we can write the likelihood function as follows:

$$P(D|m) = \prod_{i=1}^{j} f(d_i|m) \tag{4.5}$$

where d_i represents the data points and j their number. If the data points are normally distributed with expected values given by the operation $G(m)$, and each has a standard deviation σ, then the likelihood function has the form:

$$f(d_i|m) = \frac{1}{\sigma\sqrt{2\pi}} e^{-\frac{[G_i(m)-d_i]^2}{2\sigma^2}} \tag{4.6}$$

hence,

$$P(D|m) = (\frac{1}{\sigma\sqrt{2\pi}})^2 e^{-\sum_{i=1}^{j}\frac{[G_i(m)-d_i]^2}{2\sigma^2}} \tag{4.7}$$

In practice, $P(D|m)$ can be extremely small, causing floating-point overflow problems. Therefore, it is advisable to wrap the components of Equation 4.5 in logarithms and thus transform the entire acceptance/rejection process as follows:

1) Use the MCMC method with a specified step size to generate a new candidate model m_c from the previous one m_k;

2) Calculate $\log(\alpha) = \log(P(D|m_c)) - \log(P(D|m_k))$;

3) Randomly generate $t \in [0, 1]$;

4) If $\log(t) < \log(\alpha)$, then accept the new candidate parameter hypothesis and let $m_{k+1} = m_c$, otherwise, reject the step and let $m_{k+1} = m_k$.

The combination of steps 3 and 4 is equivalent to returning the candidate hypothesis m_c with probability α and returning m_k with probability $1-\alpha$. If this is the case, what is the significance of this approach? The answer is that since the result of each iteration is determined by a probability, the function will move towards the solution with a high probability and randomly in the other direction with a low probability. The condition for completing the calculation is not defined by a predefined value such as the mean square distance, but rather by the number of samples. So we can have an infinite number of samples and the result will gradually approach the high probability region where the true solution is found. In the end, we get a candidate model that is slightly different each time we run the inversion, even if we use the same initial values (Calvetti and Somersalo, 2007).

If the sampling works as expected, we will obtain a set of models that can be classified into two groups: the "tail" where the candidate models gradually approach the minimum and the candidate models that orbit the high probability region (Figure 49). For a better presentation of the results, an important step to implement before running the Metropolis-Hastings sampling is to define the number of samples for "burn-in". This step does not affect the calculation, as it only removes a number of candidate samples from the initial "tail" that are not relevant to the high probability region and ultimately the uncertainty.

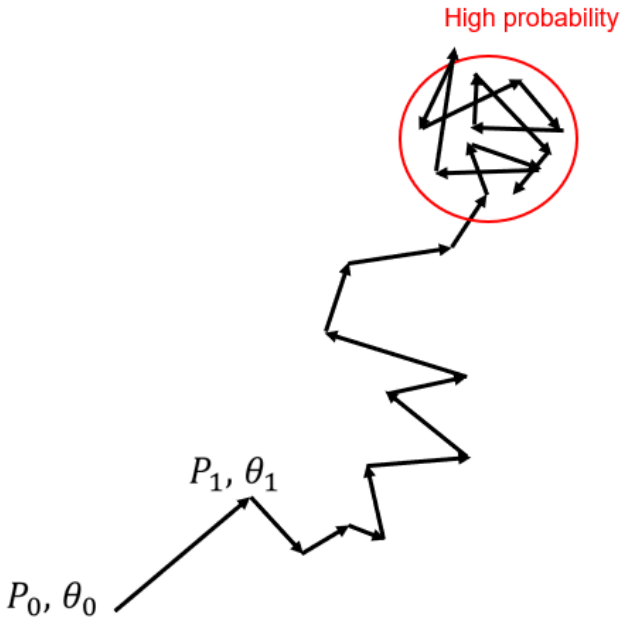

Figure 49 – Convergence process using the Metropolis-Hasting algorithm. P represents the posterior probability and θ the parameter hypothesis calculated and generated at each step.

Other methods of parameter sampling

The efficiency of Bayesian inversion is determined by the sampling method and the choice of the final solution based on the posterior distribution. For the latter, many authors often simply choose either the mean, mode or MAP of the distribution. For the former, however, we need to find a more effective sampling method other than Metropolis-Hastings, which explores the parameter space with a predefined step size and in a random direction, so it must generate a large number of samples and take a long time to deliver acceptable results. In the case of high-dimensional parameter space, there is an exponential number of directions in which to guess, but only a tiny number of directions that pass the test, making this method of sampling inefficient (Hoffman and Gelman, 2011). In the literature, we found the use of several MCMC algorithms that are considered to be a significant improvement: Hamiltonian Monte Carlo (HMC) and Dynamic Nested Sampling (DNS).

HMC is able to suppress random walk behaviour through a variable scheme that transforms the problem of sampling from a target distribution into the problem of Hamiltonian dynamics, where the potential energy is constrained by the target distribution, while the kinetic energy is unconstrained and must be specified by the implementation. It starts from a given initial set of parameter values, then for a given number of iterations a new momentum vector is sampled and

the current value of the parameter is updated using the leapfrog integrator, defined by step size and number of steps. A Metropolis acceptance step is then applied and a decision is made whether to update to the new state or keep the existing state. In this way, the correlation between successive sampled states is reduced and the typical set glides towards new unexplored neighborhoods, thus maximizing the utility of computational resources (Brooks et al., 2011; Betancourt, 2018).

On the other hand, whereas MCMC methods attempt to generate samples directly from the posterior, DNS instead splits the posterior into many nested slices, generates samples from each of them, and then recombines the samples to reconstruct the original distribution using the appropriate weights. Despite certain drawbacks, such as the need of a pre-transform and the sensitivity of the execution time to the size of the prior, this method has proved robust to complex, multi-modal problems (Speagle, 2020).

4.2 Fast Bayesian inversion (fBi)

4.2.1 Preprocessing for fast Bayesian inversion

Terrain correction

Terrain correction is an essential phase of the inversion of the Hapke model. The metadata of a Pleiades image provides an identical geometric acquisition configuration for each pixel in the image. In fact, the surface is not uniformly flat, so the slope and orientation of each pixel can vary considerably. We determined these for each pixel using the Pleiades DEM (Labarre et al., 2019). Given a constant phase angle, we calculated a new measurement configuration for each pixel using the law of spherical cosines. This calculation is applied to both incidence and emergence angles, allowing us to refine the accuracy of the inversion process by taking into account the influence of the terrain on the radiometric data. Let i' be the new solar zenith angle, e' the new viewing zenith angle and ϕ' the new relative azimuth angle. The geometric correction formulae can be written as follows:

$$\cos e' = \cos i \times \cos \vartheta + \sin i \times sin\vartheta \times \cos\left(\phi_i - \varphi\right) \tag{4.8}$$

$$\cos i' = \cos e \times \cos \vartheta + \sin e \times sin\vartheta \times \cos\left(\phi_e - \varphi\right) \tag{4.9}$$

$$\cos a' = \frac{\cos g - \cos i' \times \cos e'}{\sin i' \times \sin e'} \tag{4.10}$$

where i and ϕ_i are the initial solar zenith and azimuth angles, e and ϕ_e are the initial viewing zenith and azimuth angles, ϑ and φ are the slope and orientation of the terrain, and g is the phase angle. The local geometric configuration of certain steeply inclined pixels may indicate no direct illumination (shadow) or occultation of the satellite, as the solar or viewing zenith angle may exceed 90°. These are only a few pixels that have been filtered out. If either i' or e' equals zero, ϕ' is set to zero instead of Equation 4.10.

It is worth mentioning how to determine slope and aspect from elevation data. We have simply used the Slope and Aspect tools within the Geospatial Data Abstraction Library (GDAL), which are implemented in QGIS, a free and open source geographic information system (GIS) software [1]. There are two sets of formulae, one from Horn (1981) for rough terrain and the other from Zevenbergen and Thorne (1987) for smoother terrain.

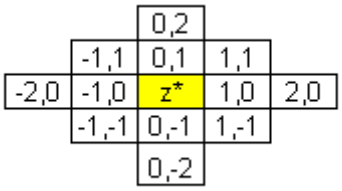

Figure 50 – Raster file neighborhoods [2]

In all the Pleiades images, we have observed that the variation in elevation is several times greater than the planar resolution. It is therefore reasonable to apply Horn's formulae. For a digitally meshed surface, the slope is defined as the magnitude of the first derivative of the surface function $z(x, y)$:

$$\vartheta = \sqrt{(\frac{\partial z}{\partial x})^2 + (\frac{\partial z}{\partial y})^2} \tag{4.11}$$

with

$$\frac{\partial z}{\partial x} \approx \frac{(z_{1,1} + 2z_{1,0} + z_{1,-1}) - (z_{-1,1} + 2z_{-1,0} + z_{-1,-1})}{8\Delta x} \tag{4.12}$$

$$\frac{\partial z}{\partial x} \approx \frac{(z_{1,1} + 2z_{0,1} + z_{-1,1}) - (z_{1,-1} + 2z_{0,-1} + z_{-1,-1})}{8\Delta x} \tag{4.13}$$

where different z corresponds to the location in Figure 50. The orientation is expressed in Figure 4.14:

$$\varphi = \frac{3\pi}{2} - \arctan\left(\frac{\partial z}{\partial x}, \frac{\partial z}{\partial y}\right) \tag{4.14}$$

Note that the application of terrain correction differs between the two Pleiades datasets. In the Asal-Ghoubbet rift, each image has only one initial configuration, which applies to all the pixels. On the Moon, each image of each channel is accompanied by four images representing the Sun zenith angles, the Sun azimuth angles, the observation zenith angles, and the observation azimuth angles. This means that each pixel has a unique geometric configuration. Importing all these maps and correcting the terrain for each pixel adds an extra layer of memory and computation.

1. https://www.qgis.org/
2. https://spatialanalysisonline.com/HTML/index.html?raster_models.htm

Filtering of invalid geometrical configurations (exclusive to the Pleiades Moon data set)

The reason why we need to limit the SZA and VZA to less than 70° was mentioned in Section 2.2.2. After performing the terrain correction for each pixel, we apply this filter to the new configuration before passing the BRF and configuration of each pixel to the next step.

Photometric normalization

Whereas terrain correction assigns a unique geometric configuration to each pixel in the image, the fast Bayesian inversion method assumes that all pixels have the same geometric configuration. It is therefore necessary to carry out a photometric normalization, which consists of calculating the BRDF of each pixel in a reference configuration defined by the user (i'', e'', g). To do this, we inverted the RTLS model for the Pleiades data from the Asal-Ghoubbet rift and the RPV model for the Pleiades data from the Moon, then ran it with the retrieved parameters to calculate the BRDF of the surface in the reference configuration. The reason why we use different BRDF models is that the Pleiades data on the Asal-Ghoubbet rift does not have a phase angle < 3°, unlike the Moon. The inversion of these models is performed using the simplex algorithm (Nelder and Mead, 1965). At this stage we obtain the model parameters for $r(i, e, g) = r(i', e', g)$, with the reflection factor and the phase angle remaining constant after the inversion of the RTLS or RPV models.

We then recalculate the normalized reflectance factors for each pixel in the reference configuration defined by the user. In the case of the Asal-Ghoubbet rift, this geometric configuration is the same as that declared in the auxiliary data for the 21 Pleiades images, in order to preserve the geometry of the acquisition. In the case of the Moon, we use the geometric configuration at the origin of the selenographic coordinate system, which is captured by the largest number of Pleiades images and therefore has the most detailed BRDF.

In short, we start with the same geometric configuration for all pixels (Figure 51A). Terrain correction consists of removing topographical effects by making all pixels perfectly horizontal, without changing their radiometry. This modifies the geometric configuration of each pixel (Figure 51B). It is only at the photometric normalization stage that new BRDFs corresponding to a unique geometric configuration for all pixels are computed using the RTLS (or RPV) model (Figure 51c). Finally, we do not invert the Hapke model on the Pleiades BRDFs, but on those simulated with the RTLS (or RPV) model after photometric normalization.

Data segmentation

The purpose of data segmentation is simple. By dividing the Pleiades images into smaller patches, we make it easier to carry out initial tests and check the results. What's more, we can process the calculations in parallel on several computers, reducing computing time.

In our experience, it is preferable for each image to be around 500×500 pixels in size and to represent only one spectral band, so the inversion process generally takes between half an hour and an hour. For the Asal-Ghoubbet rift, downsampling leads to images of 3234×3234 pixels. I have therefore divided the data into 6×6 equal parts, each patch being 539×539 pixels. For the Moon, I have divided the images so that each patch covers 15°×15° in selenographic coordinates,

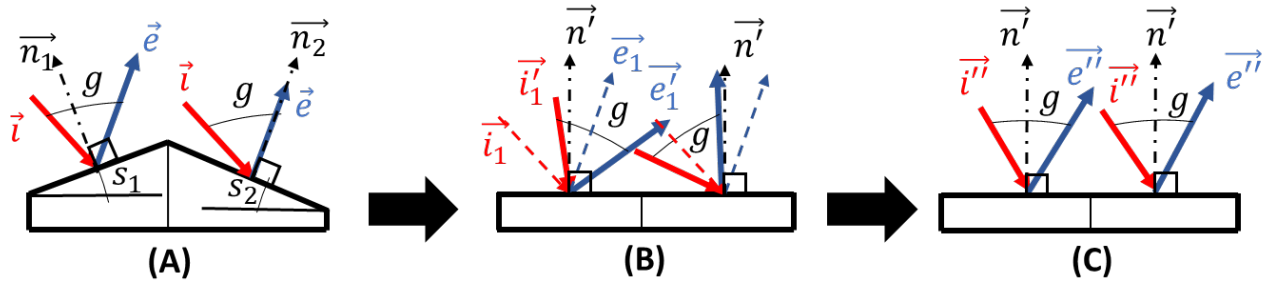

Figure 51 – Simplified graphical representation of terrain correction and photometric normalization for two pixels with different slope angles ($s1$, $s2$) (and possibly different orientations). Three stages are shown: (A) Initial condition (original BRDF, multi-configuration); (B) After terrain correction (original BRDF, multi-configuration); (C) After photometric normalization (simulated BRDF, unique configuration). $\vec{n_1}$ and $\vec{n_2}$ are the normal vector to the facets. $\vec{i}$ represents the illumination vector, $\vec{e}$ the emergence vector, and g the phase angle. The marks (′) and (”) indicate a change in the direction of the vector at each step. The subscript numbers (1,2) distinguish the two pixels.

i.e., approximately 433×433 pixels. We consider the moon in the range from -75° to 75° in longitude and latitude, which makes a total of 10 patches.

Flattening

Flattening is the process of reducing the size of the data. Originally, it is in the form of `image length` × `image width` × `number of images` × `bands`, which is incompatible with the amount of data that the fBi can digest. So we flatten the image data to one dimension by stacking it row by row. We then have a data cube of the form `flatten image data` × `number of images` × `bands`.

Finalizing the data pre-processing

At the end of data preprocessing, for each patch, we have:

• Data input: has two data cubes: one for the BRF and one for the measurement error (4% for Pleiades images); a binary mask to exclude the unwanted pixels from the inversion; and a wavelength vector of the Pleiades bands.

• Configuration input: has matrix of size `number of image` × 3. The three columns are the incidence angle i, the emergence angle e and the azimuth difference ϕ.

4.2.2 Main process

To address both the problem of effective sampling and the problem of exploring the posterior distribution, a complete framework has been proposed by Kugler et al. (2022), which takes a very different approach from the aforementioned methods. First, for sampling, they introduced the use of an algorithm called the Gaussian Locally Linear Mapping (GLLiM) model (Deleforge et al., 2015). The principle is to transform the parameters of interest into a common global parameter set that can be implemented for all conditional distributions. Thus, the cost of individual inversions (the

number of samples drawn) is transferred to this global operator and greatly reduced, allowing the algorithm to be applied to a large number of observations.

To describe the individual processes of this particular algorithm, we start with the transformation of the parameters. First we have X, the set of L individual parameters denoted as x, and Y, the set of D individual observations denoted as Y. While it is generally desirable to model a non-linear data set with a mixture of linear models, we assume that Y is a noisy image of X obtained from a K-component mixture of affine transformations. The function that maps X to Y is:

$$Y = \sum_{k=1}^{K} \mathbb{I}_{Z=k}(A_k X + b_k + \epsilon_k) \tag{4.15}$$

where $\mathbb{I}$ is the indicator function, $Z \in \{1, ..., K\}$ is a newly introduced latent variable (which can only be inferred indirectly from other observable variables through a mathematical model), matrix $A_k \in R^{D \times L}$ and vector $b_k \in R^D$ define the affine transformation, $\epsilon_k \in R^D$ is an error term that captures both observation noise and reconstruction error due to the affine transformation. Since the GLLiM model is derived assuming that the joint distribution is a mixture of Gaussian distributions (Deleforge et al., 2015), $\epsilon_k \sim \mathcal{N}(0, \Sigma_k)$, X is now a mixture of K Gaussian distributions (denoted by the subscript G), specified by $p_G(x|Z = k) = \mathcal{N}(x; c_k, \Gamma_k)$, and $p_G(Z = k) = \pi_k$. Then we can have the global model parameter $\theta = \{\pi_k, c_k, \Gamma_k, A_k, b_k, \Sigma_k\}_{k=1:K}$.

The global parameter θ is estimated by standard Expectation-Maximization (EM), an efficient iterative procedure for computing the maximum likelihood (ML) estimate in the presence of missing or hidden data. In ML estimation, we want to estimate the model parameters for which the observed data are most likely. Each iteration of the EM algorithm consists of two steps: The E-step and the M-step. In the E-step, or expectation, the missing data are estimated given the observed data and the current estimate of the model parameters. This is done using conditional expectation, which explains the choice of terminology. In the M-step, the likelihood function is maximized assuming that the missing data are known. The estimates of missing data from the E-step are used instead of the actual missing data. Convergence is ensured because the algorithm is guaranteed to increase the likelihood at each iteration (Borman, 2004). In this way, the prior and posterior distributions would be presented under the form:

$$p_G(y|X = x, \theta) = \sum_{k=1}^{K} \eta_k(x) \mathcal{N}(y; A_k x + b_k, \Sigma_k) \tag{4.16}$$

with

$$\eta_k(x) = \frac{\pi_k \mathcal{N}(x; c_k, \Gamma_k)}{\sum_{j=1}^{K} \pi_j \mathcal{N}(x; c_j, \Gamma_j)} \tag{4.17}$$

$$p_G(x|Y = y, \theta^*) = \sum_{k=1}^{K} \eta_k^*(y) \mathcal{N}(x; A_k^* x + b_k^*, \Sigma_k^*) \tag{4.18}$$

with

$$\eta_k^*(x) = \frac{\pi_k \mathcal{N}(y; c_k^*, \Gamma_k^*)}{\sum_{j=1}^{K} \pi_j^* \mathcal{N}(y; c_j^*, \Gamma_j^*)} \tag{4.19}$$

From Equation 4.19, we get a new parameterization $\theta^* = \{\pi_k, c_k^*, \Gamma_k^*, A_k^*, b_k^*, \Sigma_k^*\}_{k=1:K}$. To estimate the posterior distribution (Equation 4.18), θ is estimated from θ^* via a series of formulae:

$$c_k^* = A_k c_k + b_k \tag{4.20}$$

$$\Gamma_k^* = \Sigma_k + A_k \Gamma_k A_k^\intercal \tag{4.21}$$

$$\Sigma_k^* = (\Gamma_k^{-1} + A_k^\intercal \Sigma_k^{-1} A_k)^{-1} \tag{4.22}$$

$$A_k^* = \Sigma_k^* A_k^\intercal \Sigma_k^{-1} \tag{4.23}$$

$$b_k^* = \Sigma_k^* (\Gamma_k^{-1} c_k - A_k^\intercal \Sigma_k^{-1} b_k) \tag{4.24}$$

To summarize, in GLLiM we first estimate the global parameter θ from the available data, then infer θ^* and finally the posterior distribution. The next step would be to improve the solution prediction using a special technique called Incremental Mixture Importance Sampling (IMIS). This is a refinement of "importance sampling", a collection of Monte Carlo methods in which a mathematical expectation about a target distribution is approximated by a weighted average of random draws from another distribution. In other words, samples are drawn from a distribution other than the one of interest, to make sampling easier. While "importance sampling" handles I samples all at once, starting with I_0 samples, IMIS successively samples J groups of B samples, using the previous group to sequentially refine the proposed distribution with additional components. Knowing that the choice of J reflects the trade-off between computational efficiency and precision, IMIS helps to exert more control over the exploration of the posterior distribution and to improve the prediction of means and modes (Kugler et al., 2022). In practice, we use different prediction methods and choose the one with the lowest residuals. The whole framework of fast Bayesian inversion is illustrated in Figure 52.

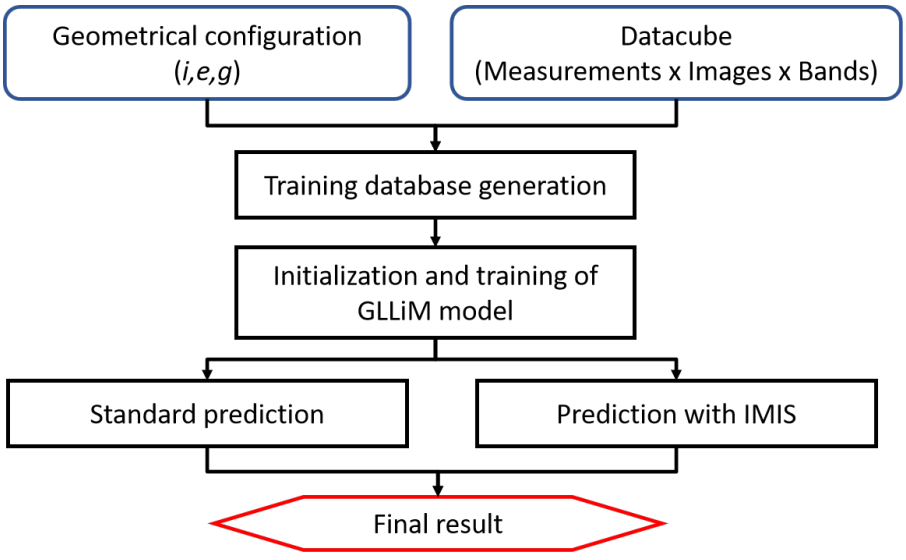

Figure 52 – Fast Bayesian inversion framework.

Fast Bayesian inversion is highly efficient for large-scale inversions, while retaining the advantages of Bayesian analysis. It improves prediction accuracy, reduces computation time, and provides information about parameter estimates thanks to the posterior prediction distribution. It is very useful for poorly constrained inverse problems where multiple solutions may coexist (e.g., Fernando et al. (2013); Schmidt and Fernando (2015); Kugler et al. (2022)).

4.2.3 Software usage

There are two versions of fBi: one is a standalone software and the other is facilitated by a web browser and requires an internet connection. Both can be used in a Windows or Linux environment, but in my experience I've had fewer errors with Linux.

Standalone, offline package

The standalone version of fBi can be downloaded from the following address `https://gitlab.inria.fr/bkugler/fastbayesianinversion`. It requires the Julia programming language (`https://julialang.org/`), chosen for its optimization for parallelism and distributed computation. After installing Julia, the user must open it and install several packages using the following commands:

```
using Pkg

Pkg.add("PyPlot")

Pkg.add("LaTeXStrings")

Pkg.add("JSON")

Pkg.add("Colors")

Pkg.add("Formatting")

Pkg.add("MAT")

Pkg.add("Conda")

Pkg.add("TensorCast")

Pkg.add("Plots")

Pkg.add(url="https://gitlab.inria.fr/bkugler/fastbayesianinversion")

ENV["PYTHON"]="/soft2/x86_64/gcc_6.3.0/anaconda3_2019.10/bin/python"
```

To test, we input:

```
build PyCall

build PyPlot
```

If a package does not install, we recommended deleting everything in the `.julia/environments` directory (it may be a hidden folder) and install the packages from scratch. After adjusting the directories in `fastbayesianinversion/playground/env.jl` we can modify three files `hapke_models/models.jl`, `manuscrit/inversion.jl` and `manuscrit/prerequsite.jl` in `fastbayesianinversion/playground`. The targets for modification are the fBi parameters, the type

of radiative transfer model and the input and output directories. Unfortunately, these three files are currently missing from the official fBi installation link and are reserved for personal use. However, we can provide them on request. To launch the software, simply type the following command line in the terminal:

```
julia --threads X <address of inversion.jl> > <address of log file> &
```

where `X` is the number of threads. The value of `X` depends on the processing capacity of the computer. At the moment, we haven't designed a script for batch processing, so we have to change the parameters manually each time.

Online version: planetGLLiM

The home page for this version can be found at https://gitlab.inria.fr/kernelo-mistis/planet-gllim-front-end. To use it, the user must install Docker (https://www.docker.com/), a versatile platform that lets you package and run an application inside a container, a lightweight, isolated environment. This separation and security allows multiple containers to run simultaneously on the same host. You will also need to obtain a login key from the Institut national de recherche en sciences et technologies du numérique (INRIA). To run the program, we first open the terminal and log in with the command line:

```
docker login registry.gitlab.inria.fr
```

Then go to the directory `planet-gllim-front-end/build`, update the program using:

```
docker compose pull
```

To activate the program, input:

```
docker compose up
```

then open a browser, go to http://0.0.0.0:8080/simulation, declare the input directories and modify the fBi parameters. Once finished, we can select "Save configuration" to finalize the input and click "Start" to begin the inversion. Once the inversion is complete, we can download the results, which are a `.zip` file containing the prediction of the normal solution by the k-mean algorithm and the IMIS prediction, each with two centroids, a mean and the corresponding standard deviations.

4.3 Evaluation of the accuracy of the surface photometric parameters estimations

Because of the non-linearity of the model, estimating a global solution by inversion is challenging. The lack of prior knowledge about parameter values often turns the inverse problem into an attempt to identify an optimal combination of variables that reduces the gap between observations and model predictions through iterative numerical analysis. Therefore, we calculated the root mean square error (RMSE) of the reconstructed BRF as follows:

$$RMSE = \frac{1}{N}\sqrt{\sum_{k=1}^{n}(r_k - r(i_k, e_k, g_k))^2} \tag{4.25}$$

where n is the number of data points (number of images), r_k is the measured reflectance and r is the reflectance predicted by the model. r is calculated using the direct Hapke model on the retrieved parameters and the configuration obtained after terrain correction. The solution with the lowest RMSE is then selected. The fast Bayesian inversion also provides the standard deviation (SD) of each parameter for each pixel, which is useful for understanding the constraints on each parameter during the inversion.

4.4 Test the individual Hapke model inversion

In this section, we would like to demonstrate the capability of two inversion schemes: Bayesian inversion using MCMC sampling and fast Bayesian inversion on two versions of the Hapke model. We tested these methods on different data sets to those used for massive inversion.

4.4.1 Framing camera data of Dawn spacecraft (with 4-parameter Hapke model)

This part offers an exciting extension of our previous work, applying the same inversion and interpretation methods to planetary surfaces. Initial results are promising and demonstrate the effectiveness of the inversion approach. Although further context and data conditions are required to confirm the validity of the dataset and justify the use of the Hapke model inversion, this work has strong potential for wider application. As the project is currently under review, we will refrain from sharing the interpretation of our results at this stage.

NASA's Dawn mission was designed to study two extraterrestrial bodies: the giant asteroid (4)Vesta and the dwarf planet Ceres, both located in the main asteroid belt between Mars and Jupiter. On (4)Vesta, certain craters, avalanches, cliffs and ejecta deposits show unexpected and unexplained variations in brightness as a function of phase angle. Focusing on the avalanches in Cornelia crater (9°S, 226°E), we aim to study the granular segregation resulting from avalanches (Figure 53) in order to improve our understanding of the microphysical properties of airless planetary regoliths.

The inversion of the Hapke model has made it possible to extract the physical properties of the grains in different terrain units. Amande Roque-Bernard carried out the preparatory work by collecting and processing the data, which includes multi-angle images from the Framing Camera of the Dawn spacecraft, with incidence and phase angles ranging from 10° to 75°. This wide range of phase angles is within the scope of the model. However, as shown in Figure 55, measurements at low phase angles (< 20°) are far too few to constrain the hotspot parameters. We therefore opted for the 4-parameter version including SSA (ω), the photometric roughness ($\bar{\theta}$), and the two HG phase angle parameters (b and c).

Figure 54 shows one of the results of Bayesian inversion using MCMC. Unlike fBi, we are able to keep track of all samples and we choose the best solution with the lowest RMSE between the mean and centroids, as shown above. In Figure 54(a), ω is the most constrained parameter, while c is the least constrained, based on the confidence interval. It seems that with a sample size of 5×10^5 the parameters are stabilized (Figure 54(b)). In parallel,, figure 55 shows the BRF curves reconstructed from the Hapke parameters obtained by the two inversion methods. The results are

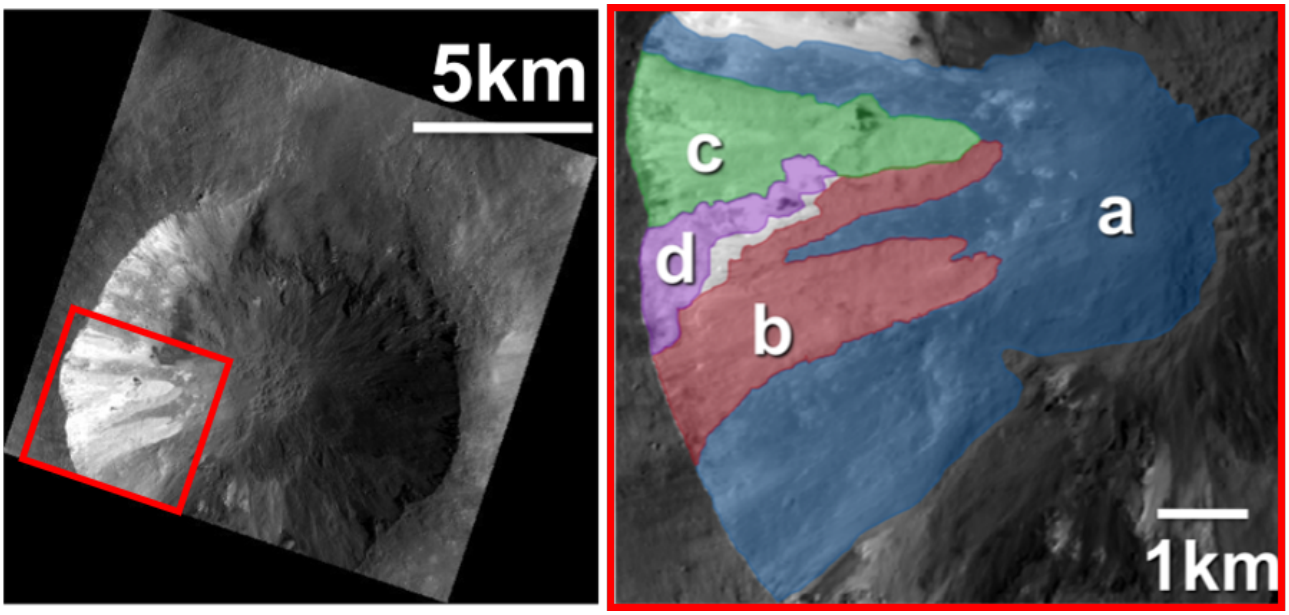

Figure 53 – Left panel: Cornelia crater as seen by the Framing Camera in the panchromatic band, with an average GSD of 20 m. The red rectangle corresponds to the studied area. Right panel: delimitation of four avalanches referenced by a letter.

visually similar, although fBi does not provide us with a set of samples for plotting the confidence interval. This similarity is also shown in Table 4.1, and the RMSE values are below 0.02, which is in the range recommended by Fernando et al. (2013). We can therefore conclude that both methods give acceptable results. The MCMC method gives a slightly better result in terms of RMSE, but slightly worse in terms of standard deviation of the parameters, which means that the sampling is not as efficient. In addition, the computation time for MCMC is considerably longer (a few hours for MCMC and a few seconds for fBi).

Site	ω	$\overline{\theta}$ (°)	b	c	RMSE
Bayesian inversion with MCMC					
avalanche a	0.74 ± 0.08	49.13 ± 6.28	0.33 ± 0.1	0.55 ± 0.23	0.0105
avalanche b	0.78 ± 0.06	50.69 ± 9.39	0.31 ± 0.05	0.78 ± 0.17	0.013
avalanche c	0.78 ± 0.05	48.48 ± 4.5	0.34 ± 0.06	0.72 ± 0.19	0.012
avalanche d	0.78 ± 0.04	50.42 ± 4.12	0.33 ± 0.04	0.83 ± 0.13	0.0177
Fast Bayesian inversion					
avalanche a	0.72 ± 0.05	50.29 ± 4.26	0.29 ± 0.05	0.69 ± 0.15	0.0111
avalanche b	0.78 ± 0.03	49.39 ± 2.83	0.32 ± 0.03	0.75 ± 0.11	0.0151
avalanche c	0.77 ± 0.04	45.79 ± 4.83	0.35 ± 0.04	0.72 ± 0.15	0.0136
avalanche d	0.79 ± 0.04	50.25 ± 3.46	0.33 ± 0.03	0.84 ± 0.12	0.0181

Table 4.1 – Inversion result Vesta data using Bayesian inversion with MCMC sampling and fast Bayesian inversion.

4.4.2 SHINE data (with the 6-parameter Hapke model)

Let us first recall the context and the state of the SHINE data presented in section 2.4.1. As there are many measurements with low phase angles, we can invert the 6-parameter Hapke model. We

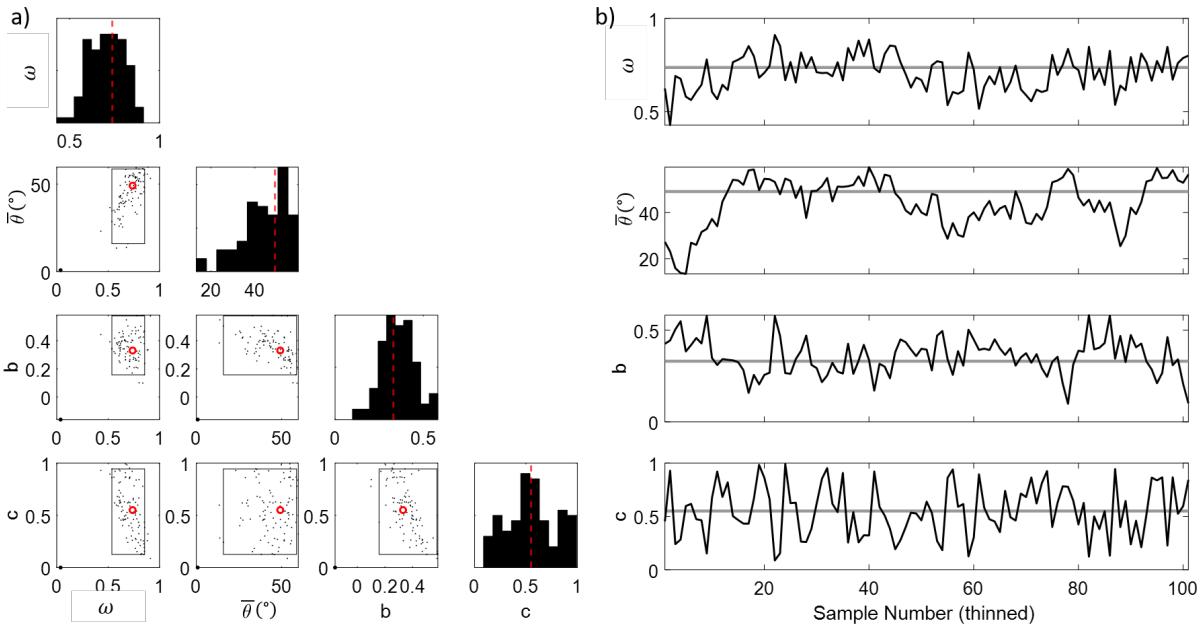

Figure 54 – Result of Bayesian inversion using MCMC sampling over the avalanche area a. a) The bar graphs represent the posterior distribution of each parameter. The scatter plots show the distribution in terms of relationship between pairs of parameters. The red circles and red dashed lines highlight the chosen solution. The black rectangles represent the 95% confidence region. b) The thinned sampling progress, where samples are chosen at regular intervals.

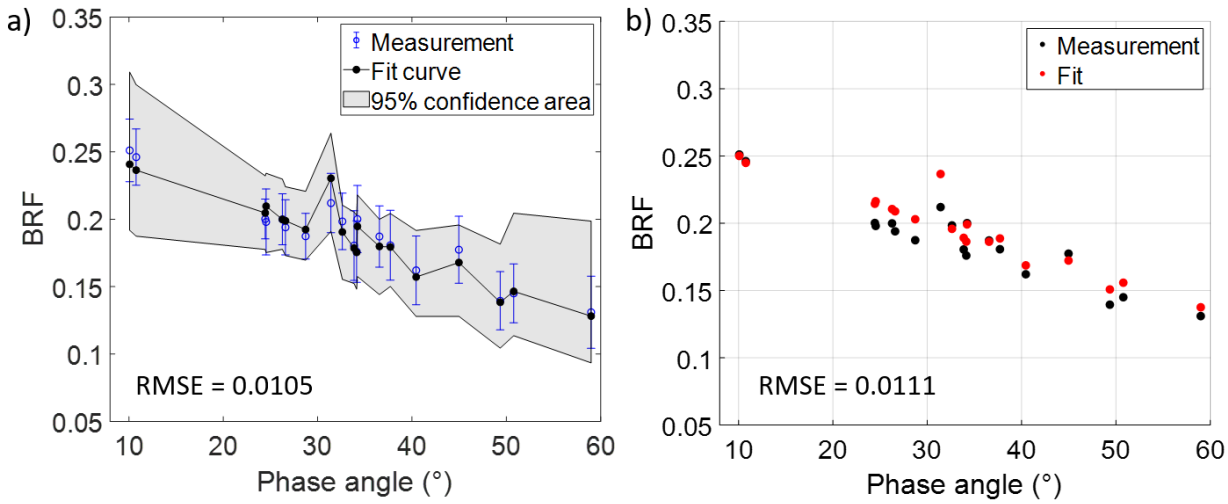

Figure 55 – Measurement and reconstruction the BRF curve, using the Hapke parameters estimated by a) Bayesian inversion with MCMC sampling and b) fast Bayesian inversion.

will mainly present the results of Bayesian inversion with MCMC, as we have shown that the results are similar when using the fBi.

The posterior distribution and sampling progress resulting from the MCMC method applied to Djibouti T sample are shown in Figure 56. In subplot (a), the parameters are suitably constrained, with the exception of the parameter h, whose 95% confidence interval covers almost the entire defined limit [0,1]. The posterior distributions generally show a single peak, while the parameter h appears to have two modes. The distributions of the two hotspot parameters h and B_0 have a peak close to the limit of 0 or 1. This is of concern because if B_0 approaches zero, we would have

the 4-parameter Hapke model with the value of h being non-sequential. We can also observe the unconstrained nature of h in subplot (b), where samples can deviate significantly from the expected solution at the end of the sampling process.

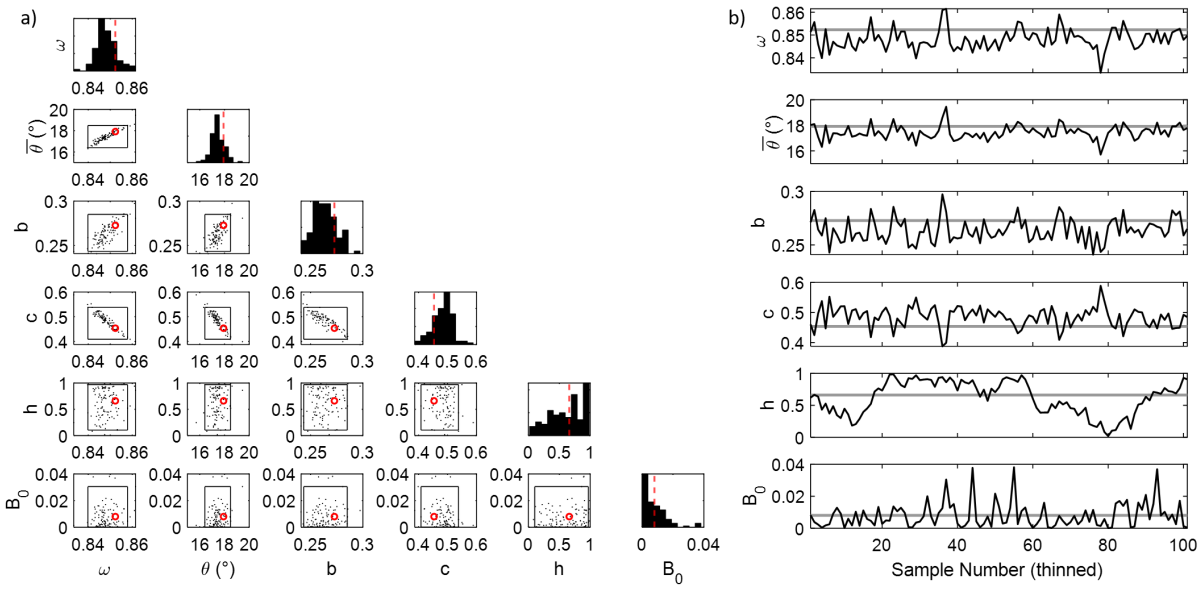

Figure 56 – Result of Bayesian inversion using MCMC sampling on Djibouti T sample from the SHINE data set (Band 1: 520-600 nm). The presentation is similar to Figure 54, but with six Hapke parameters.

Figure 57 compares the BRF curves constructed from the parameters estimated by both methods. Again we see many similarities, with only a small difference at large phase angles. The reason why there are several measurement points at the same phase angle is that many off-main-plane measurements were made with a different geometric configuration but the same phase angle. This is why we don't show a confidence interval, so as not to clutter up the graph. The RMSE in both cases is greater than 0.02, which could be due to the high BRF values. The value of 0.02 is considered by Fernando et al. (2016), whose work we often refer to because of the similarity in terms of inversion and method of interpreting the results. Indeed, RMSE evaluation is sensitive to outliers and high amplitude data. In this case, we must either relax our requirement and set the RMSE limit higher, or adopt another measure called relative RMSE (RRMSE), expressed as a percentage. This is a normalized version of the RMSE, which means that it is adjusted for the range of the data. It is useful for comparing the accuracy of different models or data sets operating at different scales.

$$RRMSE = \frac{1}{N}\sqrt{\sum_{k=1}^{n}\frac{(r_k - r(i_k, e_k, g_k))^2}{r_k^2}} \tag{4.26}$$

However, there is little consistent, meaningful, quantitative criterion for defining an appropriate error for RMS residuals (Helfenstein and Shepard, 2011). Although the use of RMSE and RRMSE is widespread, there is no consensus on which value is best. For example, Cord et al. (2005) use 0.03 for RMSE, 0.05 for Li et al. (2019) and 0.06 for Fornasier et al. (2015). As for the RRMSE, Belgacem et al. (2021) take the value of 30%, while it is 20% for Hasselmann et al. (2016). Therefore, we have to make a decision based on the data condition. The RRMSE of the results in Figure 57 is 7% and

8%, which can be considered satisfactory in most cases.

So far, we have performed Bayesian inversion on all the SHINE measurements performed on the samples collected in the Asal-Ghoubbet rift (sites F, T and R) (Table 4.2). Based on the inversion quality assessment established previously, we can see that the results of site F and site T are satisfactory. The results of site R showed many problems, such as high RMSE and parameters close to their boundary values. It was therefore decided to exclude this site from future analysis.

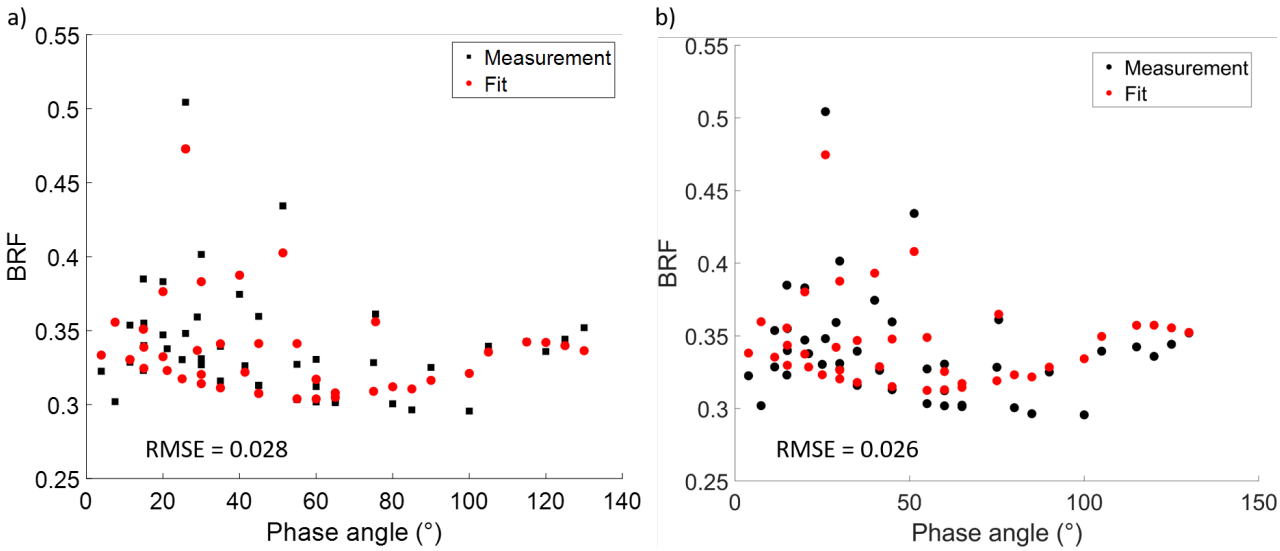

Figure 57 – Measurement and reconstruction BRF curve, using the estimated Hapke parameters from Figure 56 and a) Bayesian inversion with MCMC; b) Fast Bayesian inversion.

Channel	ω	$\overline{\theta}$ (°)	b	c	h	B_0	RMSE
Asal-Ghoubbet rift site F							
B0	0.59 ± 0.01	22.66 ± 0.59	0.29 ± 0.01	0.50 ± 0.02	0.30 ± 0.30	0.01 ± 0.04	0.024
B1	0.67 ± 0.0	16.25 ± 0.11	0.27 ± 0.0	0.72 ± 0.01	0.77 ± 0.05	0.01 ± 0.04	0.034
B2	0.8 ± 0.0	20.03 ± 0.32	0.26 ± 0.0	0.62 ± 0.02	0.62 ± 0.02	0.0 ± 0.02	0.040
B3	0.88 ± 0.02	21.86 ± 0.98	0.32 ± 0.02	0.43 ± 0.05	0.39 ± 0.02	0.02 ± 0.06	0.042
Asal-Ghoubbet rift site T							
B0	0.78 ± 0.05	20.69 ± 3.89	0.29 ± 0.13	0.34 ± 0.21	0.51 ± 0.29	0.39 ± 0.27	0.028
B1	0.85 ± 0.0	17.92 ± 0.35	0.27 ± 0.01	0.45 ± 0.03	0.66 ± 0.23	0.01 ± 0.01	0.025
B2	0.9 ± 0.01	17.63 ± 0.28	0.3 ± 0.01	0.39 ± 0.02	0.58 ± 0.33	0.01 ± 0.03	0.027
B3	0.92 ± 0.0	15.33 ± 0.11	0.3 ± 0.0	0.45 ± 0.01	0.54 ± 0.02	0.0 ± 0.02	0.033
Asal-Ghoubbet rift site R							
B0	0.43 ± 0.01	4.31 ± 2.13	0.49 ± 0.01	0.45 ± 0.03	0.05 ± 0.02	0.97 ± 0.04	0.118
B1	0.86 ± 0.0	10.69 ± 0.68	1.0 ± 0.0	0.06 ± 0.02	0.13 ± 0.06	0.35 ± 0.03	0.060
B2	0.87 ± 0.0	11.63 ± 0.28	0.88 ± 0.0	0.02 ± 0.0	0.1 ± 0.09	0.3 ± 0.06	0.052
B3	0.9 ± 0.01	11.69 ± 1.52	0.93 ± 0.04	0.01 ± 0.01	0.44 ± 0.03	0.37 ± 0.03	0.038

Table 4.2 – Inversion result of SHINE data using Bayesian inversion with MCMC sampling. The SHINE chanels are B0 (490 nm), B1 (560 nm), B2 (650 nm), B3 (840 nm).

We also performed an fBi inversion on the green channel of SHINE for site T (Table 4.3), to verify the results in Table 4.2. As expected, they are similar in terms of RMSE, parameters and SD values.

Channel	ω	$\overline{\theta}$ (°)	b	c	h	B_0	RMSE
B1	0.86 ± 0.0	18.03 ± 0.37	0.28 ± 0.01	0.41 ± 0.02	0.97 ± 0.03	0.01 ± 0.01	0.026

Table 4.3 – Inversion result of SHINE data of site T, channel B1 (560 nm), using fast Bayesian inversion.

We will now analyze the results of table 4.2 in light of the information we have.

• Site F, which contains very fine calcite and quartz silt, is easily recognizable by its brightness on a satellite image. Therefore its SSA (ω) is high, 0.6 or more. The photometric roughness is quite high (around 20°) for a relatively flat plain and is consistent across the four channels. The sample from site F also shows wider scattering lobes corresponding to a low value of b, which can be interpreted as irregular, rough particles. However, Figure 110 shows that this is not the case, but that very fine silt tends to clump together in the presence of moisture, making the sample rougher than normal. The parameter c is rather difficult to interpret as it varies from channel to channel. However, its mean value of 0.57 tends to show that the scattering of site F is equally in the forward and backward directions. Together they show that this sample contains clumped particles with moderate density. In contrast, B_0 approaches zero, which invalidates the results of h...

• Site T, which contains limestone slabs, is also bright. The SSA values are even higher than those of site F, which is normal because its reflectance spectrum is higher (Figure 126 and 127). The proportion of limestone may be higher. $\overline{\theta}$ varies from 15° to 20°. b is about 0.3, indicating a broad diffusion lobe. c is between 0.3 and 0.45, showing a slight preference for forward scattering, probably due to the quartz and crystal structure. Together they show that the sample has clumped particles and a rough surface grain, which are the features we can observe (Figure 126 and 127). Otherwise, B_0 is close to zero, which makes it difficult to interpret the h results. The exception is B_0, where $h = 0.51$ and $B_0 = 0.39$ indicate that the sample is moderately compact and opaque.

Conclusion

We have presented a number of inversion methods, each with its own advantages and disadvantages. Among all the options, we have chosen the fast Bayesian inversion developed by (Kugler et al., 2022). It allows us to deal with non-linear models such as the Hapke model, since it preserves the original capacity of Bayesian inversion: assessing uncertainty, bypassing local minima and being suitable for studying the case of multiple solutions. Moreover, the quality of the inversion is verified: the results are similar to those of the standard Bayesian inversion (MCMC sampling), while significantly reducing the computational cost. As a result, fBi will perform very well in the case of massive inversion (Chapter 5).

Chapter 5

Massive inversion of the Hapke model: Results

Introduction

Inversion of BRDF models on satellite images presents both significant challenges and opportunities. In the simplest case, researchers manually select pixels on an image, extract their BRDF, then run inversion schemes to retrieve the model parameters. This approach has been implemented by Labarre et al. (2019) on multiangular Pleiades images acquired over the Asal-Ghoubbet rift. Inversion of the Hapke model over extended areas has rarely been implemented for several reasons: (1) Insufficient coverage or inadequate geometric configurations, impacting model selection and parameter constraints; (2) The interdependence of model parameters, leading to multiple solutions (local minima) during inversion; (3) A lack of field measurements for validation; (4) Atmospheric effects affecting the photometric response of surfaces; (5) Important computational resources required to process millions, if not billions, of pixels in several spectral bands. A massive image-scale inversion would provide much wider coverage and a detailed representation of land units. In our work, we use both single (Section 4.4) and massive inversion (this chapter).

Here we present the results of large-scale inversion using the fast Bayesian inversion method described in Chapter 4 on Pleiades data from the Asal-Ghoubbet rift and the near side of the Moon. Depending on the dataset, the 4- or 6-parameter Hapke model is applied (the conditions are set out in Chapter 2), allowing multi-parameter maps to be produced. The process begins with an assessment of the quality of the inversion, followed by a detailed discussion of the observations drawn from the results. We then proceed to interpret these results, making cross-comparisons, discussing their significance and concluding with key takeaways.

5.1 Asal-Ghoubbet rift

In this section, the results will often be compared with the information in Table 2.3 and the geologic map in Figure 58.

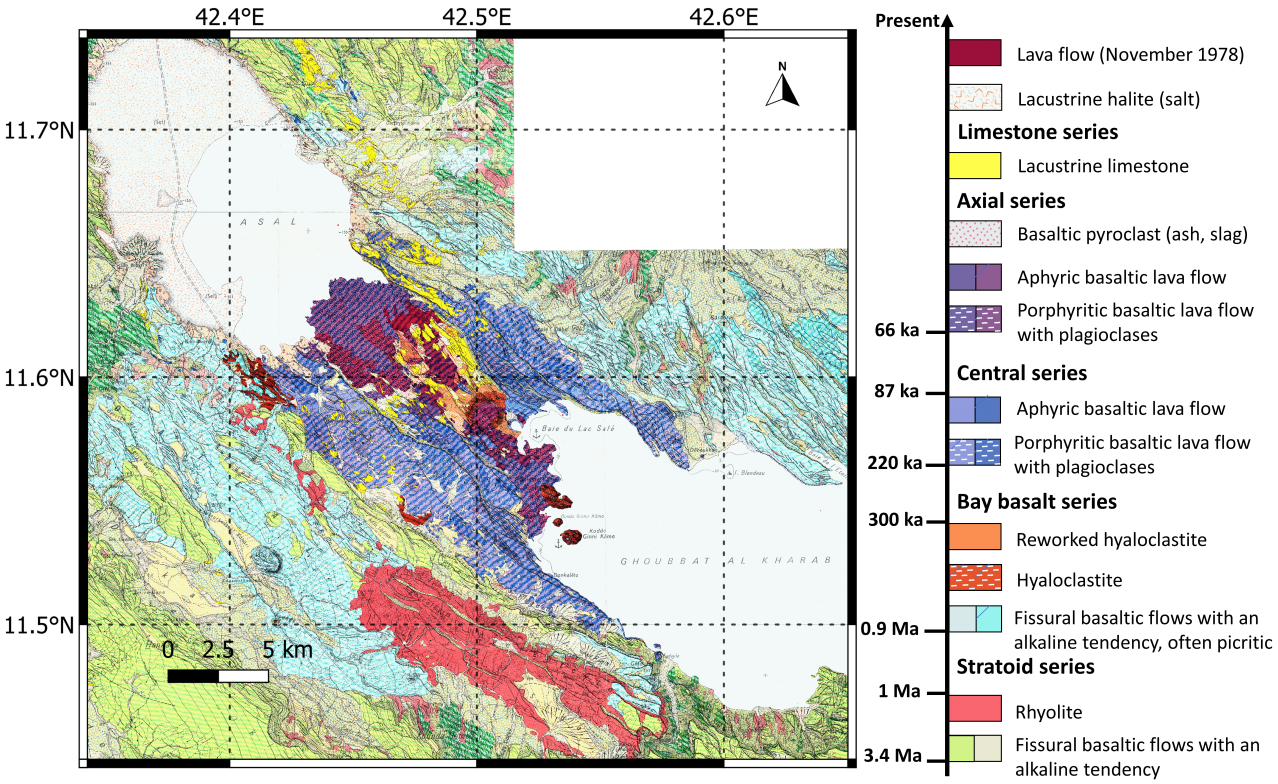

Figure 58 – Geologic map of Asal-Ghoubbet rift (after Stieltjes (1980); Pinzuti et al. (2013)).

5.1.1 Overall quality of the inversion

To assess the accuracy of the model's predictions, we consider RMSE values of 0.02 or less to be acceptable. This excludes clouds, their shadows and steep slopes where the fit is poor. As seen in Figure 59, the model reproduces the amplitude and general shape of the BRDF. A comparison between the RMSE map (Figure 60a) and the Pleiades DEM (Figure 24) clearly shows that RMSE is higher in steep rift areas. RMSE values are generally below 0.01 for most sites (Figure 60b), suggesting good agreement between predicted and observed values. For sites K and S, they vary between 0.1 and 0.12 due to cloud contamination of some images, which produced 2-3 outliers. However, the impact on inversion is moderate. The fit is also poorer at the F, H and T bright sites, with RMSE values between 0.15 and 0.2. This suggests that an increase in BRF corresponds to an increase in residuals, as shown in Figures 59 and 60b). Therefore, to verify this observation and ensure the robustness of the inversion, we calculated the relative root-mean-square error (RRMSE) at different sites. Most values are below 0.1 and around 0.06, with no significant trend.

Fernando et al. (2016) and Schmidt and Fernando (2015) have shown the importance of phase angles in BRDF analysis. Specifically, they highlighted that phase angles $> 90\,\mathrm{deg}$ and ranges of variation $> 50\,\mathrm{deg}$ are essential to effectively constrain the Hapke model parameters. With phase angles ranging from 35° to 90°, our dataset partially meets these requirements and 80% of the region meets the strict requirement of an $RMSE \leq 0.02$ (Figure 60a).

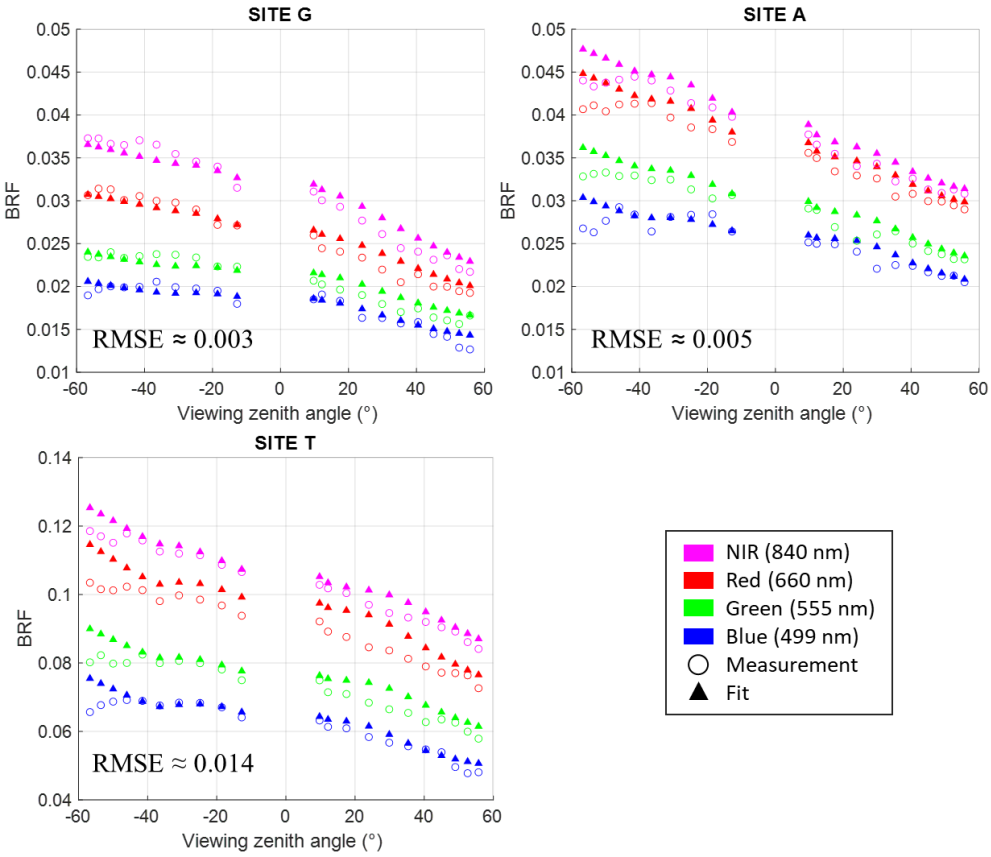

Figure 59 – Comparison between the BRF measured by Pleiades at sites G, A and T (Figure 6) (circles) and the BRF simulated by the Hapke model (triangles) in four Pleiades channels.

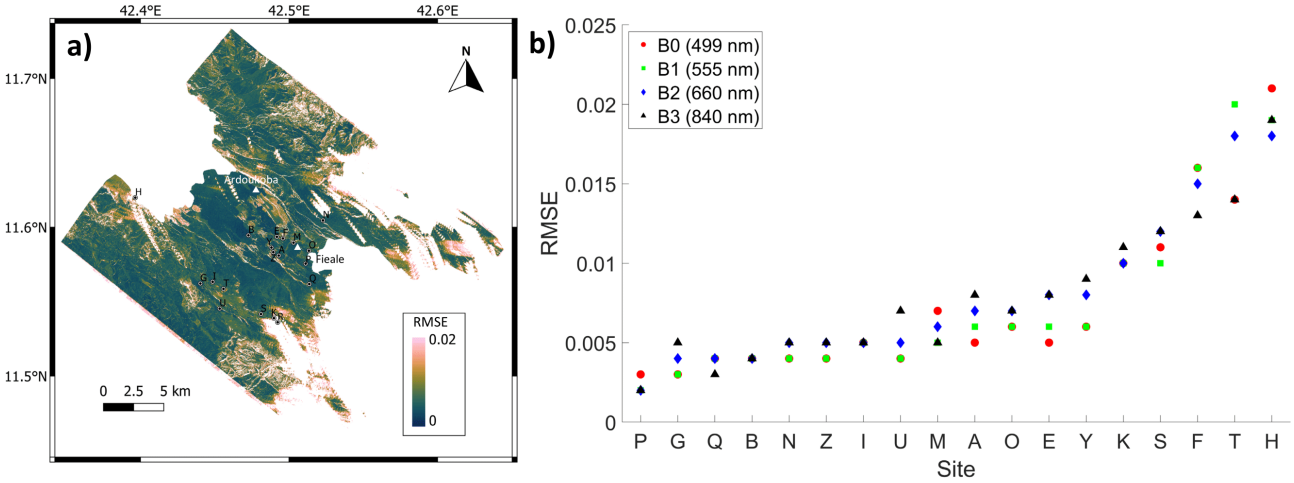

Figure 60 – Root mean square error between the measured BRF and the modeled BRF a) over the entire image in the Pleiades spectral band centered on 555 nm; b) For the 18 experimental sites in the four Pleiades spectral bands, in ascending order of value.

5.1.2 Single scattering albedo ω

Results

Figure 61a shows the single scattering albedo (SSA) map in the green band obtained by massive Bayesian inversion of the Hapke model on the Asal-Ghoubbet rift. SSA is well constrained with SD < 0.015 almost everywhere in the image (Fig. 61b). The lowest values are observed on basaltic

units, but they vary significantly between the inner floor of the rift and its two flanks. The large porphyritic basalt region on the southern shore of Lake Asal, which is predominantly composed of plagioclases, displays an average SSA value of 0.38. The Ardoukôba caldera, characterized by phyric basalt (Figure 62), has systematically lower SSA values of 0.26. Similar values are found in the center of the rift, where there is another distinct zone of phyric basalt. The basalt of the Fieale volcano, whose caldera is identified as a porphyric unit on the geologic map, is classified as phyric in our study, with SSA values decreasing progressively from 0.34 to 0.26 between the caldera and Lake Ghoubbet. The SSA values of both rift flanks composed of porphyritic and phyric basalt range from 0.45 to 0.55. This is significantly higher than in the inner rift.

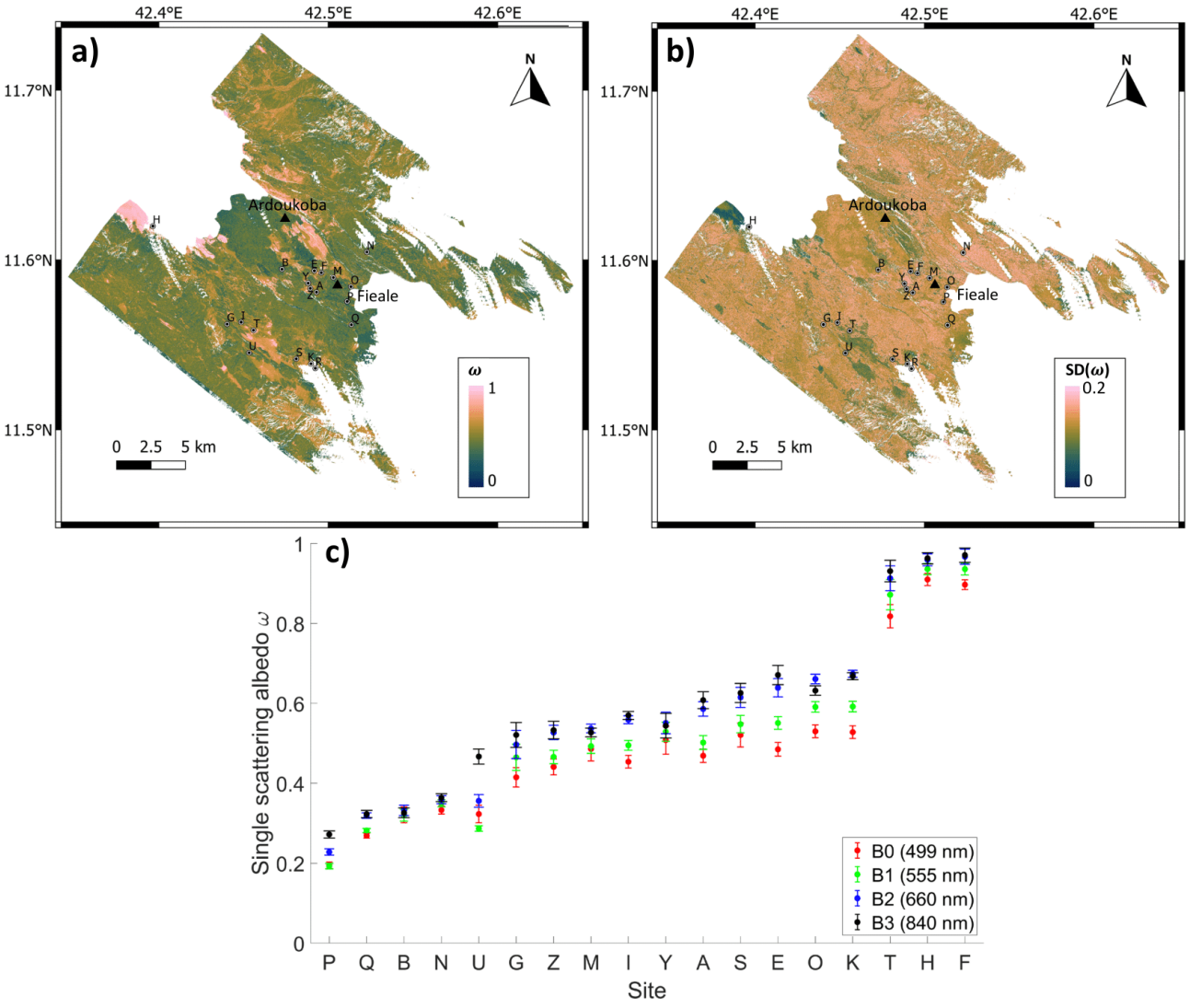

Figure 61 – Estimated single scattering albedo a-b) over the Asal-Ghoubbet rift in the Pleiades spectral band centered on 555 nm and corresponding SD map; c) Over the 18 experimental sites in the four Pleiades spectral bands, in ascending order of value.

In contrast to the low values associated with basaltic materials, several bright patches of lacustrine limestone, clearly visible on satellite images, exhibit very high SSA values of 0.9. Nearby basaltic pyroclastic units also stand out with SSA values of 0.65. They often accompany lacustrine formations, contributing to the complex geological mosaic of this region. Finally, to the southwest of the rift are several zones characterized by fissured alkaline basaltic flows, in particular hawaiite, with SSA values of 0.7.

Considering the study sites, Figure 61c shows consistent results with global observation: SSA is < 0.4 for pure basalt (P < Q < B < N), > 0.7 for lacustrine limestone, salt, sand field (T < H < F), and in between for mixed sand and lava rock or reworked hyaloclastite (U < G < Z < M < I < Y < A < S < E < O < K).

Discussion

Several surface characteristics have been reported to have significant impact on SSA. These include soil chemical composition, grain size and shape, and particle microstructure (e.g., crystals, fractures, pores). Shepard and Helfenstein (2007) stated that it could be related to soil compaction, which is assessed by soil density. SSA also decreases with increasing absorption coefficient and/or particle size (Fernando et al., 2016; Gao et al., 2021) and it tends to be higher for fine-grained soils than for coarse-grained soils (Johnson et al., 2013). This interpretation must be made with caution, as few surfaces are granular. Moreover, it would be difficult to assess grain size from SSA with no information about the refractive index of these soils. As basaltic surfaces are generally not granular, low SSA values are mainly due to their chemical composition, in particular the presence of magnesium- and iron-rich minerals, which are ubiquitous in lava flows. The impact of iron concentration on SSA has been extensively documented by Lucey (1998) and Wang et al. (2017). Their studies show that higher iron concentrations reduce the albedo across the visible and near-infrared (Vis/NIR) range, while causing minimal changes to the overall shape of the spectral continuum. The porosity of mafic minerals in basalt flows could also play a role. As noted by Hapke (2012), porosity tends to decrease SSA. However, it is difficult to measure porosity in the field. The SSA of sand and salt fields is significantly higher. For instance, the clay deposits at site F, mainly composed of calcite and quartz, and site T, consisting of powdery limestone with calcite as its main component, both have high SSA values. Ditto for site H, characterized by a salt bank containing halite and gypsum. The common feature of these sites is the presence of crystallized and glassy materials, which generally increase SSA. In addition, the texture of these materials also influences SSA. Site T is very fine-grained and compact, while site H is looser-grained, and site F has a mixture of granular and blocky materials. This nuanced analysis of chemical composition and texture enables us to understand how different geological factors affect the photometric properties of these surfaces.

Figure 61c shows that sites with medium SSA deserve particular attention. They present a varied range of mixtures (Figure 41), but this diversity does not seem to be directly correlated with significant variations in SSA. A more relevant factor seems to be the proportion of bright materials present in the mixtures. Pilorget et al. (2015) have highlighted that the BRDF pattern is primarily influenced by the properties of the most abundant, brightest or most anisotropic grains within the mixture. We note that sites E, K and O are predominantly fluvial or lacustrine deposits, characterized by a significant presence of sand and bright sediments. These geological characteristics generally translate into slightly higher SSA values, reflecting the bright nature of these materials. Conversely, sites A, G, I, M, S, Y, and Z are predominantly composed of lava rocks which, by their very nature, have darker materials and therefore lower SSA values.

By extrapolating the results obtained from the 18 study sites, we can interpret the photometric characteristics of other regions of the rift. For example, we find that the SSA of the rift flanks is influenced either by degradation or by mixing with bright materials. This corroborates the

geological map that indicates that the rift flanks, which date from 87,000 to 220,000 years ago, are older than the inner zone, which dates from 66,000 years ago to the present day (Figure 58). Weathering and erosion processes probably contributed to the mixing and alteration of the original materials, potentially increasing the SSA through the incorporation of brighter sedimentary components. Similarly, the behavior of pyroclastic units can be likened to that of compact sand or lacustrine deposits, assuming that their composition consists mainly of fine volcanic ash of medium brightness.

Comparison between SSA and lab reflectance spectra

A linear relationship is observed between measured reflectance values and estimated SSA values at different wavelengths across sites, however, it is not unique, as slopes and intercepts vary from site to site ((Figure 62). Figures 62c and d show that this relationship becomes nonlinear as SSA reaches its upper limit of 1, which could reflect an SSA saturation effect. This suggests that this relationship could be influenced by factors, such as mineral composition, grain size or other environmental conditions and the model limitation. The lack of such information underlines the need for more laboratory or field measurements to interpret remote sensing products.

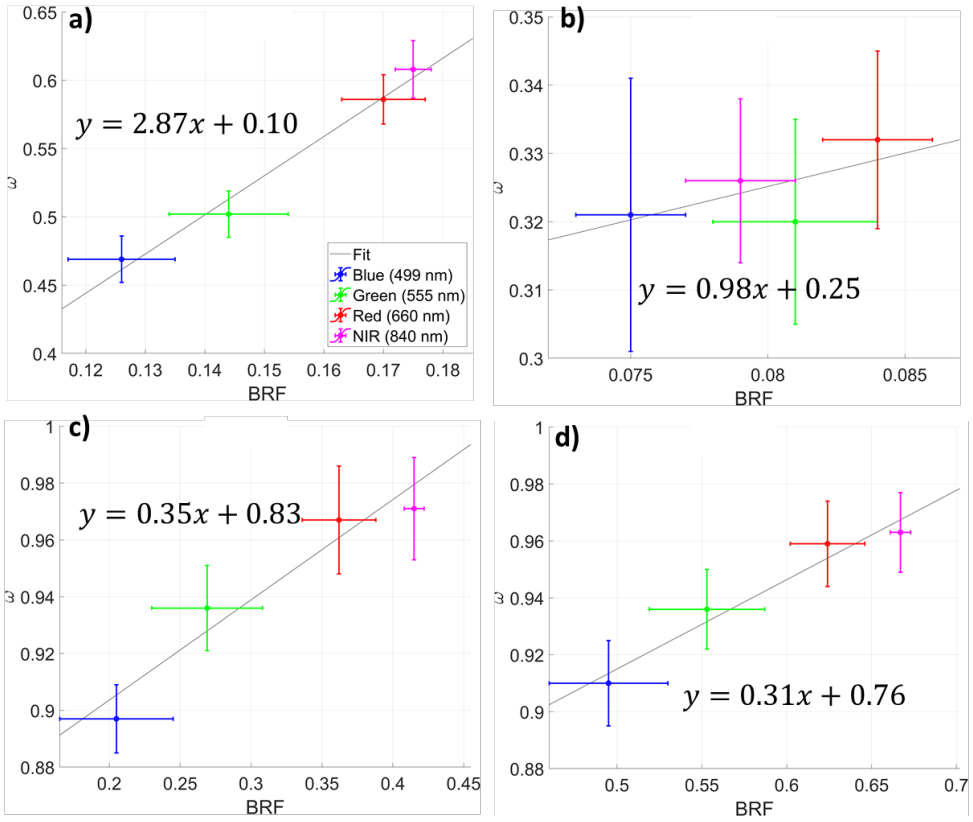

Figure 62 – Relationship between the single scattering albedo (ω) obtained by inversion of the Hapke model on the Pleiades BRDF and the bidirectional reflectance factor (BRF) of soil and rock samples from sites a) A, b) B, c) F and d) H measured in the laboratory in four spectral bands.

5.1.3 Photometric roughness $\overline{\theta}$

Results

We refer to photometric roughness as either $\overline{\theta}$ or simply "roughness". Most terrains have roughness values between 35° and 40° with a standard deviation of 2° to 3°. Areas with low roughness values are the basalt units and the salt bank west of Lake Asal (Figure 63a). The large porphyritic basalt unit has a wide range of roughness values between 10° and 45°. Surface roughness is 20° on the shores of Lake Asal, 25° in the Ardoukôba volcano region, and between 25° and 30° on the phyric basalt flow in the middle of the rift. The basaltic flows of the Fieale volcano have a surface roughness decreasing progressively from 30° to 20° from the highest to the lowest altitudes. On the salt bank of Lake Asal, roughness decreases from 20° to 5° as one moves away from the shore. These are the lowest values recorded in the Asal-Ghoubbet rift. The lacustrine and pyroclastic basalt units have a more homogeneous and higher roughness (35°-40°), as do the rift flanks (37°). Note that surface roughness cannot be accurately estimated on steep slopes.

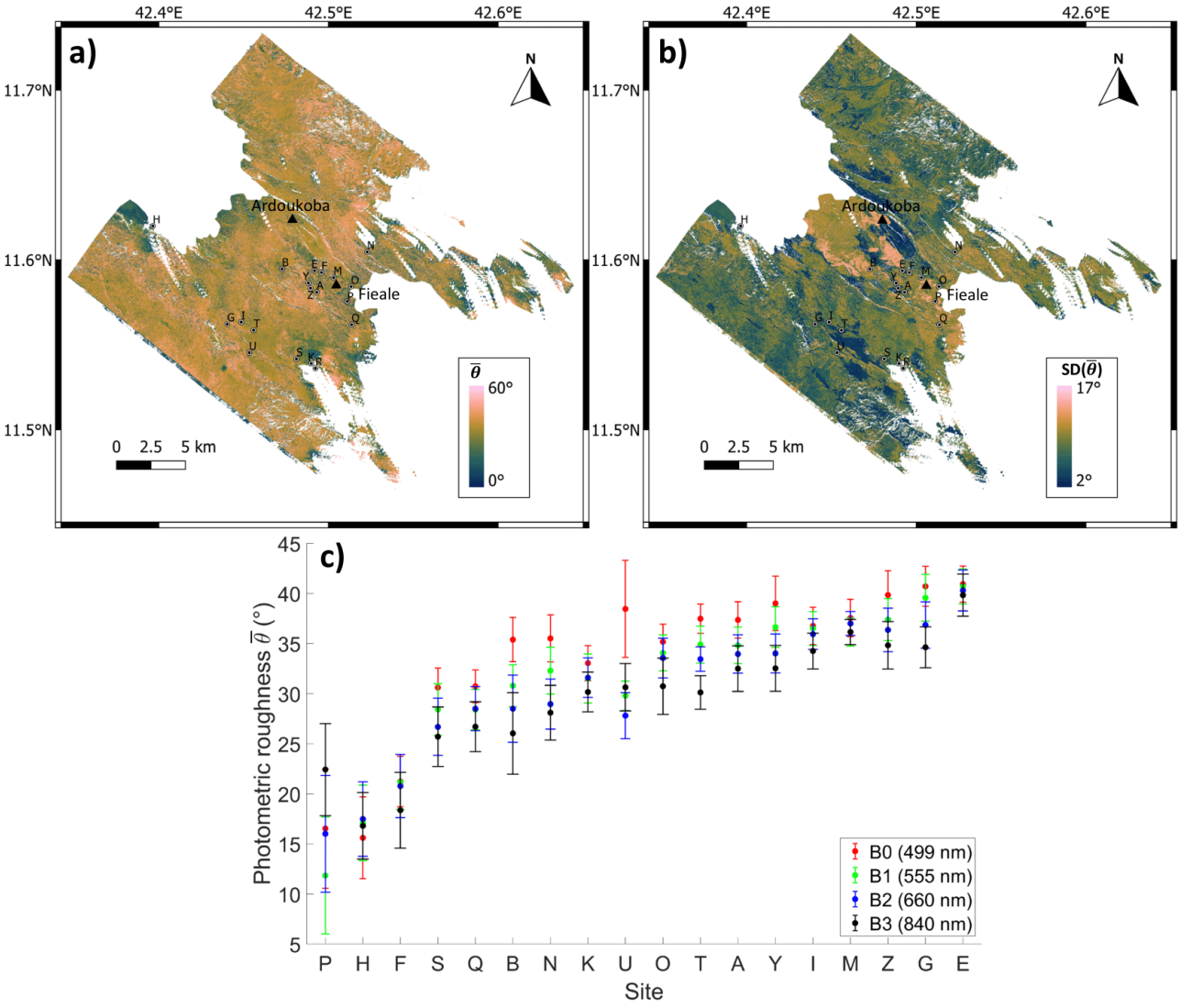

Figure 63 – Estimates photometric roughness a-b) over the Asal-Ghoubbet rift in the Pleiades band centered on 555 nm and corresponding SD map; c) Over the 18 experimental sites in the four Pleiades spectral bands, in ascending order of value.

Unlike the SD map of SSA, that of $\overline{\theta}$ shows a clear distinction of different geological units (Figure

63b). In terms of trends, it seems that the $SD(\overline{\theta})$ is disproportionate to the SSA in Figure 61a, as the lowest values correspond to the highest SSA and vice versa. We list some notable values and areas in ascending order. The lacustrine limestone unit in the centre of the map has a value of about 3°, which is the lowest. The $SD(\overline{\theta})$ at the salt shore of Lake Asal is about 6.4°. These two units happen to have the highest SSA. The large basalt area near Lake Asal has a value of ≈10.5°, the one near Lake Ghoubbet is ≈10.9°, the phyric basalt area next to the lacustrine limestone unit has the highest value: 13.6° on average.

Figure 63c shows that sites P, H and F have significantly lower photometric roughness (10-20°) than the others (30-40°). Although roughness should not vary too widely within a site, we observe that sites P, B, U and N have greater variability than the others. They are the sites where SSA was low. We also observe that roughness increases with wavelength at most sites, with the exception of sites P, H and F, previously mentioned as having the lowest roughness.

Discussion

As mentioned above, photometric roughness encompasses spatial scales ranging from several times the average inter-particle distance (100 to 1000 μm) to a maximum defined by the detector's field of view, which sets the ground sampling distance. In Earth observation, GSD can vary from a few decimeters to a few kilometers. The interpretation of is a matter of debate within the scientific community, due to the ambiguous definition of these scales (Shiltz and Bachmann, 2023). However, there is a common consensus that photometric roughness is most sensitive to the millimeter scale and below (Shepard and Helfenstein, 2007; Pilorget et al., 2016; Labarre et al., 2019). We applied the isotropic undecimated wavelet transform (IUWT) (Starck and Murtagh, 2006) to decompose the high-resolution DEMs, so as to disaggregate the roughness components at different scales, and then calculated their contribution. Our results confirm that smaller scales generally exhibit higher roughness (Figure 64). This is because smaller-scale topographical features contribute more significantly to overall surface roughness, due to their greater frequency and variation in elevation within a given area.

Jacquemoud et al. (1992) and Protopapa et al. (2020) hypothesized that, unlike other photometric parameters, $\overline{\theta}$ does not vary with wavelength. Conversely, Cord et al. (2003) have noted that when surface reflectance varies with wavelength, photometric roughness is also influenced by wavelength. The optical characteristics of minerals or grains, such as absorption and scattering, can vary as a function of wavelength. Meanwhile, as previously mentioned, the photometric behavior of natural surfaces is strongly influenced by roughness on a microscopic scale, which is linked to absorption properties. When these microscopic structures are opaque, there is a marked photometric contrast between shadowed and directly illuminated areas, leading to a situation where photometric roughness is closely related to geometric roughness. Conversely, when the grains are partly translucent, this contrast is strongly diminished, resulting in a reduced photometric roughness that is less correlated with geometric roughness. This relationship suggests that there may generally be an anti-correlation between photometric roughness and SSA for different wavelengths, at least within the solar domain and in most studied sites.

Furthermore, although there is no direct relationship between SSA and $\overline{\theta}$, there seems to be a clear anti-correlation between SSA and the variation of $\overline{\theta}$ (Figure 63b). Apparently, a high SSA

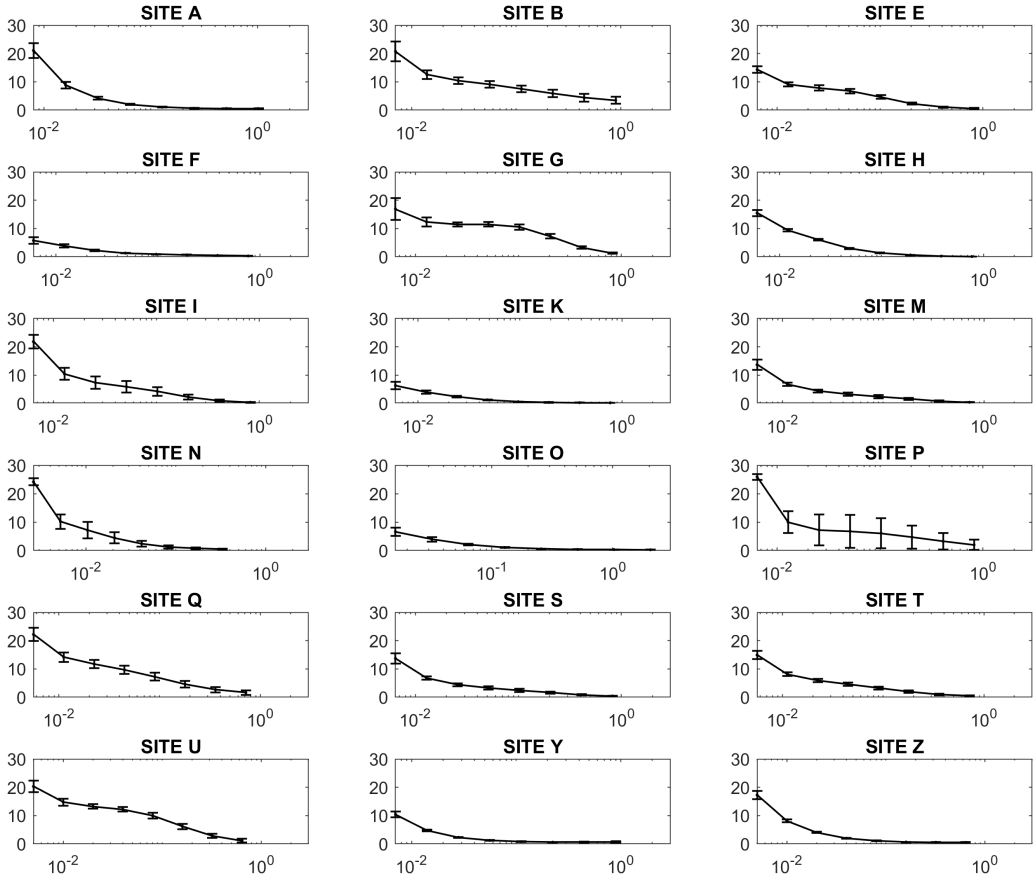

Figure 64 – Mean slope angle (°) (y-axis) across various scales (meter) (x-axis), calculated from different levels of IUWT decomposition of drone DEMs.

helps to better constrain the photometric roughness, possibly because the contrast is increased. However, this observation raises the question: does this finding have any underlying physical significance? After all, the variation in roughness is inherently a component of the roughness itself. This remains an open question as we have not been able to investigate this in depth due to time constraints.

The relationship between SSA and photometric roughness in photometric models is key for understanding surface reflectance properties. These two parameters are independently influenced by the physical properties of a surface, but are also interdependent in the way they affect BRDF. Shepard and Helfenstein (2007) have shown, through various experiments with different soil samples, that SSA and photometric roughness are intrinsically linked, providing empirical evidence of their combined impact on photometric observations. A sensitivity analysis on the Hapke model conducted by Labarre et al. (2017) also showed this coupling, which can explain up to 30% of reflectance variability. From Figs 11 and 16, it appears that SSA values below 0.8 are required to estimate photometric roughness with reasonable accuracy. Sites with these values can still be considered "opaque", and their photometric roughness corresponds more to the geometric roughness than to the surface material.

Comparison between photometric roughness and mean slope angle

Figure 65 shows the relationship between photometric roughness estimated by inversion of the Hapke model ($\bar{\theta}$) and the mean slope angle calculated from DEMs at the millimeter and

submillimeter scales ($\overline{\theta_M}$). Our results corroborate those of Labarre et al. (2019) and also show a weak correlation. Photometric roughness is larger than the calculated mean slope angle at most sites, with the exception of sites H and P. Further analysis showed a linear relationship between and SSA. Figure 65b shows that both surface roughness and SSA influence the estimation of photometric roughness. According to Hapke (2012), SSA depends on material refractive index, wavelength and grain size. This confirms the multi-scale nature of photometric roughness. Grain size represents the smallest scale of roughness, so its contribution is the most important. The linear relationship observed in Figure 65b remains unexplained, however, and needs to be validated by further field experiments. On the other hand, sites F, H and T sites with high SSA values show significant deviations. This raises several questions, for which we have no complete answer: What determines such a linear relationship? Why do sites F, H and T deviate from the correlation line? Do sites with very high SSA follow a different trend? Site M also shows an outlier, with a mean slope angle estimated to be too low, which could be a local characteristic not reflecting the geological and topographic conditions of the region.

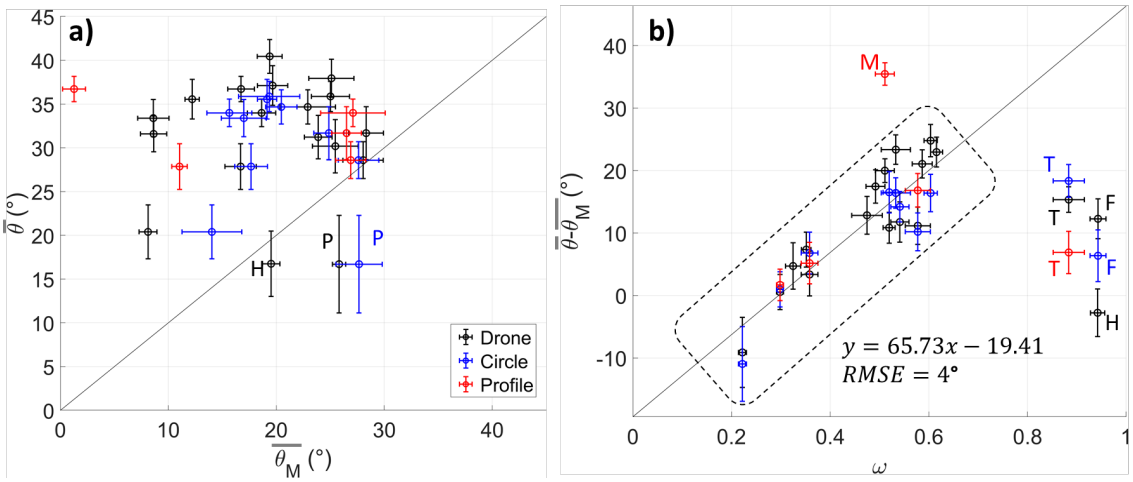

Figure 65 – Relationship between a) photometric roughness ($\overline{\theta}$) and mean slope angle ($\overline{\theta_M}$). b) $\overline{\theta}$-$\overline{\theta_M}$ and single scattering albedo (ω). Only outliers are labeled.

5.1.4 Phase function parameters b and c

Results

The double Henyey-Greenstein phase function over the Asal-Ghoubbet rift is shown on Figures 66. The latter generally exhibits broad scattering lobe characteristics, in backward and forward directions. Although both maps are noisy, the maximum SD is only 0.016, which is smaller than for SSA. Parameters and mostly range from 0.2 to 0.4 and from 0.4 to 0.6, respectively. This scattering behavior is consistent across most geological units, making it challenging to identify distinct features. The most notable exception is the salt bank, which features a very high asymmetry parameter ($b > 0.9$), indicating narrow, directional scattering lobes. This geological unit also exhibits values of $c < 0.1$, indicating predominant forward scattering. The sandy zone in the middle of the rift also stands out, with values of that can be as low as 0.2, but also close to 1 on some pixels. We also observed a high value for the parameter c, which can reach a maximum of 0.7, but it can average 0.5. In pyroclastic areas, values can be very low, at 0.15, but average 0.3.

According to Figures 66b and d, two distinct units can be identified at the center of the rift: basalt, characterized by a higher SD of b (approximately 0.2) and a lower SD of c (approximately 0.19), and a sandy field/lacustrine limestone unit, which exhibits a slightly lower SD of b (approximately 0.17) and a slightly higher SD of c (approximately 0.24). On average, the two parameters show similar standard deviation values, both at or slightly below 0.2, which is considered an acceptable result. However, the physical significance of these values remains unclear at this stage.

The results for the asymmetry parameter at the local scale corroborate the rift-scale observations. Most sites have values of $b < 0.4$, with the exception of sites H and F. The latter are very bright and therefore have a high SSA. Sites H and F have the lowest values of c while having the highest values of b. This highlights their distinct photometric responses. Figure 66 also reveals that c varies widely between the different sites within its range of variation, with no other significant features emerging. There is no clear variation in these two parameters with wavelength. Volcanic terrains exhibit broad scattering lobes and a balance between forward and backward scattering. In contrast, sites F and H characterized by high albedo and glassy grains, have narrow forward scattering lobes.

Discussion

McGuire and Hapke (1995) studied particle scattering as a function of physical characteristics: smooth, bright and spherical particles tend to exhibit narrower scattering lobes (high values of b) and greater forward scattering (low values of c). Conversely, irregular and rough particles or with internal scatterers tend to exhibit broader scattering lobes (low values of b) and greater backward scattering (high values of c). Plotting against produces an "L-shape" or "hockey-stick shaped" curve (Figure 66), which represents the transition between rough, opaque and irregular grains to smooth, clear and spherical grains. This representation highlights the influence of particle structure on light-scattering properties. Hartman and Domingue (1998) noted a behavior independent of particle size, suggesting that the effects observed are more intrinsic to the overall structure of the particle than to its scale. Cord et al. (2003) and Shepard and Helfenstein (2007) have pointed out that scattering patterns are more sensitive to the organization of grains on the surface, such as density or micro-roughness, than to the inherent optical properties of individual particles. The simulation of surface compactness carried out by Lucas et al. (2023) has further reinforced this assertion. Switching from individual particles to a group of particles provides a better understanding of how light is scattered by a surface. Souchon et al. (2011) carried out BRDF measurements on natural granular surfaces composed of volcanic materials varying in grain size (micron to millimeter), shape, surface texture, and mineralogy. This includes combinations of glass and minerals. This experiment enabled them to explore the scattering properties of planetary analogs of basaltic granular surfaces. A key finding is that these surfaces exhibit pronounced forward scattering properties, even though they contain only a small proportion of isolated translucent monocrystals or fresh glass. This extended the and parameter space and revealed new modes of light scattering. To date, the Hapke model has mainly been applied to granular surfaces encountered in the Asal-Ghoubbet rift (reworked volcanic materials, sand, salt). It also includes rocky terrains, lava flow, mixtures of granular and rocky terrains, on which similar optical behavior can be observed.

In line with the experimental results of Souchon et al. (2011), most sites exhibit irregular, rough, opaque and hollowed grains on granular surfaces ($0.2 < b < 0.4$ and $0. < c < 0.6$), which is typical of

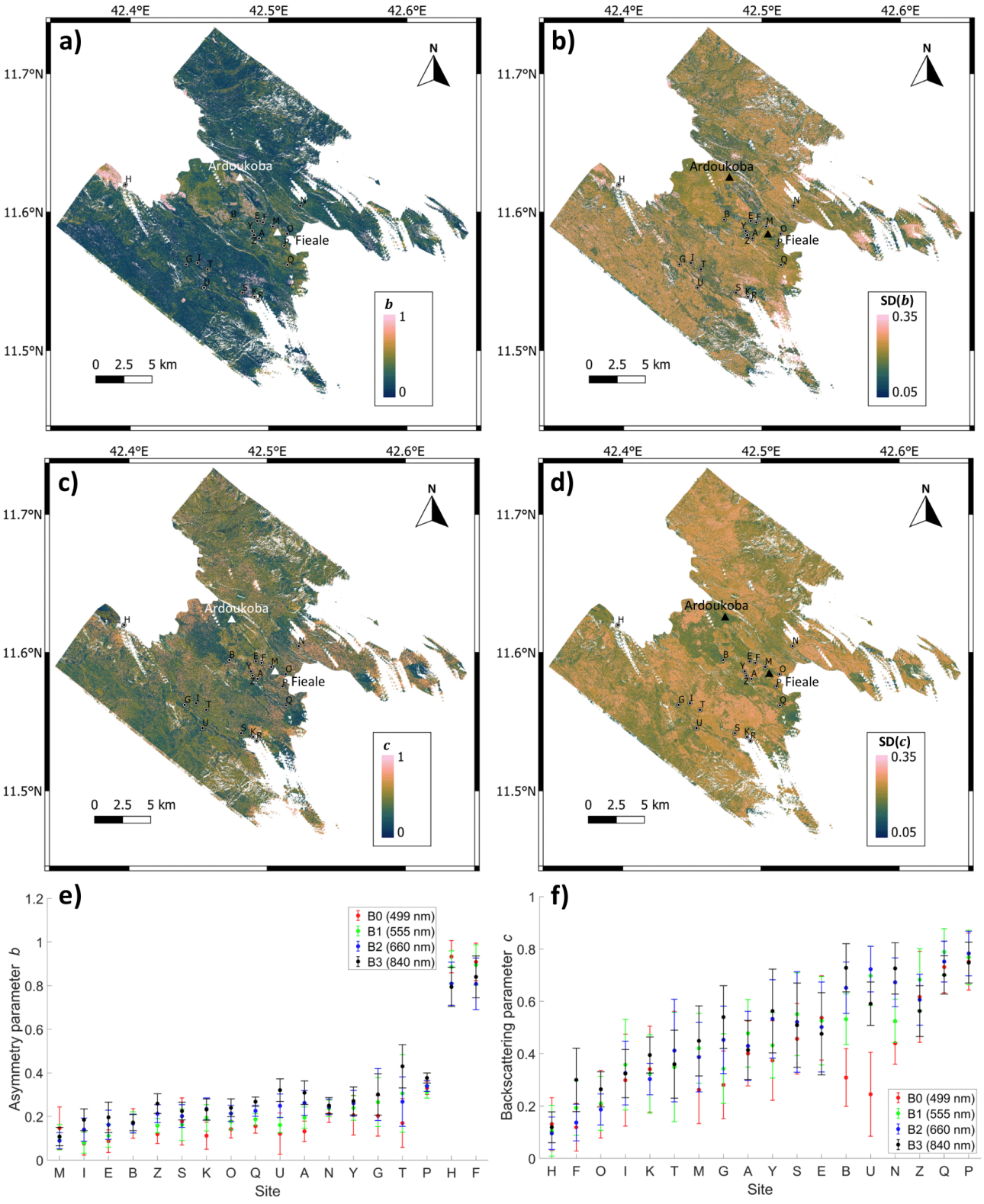

Figure 66 – Estimated asymmetry parameter and backscattering parameter over the Asal-Ghoubbet rift in the Pleiades band centered on 555 nm (a, c) and corresponding SD maps (b, d); Over the 18 experimental sites in the four Pleiades spectral bands, in ascending order of value (e, f).

pyroclastic material. Figure 17 shows three groups based on the mineral composition and location of the sites. Group 1 comprises lava flows and hyaloclastite. Sites in this group are characterized by hard, blocky lava flows, exhibiting a wide range of backscatter parameters (from 0.2 to 0.9) and low asymmetry parameters ($b < 0.3$). This suggests materials with moderate to high internal

density, consistent with surfaces composed of rough, opaque particles and hollow grains. Group 2 comprises calcareous and lacustrine deposits, mainly consisting of sand and gravel. The position of this group in the graph indicates a structure consisting of agglomerated fine particles, typical of sites I and T. However, some sites show a loose combination of rocks and gravels (e.g., sites A, K, M). There is significant overlap between groups 1 and 2, corresponding to sites containing a mixture of the two materials, characterized by low to intermediate values of b and c. Group 3 is composed of bright salt and clay, notably occupying a unique region in the graph with very high b values (> 0.8) and low c values (< 0.3). This group, which includes sites F and H, has surface characteristics similar to fresh opaque glass or isolated single crystals (Souchon et al., 2013). The mineral composition of these sites (F with calcite, quartz, albite, zeolite, palygorskite, smectite and talc, and H with halite and gypsum) supports their inclusion in this group. The diagram in Figure 67 is useful for a general understanding of the physical characteristics of surfaces. For a higher level of accuracy, interpretation becomes complicated when the sites present a mixture of materials, with the percentage contribution of each material being unknown.

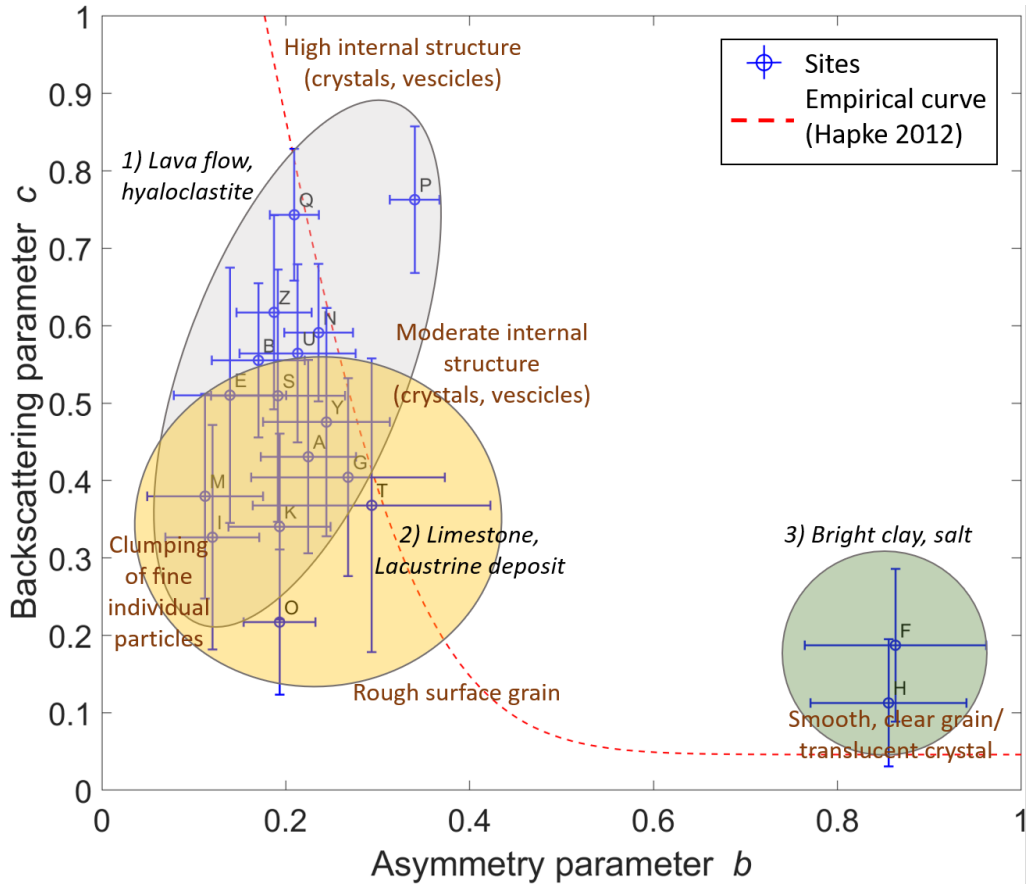

Figure 67 – Relationship between phase function parameters estimated by inversion of the Hapke model at the 18 sites studied. The results are the average of the individual results from different wavelengths. Texts in italic correspond to groups of sites and designate their main constituents, while other texts are the physical properties at the relative position on the graph (Souchon et al., 2013; Fernando et al., 2016).

5.2 The Moon

5.2.1 The near side of the Moon

As far as the results on the Moon are concerned, several locations have been mentioned using the convention (longitude, latitude). We will also mention a few distinguishable landmarks to facilitate the analysis (Figure 68).

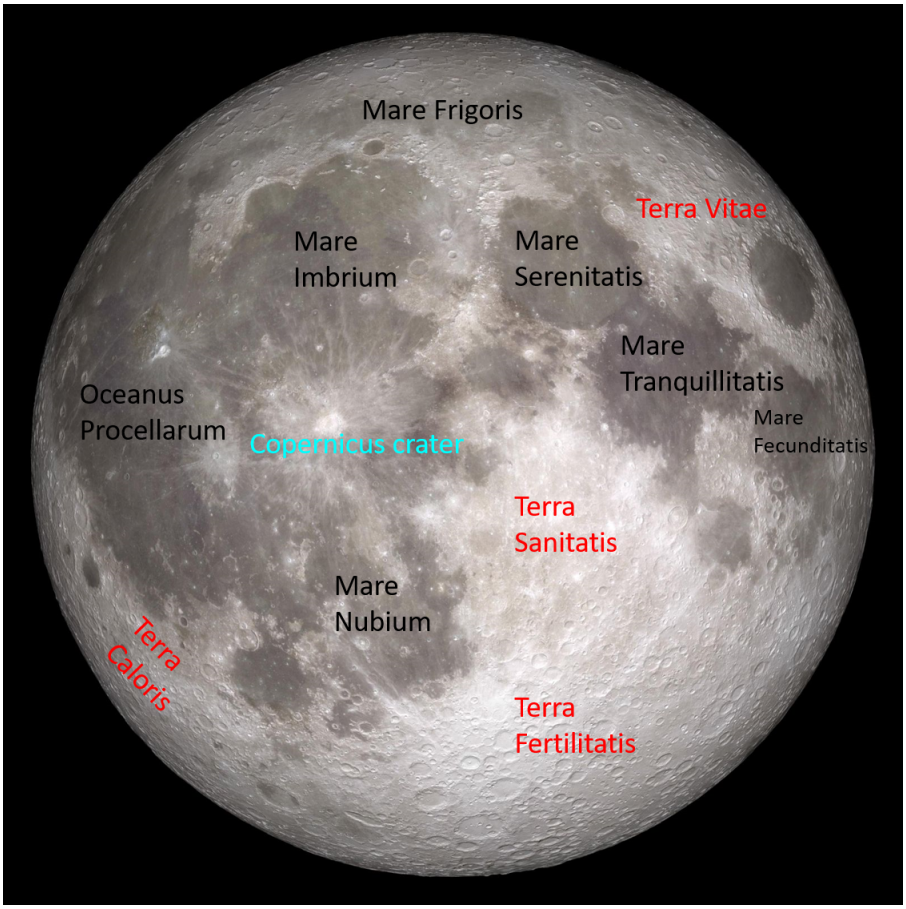

Figure 68 – Several recognizable landmarks on the near side of the Moon.

Overall quality of the inversion

The region located in the latitude interval [-45°, 45°] generally has an RMSE less than 0.05 (Figure 69). A comparison with Figure 70 shows that this value is less than 25% of the SSA value (which is between 0.2 and 0.3 in this region), which is satisfactory, although less than the results obtained for the Asal-Ghoubbet rift. The quality of the inversion improves closer to the equator, with RMSE values decreasing to 0.007. The marine regions have low RMSE values (below 0.02), while the highlands have higher RMSE (0.075 and above). This pattern is consistent with our earlier observation in section 4.4, where RMSE increases with BRF. However, these highlands are at higher latitudes, where unusually high BRF values were reported in section 2.4.2, making the results in these areas unreliable. The discussion of results for the highlands therefore focuses on a portion of Terra Sanitatis above -45° latitude. Areas where the RMSE is unacceptably high are generally found near crater rims and highlands close to the lunar limb, where steep slopes are detected, introducing outliers into the BRF measurements.

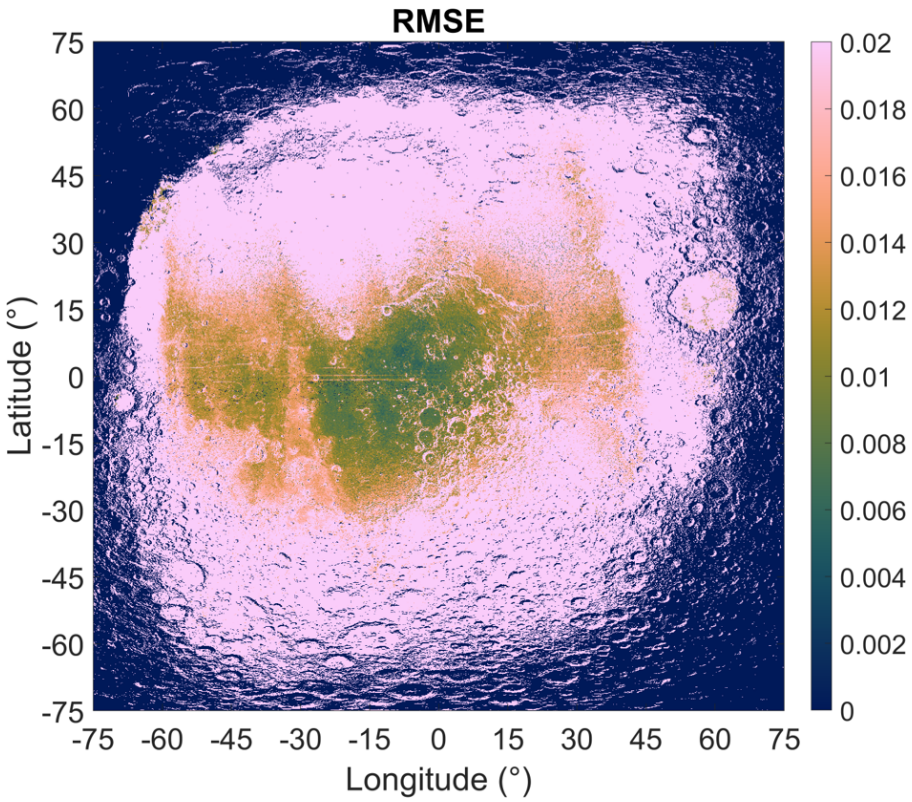

Figure 69 – RMSE map of the BRF reconstruction from the inversion of Pleiades green band images (510-590 nm), covering most of the near side of the Moon (from -75˚ to 75˚ in longitude and latitude).

Hapke parameter maps

We obtained 6 maps of the Hapke parameters, covering a large part of the near side of the Moon.

- **Single scattering albedo** ω:

As far as the SSA is concerned, we can clearly distinguish the topographic features of the Moon (Figure 70). The values from -45˚ to 45˚ in longitude and latitude are reasonable and in the range [0.1, 0.5]. From -60˚ to -45˚ and from 45˚ to 60˚ in longitude, they are still consistent with the central part, although there are some very high SSA values at the crater rim (ω approach 1). The maria tend to have a lower SSA ($0.1 < \omega < 0.3$), while the highlands have a higher SSA ($0.3 < \omega < 0.5$). It is consistent with the results of Kennelly et al. (2010); Sato et al. (2014) who used Clementine and LROC WAC data. For the region between -60˚ and -45˚ and between 45˚ and 60˚ latitude, we generally observe SSA values in the range [0.5, 0.7]. These values are higher than those obtained by Sato et al. (2014), since the maximum SSA should be around 0.5. This is probably the result of a calibration error mentioned in chapter 2, which makes regions near the pole appear brighter than the others. As far as the SD map is concerned, the swampy regions seem to have a low SD (< 0.1), whereas it is higher for the highlands ($0.1 < \omega < 0.15$). This seems to correspond to the amplitude of the SSA, since the higher the SSA, the higher the SD.

In comparison with the results obtained in the Asal-Ghoubbet rift, the SSA of the maria is similar to that of sites P, Q and B (Figure 61). This is consistent with the fact that both contain basaltic material. On the other hand, the upland SSA value can be placed in the same group as sites N, U,

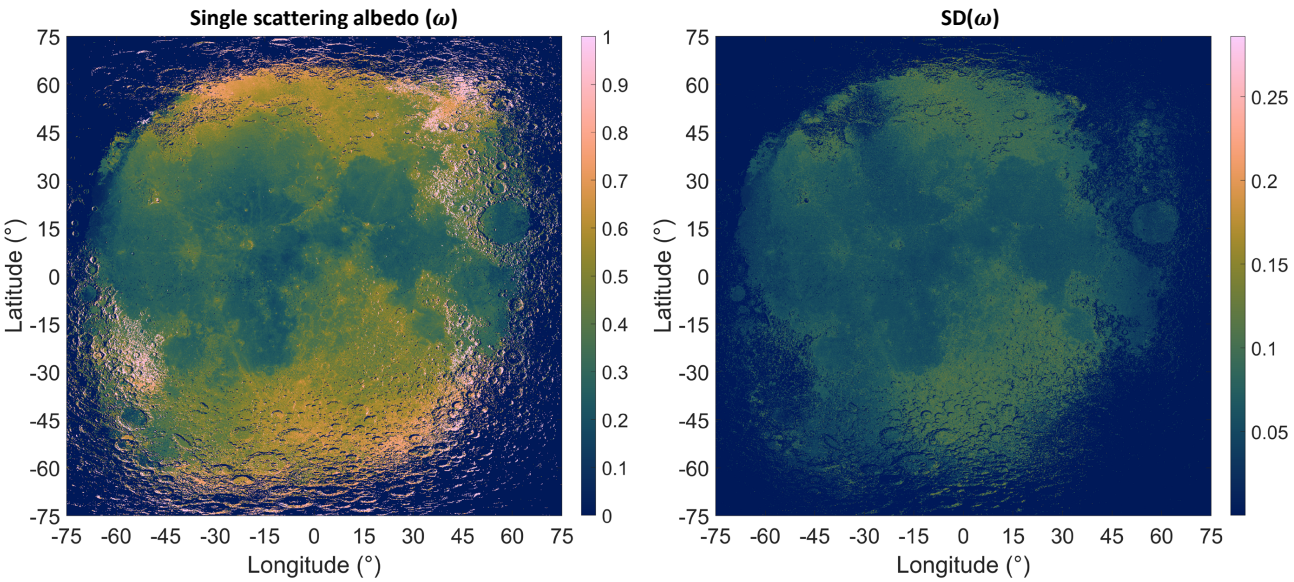

Figure 70 – Estimated single scattering albedo in the Pleiades spectral band centered on 555 nm, covering most of the near side of the Moon (from -75˚ to 75˚ in longitude and latitude) and the corresponding SD map.

M, Z, N, I, which are a mixture of basaltic and lacustrine material. In section 2.4.2, we mentioned that the lunar highlands contain mainly anorthosites. They occur as fragments or inclusions of varying size and shape in many igneous rocks, ranging in composition from granite to basalt to kimberlite (Ashwal, 2021). We can see the similarities between the two cases.

- **Photometric roughness** $\overline{\theta}$:

As far as photometric roughness is concerned, it is much more difficult to distinguish topographical features without zooming in. In general, the central region has values between 30˚ and 50˚. The western, eastern and southern edges have a roughness parameter of less than 10˚, while the northern edge has values between 35˚ and 40˚. At longitude -30˚, it is unusually low (< 15˚). This "low roughness wedge" doesn't appear in the RMSE map (Figure 69), nor in the SSA map (Figure 70). Why is this? Sensitivity analysis of Labarre et al. (2017) shows that the SSA is affected by all BRF measurements, while $\overline{\theta}$ is more affected by the highest phase angle measurements. Furthermore, this feature does not correspond to the topography, but rather to the visible edge at certain phases of the moon (Figure 19). This means that there may be some "bad" parts of the images that should have been excluded from the dataset, or that the invalid geometry filter did not work as expected on high phase angle images. Therefore, we expect this to affect the phase function parameters to some extent, while leaving the hot spot parameters unaffected.

Let us now consider several regions on the Moon (Figure 68), according to their longitude, since roughness seems to vary between these regions rather than between terrain units as in the case of SSA. Oceanus Procellarum (18.4˚,-57.4˚) has a roughness between 30˚ and 40˚. Mare Imbrium (32.8˚, -15.6˚) is an strange case, as it has roughness values of 45˚-50˚ at a lower longitude, and roughness values of $\overline{\theta} \approx 40^{\circ}$ at a higher longitude. Although the high roughness of this area does not correspond to topography or geological units, it is difficult to attribute it to the error in data pre-processing, as it has no characteristic curve, unlike the low roughness anomaly discussed earlier. Around Mare Serenitatis (28.0˚, 17.5˚), Mare Tranquillitatis (8.5˚, 31.4˚) and Mare Nubium (-21.3˚, -16.6˚), $\overline{\theta}$ is of the order of 35˚ to 40˚. On the other hand, in the highland region around (15˚,-15˚),

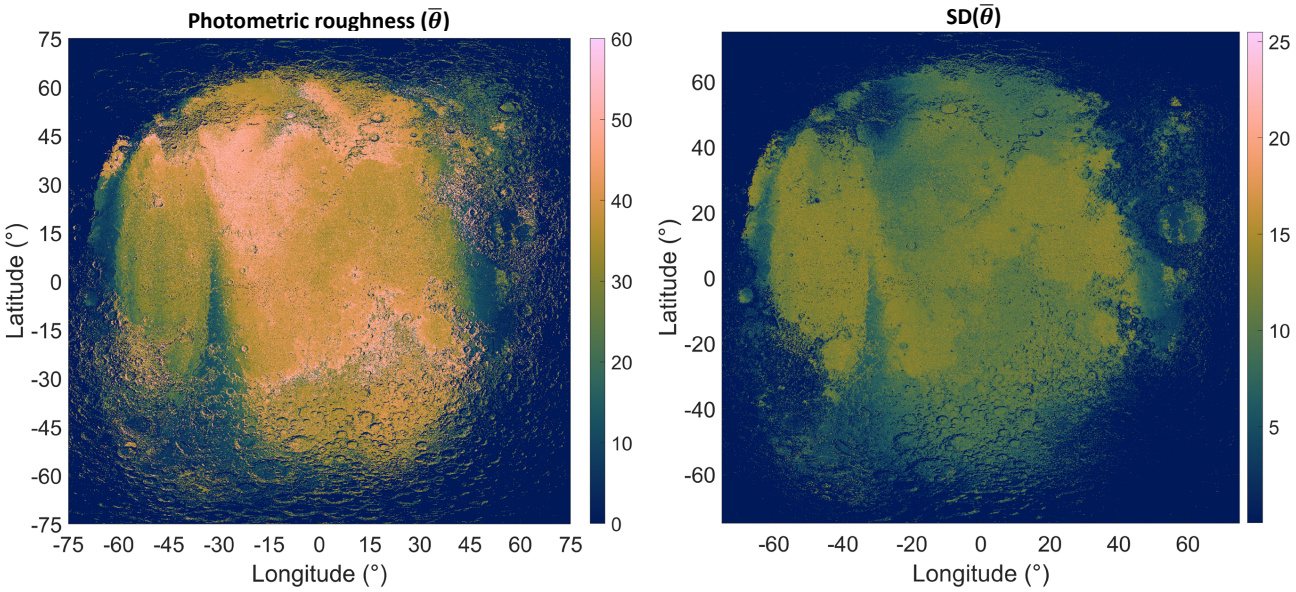

Figure 71 – Estimated photometric roughness in the spectral band of Pleiades centered on 555 nm, covering most of the near side of the Moon (from -75˚ to 75˚ in longitude and latitude) and the corresponding SD map.

$\overline{\theta}$ typically of the order of 50˚. Leaving aside any explainable or erroneous features, the maria tend to have lower photometric roughness ($30° < \overline{\theta} < 40°$) than the highlands ($40° < \overline{\theta} < 50°$). By measuring multi-resolution surface roughness, Cao et al. (2018) confirmed that maria's roughness values are lower than those of the highlands. Secondly, as the resolution increases, the roughness contrasts of the main regions become weaker. Consequently, the variation in roughness on a kilometer scale is small. In addition, as the highlands contain brighter material, it may be easier to detect shadows, hence the increase in photometric roughness. Of course, as Li et al. (2016) points out, photometric textures are sensitive to variations in brightness.

These photometric roughness values are higher than those found by Helfenstein and Shepard (1999), with $\overline{\theta} = 24°$ for the maria and $\overline{\theta} = 27°$ for the highlands and craters, and by Sato et al. (2014), with $\overline{\theta} = 23.4°$. However, if we compare these values with the results obtained in the Asal-Ghoubbet rift, ignoring the difference in scale, the wide range of maria roughness is comparable to sites with volcanic ash deposits, gravel or rock on sediment, rather than sites with bright fine silt or pure lava field. On the other hand, the roughness of the highlands is higher than any of the values obtained at the sites studied in the Asal-Ghoubbet rift. Figure 63 shows that only a few pixels in inaccessible mountains, rocky slope or very rough lava field have very large photometric roughness (above 50˚) in the decimeter to meter scale. On the basis of this observation, we formulate two hypotheses: Firstly, in the case of the lunar surface and the kilometer-scale images of the Pleiades, roughness at or below the millimeter scale is still a major component. The microscopic roughness of the Moon is simply higher than that obtained on Earth. Secondly, while the microscopic roughness is similar between the Asal-Ghoubbet rift and the Moon, the macroscopic roughness (above the millimeter scale) affects the photometric roughness and makes the difference. According to Cao et al. (2021), high roughness textural changes at the kilometer scale are related to crater obliteration at the hectometer scale, while low roughness textural changes around high roughness patterns are probably affected by smooth mare materials. Between decimeter and kilometer scales, Rosenburg et al. (2011) indicated that most of the surface exhibits fractal-like behavior, with one or two different

Hurst exponents over the given reference range. The Hurst exponent is high in the lunar highlands (median value of 0.95) and lower in the maria (median value of 0.76). According to Cai and Fa (2020), Hurst exponents estimated from LROC NAC DTMs vary from 0.7 to 0.95, (median value of 0.9) for the meter scale. There is no discernible difference in the Hurst exponent between the maria and the uplands. A value close to 1 means that roughness is stable over many measurement scales (Section 3.7.4). The Hurst exponent $H = 2 - D$ of the Asal-Ghoubbet rift is in the range [0.3,0.7], which means that the macroscopic roughness of the Asal-Ghoubbet rift is lower than that of the Moon. This could explain the difference in the overall photometric roughness.

- **Phase function parameters (b and c)**:

At first glance, parameters (b and c do not correspond well to the lunar topographic features (Figure 72). The value of b in Oceanus Procellarum is around 0.2 to 0.25. We noticed a strange vertical feature ($0.3 < b < 0.4$) in the longitude from -30° to 0° and in a wide range of latitudes, from -30° to 45°. As this coincides with the anomalously high roughness of Mare Imbrium, we suspect a data extraction error. Otherwise, the rest of Mare Imbrium and Mare Nubium have very low b, between 0.15 and 0.2. Mare Serenitatis and Mare Tranquillitatis are recognised as having slightly higher b than their surroundings, around 0.25 to 0.3. Terra Sanitatis has a slightly higher value, around 0.3 and 0.35. Overall, the entire lunar surface has a low b, implying a broad scattering lobe. The average SD value is 0.08 and below, which means that the overall constraint is decent.

Typical values of b obtained by Sato et al. (2014) in the maria are 0.25 to 0.27, of the same order of magnitude as our own for Mare Serenitatis and Mare Tranquillitatis. In the highlands, they find values in the range 0.225 to 0.255, which is significantly lower than our results. Furthermore, the b values on the Moon are similar to most of the Asal-Ghoubbet rift sites, with the exception of sites H and F, which both have very bright material (Figure 66).

On the parameter c map, we can clearly see the wedge feature at -30° longitude. Oceanus Procellarum has a wide range of values, from 0.2 to 0.9. However, the average value is 0.64. Most of Mare Imbrium and Terra Sanitatis have a value of $c \approx 0.8$. Mare Nubium, Mare Serenitatis and Mare Tranquilitatis have a similar range, from 0.6 to 0.65. We can therefore see that the Moon has c values above average or high, which favours backward scattering. This is consistent with the high photometric roughness obtained. The pattern of the SD map for the backscatter parameter is similar to that for the asymmetry parameter. However, the values are around 0.2, which means that it is more difficult to constrain.

Sato et al. (2014) found a c parameter ≈0.5 in the maria and around 0.65 to 0.72 in the highlands (after conversion to the new c parameter). Although smaller than our result, they show that the lunar surface typically has an above average or high c parameter. Lnar values are similar to those of sites U, N, Z, Q, P in the Asal-Ghoubbet rift (Figure 66). They all contain basaltic materials as major constituents. Although there are slight differences in each geological unit, the average phase function parameters of lunar particle from Sato et al. (2014) are similar to those of this work (Figure 73).

- **Parameters of the opposition effect (h and B_0)**:

It is even more difficult to observe topographic features in the width and amplitude maps of the opposition peak parameter (Figure 74). However, we can see a slight difference between the maria and the highlands. The value of the parameter h for the maria is 0.42, while that for the highlands

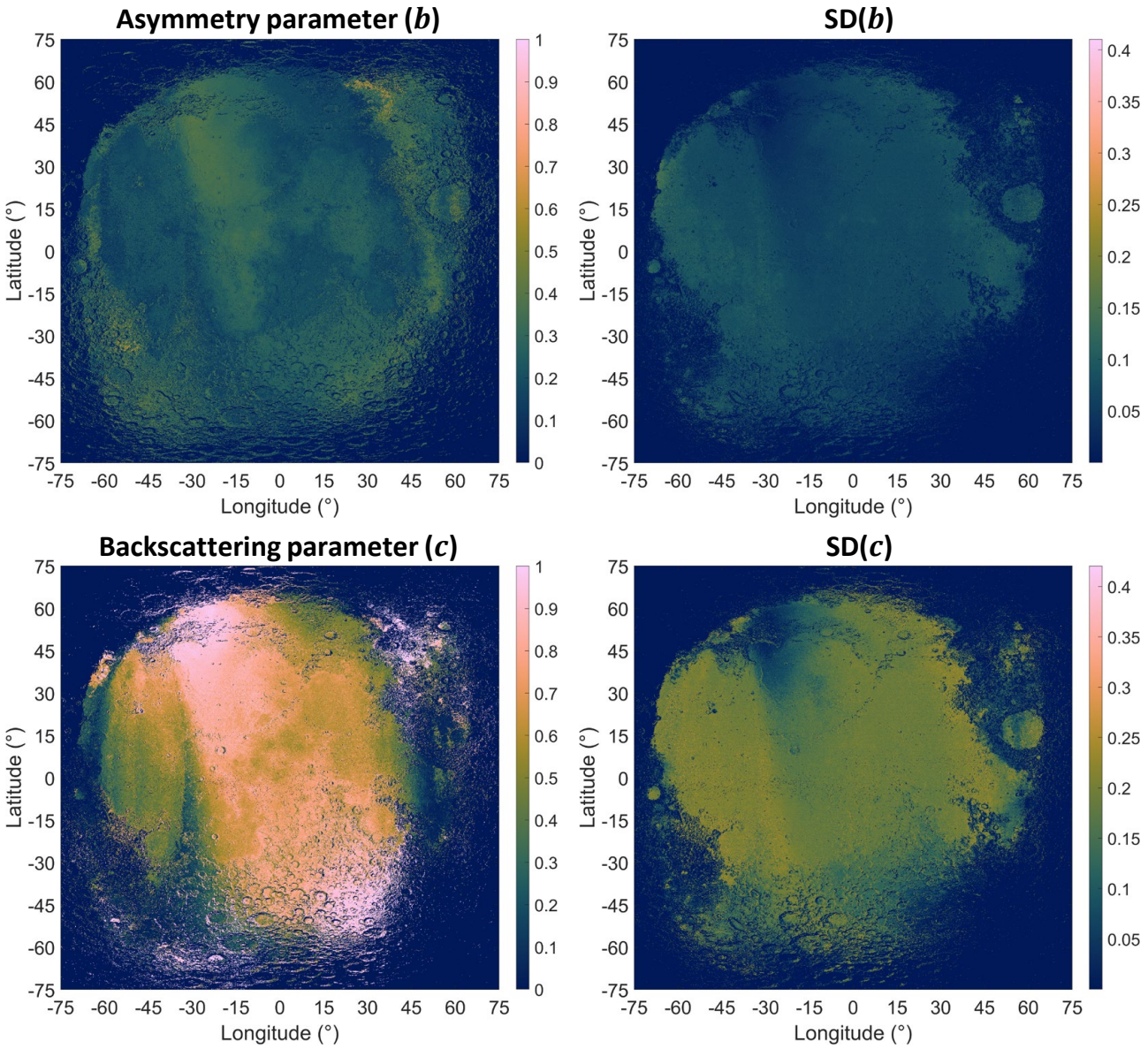

Figure 72 – Estimated HG phase function parameters (b and c) in the spectral band of Pleiades centered on 555 nm, covering most of the near side of the Moon (from -75˚ to 75˚ in longitude and latitude) and the corresponding SD maps.

is 0.49. On the basis of these results, the surface compactness of the Moon appears to be similar in the two regions. The value of the parameter B_0 is more distinguishable, with 0.46 for the maria and 0.7 for the highlands. This could mean that the highlands are more opaque than the maria in the 510-600 nm wavelength range. The SD of h and B_0 is 0.23, which is not as well constrained as other parameters.

Again, we will compare these results with other work. According to Sato et al. (2014), h is between 0.03 and 0.06 for Maria and between 0.075 and 0.1 for the highlands. These values are very low compared to ours. On the other hand, B_0 is between 1.92 and 2.08 for the maria and between 1.52 and 1.76 for the highlands. This time their values are much higher than ours. Kennelly et al. (2010) also estimated the opposition effect parameters, but their version of the Hapke model was different from ours, as they estimated both the SHOE and CBOE parameters, so the results are not comparable. In addition, we used the 4-parameter Hapke model in the Asal-Ghoubbet rift, excluding h and B_0, so we cannot compare the results with those obtained on the Moon.

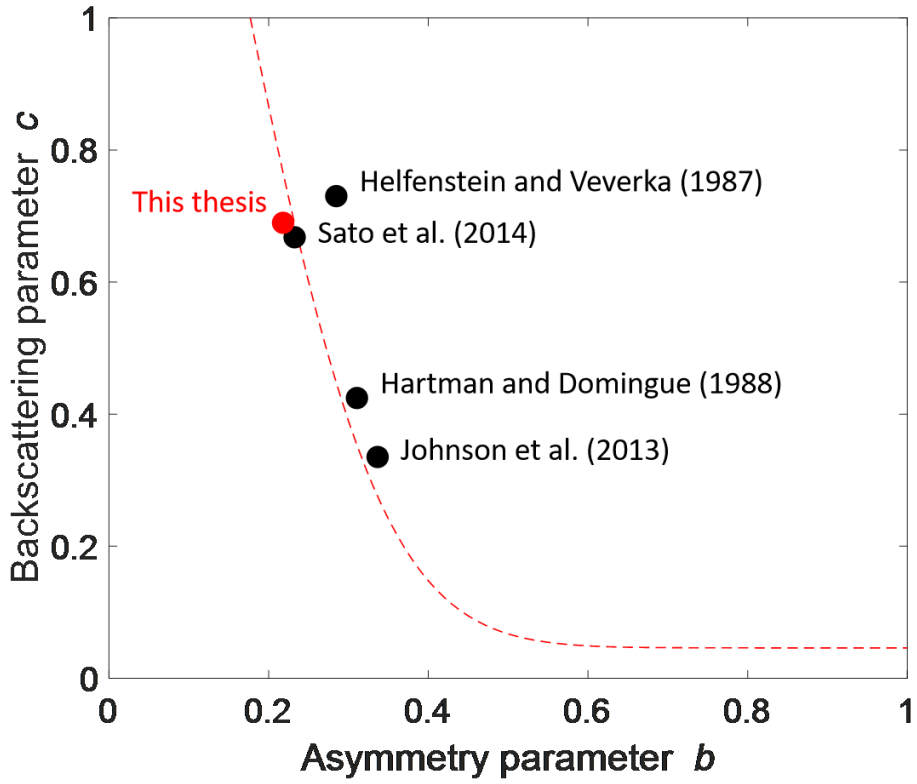

Figure 73 – Hockey-stick diagram (Hapke, 2012) of average lunar particle phase function parameters, originally created by Hapke and Sato (2016), including our result (red dot): $b = 0.21, c = 0.64$.

5.2.2 Apollo 17 landing site

In this section, we will focus on a small area, the Apollo 17 landing site in the Taurus-Littrow valley. This valley lies south of the Littrow crater on the far side of the Moon. As shown in figure 75, the valley is framed by two large mountains, the Massif Nord and the Massif Sud, and opens onto Mare Serenitatis (northwest). This site has a geological importance because it contains dark soil, lava rocks hollowed out by the impact of meteorites, and upland material from the Massif (Nguyen, 2019). This makes photometric analysis of this site interesting. However, based on the distance covered during the EVA, the valley is only about 3 × 8 km long, which represents only 6 pixels on the Pleiades images. Therefore, by extending the view by 10°, we can obtain a balanced region between the maria and the highlands, and we have more geological units to study (Figure 76c). On the Pleiades images, it covers 289 × 289 pixels, or 433.5 × 433.5 km.

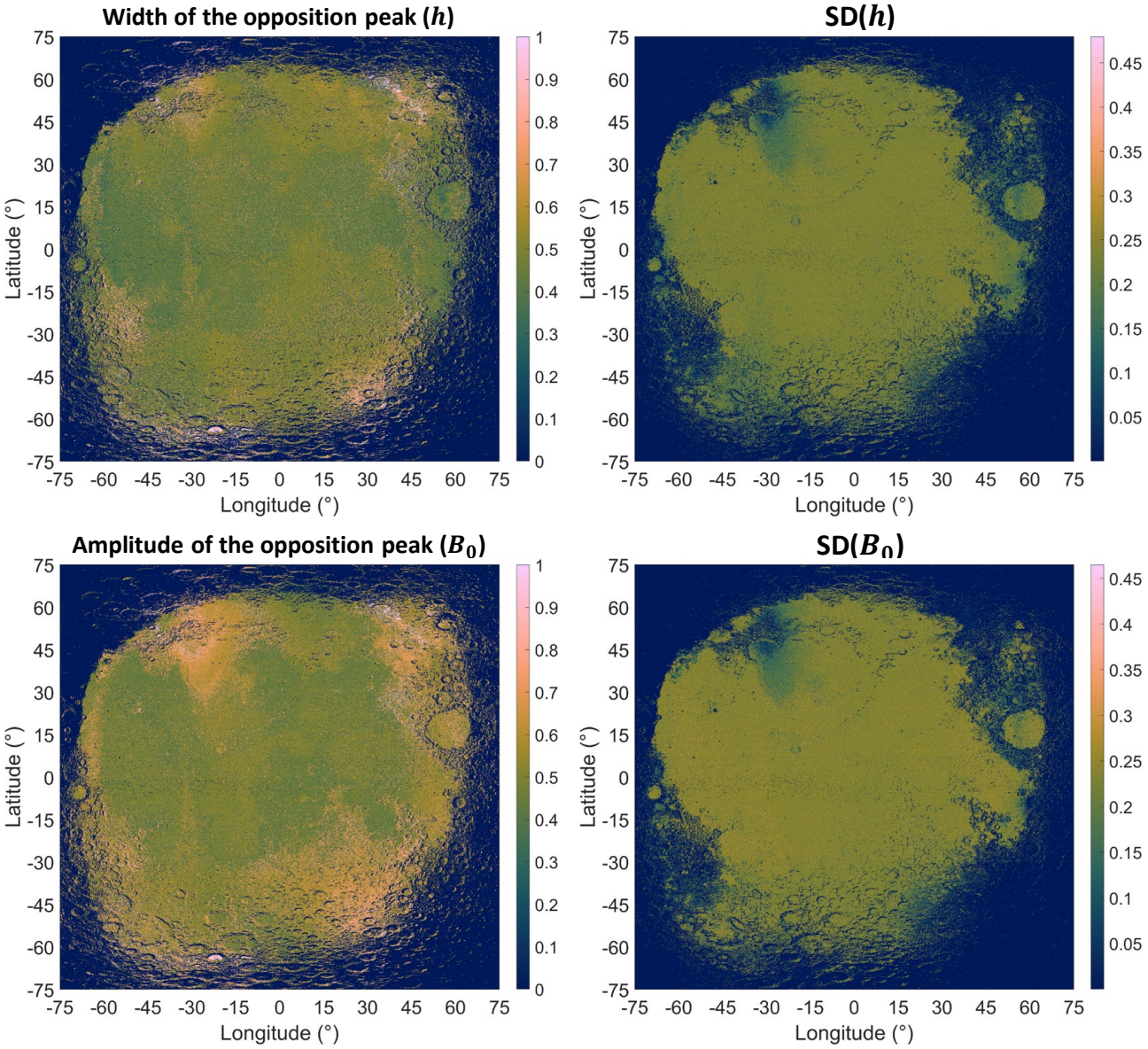

Figure 74 – Estimated opposition effect parameters (h and B_0) in the spectral band of Pleiades centered on 555 nm, covering most of the near side of the Moon (from -75˚ to 75˚ in longitude and latitude) and the corresponding SD maps.

Figure 75 – Apollo 17 landing site and surrounding region. The red square shows the extent of the 10˚×10˚ surrounding the Apollo 17 landing site.

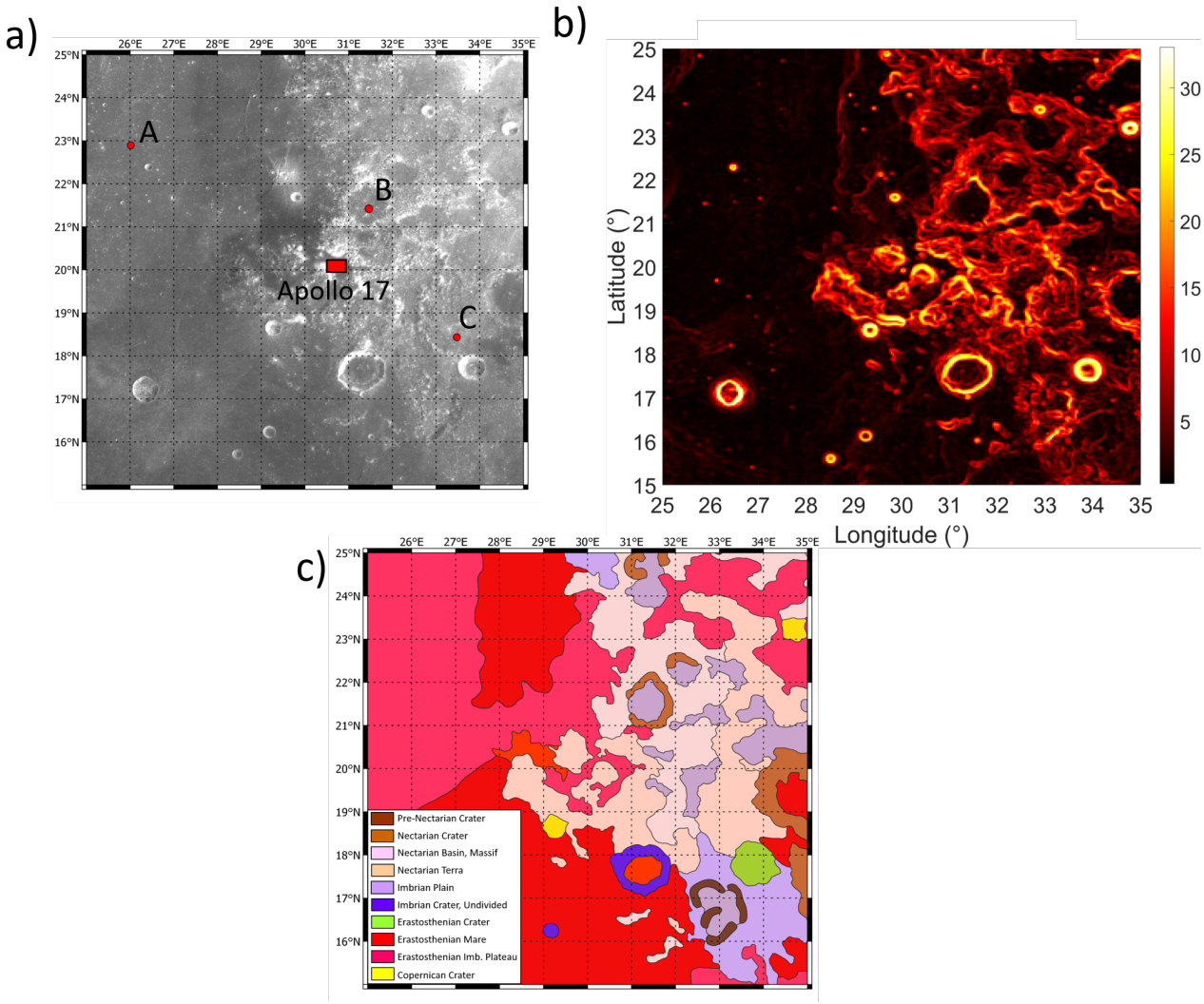

Figure 76 – Information required for detail analysis of the Hapke model inversion parameter maps: a) SELENE/Kaguya Global Lunar image to identify lunar surface features (GSD = 474 m) (Haruyama et al., 2012). Aside from Apollo 17 site, we are inspecting three points: A (mare), B (crater) and C (highlands); b) Slope map generated from LROC WAC DEM (GSD = 118 m) (Scholten et al., 2012); c) Lunar geologic map (Fortezzo et al., 2020). All the subplots are confined within 10° around the Apollo 17 landing site.

Quality of the inversion

The correlation between the RMSE map (Figure 77) and the slope map derived from the global lunar DEM (Figure 76b) is fairly straightforward: a high RMSE corresponds to a steep slope. Part of the region has a RMSE greater than 0.02, which does not meet the criteria for a good BRF fit (Fernando et al., 2013). However, the fit is good over most of the region (80%). Further analysis showed that with such a large ground sampling distance (1.1 km), there is a greater chance of encountering varied topography within the same pixel, resulting in a combined spectral response for which the inversion algorithm struggled to find a good solution. This is why steeply sloping areas have the highest errors.

Looking into the BRF, Figure 78 shows that the result is acceptable with RMSE < 0.02. However, the fit appears to be better at high phase angles, while at phase angles < 40° the measurement is

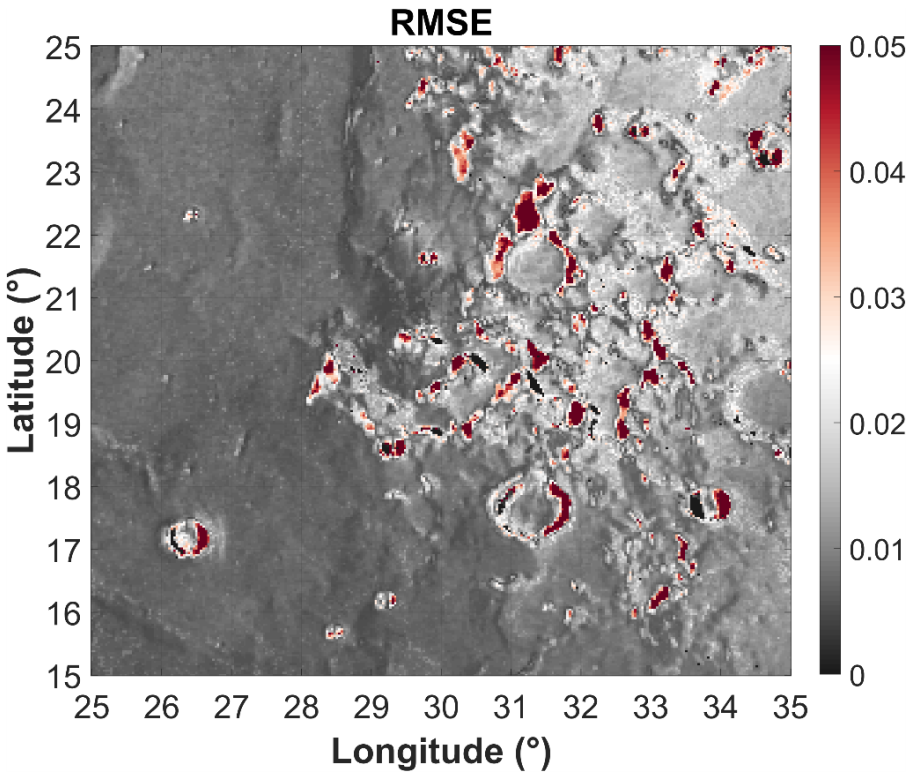

Figure 77 – RMSE map of the reconstruction BRF from the inversion of Pleiades green band images (510-590 nm), covering the region 10˚×10˚ (289×289 pixels) surrounding the Apollo 17 landing site.

underestimated by a maximum value of 0.02. The BRF fit of other points (A, B and C in Figure 76) shows a similar pattern.

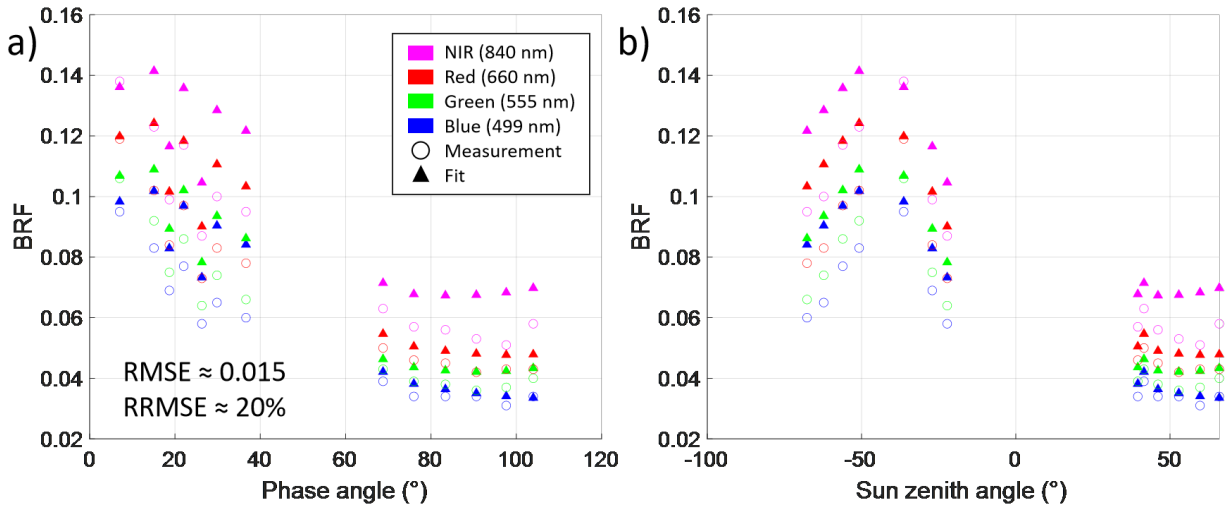

Figure 78 – Comparison between the BRF measurements (circles) of Pleiades at the Apollo 17 landing site (20.1653˚N, 30.7658˚E) and simulated by the Hapke model (triangles) in the four Pleiades channels. The same result is found for different x-axes: a) phase angle; b) sun zenith angle (SZA). For better visualization, the SZA in subplot b can take negative values when $\phi < 90^{\circ}$.

Hapke model parameter maps

Figure 79 shows the inversion result obtained using the Pleiades green band images. At first glance, as with the RMSE map, the distribution of parameter values closely follows the topography of the region, with a strong contrast between the flat and mountainous areas.

- **Single scattering albedo** ω:

The distribution of the SSA follows not only the topography but also the geological map (Figure 76c). We can clearly distinguish several units: three marshy units (Imbrian plain, Eratosthenes mare and Eratosthenes and Imbrium plateau) with mean values of 0.28, 0.22 and 0.19 respectively. These values are in line with the expectations formulated in the previous section. Surprisingly, the mixing unit between the Eratosthenes and Imbrium materials has a lower SSA than either. The highlands consist of two main units: the Nectarian Basin Massif and the Nectarian Land, both with an SSA of 0.31, which is the minimum value for this region. This could mean that there is a mixture of materials in the highlands, which is visible on the geological map (Figure 76c).

- **Photometric roughness** $\overline{\theta}$

In addition to the steep slopes, Figure 79 shows two distinct areas in terms of photometric roughness. $\overline{\theta} = 25.4$ř in the mare region and $\overline{\theta} = 21.2$ř in the highlands region. This is curious since these values are lower than those reported on global scales. Moreover, the photometric roughness of the highlands is lower than that of the maria. It seems that this region does not follow the conventional behavior of the rest of the near side of the Moon. Surprisingly, the roughness range of [20,25]° does not correspond to any of the sites investigated in the Asal-Ghoubbet rift. The lower limit is close to site F, which contains very fine silt, while the upper limit can be associated with site S, which is a smooth lava field. It is therefore highly likely that this particular region of the Moon is smooth, with the highlands displaying a lower roughness due to progressive erosion, while the roughness of the maria is slightly increased by space weathering.

- **Phase function parameter (**b **and** c**)**:

Once again, we focus on the difference between the maria and the highland. As for the asymmetry parameter, $b = 0.37$ in the maria and $b = 0.32$ in the highlands. The difference is minimal and the two units indicate the broad scattering behavior that is common on the lunar surface. As for the backscatter parameter, $c = 0.39$ in the maria and $c = 0.53$ in the highlands. These values are below the average of 0.6 found or the entire lunar near side. However, given the low photometric roughness, it is logical that this region shows a preference for forward scattering (maria) or isotropic scattering (highlands). If we relate this to the Asal-Ghoubbet rift (Figure 67), the maria may be associated with site T (bright powdery material), whereas the highlands may be associated with sites N or Y (volcanic ash, gravel, sediment).

As for the Asal-Ghoubbet rift, we can plot the b-c graph to get an idea of the characteristics of the grains. Comparison of Figures 80 and 67 shows the trace of physically processed basaltic material, which may consist of an irregular, coarse grain or a cluster of fine individual particles. We have also selected three points on Figure 76a outside the Apollo 17 site for closer examination: A for mare, B for crater and C for highland unit. The result is that their positions on the graph are close, which means that their granulometric characteristics are very similar. This implies that the entire region was covered by the same material, or at least had the same origin, but underwent

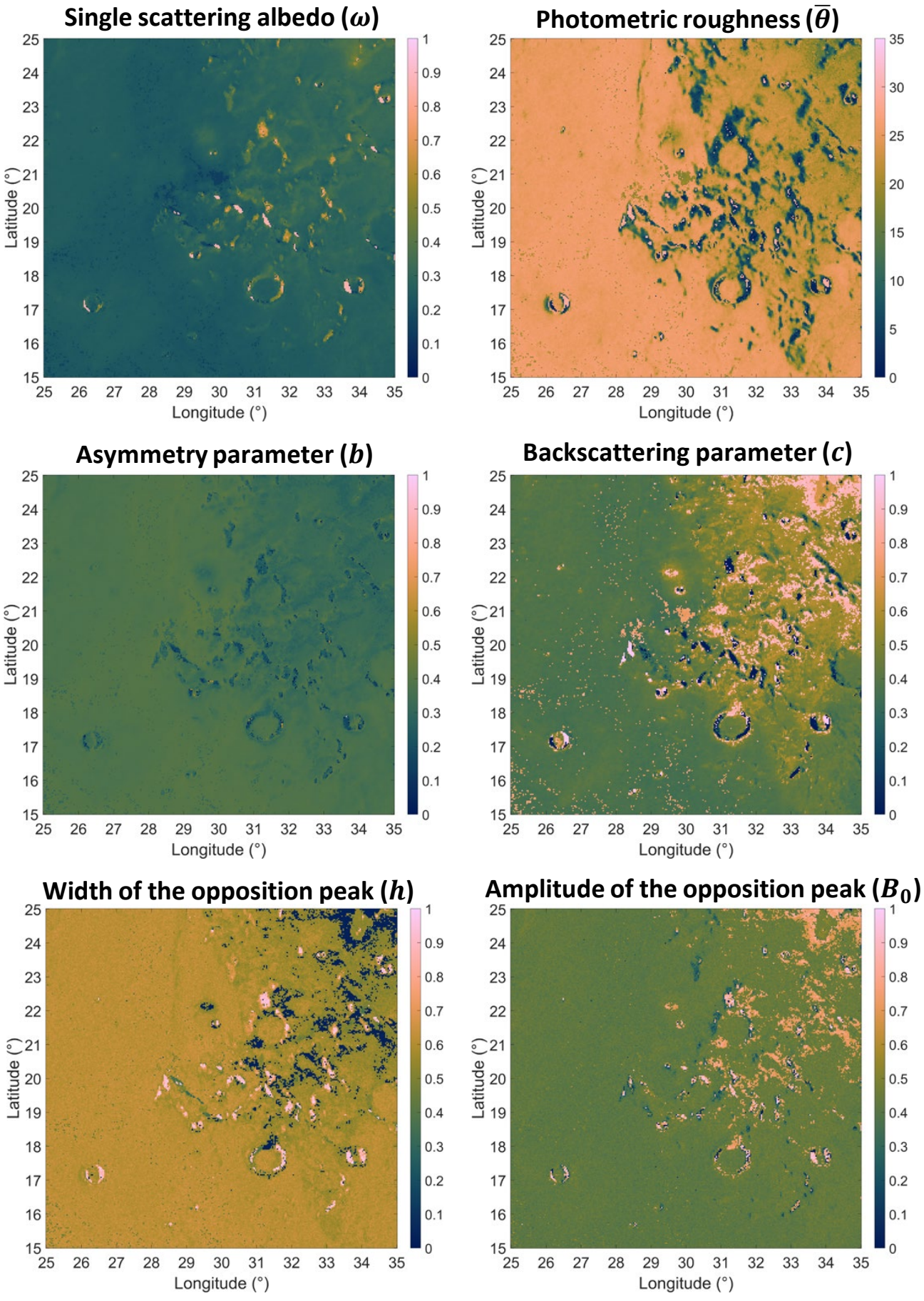

Figure 79 – Maps of Hapke model parameter estimated by inversion of Pleiades green band (510-590 nm) images, covering the region mentioned in Figure 79.

the same degree of physical alteration.

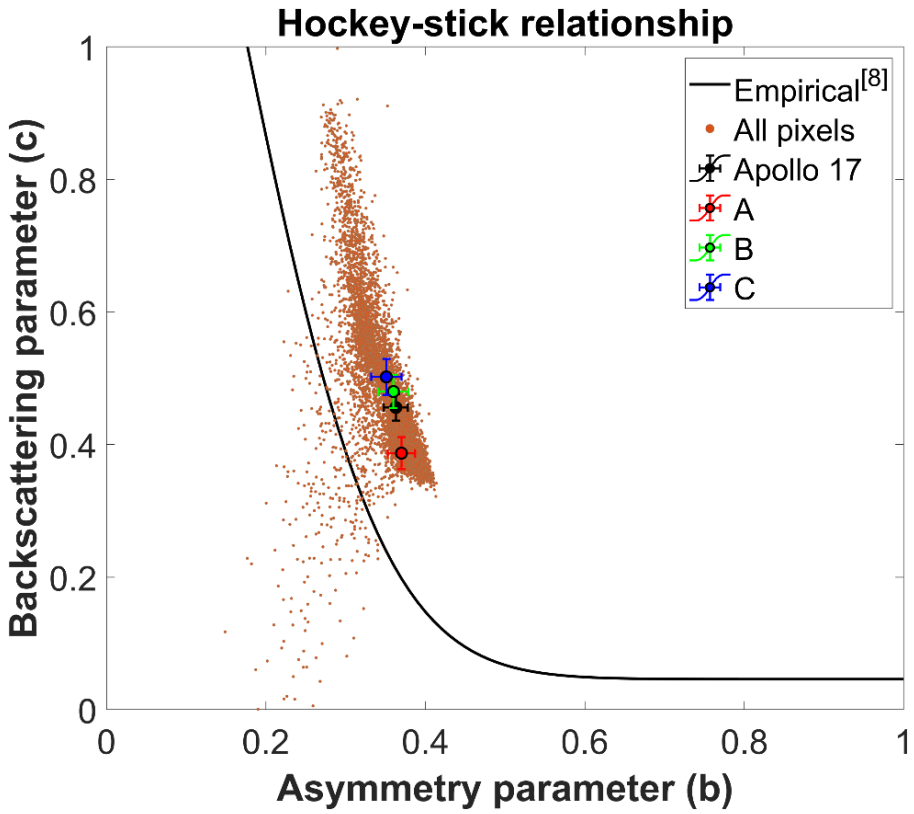

Figure 80 – b-c plot of all the pixels in the region [25, 35]° longitude, [15, 25]° latitude, obtained from Figure 79. We also plot some points of interest in Figure 76a.

• **Parameters of the opposition effect (h and B_0)**:

According to Figure 79, $h = 0.62$ in the maria and 0.56 in the highlands. The highland value is consistent with the global value, but the maria value is 0.14 higher. $B_0 = 0.42$ in the maria and 0.45 in the highlands. The maria value is consistent with the global value, but the highlands value is 0.25 lower, which is significant. At this stage, we do not have enough information to comment on the compactness of the surface. Furthermore, the lower opaqueness of the highlands in the region of interest could be linked to the lower SSA.

Hapke parameters at several points

Once again, let's look at the three points defined in Figure 76a, with a complete set of parameters for 4 Pleiades bands (Figure 81).

• The SSA levels are different, but consistent as a function of wavelength, and show the same pattern. The increase in SSA is not monotonous, since the values at 660 nm are slightly lower than those at 550 nm, contrary to the observations of Kennelly et al. (2010).

• Theoretically, in the wavelength range from 500 to 900 nm, the other parameters should remain practically constant. This is not the case for $\overline{\theta}$. Point C still has the lowest roughness with an average of 14°, but the variation is extremely large, ≈10°. The others are similar, with an average of 21°. This is consistent to our observation where highlands have a lower roughness than the maria in the region of the Apollo 17 landing site.

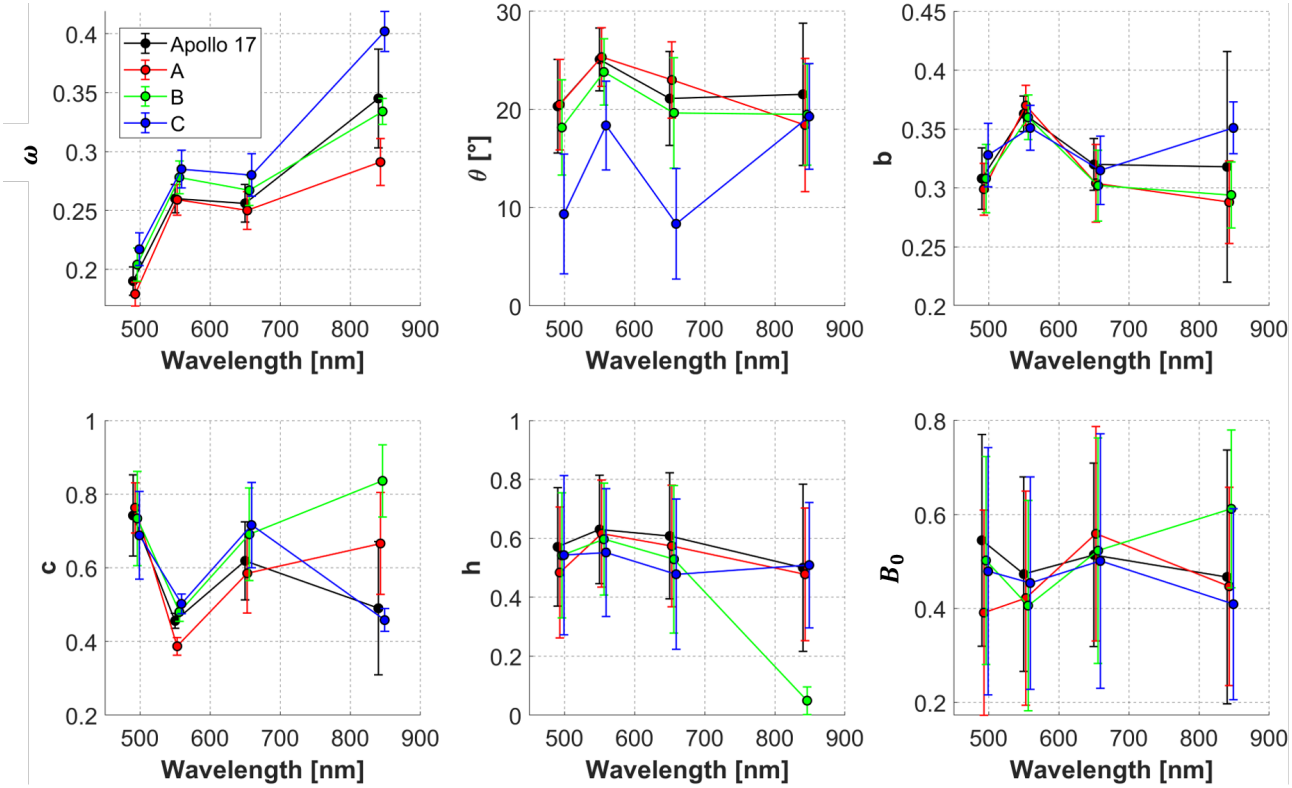

Figure 81 – Inversion result from Figure 79, which highlights some notable points in Figure 76. The graph covers the four Pleiades bands shown on the x-axis.

• b is almost the same for the four locations, with an average value of 0.33 and insignificant variation of 0.05. The same applied to c, with the exception in the fourth channel. Their variation is also larger, around 0.27. This observation is consistent with Figure 80m where c varies strongly while b does not change much.

• h and B_0 are consistently centered around 0.5, reflecting the results of the inversion on a global scale. However, the analysis is not as reliable, as the SD value is large (0.2 for h and B_0).

Finally, by analyzing a few points, we reinforce the assertion that the entire region has the same origin, deposition or alteration process, despite being in very different locations and geological units.

5.2.3 Latest results

As shown in Figure 82, the RPV model shows a good fit for data points with phase angles above 10°, but performs poorly for measurements below this threshold. This discrepancy raises immediate concerns about the reliability of the previously derived parameter maps for h and B_0. As an alternative to the RPV model, we investigated the modified RTLS model (RossThick-LiSparseReciprocal - RTLSR) proposed by Jiao et al. (2016), which has been optimized to account for hotspot effects. When we attempted to fit the Pleiades Moon data with this model, the goodness of fit was comparable to that of the RPV model. However, the RTLSR model also exhibited an underestimation of BRF values at low phase angles, and its additional parameters further increased the computational requirements. Recently, we came across the work of Ding et al. (2024), which evaluates the modified RTLS model variants of Jiao et al. (2016, 2019); Dong et al. (2019). Among them, the RTLSRC (RossThick-LiSparseReciprocalChen) model caught our attention, as it

is intended to be an extension of the RTLSR model. As shown in Figure 82, this model significantly improves the fit for certain data sets (e.g., Apollo 14 and Apollo 16), although it still underestimates BRF values at low phase angles for others (e.g., Apollo 17). The conditions under which the RTLSRC model achieves optimal performance remain poorly understood, but appear to depend heavily on the specific geometric configurations of the data set. Ding et al. (2024) investigated another variant, the RTLSRCS model (Jiao et al., 2019), which incorporates the same elements as RTLSRC but is specifically optimized for snow-covered surfaces. Since most of the lunar surface does not meet this criterion, we have not yet tested this model.

In the end, we decided to directly invert the six-parameter Hapke model using the Simplex algorithm and evaluate its performance. This model produced the best results, even for measurements at low phase angles. We therefore directly inverted the Hapke model using the simplex method, avoiding the photometric normalization required for massive Bayesian inversion, in order to assess its effectiveness in relation to the results presented in previous sections.

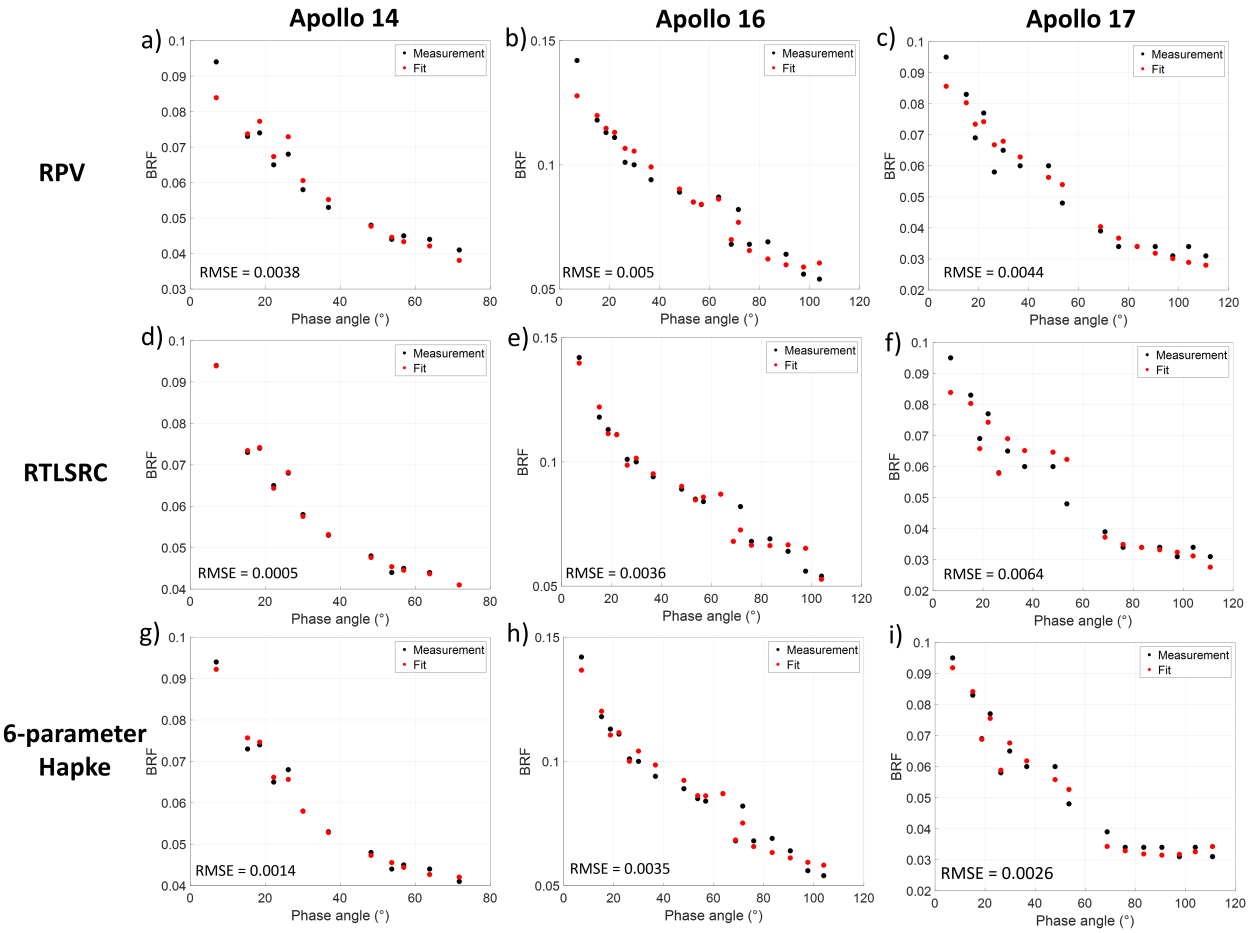

Figure 82 – Comparison of the goodness of fit of the RPV, RTLSRC (Ding et al., 2024) and 6-parameter Hapke models to Pleiades data at Apollo 14, 16 and 17 mission landing sites.

Figure 83 shows the goodness of fit for the new results. Compared with Figure 69, the improvement is substantial, with RMSE reduced by more than an order of magnitude. In particular, RMSE values for the maria are generally below 0.002, while those for the highlands are below 0.01, except in regions characterized by steep slopes or complex terrain. In addition, the Moon's topographic features are clearly visible, in line with previous observations. As before, RMSE values for the maria are lower than those for the highlands. The highest RMSE values are observed along the crater rims, where significant elevation changes result in steep slopes.

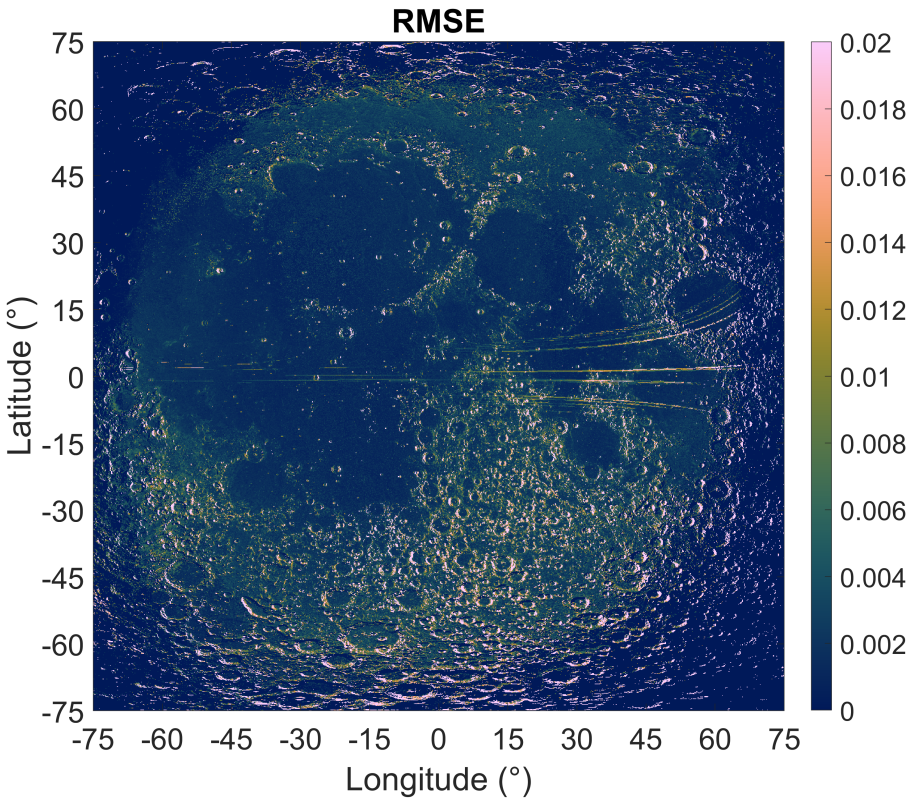

Figure 83 – New RMSE map of the BRF reconstruction from the inversion of Pleiades green band images (510-590 nm), covering most of the near side of the Moon (from -75˚ to 75˚ in longitude and latitude).

Looking at Figure 84, the topographic features are more pronounced than in the results presented earlier. In the case of SSA, a threshold of 0.6 effectively distinguishes maria from highlands: the former have values below 0.6, while the latter have higher values. This threshold is twice as high as that obtained using the RPV model for photometric normalization and fBi. This improvement is probably due to the improved fit of low phase angle data, which avoids the underestimation observed in previous models. Since most values of B_0 (representing the amplitude of the opposition peak) approach the defined upper limit, as suggested by Johnson et al. (2013), we carried out several tests in a small area near the lunar center, removing the upper limit constraint on B_0. The results showed that while most parameter values remained consistent, SSA values at the crater rims dropped significantly. The influence of B_0 on ω remains uncertain and deserves further study.

The photometric roughness presented in Figure 84b shows a clear contrast between the maria and highlands. The maria typically have roughness values between 40˚ and 50˚, while the highlands are typically between 10˚ and 20˚, as indicated by the color scale. However, roughness values show significant variation across the defined [0, 60]˚ boundary. This result differs significantly from previous global results, where maria roughness was slightly lower than highlands roughness, but is consistent with what we observed in the region surrounding the Apollo 17 landing site. As far as the phase function parameters are concerned, the results show a clear distinction between the terrains. The b parameter is generally higher and c lower for the maria. Specifically, b values range from 0.5 to 0.6 for the maria and from 0.3 to 0.4 for the highlands. Previously, the two terrains had very similar b values around 0.2-0.35, making differentiation difficult. A similar trend can be observed for the c parameter. Whereas earlier results showed uniform values of around 0.6-0.7 on

the near side of the Moon, the most recent results distinguish the maria, with c values below 0.1, from the highlands, with values varying between 0.5 and 0.6. An unusual feature has also been identified between 30° and 60° latitude and -45° to 15° longitude, corresponding to part of Mare Imbrium. This region shows a different behavior from its surroundings, particularly in the parameter maps of $\overline{\theta}$ and b. A examination of the geological map produced by Fortezzo et al. (2020) revealed no specific geological unit associated with this anomaly. If this behavior is due to geometric effects, the question arises as to why a symmetrical feature does not appear in the southern hemisphere. This anomaly remains under investigation.

A slight improvement can be seen in the parametric maps of h and B_0. The distinction between the maria and the highlands is now more pronounced. For the maria, h shows significant variation in the range 0 to 1, while B_0 also shows great variability but is centered around 0.7. In contrast, the highlands are characterized by h values consistently below 0.1 and B_0 values close to 1.

An interesting observation is the presence of artifacts along the equator, manifesting by several lines that are absent in the actual lunar images. These artifacts originate from the azimuth angle maps used during the terrain correction step, particularly at points of abrupt transition between high and low azimuth angles. Interestingly, these artifacts were not visible in the previous results, but are apparent in the current analysis. This suggests that photometric normalization can partially harmonize the data and mitigate the effects of these undesirable features, by bypassing them in the previous results.

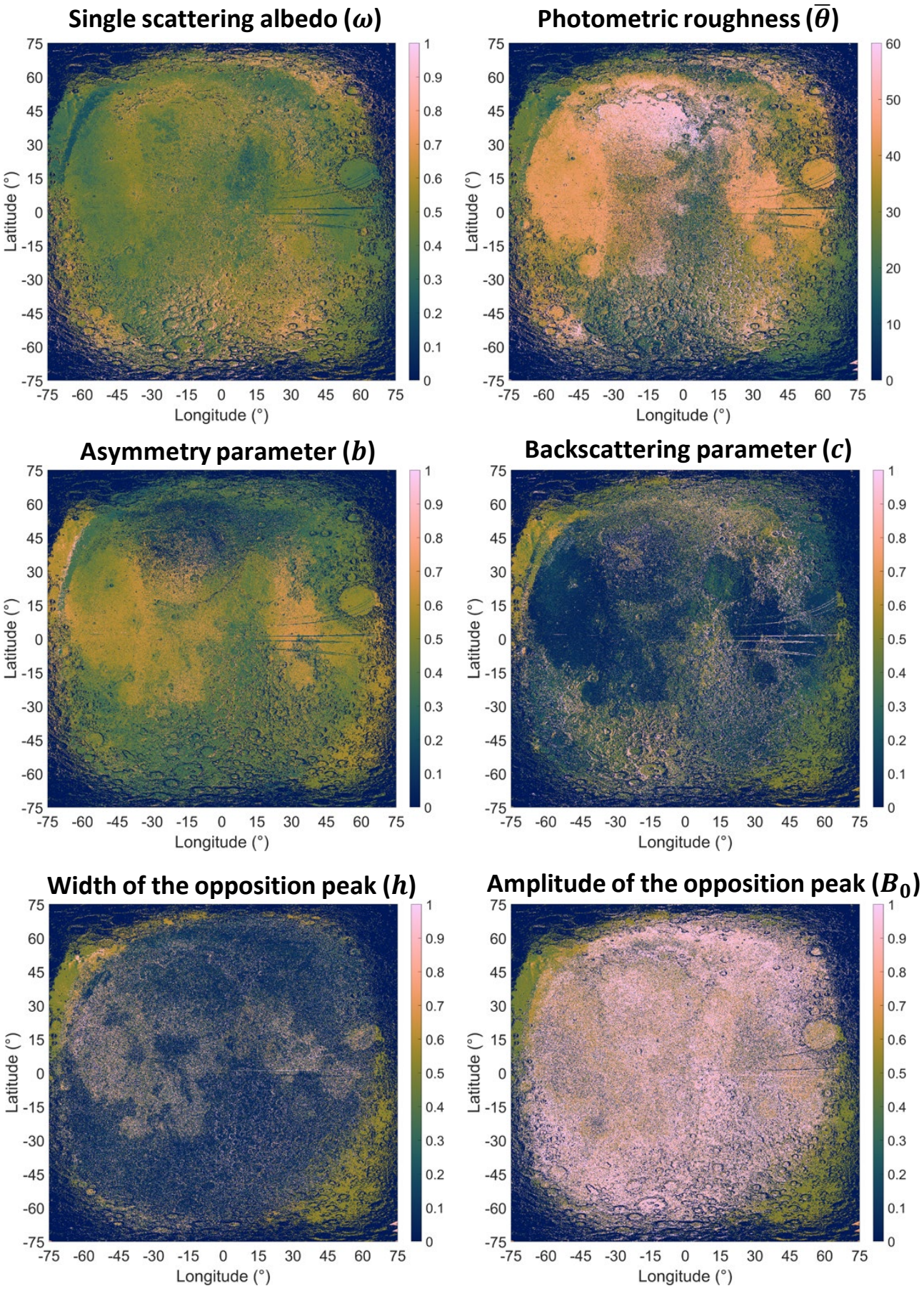

Figure 84 – New parameter maps from the inversion of Pleiades green band images (510-590 nm), covering most of the near side of the Moon (from -75° to 75° in longitude and latitude).

In conclusion, the application of the simplex algorithm to the inversion of the six-parameter

Hapke model produces clear results with high goodness of fit. However, some of these results contradict previous results presented in this thesis and those reported in the literature. Further research is required, particularly with regard to parameter ranges (particularly B_0) and the applicability of newly modified RTLS model variations. Particular attention should be paid to improving the fit at low phase angles.

Conclusion

Overall, we have demonstrated our ability to perform massive inversions using fast Bayesian inversion and obtained encouraging results. However, improvements are still expected in the case of the Moon, as we encountered several undesirable features related to condition of the data.

With regard to the results from the Asal-Ghoubbet rift, our study advances the interpretation of Hapke model parameters, linking them to field measurements. While single scattering albedo (SSA) remains the most reliable parameter to extract, as demonstrated in other studies, its validation presents a significant challenge. There is no straightforward formula relating SSA to surface reflectance from a single measurement configuration, indicating the need for further methodological development or alternative approaches to bridge the gap between theoretical models and observable quantities. Additionally, our results reinforce the close relationship between photometric roughness and SSA, emphasizing that accurate extraction of photometric roughness may depend on SSA values. Regarding phase angle parameters, their correlation with grain characteristics varies by surface type and the physical and optical properties of the materials, but the general relationship holds for most sites.

As far as the lunar results are concerned, we found a certain similarity between the Moon and the Asal-Ghoubbet rift. SSA remains the best constrained parameter for observing lunar features, and the low value of SSA on the Moon is consistent with the fact that it contains mainly the basaltic materials. The photometric roughness is generally higher on the Moon, suggesting either the difference in microscopic roughness or the different influence of macroscopic roughness on the microscopic roughness. In addition, the lunar surface favors backscattering through the phase angle parameters, with different forms of scattering lobes. Applying these data to the b-c graph, we can see that the characteristics of the grains in the basaltic terrains are similar on the Moon and on Earth. We have also obtained values for the opposition effect parameters, although these have yet to be validated and are difficult to compare them with other results due to the use of different versions of the Hapke model.

Chapter 6

BRDF simulation with a ray-tracing model

Introduction

In the previous two chapters, we showed how to analyze surface properties across various BRDF models using photometric model inversion. In this chapter, we take the opposite approach, investigating the influence of surface characteristics on BRDF models using the DART ray-tracing software applied to DEMs (Chapter 3). This approach is limited to surface roughness as represented in the DEMs and spectral properties as obtained in section 2.4.1. However, it does not take into account other essential properties, such as the physical characteristics of the grains (size, shape, micro-roughness) and porosity. These aspects have been addressed in other studies (Section 1.2.2).

In this section, we begin with an overview of the concept of ray-tracing, followed by an introduction to how the DART model works. A concise summary of the work of Wang (2022) is provided. We then explore the framework used to achieve our research objectives, building on the advances made by Legendre-Champion (2021). Finally, we present the results, followed by a discussion of their implications.

6.1 Ray-tracing

In computer graphics, ray-tracing is used to create highly realistic lighting by simulating the way light interacts with objects. It traces the path of light in the form of rays that bounce off surfaces or are absorbed or refracted by materials. Similarly, in photometry, particularly in radiative transfer models (RTMs), ray-tracing is used to simulate the transfer of radiation in a given scene, which may include the atmosphere, objects and surfaces. RTMs involve a computer realization that takes into account the geometry and radiative properties of the elements in the scene (e.g., scattering, absorption and thermal emission), as well as the light sources and sensors. The ray-tracing algorithm tracks energy exchanges in the virtual environment, simulating the quantities required, such as instrument observations and the radiation budget. The design of RTMs depends on the scientific context. Here, to study the functioning of the Earth's surface, RTMs aim to simulate radiative transfer at or near the Earth's surface (Qi, 2019; Wang, 2022).

The Monte-Carlo method simulate the scattering events experienced by a photon between

a source and receiver. It is a stochastic process that gradually converges to the exact solution after a sufficient number of trials and repetitions. This approach attracted our attention because it is considered to be the most accurate and flexible. However, it is also the most computationally expensive solution for dealing with radiative transfer problems (Goel, 1988; Myneni et al., 1989). Examples of ray-tracing models that use this method include, FLIGHT (North, 1996), Raytran (Govaerts, 1996), Drat (Lewis, 1999), LESS (Qi, 2019) and Eradiate [1]. Next, we'll take a closer look at a ray-tracing software package called "DART", which implements Monte-Carlo method.

6.2 DART ray-tracing software

6.2.1 Overview

DART (Discrete Anisotropic Radiative Transfer) has been developed at CESBIO since 1992 (Gastellu-Etchegorry et al., 1996, 2015). It is recognized as one of the most accurate and comprehensive 3D RTMs in the field of remote sensing. DART can simulate radiation budget and remote sensing data (in situ, airborne and satellite measurements) for urban and natural land surfaces, incorporating topography and atmosphere, from ultraviolet to thermal infrared. In addition, it can model solar-induced fluorescence in vegetation canopies and LiDAR signals from ground, airborne and spaceborne platforms. Its accuracy in simulating directional reflectance and brightness temperature at the bottom (BOA) and top (TOA) of the atmosphere has been validated: comparison with other models in the RAMI [2] experiment, as well as with satellite, airborne and in situ data (Malenovsky et al., 2023).

The DART working environment is composed of a stratified atmosphere and a heterogeneous three-dimensional land surface, which includes both surfaces (e.g., facets, triangles) and volumes (e.g., turbid vegetation, air, soot). These elements are arranged in a 3D voxel matrix to optimize radiation transfer and simplify the calculation of radiation fluxes at different interfaces. Environmental components, such as 3D objects, triangular clouds or DEMs, can be imported directly or generated by DART's object creation modules. Surface scattering is defined by a bidirectional scattering distribution functions (BSDF), which describes surface interactions such as reflection and transmission. BRDF models include Lambertian, RPV, Hapke, and specular scattering. The media are characterized according to their physical and optical properties. The radiant flux of outgoing radiation in any direction is determined by solving the radiative transfer equation at the local surface or volume. The iterative process ends when the radiation is fully absorbed, exits the environment, is detected by the sensor or reaches the maximum number of iterations allowed. The radiation scattered within the sensor's field of view (FOV) contributes to the corresponding measurements (Gastellu-Etchegorry et al., 1996; Yin et al., 2013).

6.2.2 DART-Lux: the latest advancement in DART software

DART-Lux (Bidirectional Path Tracing from LuxCoreRender) is one of the three DART modes and the latest in development (2022). It uses the Monte-Carlo method and is recommended for its

1. https://www.eradiate.eu/site/
2. https://rami-benchmark.jrc.ec.europa.eu/

ability to process large, complex landscape remote sensing products, as it is faster and requires less memory. It implements a bidirectional tracing algorithm to efficiently sample a group of paths connecting the light source and the sensor, and to progressively evaluate the estimate without redundant calculation. It is intuitive to sample a path by a random walk (a stochastic Markov chain) from the light source and connect it to the sensor, which is what happens in nature. That is what we call forward transport of light or ray tracing. Although counter-intuitive, it is also possible to sample a path by a random walk from the sensor and connect it to the light source. This sampling method, known as adjoint transport, importance transport or backward path tracing, has been shown to be more efficient than light transport for image simulation, and has therefore been incorporated into DART-Lux (Wang et al., 2017).

In the 1992 version, DART used an iterative discrete ordinate method (DART-FT) to track radiation from the source through the environment to the sensor. Compared to DART-FT, DART-Lux offers major advantages for simulating remote sensing images and BRF, particularly for complex environments with millions of facets (in term memory allocation and simulation computation time). The differences between the two modes are as follows:

• End-to-end simulation: DART-Lux samples the paths that contribute uniquely to the simulated image, while DART-FT tracks all possible paths.

• Efficient path generation strategy: bidirectional random walk and vertex connection methods generate a group of paths in less time.

• Depth-first strategy: the random walk requires much less memory than the breadth-first strategy of DART-FT, whose memory demand increases considerably with the scattering order.

• Data organisation: instead of storing multiple objects like in DART-FT, DART-Lux converts them into a single one. Therefore, DART-Lux uses much less memory and time than DART-FT.

DART-Lux proved to be a significant improvement over DART-FT. It was therefore chosen for this work.

6.3 BRDF simulation framework

Having presented the general principles of DART, we now turn to the BRDF simulation framework developed specifically for this thesis.

6.3.1 Preparation

a) Site classification

Terrain can take various forms, and the complexity of input DEMs increases when dealing with mixed terrain containing several spectral components. In DART, it is essential to assign specific spectra to each element in a scene. However, since the DEM is treated as a single component, it becomes necessary in some cases to divide the DEM into separate components. Based on the reflectance spectra of the soil/rock samples and the homogeneity of the individual sites, we classify the sites into three groups:

- Relatively homogeneous: In this group, there is only one type of material, or several types but with very similar reflectance spectra. The DEMs do not require further processing. The majority of the Asal-Ghoubbet rift DEMs and all the DEMs produced from the astronaut photographs belong to this group.
- Inhomogeneous but physically distinguishable: In this group, there are at least two different materials that can be easily separated by image processing because they are at different elevations or have very different physical properties. In site E of Asal-Ghoubbet rift, a layer of rock lies on a layer of sand (Figure 85a) with different reflectance spectra (Appendix 6.4.3).
- Inhomogeneous and physically indistinguishable: In this group, there are at least two different materials that cannot be separated by simple image processing because they are similar in terms of physical characteristics and spectral properties. Site I contains three components: sand and a slab of rock with similar spectral properties, and another type of rock with different spectral measurements (see Figure 85b and Appendix 6.4.3).

(a) (b)

Figure 85 – Close-up photos of a) site E and b) site I in the Asal-Ghoubbet rift.

For the second group, we describe the process of separating the components of the DEM:

• Edge detection using Sobel algorithm Sobel and Feldman (1973): In MATLAB, the command is `[~,~,Gx,Gy] = edge(DEM)`, with `Gx` and `Gy` two images which contain at each point the approximations of the horizontal and vertical derivatives. We then calculate the magnitude of the gradient at each pixel $G = \sqrt{G_x^2 + G_y^2}$. Finally, we define a threshold for the image `G` and create a prototype mask of two values, one for values above and one for values below the threshold. The choice of threshold is based on a process of trial and error. A histogram of values with `G` can help to make a choice.

• Dilation and Erosion: This is an optional step which allows the edges to be surrounded. The MATLAB functions are `imdilate()` and `imerode()`.

• Fill the hole: This is carried out to take into account all the values inside the edges, recognized as a filter for rocks. The MATLAB function is `imfill()`. We now have a usable mask that separates the DEM components (Figure 86).

• Apply the mask: For the upper layer (rocks), we declare that pixels that are not rocks are at the lowest elevation (within the range of the original DEM), while pixels that are recognized as rocks retain the original elevation. The same applies to the lower layer (sand). So when we input the two DEMs into DART, we can overlay them and the virtual light will only interact with the important

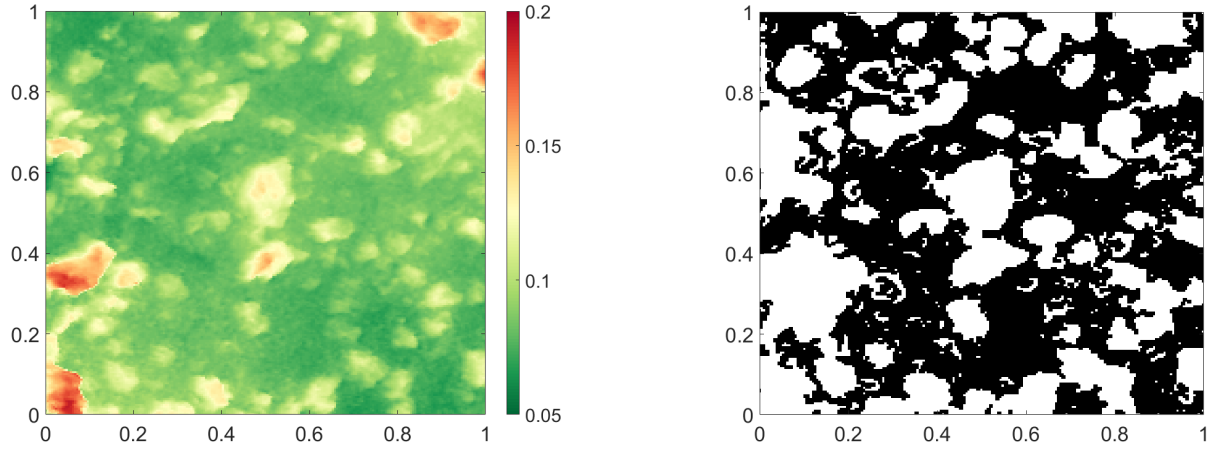

(a) (b)

Figure 86 – a) Part of the DEM of site E. The color bar represents the elevation; b) Corresponding mask generated by the DEM component separation process. As can be seen, the identification of the rock layer is imperfect, but most of the pixels belonging to this layer have been identified. All axes are in meters.

parts. This has been done to avoid any pixel having no value, which could have a negative effect on the next step.

For the third group (inhomogenous and physically indistinguishable), we would need an orthophoto of the scene, in order to separate the different DEM components using a color gradient filter. However, due to time constraints, we have not tested this.

b) Detrending

Detrending is necessary because we wish to simulate the BRDF of the surface with its normal vector overlapping the nadir, in order to avoid large-scale topographic effects. This process was described in Section 3.7.4.

c) DEM conversion to suitable format

Since DART has simulated light rays reflecting off facets, we need to import DEMs in the appropriate format to represent facets in 3D geometry, such as `.OBJ` files containing:

- The list of vertices, with the pattern 'v x z -y', where (x, y, z) are their coordinates in right-handed orientation of the GIS (x to the right, y outward, z upward).
- The list of faces, with the pattern 'f v1 v2 v3', where v1, v2, and v3 are the indices (starting from 1) of the previously defined vertices that form the face.

Conversion from `.TIF` to `.OBJ` is essential. Our default `OBJ` files are created using alternating triangles as faces, to avoid artefacts (Figure 87). All these steps are contained in a Python script, written by Legendre-Champion (2021).

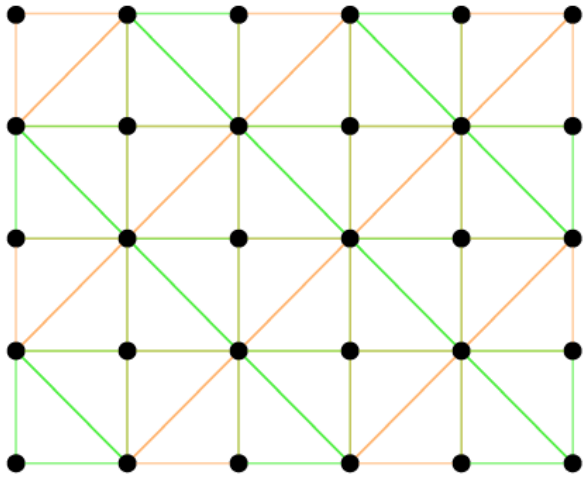

Figure 87 – Triangulation of a regular grid by regularly alternating SW-NE NW-SE diagonals (Legendre-Champion, 2021).

d) Specifying and importing input parameters into DART

Here we show what is common to all our simulations. We can use DART's graphical user interface (GUI) to define all the parameters required to run a simulation. A GUI is available for:

- Importing/managing 3D objects and DEMs.
- Defining and assigning optical and temperature properties
- Configuring the atmosphere (geometry, vertical profile and optical properties of gases, aerosols and/or clouds).
- Selecting the type of product.

All the input parameters are encoded in an extensible markup language (`.XML`) to facilitate access to the data. We can speed up the process by creating a default input folder common to all simulations and placing it in `user\_data/simulations/<name of simulation>`. Here is our common input data for the different simulations:

- A totally dark background on which to place the DEM, named "Lambertian_black", whose reflectance spectra set to zero at all wavelength. This is necessary if we want to simulate the DEM in a isolated scene.
- Four spectral intervals depending on the Pleiades satellite:
  - B0: Central wavelength 0.49 μm, spectral bandwidth 0.08 μm
  - B1: Central wavelength 0.55 μm, spectral bandwidth 0.08 μm
  - B2: Central wavelength 0.66 μm, spectral bandwidth 0.08 μm
  - B3: Central wavelength 0.845 μm, spectral bandwidth 0.14 μm
- The target sample density per direction is set at 15000. This value was chosen because 15000 rays $\times$ 360° (in azimuth) $\times$ 90° (in elevation) $\simeq$ 500 million rays, for a more accurate map with an error of about 0.2% and a ray-tracing time of about half an hour, as recommended by Legendre-Champion (2021).

- Direction input parameters: Similar to the configuration of the Pleiades image in the Asal-Ghoubbet rift.
    - Sun zenith angle [°] = 38.0
    - Sun azimuth angle [°] = 0.0
- Surface reflectance model: Hapke 2012.

This default data import step also comes from a python script written by Legendre-Champion (2021). On a case-by-case basis, the differences between the simulations are the DEM and the ground reflectance spectra. In the DART user interface, the DEM in `.OBJ` format can be declared in "Parameters/Editor...", then when a new window opens, go to "Earth Scene: 3D imported object / Point objects". However, for very large files, it is recommended that you use the Python code, as the interface will become unresponsive. For spectra, you first need to create a text file for each soil type, with the following header:

```
wavelength reflectance direct_transmittance diffuse_transmittance
```

The wavelength and reflectance are taken directly from the ASD measurements mentioned above. The last two columns are assumed to have zeros only. Next, from the DART interface, we go to "Tools/DART Database Manager". When a new window opens, choose "Import" and then select all the newly generated spectra text files and choose "Add to database". This will change the database format from `.txt` to `.db`. Subsequently, in Parameter Editor, search for the Hapke surface characteristics in "Optical and temperature properties" and select the appropriate spectra file in the "Transmittance database" tab.

6.3.2 Simulation choice

In this section, we show the differences between the simulations. We have run a series of simulations on DEMs from the Asal-Ghoubbet rift, all of which differ in terms of surface reflectance, roughness and spectral properties, in order to make cross-comparisons. First, we need to clarify how we define the interaction of radiation at the surface, which includes reflectance, transmittance, absorptance and emission. As far as reflectance models are concerned, we use two models: the Lambertian model and the Hapke model. The diffuse Lambertian model assumes that the light reflected from a surface depends only on the normal to the surface and the direction of the light. A Lambertian surface is therefore equally luminous in all directions. We have chosen this model to be able to use the reflectance spectra measured in the laboratory (see Section 2.4.1 and Appendix 6.4.3). On the other hand, the Hapke reflectance model depends on the Hapke parameters estimated by inversion on the SHINE instrument (see Chapter 4). The transmittance of the soil samples was set to zero. Finally, as far as thermal emission from soil is concerned, it is outside the scope of our study (the solar domain).

In addition to model selection, we also run simulations on the different DEMs and their decomposed components, in order to study the BRDF of surfaces with different surface roughness.

6.3.3 Main process

When you click on "Run/DART", the software runs sequentially through four main modules:

- Direction: subdivides space into user-defined discrete directions for radiation transfer.
- Phase: calculates optical bandwidth properties, temperature properties and scattering phase functions.
- Maket: creates a 3D model of the Earth's surface and atmosphere, assigns temperature and optical properties to each element in the scene and calculates vertical profiles of the atmosphere (pressure, temperature, density).
- Dart: simulates the transfer of radiation on the ground and in the atmosphere, and generates the necessary measurements.

6.3.4 Output

To visualize the BRF obtained in the DART software, we can go to "View/Directional Reflectance-Temperature/View BRF Map (Bi-directional mode)" and open the file `BRFmap.mp#` in the directory:

`user_data/simulations/<name of simulation>/output/BAND<number>/BRF/ITERX/IMAGE_DART/`

The simulated BRF is stored in ILWIS (Integrated Land and Water Information System) files. To read it, we need the text file `BRFmap.mpr` storing the metadata and the binary file `BRFmap.mp#` containing the raster data. ILWIS is a geographic information system (GIS) and remote sensing software for both vector and raster processing. Its enables data to be digitized, edited, analyzed and displayed, and high-quality maps to be produced. To read the ILWIS files, we also have a Python code for converting them into `.csv` files that can be read by MATLAB to visualize the BRF.

6.3.5 Known errors

Error with Database manager

In case we cannot import the sample spectra into DART, we can overwrite the old `Lambertian_mineral.db` with the new one that works.

Memory overload

When this problem occurs, a few changes need to be made:

- Open `DART/bin/DARTIHMLauncher.bat` and add `-Xmx64g` after `-XX:MaxHeapFreeRatio=60` if the user decides to allocate 64 GB of RAM (or any other value).
- Do the same with `DART/bin/DARTIHMSimulationEditor.bat` if the user tries to import a large OBJ into the Editor.
- Open `dart-maket.sh` in either `DART/tools/linux` or `DART/tools/window`, add `-Xmx64g` after `-Dj3d.rend=noop`.

If nothing works, you will have to reduce the size of the DEM or the resolution.

6.4 Simulation results and discussion

For the tests, we generally choose sites A (undulating gravel field), F (flat sand field) and U (basalt boulder field) of the Asal-Ghoubbet rift, as their roughness is characteristic and representative. In other cases, as the SHINE dataset only contains BRF measurements from sites F (very fine silt), R (granular terrain) and T (slab limestone), we sometimes use DEMs from these sites as well. Our simulations do not contain any atmosphere (BOA simulation). The general strategy is to test the simulation on two models: the Lambertian model (which depends on the measurement of reflectance spectra in Appendix 6.4.3) and the Hapke model (which depends on the inversion results in Section 4.4). For each model, we test the original DEM and its decomposed roughness components (Section 3.8.2).

6.4.1 Lambertian model

Between different SHINE channels and DEMs

As shown in Figure 88, when moving from one wavelength to another, the BRF pattern does not change, but rather the amplitude. As far as the BRF pattern is concerned, site A has a constant slope from -70° to 70° in emergence angle. Site F, on the other hand, has a gentle slope from -80° to 80°, as well as the highest amplitude. Unlike site U, which is the roughest of the three sites, the BRF of these two sites does not show a hot spot. It is interesting to note that the hot spot does not appear directly at the angle of incidence (-38°), but at around -50°.

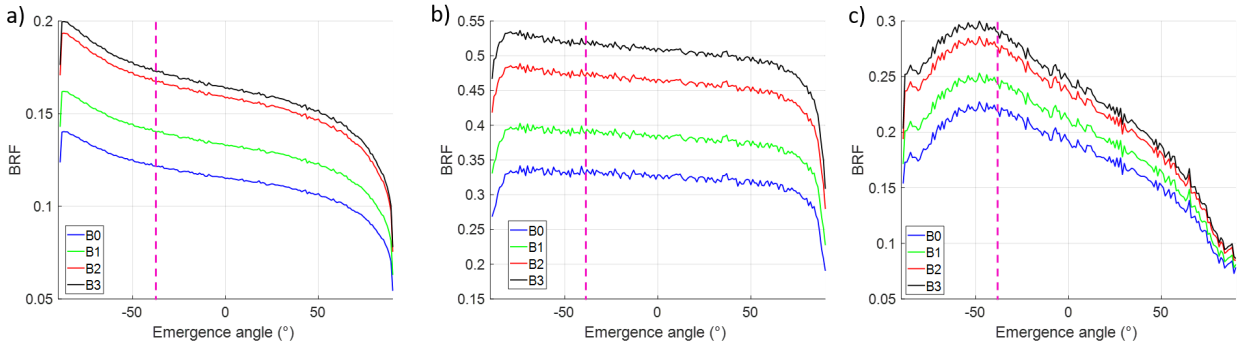

Figure 88 – Simulation of the BRF of a) site A; b) site F and c) site U, in the principal plan ($\phi = 0°$ or 180°) using the Lambertian model, the drone DEM and the spectral measurements. Sun incidence angle of -38° (the dashed vertical line). The four SHINE bands are B0 (450-530 nm), B1 (520-600 nm), B2 (610-690 nm) and B3 (775-915 nm).

In Figures 89, 90 and 91, we can see the complete BRF pattern, as well as the effects mentioned. We can see that the BRF behaves like a gradual slope, with no clear hot spot, for the homogeneous sites (site A with $\overline{\theta_M} = 22.91°$ and site F with $\overline{\theta_M} = 8.12°$). The finer the grain (the lower the roughness), the gentler the slope. On the other hand, rough sites like site U (with $\overline{\theta_M} = 28.32°$) will have a surge of BRF near the incidence.

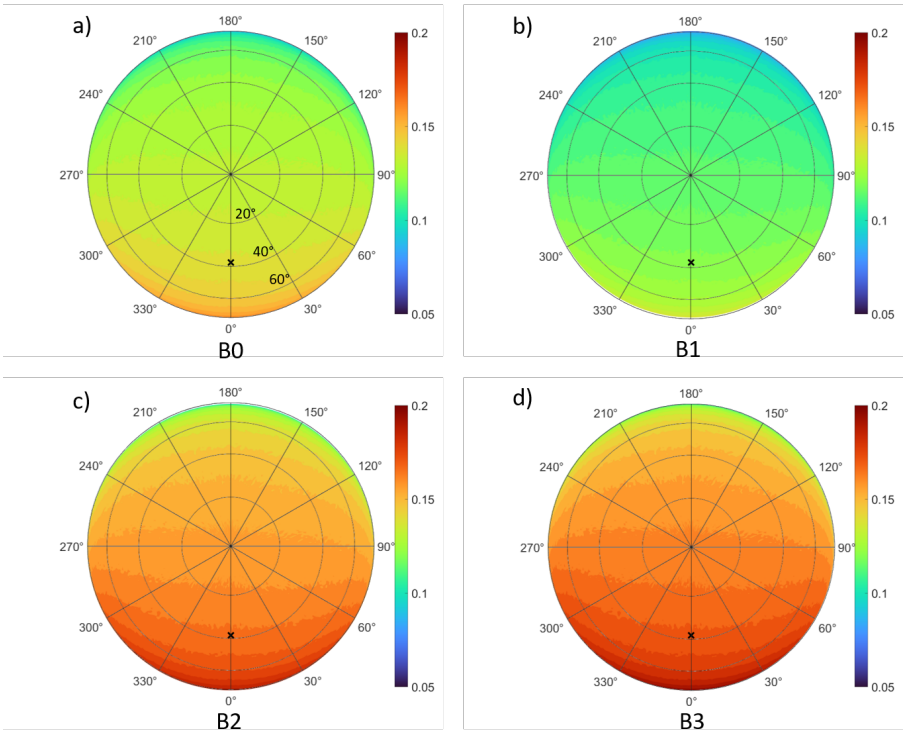

Figure 89 – Simulation of the BRF of site A using the Lambertian model, the drone DEM and the spectral measurements. a) B0 (450-530 nm); b) B1 (520-600 nm); c) B2 (610-690 nm); d) B3 (775-915 nm). Sun incidence angle of -38° (indicated by the symbol ("×")).

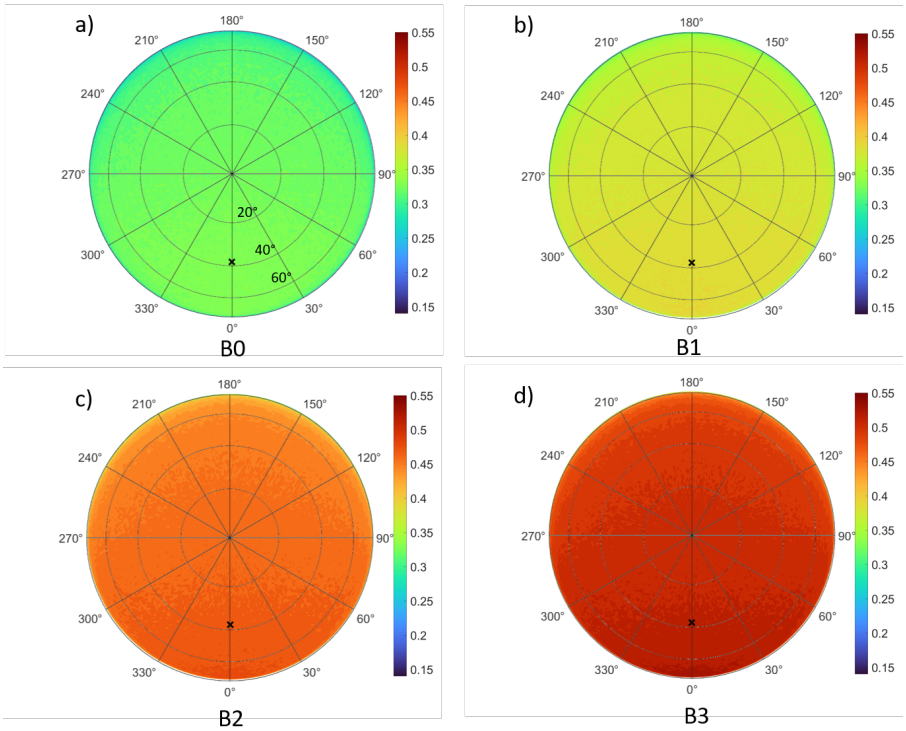

Figure 90 – Simulation of the BRF of site F using the drone DEM, spectral measurements and the same configuration as in Figure 89.

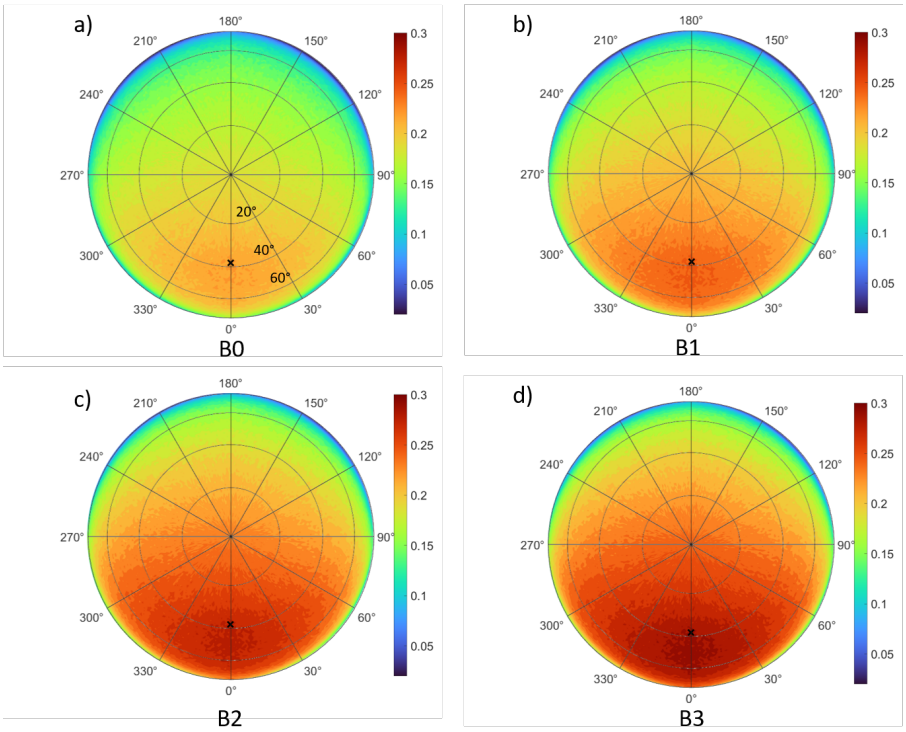

Figure 91 – simulation of the BRF of site U using the drone DEM, spectral measurements and the same configuration as in Figure 89.

Between different DEM roughness components

Figure 92 shows the BRF behaviors of each roughness component of the DEM. The form, waviness and roughness components for site A has $\overline{\theta_M}$ equal to 0.98˚, 2.99˚ and 25.01˚. For form and waviness, the BRF stabilizes around the value of 0.22, with visible zigzag variation. The roughness component shows a peak amplitude between approximately -75˚ to -68˚. The highest values exceed those of B1 BRF in Figure 88a. For site F, we keep in mind that the $\overline{\theta_M}$ values of the DEM components are 0.76˚, 2.38˚ and 9.49˚ respectively. The three BRFs behave mainly as a flat plateau at around 0.263, which is smaller than what we encountered in Figure 88b. At site U, the $\overline{\theta_M}$ values of the DEM components are 3.27˚, 20.08˚ and 29.76˚. Unsurprisingly, the form component with the lowest roughness produces an almost constant BRF of around 0.25. On the other hand, the waviness and roughness components show a hot spot around -50˚. These BRFs are very similar to those in Figure 88c, both in terms of amplitude and shape. For the Lambertian simulation, the hot spot may appear when using a DEM with $\overline{\theta_M}$ as low as 20˚. However, we have not tested the cases where $\overline{\theta_M}$ is between 10˚ and 20˚.

Figures 93, 94 and 95 show the full BRF for the DEM components in Figure 92.

6.4.2 The Hapke model

Between different SHINE channels and DEMs

As in the case of Lambertian inversion, we observe a change in amplitude only when we move from one wavelength to another (Figure 96). The increase in amplitude, which should be a phenomenon of the opposition effect, does not appear exactly at the angle of incidence (38˚).

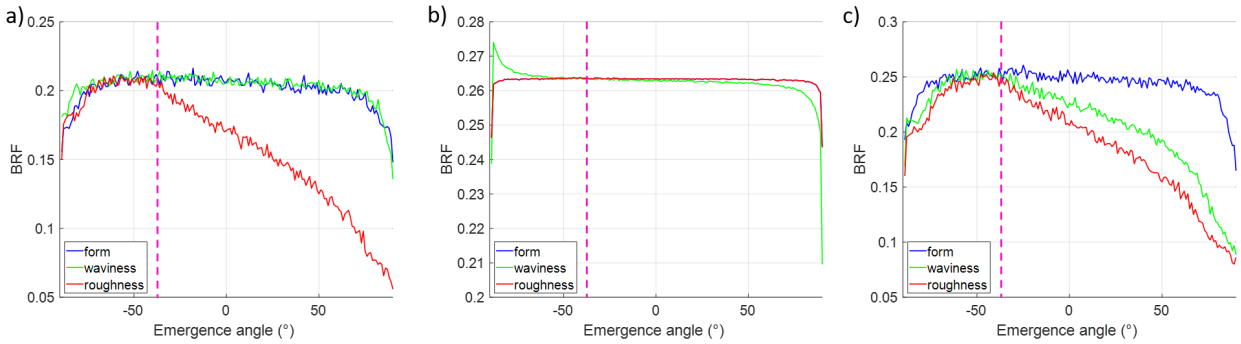

Figure 92 – Simulation of the BRF on decomposed drone DEMs of a) site A; b) site F and c) site U in the principal plane, using the Lambertian model. B1 channel (560-600 nm).

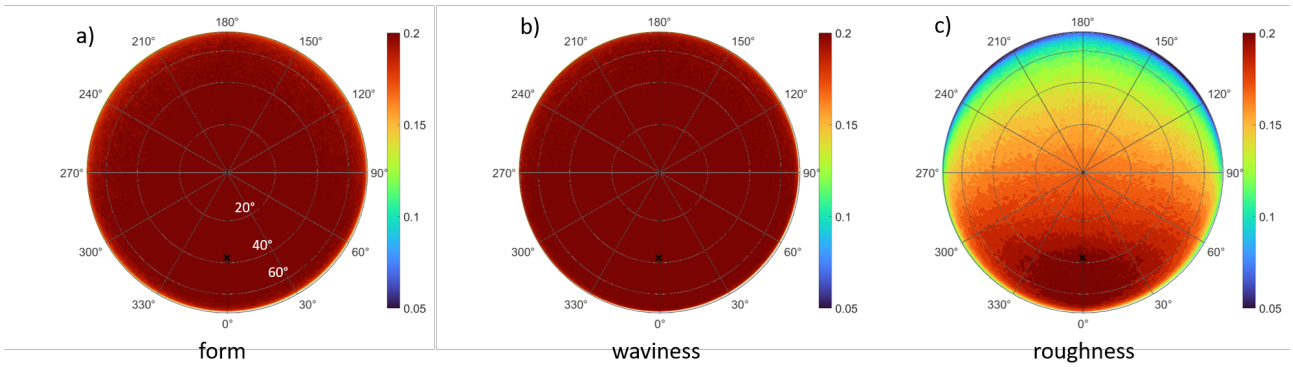

Figure 93 – Simulation of the BRF on decomposed drone DEMs of site A using the Lambertian model and spectral measurements. (a) Form; b) waviness; c) roughness. B1 channel (520-600 nm) and sun incidence angle of 38° (indicated by the symbol ("×")).

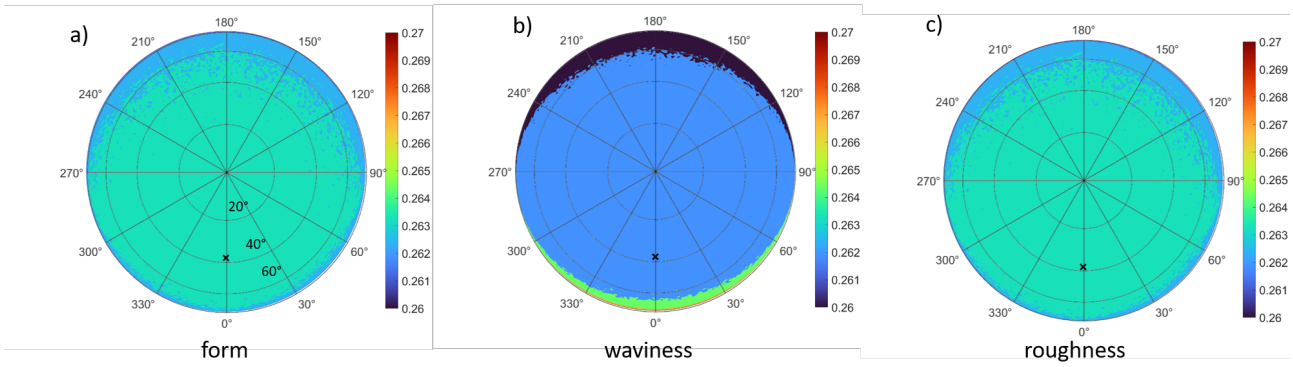

Figure 94 – Simulation of the BRF on decomposed drone DEMs of site F using spectral measurements. (a) Form; b) waviness; c) roughness. Same configuration as in Figure 93.

The maximum value is around -70°. Note that $\overline{\theta_M}$ is equal to 8.12° and 18.64° for sites F and T, respectively. The hot spot effect can therefore still be seen at sites with low roughness (< 10°), unlike the Lambertian inversion.

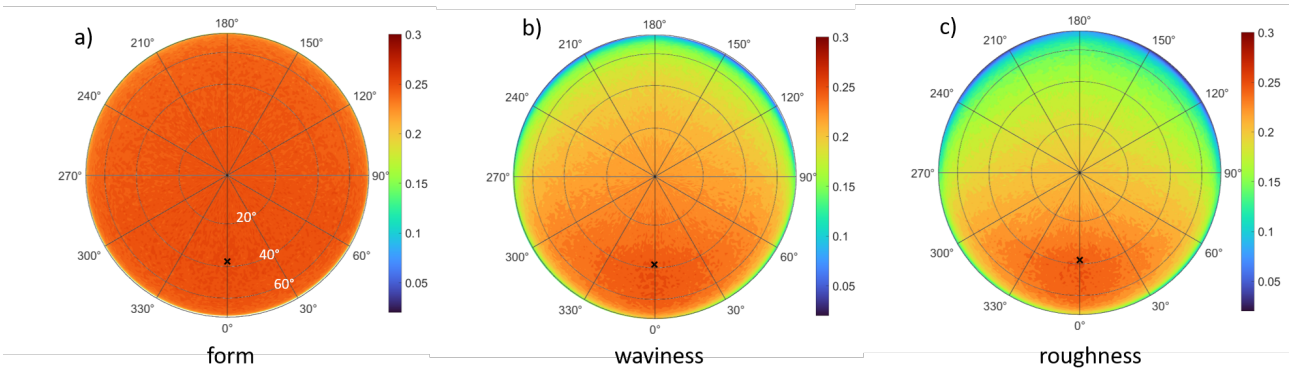

Figure 95 – Simulation of the BRF on decomposed drone DEMs of site U using spectral measurements. (a) Form; b) waviness; c) roughness). Same configuration as in Figure 93.

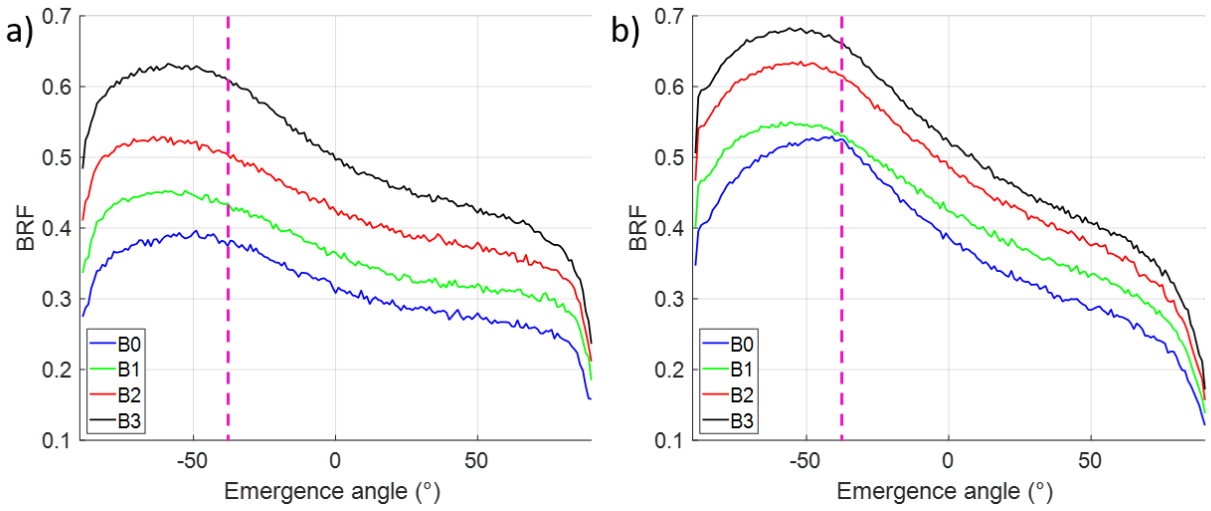

Figure 96 – Simulation of the BRF of a) site F and b) site T in the principal plane using the Hapke model, drone DEM and spectral measurements. Sun incidence angle of -38° (the dashed vertical line). The Hapke model parameters are obtained by using fBi on the SHINE BRF (see Section 4.4.2).

As before, we present the complete BRF in Figures 97 and 98.

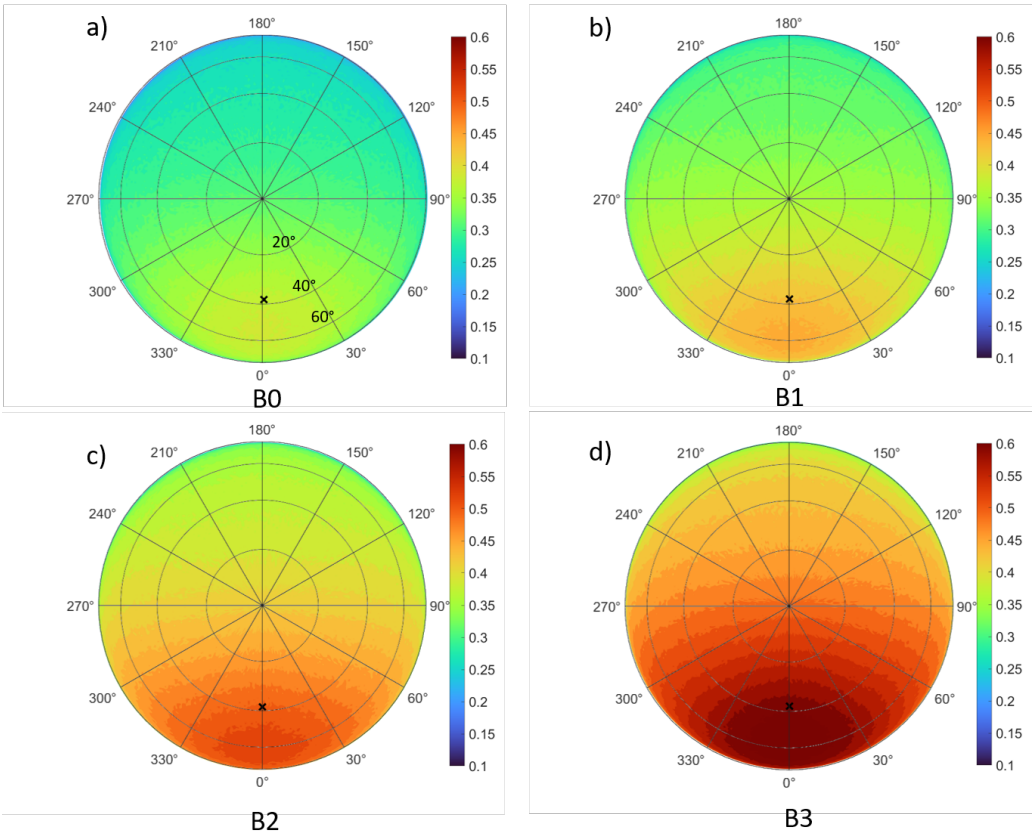

Figure 97 – Simulation of the BRF of site F using the Hapke model, the drone DEM and spectral measurements. Sun viewing angle of 38° (indicated by the symbol ("×")).

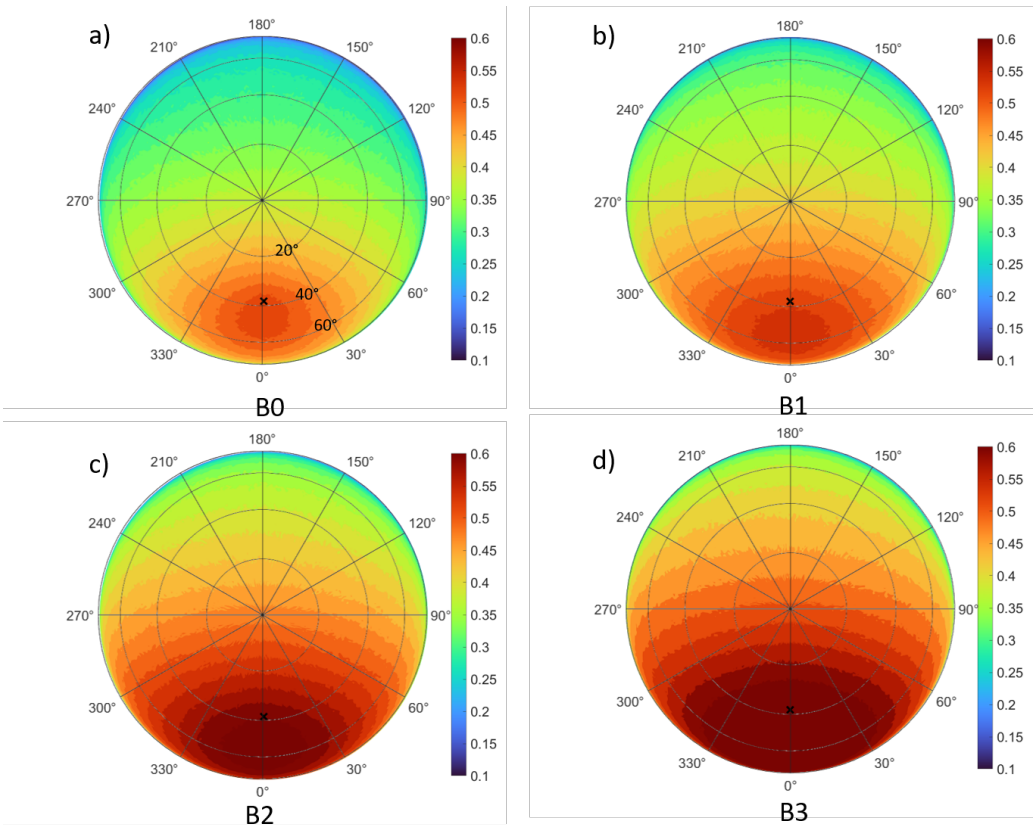

Figure 98 – Simulation of the BRF of site T using the Hapke model, the drone DEM, spectral measurements. Same configuration as in Figure 97.

Between different DEM roughness components

In Figure 99a, the BRFs of site F at different scales coincide between -60˚ and 0˚. The form and waviness components almost overlap. This behavior makes sense if we consider the low roughness values: $\overline{\theta_M}$ = 0.76˚, 2.38˚ and 9.49˚ for form, waviness and roughness. The BRFs of site T in Figure 99b are quite similar, with the form scale being consistently larger than the other two. In the two graphs, the opposition peaks between -70˚ and -38˚ are not well defined. If we look at the roughness value of site T, $\overline{\theta_M}$ = 1.26˚, 7.49˚ and 20.56˚. Based on these observations, it appears that the DEMs with lower roughness tend to scatter light more.

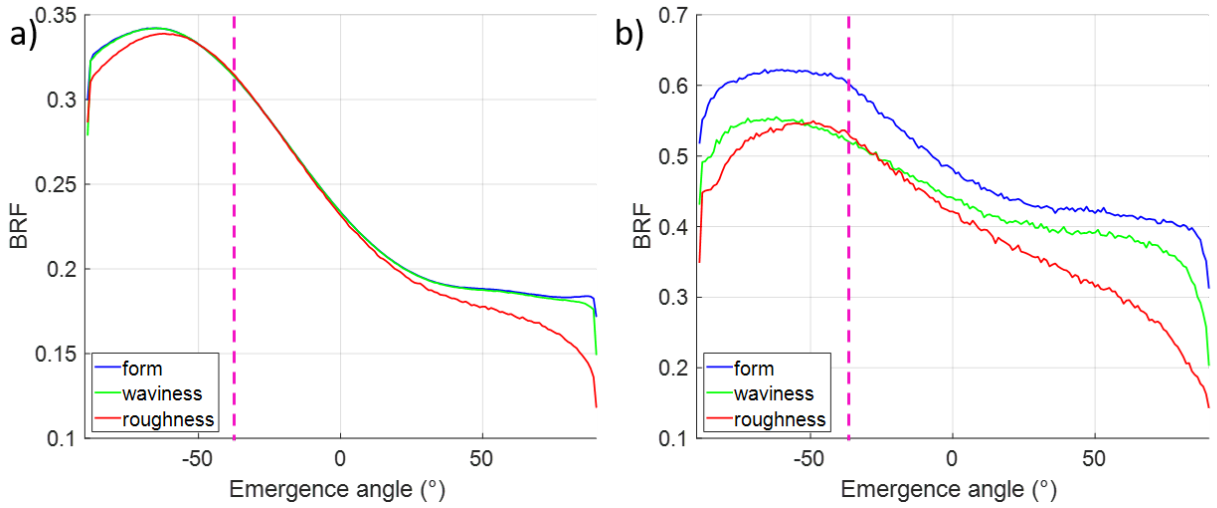

Figure 99 – Simulation of the BRF of decomposed drone DEMs of a) site F and b) site T in the principal plane, using the Hapke model. B1 channel (560-600 nm).

The complete BRFs are shown in Figures 100 and 101.

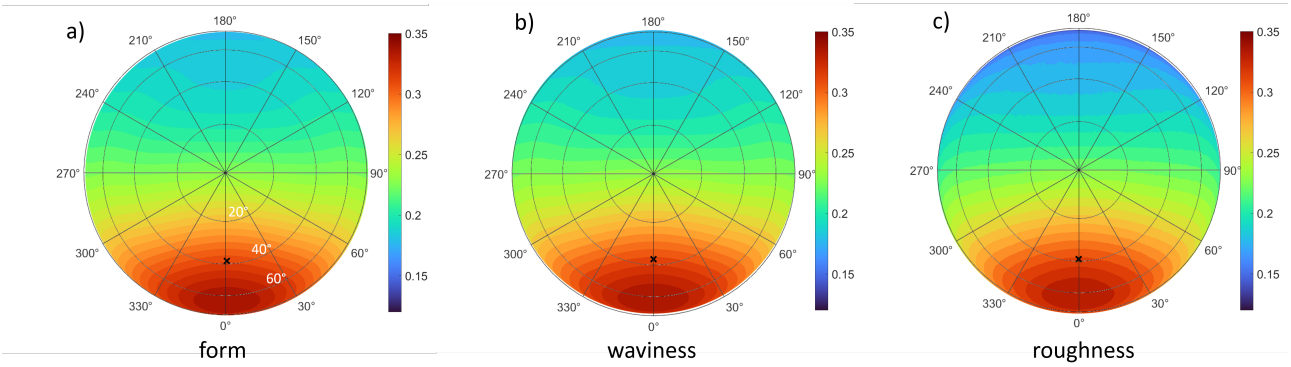

Figure 100 – Simulation of the BRF of decomposed drone DEMs of site F using the Hapke model (parameters from Section 4.4) and spectral measurements. (a) Form; b) waviness; c) roughness). Sun incidence angle of 38˚ (indicated by the symbol ("×")) and B1 channel (520-600 nm).

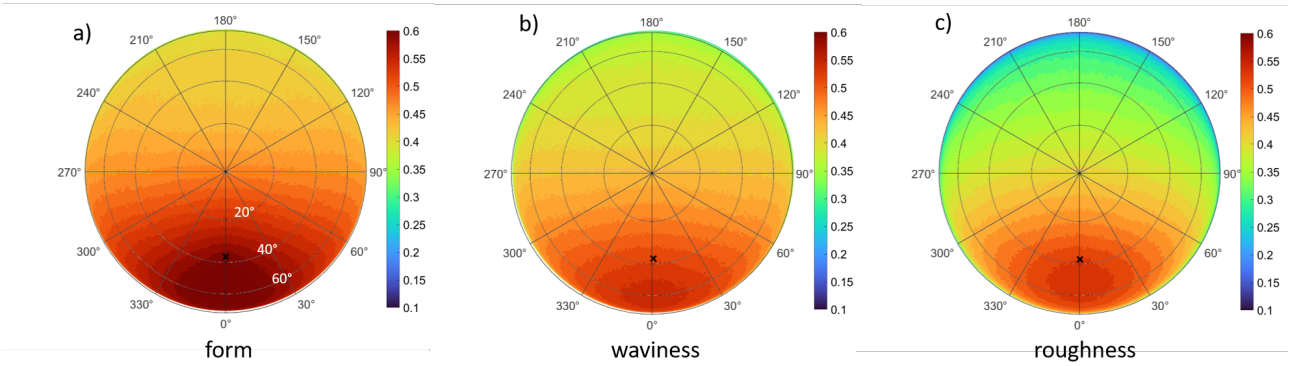

Figure 101 – Simulation of the BRF of decomposed drone DEMs of site T using the Hapke model (parameters from Section 4.4) and spectral measurements. (a) Form; b) waviness; c) roughness). Sun incidence angle of 38° (indicated by the symbol ("×")) and B1 channel (520-600 nm).

6.4.3 Other simulations

For different solar azimuth angles, we observe only a corresponding rotation of the BRF shape, with no significant effect. We also simulated the decomposition of site E into several parts (rock and sand), as described in Section 6.3.1. We chose the Lambertian model in order to be able to to use the reflectance spectra of these materials. From Figure 102, the BRF patterns are not significantly different from each other. However, it is rather strange that the two simulations almost overlap, while the combination of the two is slightly lower in amplitude. We have not found a reasonable explanation for this result. $\overline{\theta_M}$ = 19.39°. As the BRF does not show a clear increase in amplitude near the angle of incidence, combined with the previous observations, the simulation using DEMs with $\overline{\theta_M}$ < 20° has no opposition effect.

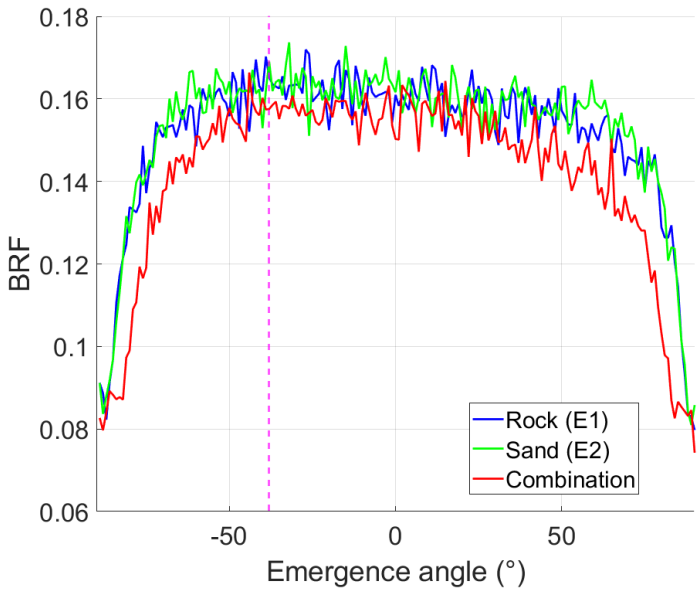

Figure 102 – Simulation of the BRF of site E in the principal plane using drone DEM, spectra E1 and E2 (Figures 108 and 109). a) The E1 spectrum (rock) is applied indiscriminately to the entire DEM; b) Similar to (a) but using the E2 spectrum (powder); c) Assigning E1 and E2 to the corresponding areas of the DEM. B1 channel (520-600 nm).

Conclusion

We presented DART, a robust ray-tracing software package used to simulate the bidirectional reflectance factor of bare soil using DEMs and spectral measurements. After detailing the use of the software, we presented simulation results for several sites of the Asal-Ghoubbet rift, using both Lambertian and Hapke models. As expected, the change in wavelength did not alter the BRDF pattern. The Lambertian model produced an isotropic BRDF for flat terrains; however, as surface roughness increased, the opposition effect became more apparent, with a mean slope angle of 20° identified as the lower threshold for generating a pronounced effect. In contrast, the Hapke model always produced an opposition effect, whatever the surface roughness. A notable feature of the simulated opposition surges is that the peak does not generally coincide with the angle of incidence, but rather occurs at a higher angle in the backscattering direction (more negative emergence angle).

General conclusion and perspectives

From the outset, we defined our main objective as being to study the properties of planetary surface using photometric modelling in the solar domain. In achieving this objective, we have obtained a number of results, the importance of which we will explain and add a few perspectives.

- **Massive inversion of the Hapke model with fast Bayesian inversion**

An innovative aspect of our research is the development of a new framework for massive inversion of the Hapke model using fast Bayesian inversion (fBi). This framework includes preprocessing to improve the accuracy of the geometry, the inversion process, quality assessment and interpretation of the results. To date, massive inversion has rarely been attempted. For example, Sato et al. (2014) carried out a massive inversion of the entire lunar surface using over 60,000 LROC WAC images, an impressive achievement. However, the immense workload involved in such an undertaking makes it difficult to standardize and replicate. In contrast, our approach uses only a few dozen co-registered multi-angular images, greatly simplifying the process. In addition, Fernando et al. (2016) applied a Bayesian Monte Carlo approach using CRISM data, but their results did not achieve pixel continuity, which limits its applicability. In our research, we tested both the Bayesian Monte Carlo and fast Bayesian inversion methods. Although both approaches produced similar results, fast Bayesian inversion delivered solutions up to a hundred times faster due to its more efficient sampling method. This efficiency makes fBi a promising tool for large-scale photometric studies.

To our knowledge, this is the first time that such an inversion has been carried out over a large area of the Earth. It has also been shown to be applicable on the Moon with the Pleiades multi-angular data set. The wide coverage provided by the massive inversion can reveal valuable information about the landscape, including how geological units fit together. It can also detect new surface features that might otherwise go unnoticed in a local analysis. Its potential goes beyond simple data processing and opens up prospects for the development of innovative methods for analyzing multi-angular photometric data.

However, much remains to be done. Whether on the Asal-Ghoubbet rift or on the Moon, massive inversion has only been carried out on the green band of Pleiades, leaving the red, blue and near-infrared bands largely unexplored due to time constraints. Although this task is time-consuming, it would be relatively straightforward if one followed the established framework. In terms of time efficiency, the fast Bayesian inversion framework does not currently have an automated mass processing capability. The current process still requires a lot of work, as each patch has to be submitted manually, one by one, per computer. In addition, there is scope for further optimization in key areas such as BRF extraction, terrain correction, photometric normalization and RMSE calculation, particularly for the management of large geometric configuration matrices.

Addressing these challenges would allow us to perform a massive inversion for the Asal-Ghoubbet Rift at the original resolution of 2 meters compared with the current resolution of 10 meters, which would significantly improve the accuracy and level of detail of the analysis.

Sub-optimal data conditions remain an unresolved issue, preventing better inversion results. For example, the absence of low phase angle measurements in the Asal-Ghoubbet rift forced us to exclude the opposition effect term; poor inversion quality on the lunar edge and significant artifacts appear in several of the Hapke parameter maps for the Moon. To improve the quality of the inversion, data acquisition should favor measurements along the principal plane, where the incidence, emergence and normal vectors are aligned, in order to maximize the recovery of photometric information, as recommended by Schmidt and Bourguignon (2019). However, it is difficult to obtain this alignment with satellite data. An alternative is to select a plane offset by about 30° from the principal plane, as well as other geometries that better sample the scattering lobes of the phase function, as suggested by Kugler (2021). When using Earth observation satellites such as Pleiades to perform inversions, accurate extraction of Hapke model parameters is generally limited to regions close to the center of the Moon (between -60° and 60° in longitude and latitude). As we get closer to the edge, the accuracy of the inversion decreases, unless the satellite's orbital radius can be increased, which would give the geometric configurations a greater range. This would, however, reduce its remote sensing capabilities on Earth, which is a dilemma. Finally, a possible solution to the problem of artifacts is to request and process additional lunar images with smaller phase angle intervals, which could remove outliers and improve the overall quality of the inversion.

- **Interpretation of Hapke model parameters**

By using fast Bayesian inversion, we have considerably accelerated the calculation and have been able to obtain the parameters of the Hapke model from a variety of terrains and at different scales. This facilitates cross-comparisons and improves our interpretation of the parameters by establishing links with field measurements. Although the single scattering albedo (SSA) is relatively easy to constrain, it remains difficult to validate. This highlights the need for further methodological development or alternative approaches to bridge the gap between theoretical models and observations. In addition, there is a notable relationship between low to moderate SSA, mean slope angle calculated from DEMs and photometric roughness, which provides insight into surface properties. For the Henyey-Greenstein phase function parameters, grain characteristics can be deduced using the interpretation system outlined by McGuire and Hapke (1995), Souchon et al. (2011) and Pilorget et al. (2015), in particular through the use of the b-c plot. However, the potential of the Hapke model has not yet been fully explored in this work. Although we have derived parameters related to surface porosity and grain opacity (opposition effect parameters), we currently lack the means to measure and validate these parameters.

Through the creation of a preliminary database of Hapke model parameter, we hypothesise that each BRDF pattern can be uniquely associated with a particular terrain, in the same way that spectral measurements are associated with chemical composition. In our case, these BRDF patterns are likely to represent a mixture of predominantly physical signatures, with some minor contributions from chemical signatures. This new concept has the potential to open up a new avenue of photometric research aimed at improving our understanding of planetary surfaces. Future results can be compared and related to this database, helping us to predict the

characteristics of planetary surfaces.

In addition, there is still much to learn from the results obtained from the near side of the Moon, as further analysis is required at additional landing sites than that of Apollo 17. With the inclusion of ground data from these other sites, this deeper analysis is essential to provide a more complete picture of the lunar surface.

- **Surface roughness investigation**

We have developed a framework for studying surface roughness based on six important roughness parameters: mean slope angle, root mean square height, autocorrelation length, Z_S parameter, tortuosity, and fractal dimension, building on the seminal work of Shepard et al. (2001), Bretar et al. (2013), Labarre et al. (2017), and Labarre et al. (2019). Each of these parameters captures different aspects of roughness, such as vertical and horizontal variation, surface repetitiveness and scaling behavior. This framework has been applied to DEMs of the Asal-Ghoubbet Rift, as well as DEMs generated from ground photographs of the Apollo astronauts and a LROC DEM of the Apollo 17 landing site.

This analysis is crucial not only for characterizing the surface, but also for validating photometric roughness and BRDF simulations using ray-tracing methods. In addition, similar to the Hapke model parameter database, this study generates a database of roughness parameters corresponding to many types of surface. This database can also serve as a reference for future work, contributing to the characterization of planetary surfaces.

The Asal-Ghoubbet rift and the lunar surface present a variety of terrain types. Just as we have developed a preliminary database of Hapke model parameters, we anticipate that future research will explore even more varied terrain types, enriching the database of roughness parameters that we have established. In addition, we have yet to investigate the roughness parameters associated with the Shkuratov model, as well as those of scattering models using radar data and thermal models. The study of these models could offer entirely new perspectives and improve our understanding of surface roughness from a variety of viewpoints and methods.

- **BRDF simulation using ray-tracing model**

The final contribution of this thesis is the simulation of the BRDF using DEMs, spectral measurements and the results of the Hapke model inversion. We found that while spectral measurements mainly affect the intensity of the BRDF, they do not change its overall pattern. Surface roughness, on the other hand, affects both intensity and pattern in the Lambertian model, whereas it mainly affects intensity in the Hapke model. An interesting phenomenon observed in our simulations, particularly at an angle of incidence of 38°, was that the opposition effect tended to occur close to the direction of incidence, but not directly in that direction. This observation merits further investigation.

These simulations have improved our understanding of the effect of surface roughness on surface scattering. However, this work is incomplete. Due to time constraints, we have not been able to perform a sufficient number of tests to fully understand the inner workings of the DART ray-tracing model. Future simulations should explore different incidence angles, perform sensitivity analyses of the Hapke model and include atmospheric effects to refine the results. In addition, goniometer measurements have only been completed at three of the nineteen sites in

the Asal-Ghoubbet rift. Obtaining additional measurements would allow us to simulate more BRDF scenarios. In addition, DEMs have yet to be generated from the images of the soil samples collected. Producing micrometre scale DEMs from these images would allow us to further investigate the effect of roughness on BRDF at this particular scale.

Appendix

A) List of articles that use the Hapke model

We have compiled a list of articles that explicitly mention the version(s) of the Hapke model used, in chronological order. To begin with, we specify the meaning of the content in several columns about the elements of the model:

- For versions:
  - IMSA: Isotropic Multiple Scattering Approximation
  - AMSA: Anisotropic Multiple Scattering Approximation
- For phase function $p(g)$:
  - HG1, 2, 3: Henyey-Greenstein single/double/triple phase function
  - LP1, 2: Legendre polynomial single/double phase function
  - CS: Cornette and Shanks (1992) phase function
  - 1: Set to unity
- For other terms: Coherent backscattering opposition effect term B_{CBOE}, shadowing function S and porosity factor K
  - 0: Not included in the model / Not mentioned
  - 1: Implemented and included in the model
  - 2: Tested both cases – with and without the mentioned term

	Author(s)	Topic	Object of Interest	Version	$p(g)$	B_{CBOE}	S	K	Inversion method	Data/ Instruments
1	Pinty et al. (1989)	Model application	Mock + field data (plowed field)	IMSA	LP1	0	0	0		
2	Jacquemoud et al. (1992)	SOILSPECT - soil with humidity	Lab samples	IMSA	LP2	0	0	0	Simplex	
3	Lucey (1998)	Optical constant of Olivine and Pyroxene	Lab samples	IMSA	LP1	0	0	0		
4	Cord et al. (2005)	Photometric contribution	Lab samples	IMSA	HG2	0	1	0		
5	Soderblom et al. (2006)	Surface photometric function modelling	Mars	AMSA	HG1	0	0	0	Levenberg-Marquardt	Hubble Space Telescope WFPC2
6	Giuranna et al. (2007)	Properties of ice cap	Mars	AMSA	LP1	0	0	0		PFS - MEX
7	Gunderson et al. (2007)	Photometric signatures of liquid water	Lab samples		HG2	0	0	0		
8	Shepard and Helfenstein (2007)	Model testing	Lab samples	AMSA	HG2,3	1	0	0		
9	Schröder and Keller (2009)	Phase curve	Titan	AMSA	HG1	1	0	0	Levenberg-Marquardt	Descent Imager/Spectral Radiometer (Huygens)

10	Warell and Davidsson (2010)	Spectral analysis	Mercury	AMSA	HG1	0	1	0		NASA Infrared Telescope Facility (IRTF)
11	Wu et al. (2009)	Photometric properties	China desert	AMSA	HG2, LP1	0	1	0		
12	Bhattacharjee et al. (2011)	BRDF of pyroxenes	Lab samples	IMSA	HG1	0	0	0		
13	Kennelly et al. (2010)	Calibration, absolute lunar radiance	Moon	AMSA	HG2	1	1	0		Clementine
14	Leyrat et al. (2010)	Surface inhomogeneities	Steins	AMSA	HG1	1	1	0		Rosetta/OSIRIS
15	Miller et al. (2011)	Opposition surge	Phoebe	IMSA	HG1	1	1	0		New Mexico State University (NMSU) 1-m telescope
16	Cull et al. (2010)	Subsurface ice composition	Mars Phoenix landing site	IMSA	HG1	0	0.1	1	Least-square Grid-search/gradient-follower (GSGF)	Phoenix Surface Stereo Imager (SSI) on NASA's Mars Phoenix Lander
17	Helfenstein and Shepard (2011)	Model testing	Lab samples	AMSA	HG2	1	1	1		
18	Souchon et al. (2011)	Model study	Lab samples	IMSA	HG2	0	1	0	Genetic algorithm	
19	Žižka and Vokrouhlický (2011)	Solar radiation pressure	(99942) Apophis	IMSA	HG1	0	0	0		

20	Yang et al. (2011)	Soil water thickness	Earth	IMSA	SOILS PECT	0	0	0	Powell's method, Ant Colony Algorithm	Sentinel-2 MSI
21	Deb and Sen (2011)	Scattering intensity & particle size	Lab samples	IMSA	HG2	0	0	0		
22	Spjuth et al. (2012)	Disk-resolved photometry	(2867) Steins	AMSA	HG1, 2, 3	1	1	2	Levenberg-Marquartz	OSIRIS
23	Dalton III and Pitman (2012)	Retrieve optical constants	Lab sample (Hydrated sulfates)	IMSA	HG2	0	0	0		
24	Fernando et al. (2013)	Photometric properties	Mars	IMSA	HG2	0	1	0	Bayesian	CRISM/MRO
25	Johnson et al. (2013)	Spectrogoniometry and modeling	Lab samples	IMSA	HG1,2	0	0	0		
26	Jost et al. (2013)	Bidirectional reflectance of ice	Lab samples		HG1,2,3	0	0	0	Particle Swarm Optimization -> Levenberg-Marquadt	
27	Souchon et al. (2013)	Spectrophotometric properties	Moon	IMSA	HG2	0	1	0	Genetic algorithm	AMIE (SMART-1) & M3 (Chandrayaan-1)
28	Xu et al. (2013)	Modeling polarized radiative transfer	Titan	AMSA	HG1	1	0	0		
29	Pommerol et al. (2013)	Photometric properties	Mars soil analogs (dry, wet, icy)	IMSA	HG2	0	1	0	Particle Swarm Optimization -> Levenberg-Marquadt	

30	Li et al. (2013)	Spectroscopy	Asteroid (4) Vesta	IMSA	HG1	0	1	0		Dawn Framing Camera
31	Ciarniello et al. (2014)	Model testing		IMSA, AMSA	HG2	1	1	0		LROC NAC
32	Clegg et al. (2014)	Photometric properties of blast zones	Moon	IMSA	HG2	1	1	0		
33	Grumpe et al. (2014)	DEM construction - photoclinometry	Moon	AMSA	HG2, CS	1	0	0		
34	Lemelin et al. (2013)	Mineral mapping	Moon	IMSA	LP1	0	0	0		LROC, Clementine
35	Sato et al. (2014)	Hapke parameter map	Moon	IMSA	HG2	0	1	1	Levenberg-Marquardt	LROC WAC
36	Wöhler et al. (2014)	Topographic, photometric and spectral analysis	Moon	AMSA	HG2	0	1	0	Levenberg-Marquardt	M3
37	Wong et al. (2014)	Reflectance Modelling	Moon	AMSA	HG2	0	1	0		Chang'E-1 IIM
38	Bachmann et al. (2014)	Investigate phase angle dependence, density effects	Lab sample (sand)	IMSA	HG2	0	1	0		
39	Carli et al. (2014)	Optical const, mineralogy, particle size distribution	Lab sample (plagioclase-mafic mixture)	IMSA	HG2	0	1	0		Spectrometer + goniometer at IAPS-INAF
40	Ciarniello, M. et al. (2015)	Photometric properties	67P	IMSA	HG2	0	1	0		VIRTIS-M onboard Rosetta
41	Feaga et al. (2015)	Geomorphology + photospectrometry	67P	IMSA	HG2	0	1	0		Rosetta Alice

42	Fornasier et al. (2015)	Spectrophotometric properties	67P	IMSA	HG2	0	1	0		Rosetta-OSIRIS
XX	Jin et al. (2015)	Photometric properties	Moon	IMSA	HG2	1	1	1		
43	La Forgia et al. (2015)	Geomorphology and spectrophotometry	67P	IMSA	HG2	0	1	0		Rosetta Philae
44	Masoumzadeh et al. (2015)	Photometric analysis	Lutetia	IMSA	HG2	0	1	0	Simplex	Rosetta-OSIRIS
45	Reddy et al. (2015)	Photometric properties	Ceres	IMSA	HG2	0	1	0		Dawn Framing Camera
46	Schmidt and Fernando (2015)	Uncertainties on Hapke model parameters		IMSA	HG2	0	1	0	Bayesian	
47	Sun et al. (2015)	BRDF model assessment	Lab samples	AMSA	HG2	0	1	0	Gauss–Newton or Levenberg – Marquardt	
48	Fernando et al. (2015)	Physical properties map	Mars	IMSA	HG2	0	1	0	Bayesian	CRISM
49	Clegg-Watkins et al. (2016)	Photometric characterization	Moon	IMSA	HG2	0	1	0	Simplex (Generalized Reduced Gradient Algorithm)	LROC NAC
50	Carvano and Davalos (2015)	Classification of asteroids		AMSA	HG2	0	1	0		Sloan Digital Sky Survey (SDSS)
121	Domingue et al. (2016a)	Disk-resolved measurement	Mercury	IMSA	HG2	1	1	1		MESSENGER

122	Domingue et al. (2016b)	Regional spectrophotometric properties	951 Gaspra	IMSA	HG2, LP1	0	1	0		Galileo Solid State Imager
51	Feller et al. (2016)	Spectrophotometric properties	67P	IMSA	HG2	1	1.1	1.2	L-BFGS-B	Rosetta-OSIRIS
52	Fernando et al. (2016)	Surface microtexture, geological processes characterization	Mars	IMSA	HG2	0	1	0	Bayesian	CRISM
53	Hasselmann et al. (2016)	Disk-resolved photometric analysis	Lutetia	IMSA	HG2	1	1	1	L-BFGS-B (in Scipy)	Rosetta-OSIRIS
54	Pilorget et al. (2016)	Grain-scale physical and compositional properties	Lab samples	IMSA	HG2	0	0	0	Bayesian	
55	Sun et al. (2016)	Effect of particle size	Lab samples	IMSA	LP2	0	0	0	Isqnonlin (MATLAB)	
56	Kar et al. (2016)	Photometry, porosity	Lab sample (regolith analoges)	IMSA	HG1	0	0	1		Miniature goniometer
57	Bachmann et al. (2017)	Field+Lab comparison	Lab samples	IMSA	HG2	1	0	1	Simplex, LM	
58	Ciarniello et al. (2017)	Photometric correction	Ceres	IMSA	HG2	0	1	0		VIR imaging spectrometer (Dawn)
59	Labarre et al. (2017)	Surface roughness retrieval	Djibuti	AMSA	HG2	1	1	1	Bayesian	
60	Lapotre et al. (2017)	Compositional analysis	Lab samples	IMSA	1	0	0	0	Bayesian	

61	Protopapa et al. (2017)	Global surface composition	Pluto	IMSA	HG1	0	1	0	Levenberg-Marquardt	New Horizons
62	Schröder et al. (2017)	Spectrophotometric properties	Ceres	AMSA	HG2	1	1	0	Levenberg-Marquardt	Dawn Framing Camera
63	Davalos et al. (2017)	Optical constant	Lab sample (meteorites)	IMSA	HG2	0	0	1		
64	Wang et al. (2017)	Submicroscopic metallic iron	Moon	IMSA	LP	0	0	0		Chang'E-3 Yutu
65	Eon et al. (2018)	Retrieval of Sediment Fill Factor	California	IMSA	1	1	0	0	Simplex	
66	Schröder, Stefan E. et al. (2018)	Opposition effect	Ceres	IMSA	HG2	0	1	0	Levenberg-Marquardt	Dawn Framing Camera
67	Tatsumi et al. (2018)	Disk-integrated photometry	25143 Itokawa	IMSA	HG2	2	1	2		AMICA/Hayabusa
68	Raut et al. (2018)	Far-Ultraviolet Photometric Response	Apollo Soil 10084 (A11)	IMSA	HG2	0	0	1		SwURC
123	Domingue et al. (2019a)	Photometric standardization	Mercury	IMSA	HG2	0	1	0		MESSENGER MASCS
124	Domingue et al. (2019b)	Photometric variability	Mercury	IMSA	HG2	0	1	0		MESSENGER MASCS
69	Labarre et al. (2019)	Surface roughness retrieval - ground truth	Asal-Ghoubbet rift	AMSA	HG2	0	1	1	Bayesian	Drone, field goniometer, handheld camera
70	Li et al. (2019)	Spectrophotometric modeling and mapping	Ceres	IMSA	HG1,2	0	1	0		Dawn Framing Camera

71	Schmidt and Bourguignon (2019)	Efficiency of BRDF sampling		IMSA	HG2	0	1	0	Bayesian	
72	Ciarniello et al. (2019)	Mineralogy, composition	Saturn's main rings	IMSA	HG1	0	0	0		VIMS - Cassini
73	Lin et al. (2019)	Hydrated minerals spectroscopy	Mars	IMSA	1	0	0	0		CRISM (MRO)
74	Foote et al. (2020)	Bidirectional and directional hemispheric reflectance	Moon + Lab samples	IMSA	HG2	0	1	0		Diviner (LRO)
XX	Gou et al. (2020)	Space weathering	Moon	IMSA	LP1	0	0	0		Chang'E-4 VNIS
75	Protopapa et al. (2020)	Photometric properties	Pluto	IMSA	HG2	0	1	0	Levenberg-Marquartz	MVIC (New Horizon)
76	Tenthoff et al. (2020)	High-res DTM by photoclinometry	Mercury	AMSA	HG2	0	1	0	Levenberg-Marquardt	MESSENGER
77	Xu et al. (2020)	Photometric Correction	Moon	IMSA	HG2	0	0	0	MPFIT-Robust	IIM (Chang'E 1)
78	Zeeshan and Sayyad (2020)	Spectra modeling	Moon	IMSA	LP2	0	0	0		Chandrayaan-1
79	Belgacem et al. (2020)	Regional study of Europa's photometry	Europa	IMSA	HG2	0	1	0	Bayesian	Voyager's Imaging Science System and New Horizons' LOng Range Reconnaissance Imager

80	Eon et al. (2020)	Retrieval of Sediment Filling Factor		IMSA	HG3	0	0	1	Simplex	GRIT-T goniometer + NASA G-LiHT
81	Foote et al. (2020)	Bolometric hemispheric reflectance	Lab and Diviner (IR)	IMSA	HG2	0	1	0		Bloomsburg University Goniometer (BUG)
82	Liang et al. (2020)	Spectrophotometry	Mars (Gale crater)	IMSA	HG1,2	0	1	0		Mars Hand Lens Imager goniometer of Mars Science Laboratory (MSL) rover
83	Zhang et al. (2020)	Soil moisture content	Earth	IMSA		0	0	0		Field goniometer
84	Belgacem et al. (2021)	Regional photometry	Ganymede	IMSA	HG2	0	1	0	Bayesian	Voyager's Imaging Science System and New Horizons' LOng Range Reconnaissance Imager
85	Gao et al. (2021)	Tidal flat -> Soil moisture content	Earth	IMSA	LP2	0	0	0	Particle Swarm Optimization	OSIRIS-REx Camera Suite (OCAMS)

86	Golish et al. (2021)	Photometric modeling	Bennu	IMSA	HG1,2	0	1	0		OSIRIS-REx Camera Suite (OCAMS)
87	Hess et al. (2021)	Darkening agents	Moon	IMSA	HG2	1	0	0	Bayesian	
88	Li et al. (2021)	Photometric modeling and mapping	Bennu	IMSA	HG1	0	1	0.1	Levenberg-Marquartz	OSIRIS-Rex
89	Pilorget and Fernando (2021)	Mineral abundances	Mars	IMSA	HG2	0	1	0	Bayesian	
90	Zhou et al. (2021)	Photometric Parameters of Minerals	Lab samples	IMSA	LP1	0	0	0	Bayesian	
91	Valantinas et al. (2021)	Multi-angular observations of slope streaks	Mars	IMSA	1	0	0	0		CaSSIS (TGO)
92	Fayolle et al. (2021)	Spectra comparison, Retrieve optical constants	New Horizon, lab sample (tholins)	IMSA	1	1	0	1	Least-square	SHADOW at IPAG
93	Kar et al. (2021)	Photometry, porosity, particle sizes	Lab sample (regolith analoges)	IMSA	HG1	0	0	1		Miniature goniometer
94	Merlin, F. et al. (2021)	Composition and particle size	Meteorite mixtures (Bennu analog)	IMSA	1	0	0	0		
125	Mishra et al. (2021b)	Bayesian analysis	Europa	IMSA	HG2	0	0	1		Juno's near-IR spectrometer JIRAM

126	Mishra et al. (2021a)	Bayesian analysis	Europa	IMSA	HG2	0	0	1		Galileo Near Infrared Mapping Spectrometer (NIMS)
95	Sun and Lucey (2021)	Unmixing Mineral Abundance	Lab sample	IMSA	LP	0	0	1		
96	Ye et al. (2021)	VIS/NIR and MIR Optical Constants	Lab samples (Gypsum and Bassanite)	IMSA	LP	0	0	0		
97	Ding et al. (2022)	Soil characteristics	Field + Lab	IMSA	HG2, LP2	0	0	0		
98	Zhou et al. (2022)	Simulated Spectral Databases	Moon	AMSA	LP1	0	0	0		
99	Xu, T. Y. et al. (2022)	Rover Spectrophotometry	Moon	AMSA	HG2	1	1	1	Bayesian	PCAM (Chang'E 3)
100	Buratti et al. (2022)	Observations and Modeling of the Opposition Surges	Icy Moons of Saturn	IMSA	HG1	1	1	1		VIMS - Cassini
101	Chen et al. (2022)	Mineralogical properties of regolith	Moon (SPA)	IMSA	HG2	0	0	1		VNIS (Yutu 2 - Chang'E 4)
102	Gimar et al. (2022)	Spectra comparison	Lab sample (Lunar simulants, A11 sample)	IMSA	HG2	0	0	1	Levenberg-Marquardt	Southwest Ultraviolet Reflectance Chamber (SwURC)
103	Hess et al. (2022)	DEM construction, SfS, Atm correction	Mars	AMSA	HG2	0	0	0		CTX, HiRISE of MRO

104	Humes et al. (2022)	Spectroscopy	Jupiter Trojan asteroids	IMSA	1	0	0	0		Hubble Space Telescope
105	Johnson et al. (2022)	Spectro-photometric properties	Mars	IMSA	HG1,2	0	1	0		Mastcam and Navcam of Curiosity rover
106	Lowry et al. (2022)	Thermal Infrared Spectroscopy	Trojan Asteroids and (944) Hidalgo	IMSA	1	0	0	0		
107	Pascuzzo et al. (2022)	Martian water ice	Mars	IMSA	LP	0	0	1		FRT-CRISM
108	Rucks et al. (2022)	VIS-MIR optical constant	Lab samples (Orthopyroxenes)	IMSA	LP	0	0	1		
109	Sadrian et al. (2022)	Reflectance spectroscopy		IMSA	1	0	0	0	MATLAB fzero	
110	Sun and Lucey (2022)	Near-infrared spectroscopy		IMSA	LP, HG2	0	0	0		Yutu-2 rover, Kaguya Multiband Imager
111	Verbiscer et al. (2022)	Spectroscopy	Dwarf Planets and Large KBOs	IMSA	HG2	1	1	1		New Horizon LORRI
112	Wise and Mars (2022)	Spectroscopy	Lab samples	IMSA	HG1	0	0	0	Levenberg-Marquardt	Portable VNIR/SWIR Field Spec Pro spectrometer + a goniometer
113	Wohlfarth and Wöhler (2022)	Spectroscopy	Mercury	AMSA	HG2	0	1	0	Levenberg-Marquardt	Telescope

114	Angrisani et al. (2023)	Spectral properties	V-type asteroid	IMSA	1	0	0	0		NASA Infrared Telescope Facility (IRTF)
115	Marshal et al. (2023)	Photometry	Moon	AMSA	HG2	0	1	0		LROC NAC
116	Munaretto et al. (2023)	Spectrophotometric properties	Mercury	IMSA	HG2	0	1	0		MESSENGER/ MDIS observations (WAC, MASCS-VIRS)
117	Nagori et al. (2023)	Photometric parameters	Moon (A11,12,14,16,17)	IMSA	HG1	0	0	0		TMC (Chandrayaan - 1/2) + BUG Observation
118	Shiltz and Bachmann (2023)	Alternative to Hapke's macroscopic roughness correction	Lab sample	IMSA	HG2	0	1	0		Spectro-gonio-radiometer
119	Sun et al. (2022)	Spectral Unmixing of Hyperspectral Imagery		IMSA	1	0	0	0		
120	Zhuang et al. (2023)	Visible and near-infrared reflectance spectra	Lab sample (igneous rock and powder)		LP	0	0	0		

121	Sheng et al. (2024)	Soil aggregate size	Lab sample (cultivated soil)	IMSA	HG2	0	1	1	Bayesian inversion with MCMC	Northeast Normal University Laboratory Goniospectrometer System (NENULGS)

B) List of samples from CAROLiNA project

(a)

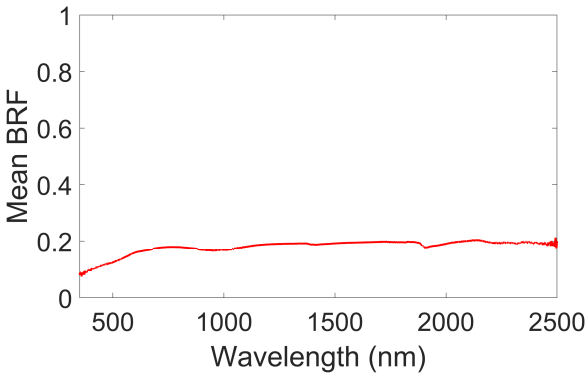

(b)

Figure 103 – Sample A : Anorthite, Diopside, Hématite et Smectite. a) Sample image; b) Spectra measurement with ASD

(a)

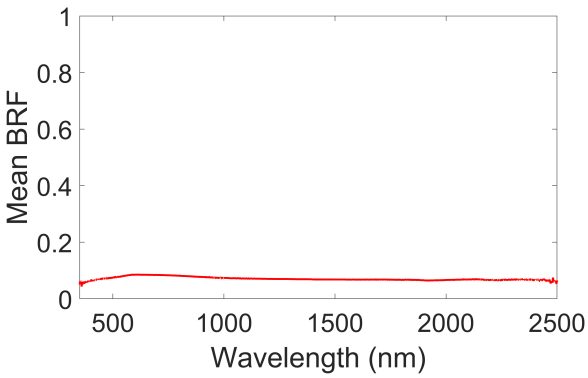

(b)

Figure 104 – Sample B. a) Sample image; b) Spectra measurement with ASD

(a)

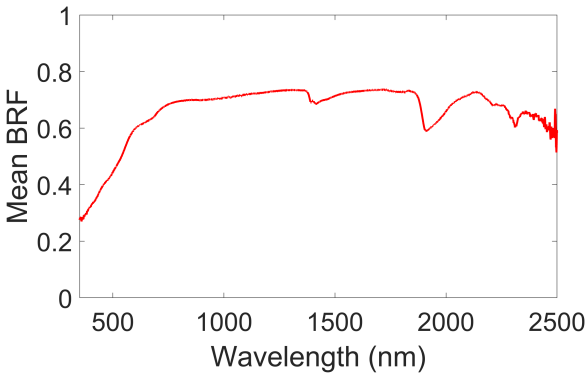

(b)

Figure 105 – Sample C1: Calcite, a little quartz, Feldspath (plagioclase), Palygorskite désordonnée, Talc ? and Smectite. a) Sample image; b) Spectra measurement with ASD

(a)

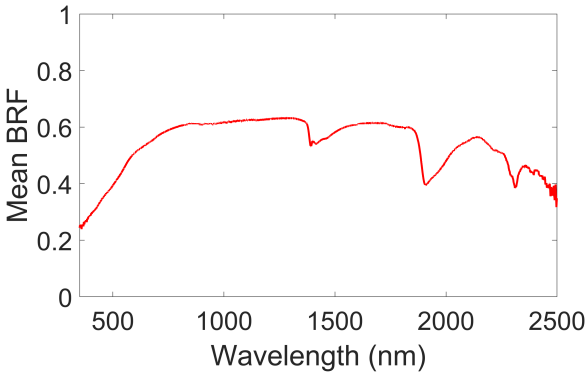

(b)

Figure 106 – Sample C2: Calcite, a little quartz, Feldspath (plagioclase), Palygorskite désordonnée, Talc ? and Smectite. a) Sample image; b) Spectra measurement with ASD

(a)

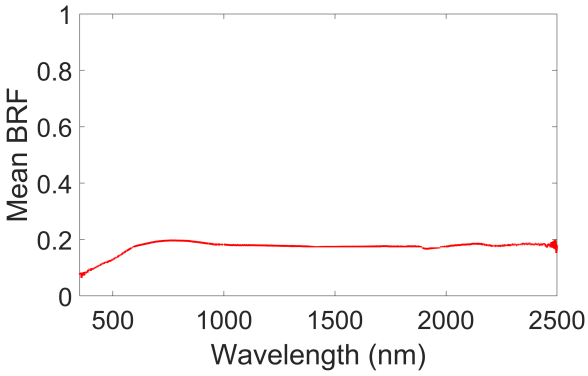

(b)

Figure 107 – Sample D: Diopside, Anorthite and Smectite. a) Sample image; b) Spectra measurement with ASD

(a)

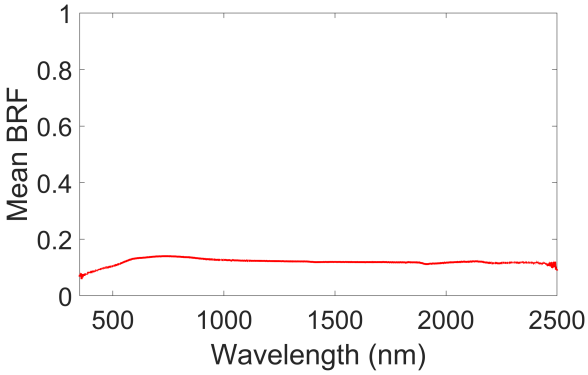

(b)

Figure 108 – Sample E1: Quartz, Calcite, Albite, Amphibole, disordered Palygorskite, trace of Talc and Smectite. a) Sample image; b) Spectra measurement with ASD

(a)

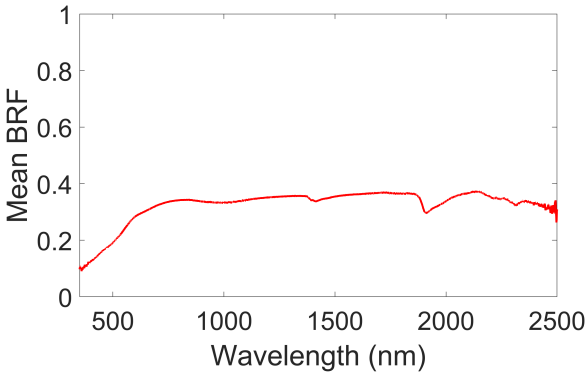

(b)

Figure 109 – Sample E2: Anorthite, Calcite, Amphibole, Quartz, Augite. Clay phase at 7Å, and Smectite, traces of Talc?. a) Sample image; b) Spectra measurement with ASD

(a)

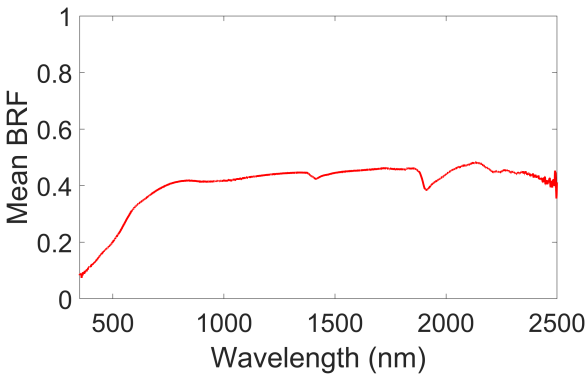

(b)

Figure 110 – Sample F: Calcite, Quartz, Albite, Zeolithe, disordered Palygorskite and Smectite, Talc. a) Sample image; b) Spectra measurement with ASD

(a)

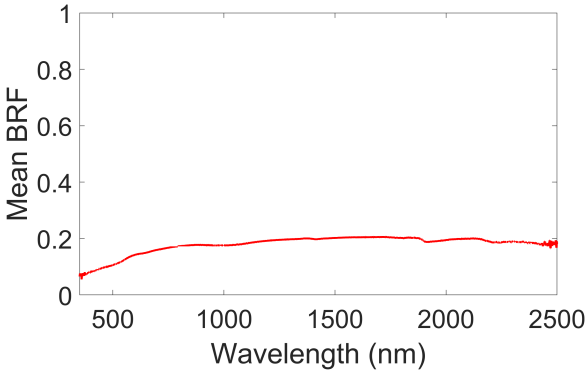

(b)

Figure 111 – Sample G. a) Sample image; b) Spectra measurement with ASD

(a)

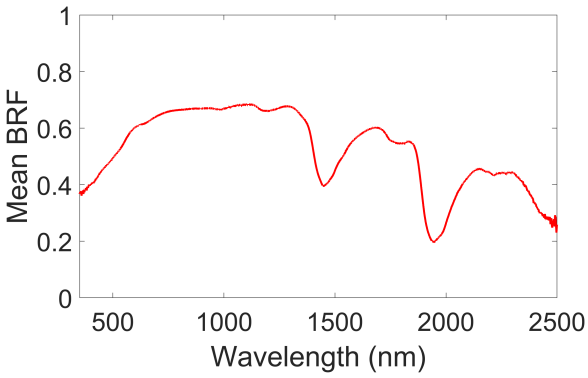

(b)

Figure 112 – Sample H1: Halite, Barium, Gypsum. a) Sample image; b) Spectra measurement with ASD

(a)

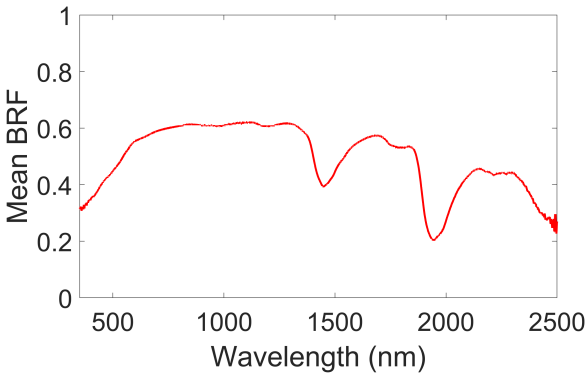

(b)

Figure 113 – Sample H2: Halite, Barium, Gypsum. a) Sample image; b) Spectra measurement with ASD

(a)

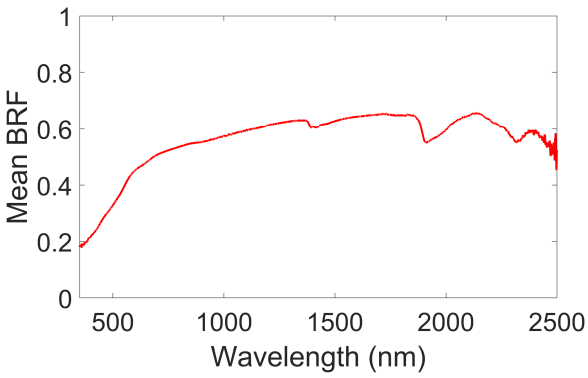

(b)

Figure 114 – Sample I11. a) Sample image; b) Spectra measurement with ASD

(a)

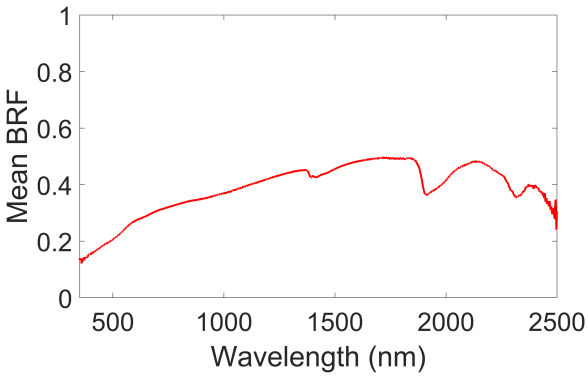

(b)

Figure 115 – Sample I12. a) Sample image; b) Spectra measurement with ASD

(a)

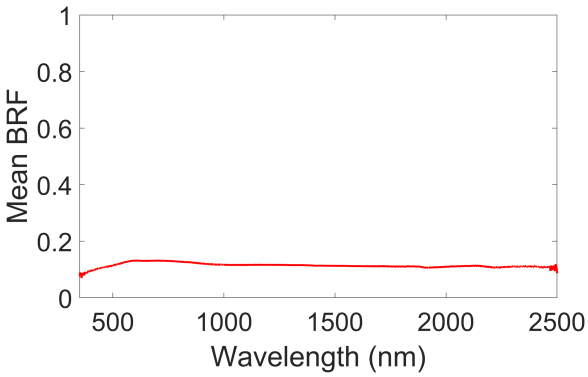

(b)

Figure 116 – Sample I2. a) Sample image; b) Spectra measurement with ASD

(a)

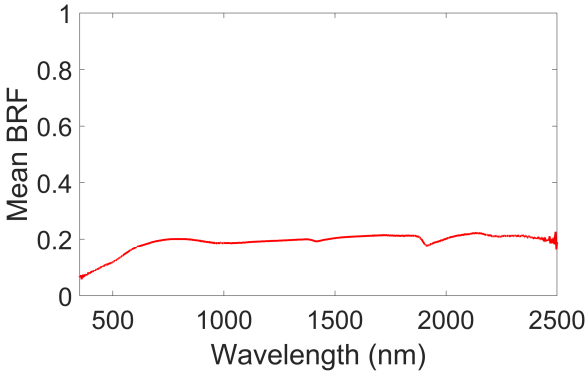

(b)

Figure 117 – Sample K: Diopside, Anorthite and traces of Smectite. a) Sample image; b) Spectra measurement with ASD

(a)

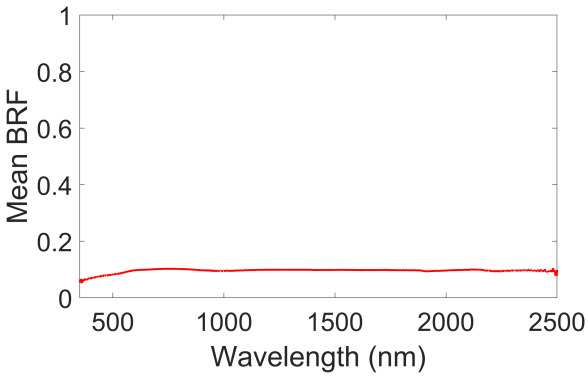

(b)

Figure 118 – Sample M: Diopside or Hedenburgite, Anorthite, Chlorite and Smectite, traces of Palygorskite , Mica?. a) Sample image; b) Spectra measurement with ASD

(a)

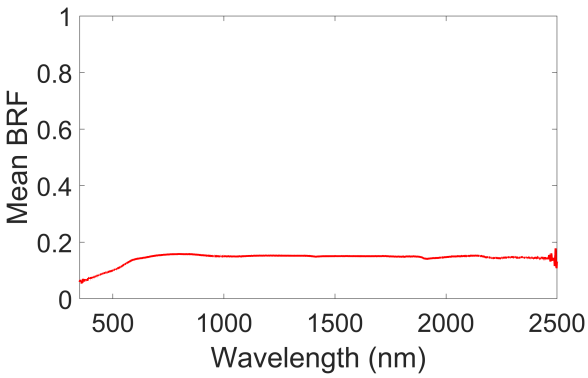

(b)

Figure 119 – Sample N1: Diopside, Anorthite, Amphibole, Chlorite and Smectite, trace of Talc ?. a) Sample image; b) Spectra measurement with ASD

(a)

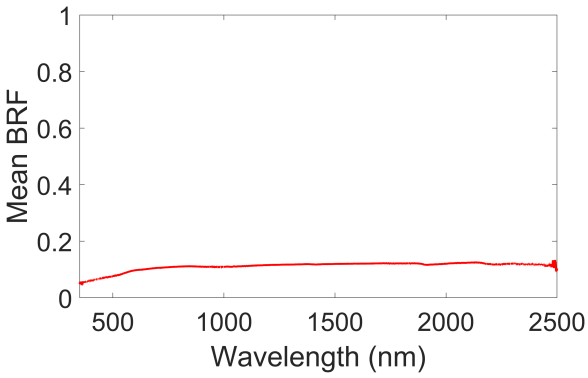

(b)

Figure 120 – Sample N2: Diopside, Anorthite, Amphibole, Chlorite and Smectite, trace of Talc ?. a) Sample image; b) Spectra measurement with ASD

(a)

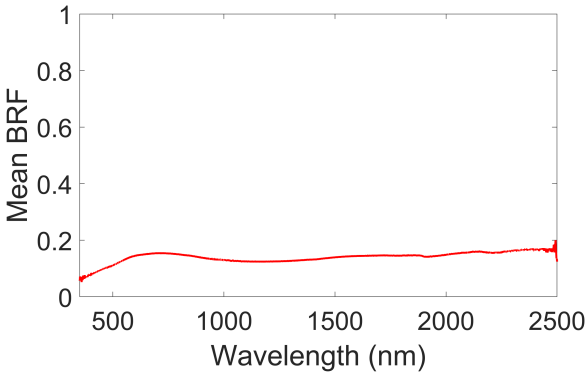

(b)

Figure 121 – Sample O: Anorthite, Diopside and Smectite. a) Sample image; b) Spectra measurement with ASD

(a)

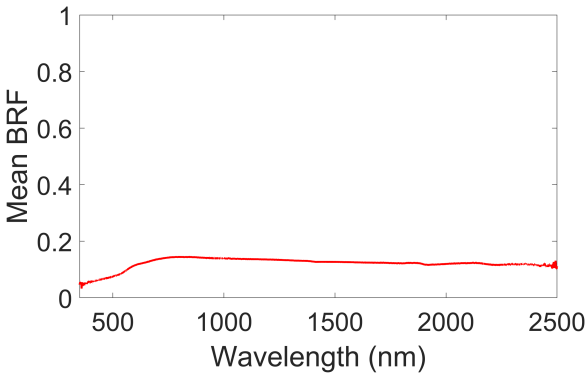

(b)

Figure 122 – Sample P. a) Sample image; b) Spectra measurement with ASD

(a)

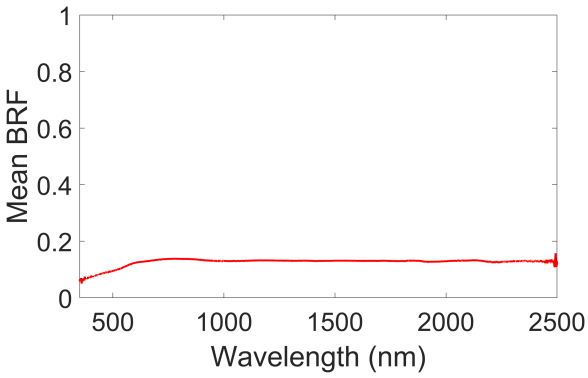

(b)

Figure 123 – Sample Q: Diopside and Smectite. a) Sample image; b) Spectra measurement with ASD

(a)

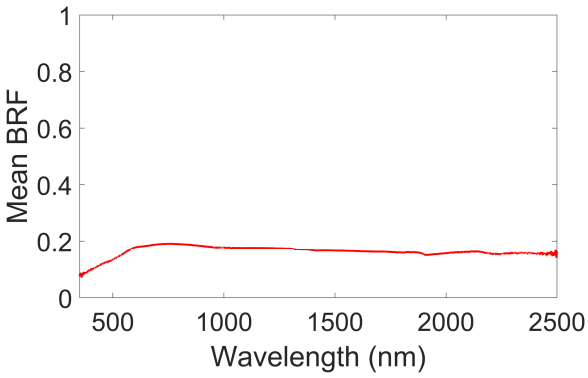

(b)

Figure 124 – Sample R1: Bytownite, Anorthite and Vermiculite to be confirmed on oriented slide, 1 unidentified peak at 5.58Å, traces of disordered Palygorskite. a) Sample image; b) Spectra measurement with ASD

(a)

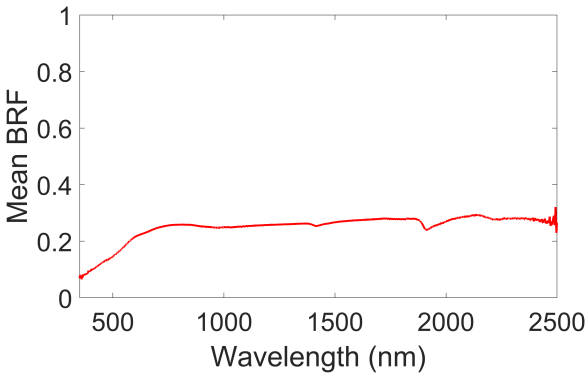

(b)

Figure 125 – Sample R2: Bytownite, Anorthite and Vermiculite to be confirmed on oriented slide, 1 unidentified peak at 5.58Å, traces of disordered Palygorskite. a) Sample image; b) Spectra measurement with ASD

(a)

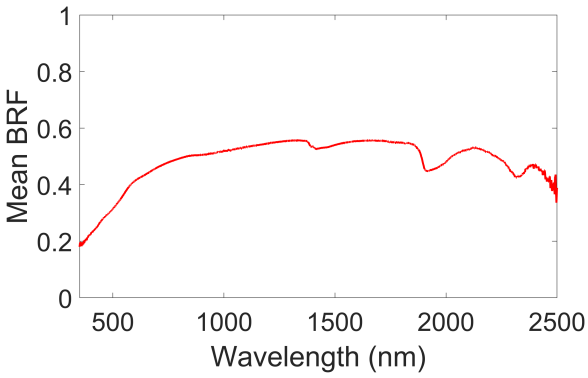

(b)

Figure 126 – Sample T1: Calcite, Muscovite or Calcite Mg, Quartz, disordered Palygorskite, Smectite. a) Sample image; b) Spectra measurement with ASD

(a)

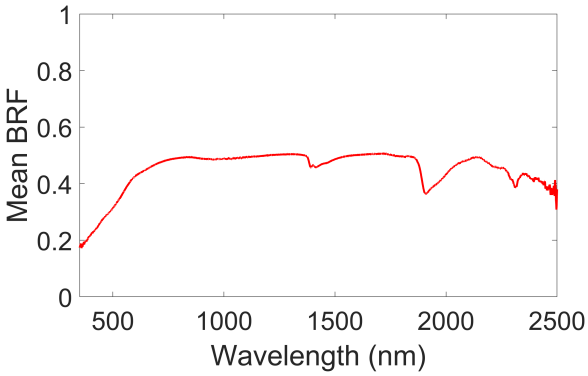

(b)

Figure 127 – Sample T2: Calcite, Muscovite or Calcite Mg, Quartz, disordered Palygorskite, Smectite. a) Sample image; b) Spectra measurement with ASD

(a)

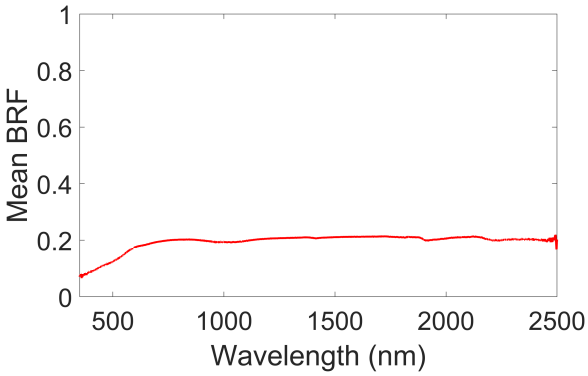

(b)

Figure 128 – Sample U. a) Sample image; b) Spectra measurement with ASD

(a)

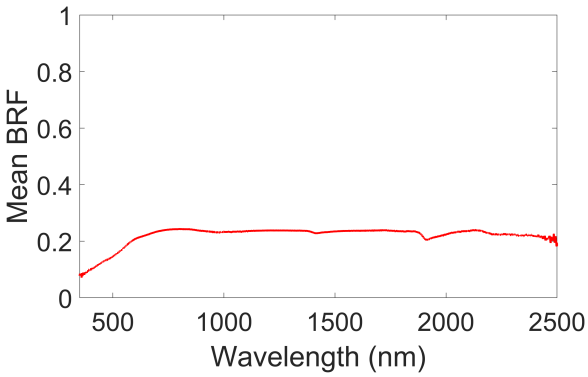

(b)

Figure 129 – Sample V1: Diopside, Anorthite (Anorthoclase), Calcite, Smectite, traces of disordered Palygorskite, 1 unidentified phase. a) Sample image; b) Spectra measurement with ASD

(a)

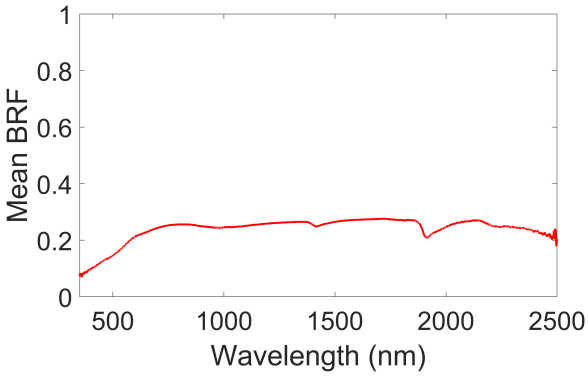

(b)

Figure 130 – Sample V2: Anorthite, Hedenbergite, Anorthoclase, Smectite/Chlorite to be specified, traces of disordered Palygorskite. a) Sample image; b) Spectra measurement with ASD

(a)

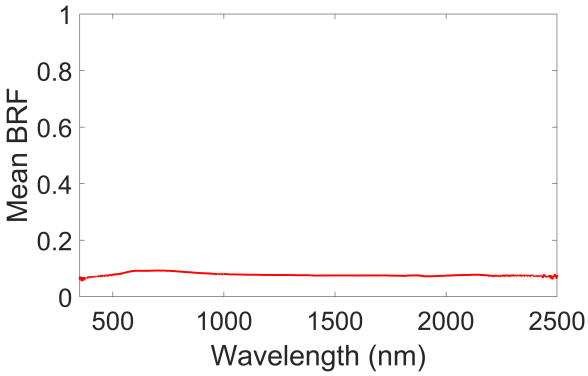

(b)

Figure 131 – Sample X1: Anorthite, Diopside, and Smectite. a) Sample image; b) Spectra measurement with ASD

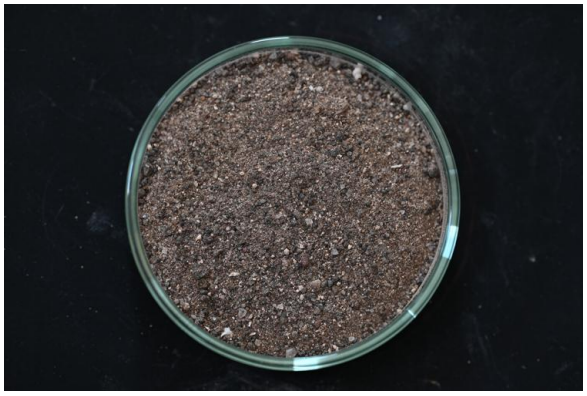

(a)

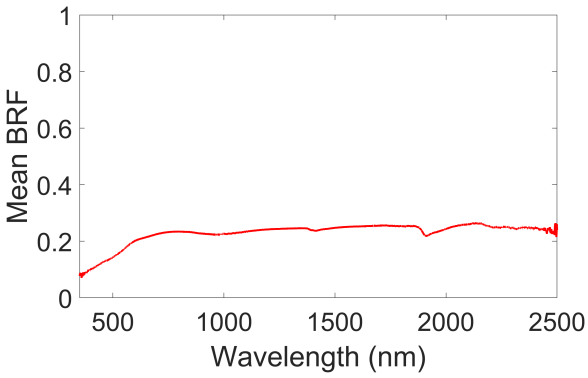

(b)

Figure 132 – Sample X2: Anorthite, Quartz, Augite, Zeolite, Smectite, disordered Palygorskite, trace of Talc, 2 unidentified peaks. a) Sample image; b) Spectra measurement with ASD

(a)

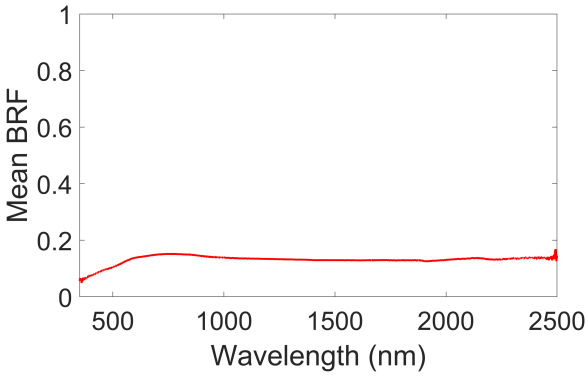

(b)

Figure 133 – Sample Y1: Anorthite, Diopside and Smectite. a) Sample image; b) Spectra measurement with ASD

(a)

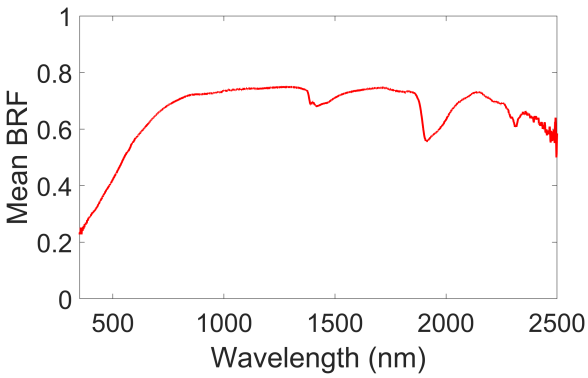

(b)

Figure 134 – Sample Y2:Calcite, Halite, Anorthite and Calcite Mg, disordered Palygorskite. a) Sample image; b) Spectra measurement with ASD

Bibliography

Akimov, L. (1975). Influence of mesorelief on the brightness distribution over a planetary disk. *Sov. Astron. AJ (Engl. Transl.), v. 19, no. 3, pp. 385-388*. Link.

Akimov, L. (1988). Light reflection by the Moon. i. *Kinematika i Fizika Nebesnykh Tel*, 4:3–10. Link.

Alsadik, B. and Abdulateef, N. A. (2022). Epipolar geometry between photogrammetry and computer vision – a computational guide. *ISPRS Annals of the Photogrammetry, Remote Sensing and Spatial Information Sciences*, V-5-2022:25–32. doi: 10.5194/isprs-annals-V-5-2022-25-2022.

Angrisani, M., Palomba, E., Longobardo, A., Raponi, A., Dirri, F., and Gisellu, C. (2023). A new prospect to analyse the spectral properties of v-type asteroids. *Icarus*, 390:115320. doi: 10.1016/j.icarus.2022.115320.

Apostol, T. (1973). *Mathematical Analysis*. Pearson (2nd edition).

Arab-Sedze, M. (2013). *Complémentarité des systèmes Radar en bande L et LiDAR pour l'étude des terrains volcaniques - Cas du Piton de le Fournaise (Ile de La Réunion)*. PhD thesis. Spécialité Sciences de la Terre, de l'environnement et des planètes, Institut de Physique du Globe de Paris. url: https://www.ipgp.fr/%7Ejacquemoud/publications/these_Sedze_2013.pdf.

Arfken, G. B., Weber, H. J., and Harris, F. E. (2012). *Mathematical Methods for Physicists: A Comprehensive Guide*. Academic Press, 7th edition. doi: 10.1016/C2009-0-30629-7.

Ashwal, L. D. (2021). Anorthosites. In Alderton, D. and Elias, S. A., editors, *Encyclopedia of Geology (Second Edition)*, pages 130–144. Academic Press, Oxford, second edition edition. doi: 10.1016/B978-0-12-409548-9.12461-3.

Aster, R. C., Borchers, B., and Thurber, C. H. (2013). *Parameter Estimation and Inverse Problems*. Elsevier. doi: 10.1016/C2009-0-61134-X.

Bachmann, C., Eon, R., Ambeau, B., Harms, J., Badura, G., and Griffo, C. (2017). Modeling and intercomparison of field and laboratory hyperspectral goniometer measurements with G-LiHT imagery of the Algodones Dunes. *Journal of Applied Remote Sensing*, 12:1. doi: 10.1117/1.JRS.12.012005.

Bachmann, C. M., Philpot, W., Abelev, A., and Korwan, D. (2014). Phase angle dependence of sand density observable in hyperspectral reflectance. *Remote Sensing of Environment*, 150:53–65. doi: 10.1016/j.rse.2014.03.024.

Bandfield, J. L., Hayne, P. O., Williams, J.-P., Greenhagen, B. T., and Paige, D. A. (2015). Lunar surface roughness derived from LRO Diviner radiometer observations. *Icarus*, 248:357–372. doi: 10.1016/j.icarus.2014.11.009.

Barker, M., Chabot, N., Mazarico, E., Siegler, M., Martinez-Camacho, J., Hamill, C., and Bertone, S. (2022). New constraints on the volatile deposit in Mercury's north polar crater, Prokofiev. *The Planetary Science Journal*, 3:188. doi: 10.3847/PSJ/ac7d5a.

Belgacem, I., Schmidt, F., and Jonniaux, G. (2020). Regional study of Europa's photometry. *Icarus*, 338:113525. doi: 10.1016/j.icarus.2019.113525.

Belgacem, I., Schmidt, F., and Jonniaux, G. (2021). Regional study of Ganymede's photometry. *Icarus*, 369:114631. doi: 10.1016/j.icarus.2021.114631.

Bertuzzi, P., Rauws, G., and Courault, D. (1990). Testing roughness indices to estimate soil surface roughness changes due to simulated rainfall. *Soil and Tillage Research*, 17(1):87–99. doi: 10.1016/0167-1987(90)90008-2.

Besl, P. and McKay, N. D. (1992). A method for registration of 3-D shapes. *IEEE Transactions on Pattern Analysis and Machine Intelligence*, 14(2):239–256. doi: 10.1109/34.121791.

Betancourt, M. (2018). A conceptual introduction to Hamiltonian Monte Carlo. Link.

Bhattacharjee, C., Deb, D., Das, H. S., Sen, A. K., and Gupta, R. (2011). Modelling laboratory data of bidirectional reflectance of a regolith surface containing alumina. *Publications of the Astronomical Society of Australia*, 28(3):261–265. doi: 10.1071/as10025.

Blaes, X. and Defourny, P. (2008). Characterizing bidimensional roughness of agricultural soil surfaces for SAR modeling. *IEEE Transactions on Geoscience and Remote Sensing*, 46(12):4050–4061. doi: 10.1109/TGRS.2008.2002769.

Bland, M. T., Kirk, R. L., Galuszka, D. M., Mayer, D. P., Beyer, R. A., and Fergason, R. L. (2021). How well do we know Europa's topography? An evaluation of the variability in Digital Terrain Models of Europa. *Remote Sensing*, 13(24). doi: 10.3390/rs13245097.

Bonnefoy, L. E., Lucas, A., Hayes, A. G., Rodriguez, S., Poggiali, V., Lalich, D. E., Lorenz, R. D., and Gall, A. L. (2022). Composition, roughness, and topography from radar backscatter at Selk Crater, the Dragonfly landing site. *The Planetary Science Journal*, 3(8):201. doi: 10.3847/PSJ/ac8428.

Borman, S. (2004). The Expectation Maximization algorithm: A short tutorial. Link.

Bretar, F., Arab-Sedze, M., Champion, J., Pierrot-Deseilligny, M., Heggy, E., and Jacquemoud, S. (2013). An advanced photogrammetric method to measure surface roughness: Application to volcanic terrains in the Piton de la Fournaise, Reunion Island. *Remote Sensing of Environment*, 135:1–11. doi: 10.1016/j.rse.2013.03.026.

Brooks, S., Gelman, A., Jones, G., and Meng, X.-L. (2011). *Handbook of Markov Chain Monte Carlo*. Chapman and Hall/CRC. doi: 10.1201/b10905.

Brožová, N., Baggio, T., D'Agostino, V., Bühler, Y., and Bebi, P. (2021). Multiscale analysis of surface roughness for the improvement of natural hazard modelling. *Natural Hazards and Earth System Sciences*, 21(11):3539–3562. doi: 10.5194/nhess-21-3539-2021.

Brummelen, G. V. (2013). *Heavenly Mathematics: The Forgotten Art of Spherical Trigonometry*. Princeton University Press. Link.

Buratti, B. J., Hillier, J. H., Dalba, P. A., Hicks, M. D., Mosher, J. A., Hendrix, A. R., Abramson, L., and Akhter, N. (2022). Observations and modeling of the opposition surges of the icy moons of Saturn based on Cassini visual infrared mapping spectrometer data. *The Planetary Science Journal*, 3(8):200. doi: 10.3847/PSJ/ac867e.

Cai, Y. and Fa, W. (2020). Meter-scale topographic roughness of the Moon: The effect of small impact craters. *Journal of Geophysical Research: Planets*, 125(8):e2020JE006429. doi: 10.1029/2020JE006429.

Calvetti, D. and Somersalo, E. (2007). *An Introduction to Bayesian Scientific Computing*. Springer New York, NY. doi: 10.1007/978-0-387-73394-4.

Campbell, H., Hess, P., and Rutherford, M. (1978). Ilmenite crystallization in non-mare basalts. In *Presentation at Lunar and Planetary Science Conference 9th, Houston*, volume 1, pages 149–151. Pergamon Press, Inc. Link.

Cao, W., Cai, Z., and Ye, B. (2018). Measuring multiresolution surface roughness using v-system. *IEEE Transactions on Geoscience and Remote Sensing*, 56(3):1497–1506. doi: 10.1109/TGRS.2017.2764519.

Cao, W., Meng, Z., Dong, X., Lei, J., Xie, M., Yang, J., and Cai, Z. (2021). Reunderstanding geomorphological features in Chang'E-5 sampling region based on multiscale roughness model. *IEEE Journal of Selected Topics in Applied Earth Observations and Remote Sensing*, 14:9106–9116. doi: 10.1109/JSTARS.2021.3110731.

Carli, C., Ciarniello, M., Capaccioni, F., Serventi, G., and Sgavetti, M. (2014). Spectral variability of plagioclase–mafic mixtures (2): Investigation of the optical constant and retrieved mineral abundance dependence on particle size distribution. *Icarus*, 235:207–219. doi: 10.1016/j.icarus.2014.03.022.

Carvano, J. and Davalos, J. (2015). Shape and solar phase angle effects on the taxonomic classification of asteroids. *Astronomy & Astrophysics*, 580:A98. doi: 10.1051/0004-6361/201526268.

Ceamanos, X., Douté, S., Fernando, J., Schmidt, F., Pinet, P., and Lyapustin, A. (2013). Surface reflectance of Mars observed by CRISM/MRO: 1. Multi-angle approach for retrieval of surface reflectance from CRISM observations (MARS-ReCO). *Journal of Geophysical Research (Planets)*, 118:514–533. doi: 10.1029/2012JE004195.

Chen, J., Ling, Z., Jolliff, B. L., Sun, L., Qiao, L., Liu, J., Fu, X., Zhang, J., Li, B., Liu, C., Qi, X., Lu, X., He, Z., and Xu, R. (2022). Radiative Transfer Modeling of Chang'E-4 Spectroscopic Observations and Interpretation of the South Pole-Aitken Compositional Anomaly. *The Astrophysical Journal Letters*, 931(2):L24. doi: 10.3847/2041-8213/ac6e6c.

Chouteau, F., Gabet, L., Fraisse, R., Bonfort, T., Harnoufi, B., Greiner, V., Le Goff, M., Ortner, M., and Paveau, V. (2022). Joint super-resolution and image restoration for PlÉiades Neo imagery. *The International Archives of the Photogrammetry, Remote Sensing and Spatial Information Sciences*, XLIII-B1-2022:9–15. doi: 10.5194/isprs-archives-XLIII-B1-2022-9-2022.

Ciarniello, M., Capaccioni, F., and Filacchione, G. (2014). A test of Hapke's model by means of Monte Carlo ray-tracing. *Icarus*, 237:293–305. doi: 10.1016/j.icarus.2014.04.045.

Ciarniello, M., De Sanctis, M. C., Ammannito, E., Raponi, A., Longobardo, A., Palomba, E., Carrozzo, F. G., Tosi, F., Li, J.-Y., Schröder, S. E., Zambon, F., Frigeri, A., Fonte, S., Giardino, M., Pieters, C. M., Raymond, C. A., and Russell, C. T. (2017). Spectrophotometric properties of dwarf planet Ceres from the VIR spectrometer on board the Dawn mission. *A&A*, 598:A130. doi: 10.1051/0004-6361/201629490.

Ciarniello, M., Filacchione, G., D'Aversa, E., Capaccioni, F., Nicholson, P., Cuzzi, J., Clark, R., Hedman, M., Dalle Ore, C., Cerroni, P., Plainaki, C., and Spilker, L. (2019). Cassini-VIMS observations of Saturn's main rings: Ii. A spectrophotometric study by means of Monte Carlo ray-tracing and Hapke's theory. *Icarus*, 317:242–265. doi: 10.1016/j.icarus.2018.07.010.

Ciarniello, M., Capaccioni, F., Filacchione, G., Raponi, A., Tosi, F., De Sanctis, M. C., Capria, M. T., Erard, S., Bockelee-Morvan, D., Leyrat, C., Arnold, G., Barucci, A., Beck, P., Bellucci, G., Fornasier, S., Longobardo, A., Mottola, S., Palomba, E., Quirico, E., and Schmitt, B. (2015). Photometric properties of comet 67P/Churyumov-Gerasimenko from VIRTIS-M onboard Rosetta. *A&A*, 583:A31. doi: 10.1051/0004-6361/201526307.

Cierniewski, J. (1987). A model for soil surface roughness influence on the spectral response of bare soils in the visible and near-infrared range. *Remote Sensing of Environment*, 23(1):97–115. doi: 10.1016/0034-4257(87)90073-3.

Clegg, R. N., Jolliff, B. L., Robinson, M. S., Hapke, B. W., and Plescia, J. B. (2014). Effects of rocket exhaust on lunar soil reflectance properties. *Icarus*, 227:176–194. doi: 10.1016/j.icarus.2013.09.013.

Clegg-Watkins, R., Jolliff, B., Boyd, A., Robinson, M., Wagner, R., Stopar, J., Plescia, J., and Speyerer, E. (2016). Photometric characterization of the Chang'E-3 landing site using LROC NAC images. *Icarus*, 273:84–95. doi: 10.1016/j.icarus.2015.12.010.

Cooper, K. D. and Smith, J. A. (1985). A Monte Carlo reflectance model for soil surfaces with three-dimensional structure. *IEEE Transactions on Geoscience and Remote Sensing*, GE-23(5):668–673. doi: 10.1109/TGRS.1985.289385.

Cord, A. M., Pinet, P. C., Daydou, Y., and Chevrel, S. D. (2003). Planetary regolith surface analogs: Optimized determination of hapke parameters using multi-angular spectro-imaging laboratory data. *Icarus*, 165(2):414–427. doi: 10.1016/S0019-1035(03)00204-5.

Cord, A. M., Pinet, P. C., Daydou, Y., and Chevrel, S. D. (2005). Experimental determination of the surface photometric contribution in the spectral reflectance deconvolution processes for a simulated martian crater-like regolithic target. *Icarus*, 175(1):78–91. doi: 10.1016/j.icarus.2004.08.010.

Correll, N., Hayes, B., Heckman, C., and Roncone, A. (2022). *Introduction to Autonomous Robots: Mechanisms, Sensors, Actuators, and Algorithms*. MIT Press, Cambridge, MA, 1st edition.

Crawford, I. A., Joy, K. H., and Anand, M. (2014). Chapter 25 - Lunar exploration. In Spohn, T., Breuer, D., and Johnson, T. V., editors, *Encyclopedia of the Solar System (Third Edition)*, pages 555–579. Elsevier, Boston, third edition edition. doi: 10.1016/B978-0-12-415845-0.00025-6.

Cull, S., Arvidson, R. E., Mellon, M. T., Skemer, P., Shaw, A., and Morris, R. V. (2010). Compositions of subsurface ices at the Mars Phoenix landing site. *Geophysical Research Letters*, 37(24). doi: 10.1029/2010GL045372.

Dalton III, J. B. and Pitman, K. M. (2012). Low temperature optical constants of some hydrated sulfates relevant to planetary surfaces. *Journal of Geophysical Research: Planets*, 117(E9). doi: 10.1029/2011JE004036.

Daubechies, I. (1990). The wavelet transform, time-frequency localization and signal analysis. *IEEE Transactions on Information Theory*, 36(5):961–1005. doi: 10.1109/18.57199.

Davalos, J. A., Carvano, J. M., and Blanco, J. (2017). Numerical determination of visible/NIR optical constants from laboratory spectra of HED meteorites. *Icarus*, 285:275–290. doi: 10.1016/j.icarus.2016.10.022.

Deb, D. and Sen, A. (2011). Light scattering from regolith: Intensity versus particle size behavior. *Earth, Moon, and Planets*, 108. doi: 10.1007/s11038-011-9384-5.

Deleforge, A., Forbes, F., and Horaud, R. (2015). High-dimensional regression with gaussian mixtures and partially-latent response variables. *Statistics and Computing*, 25:893–911. doi: 10.1007/s11222-014-9461-5.

D'Errico, J. (2024). fminsearchbnd, fminsearchcon. Link.

Ding, A., Jiao, Z., Kokhanovsky, A., Zhang, X., Guo, J., Zhao, P., Zhang, M., Jiang, H., and Xu, K. (2024). Evaluating the performance of the Enhanced Ross-Li models in characterizing BRDF/albedo/NBAR characteristics for various land cover types in the POLDER database. *Remote Sensing*, 16(12). doi: 10.3390/rs16122119.

Ding, A., Ma, H., Liang, S., and He, T. (2022). Extension of the Hapke model to the spectral domain to characterize soil physical properties. *Remote Sensing of Environment*, 269:112843. doi: 10.1016/j.rse.2021.112843.

Domingue, D. L., D'Amore, M., Ferrari, S., Helbert, J., and Izenberg, N. R. (2019a). Analysis of the MESSENGER MASCS photometric targets part i: Photometric standardization for examining spectral variability across Mercury's surface. *Icarus*, 319:247–263. doi: 10.1016/j.icarus.2018.07.019.

Domingue, D. L., D'Amore, M., Ferrari, S., Helbert, J., and Izenberg, N. R. (2019b). Analysis of the MESSENGER MASCS photometric targets part ii: Photometric variability between geomorphological units. *Icarus*, 319:140–246. doi: 10.1016/j.icarus.2018.07.018.

Domingue, D. L., Denevi, B. W., Murchie, S. L., and Hash, C. D. (2016a). Application of multiple photometric models to disk-resolved measurements of Mercury's surface: Insights into Mercury's regolith characteristics. *Icarus*, 268:172–203. doi: 10.1016/j.icarus.2015.11.040.

Domingue, D. L., Vilas, F., Choo, T., Stockstill-Cahill, K. R., Cahill, J. T., and Hendrix, A. R. (2016b). Regional spectrophotometric properties of 951 Gaspra. *Icarus*, 280:340–358. MicroMars to MegaMars. doi: 10.1016/j.icarus.2016.07.011.

Dong, Y., Jiao, Z., Cui, L., Zhang, H., Zhang, X., Yin, S., Ding, A., Chang, Y., Xie, R., and Guo, J. (2019). Assessment of the hotspot effect for the PROSAIL model with POLDER hotspot observations based on the hotspot-enhanced kernel-driven BRDF model. *IEEE Transactions on Geoscience and Remote Sensing*, 57(10):8048–8064. doi: 10.1109/TGRS.2019.2917923.

Drossart, P. (1993). Optics on a fractal surface and the photometry of the regoliths. *Planetary and Space Science*, 41(5):381–393. doi: 10.1016/0032-0633(93)90072-A.

Du, S., Zheng, N., Xiong, L., Ying, S., and Xue, J. (2010). Scaling iterative closest point algorithm for registration of m–D point sets. *Journal of Visual Communication and Image Representation*, 21(5):442–452. Special issue on Multi-camera Imaging, Coding and Innovative Display.

Efford, N. D. (1993). Scattering laws for reflected solar radiation and the characterisation of terrain roughness. *International Journal of Remote Sensing*, 14(6):1055–1080. doi: 10.1080/01431169308904396.

Egan, W. G. and Hilgeman, T. (1978). Spectral reflectance of particulate materials: a Monte Carlo model including asperity scattering. *Appl. Opt.*, 17(2):245–252. doi: 10.1364/AO.17.000245.

Eon, R. S., Bachmann, C. M., and Gerace, A. D. (2018). Retrieval of sediment fill factor by inversion of a modified hapke model applied to sampled HCRF from airborne and satellite imagery. *Remote Sensing*, 10(11). doi: 10.3390/rs101117585.

Eon, R. S., Bachmann, C. M., Lapszynski, C. S., Tyler, A. C., and Goldsmith, S. (2020). Retrieval of sediment filling factor in a salt panne from multi-view hyperspectral imagery. *Remote Sensing*, 12(3). doi: 10.3390/rs12030422.

Fa, W., Wieczorek, M. A., and Heggy, E. (2011). Modeling polarimetric radar scattering from the lunar surface: Study on the effect of physical properties of the regolith layer. *Journal of Geophysical Research: Planets*, 116(E3). doi: 10.1029/2010JE003649.

Fayolle, M., Quirico, E., Schmitt, B., Jovanovic, L., Gautier, T., Carrasco, N., Grundy, W., Vuitton, V., Poch, O., Protopapa, S., Young, L., Cruikshank, D., Dalle Ore, C., Bertrand, T., and Stern, A. (2021). Testing tholins as analogues of the dark reddish material covering Pluto's Cthulhu region. *Icarus*, 367:114574. doi: 10.1016/j.icarus.2021.114574.

Feaga, L. M., Protopapa, S., Schindhelm, R., Stern, S. A., A'Hearn, M. F., Bertaux, J. L., Feldman, P. D., Parker, J. W., Steffl, A. J., and Weaver, H. A. (2015). Far-UV phase dependence and surface characteristics of comet 67P/Churyumov-Gerasimenko as observed with Rosetta Alice. *Astronomy & Astrophysics*, 583:A27. doi: 10.1051/0004-6361/201526671.

Feller, C., Fornasier, S., Hasselmann, P. H., Barucci, A., Preusker, F., Scholten, F., Jorda, L., Pommerol, A., Sierks, H., Agarwal, J., A'Hearn, M., Bertaux, J.-L., Bertini, I., Boudreault, S., Cremonese, G., Da Deppo, V., Davidsson, B., Debei, S., Cecco, M., and Rodrigo, R. (2016). Decimetre-scaled spectrophotometric properties of the nucleus of comet 67P/Churyumov-Gerasimenko from OSIRIS observations. *Monthly Notices of the Royal Astronomical Society*, 462:S287–S303. doi: 10.1093/mnras/stw2511.

Fernando, J., Schmidt, F., Ceamanos, X., Pinet, P., Douté, S., and Daydou, Y. (2013). Surface reflectance of Mars observed by CRISM/MRO: 2. Estimation of surface photometric properties in Gusev Crater and Meridiani Planum. *Journal of Geophysical Research: Planets*, 118(3):534–559. doi: 10.1029/2012JE004194.

Fernando, J., Schmidt, F., and Douté, S. (2016). Martian surface microtexture from orbital CRISM multi-angular observations: A new perspective for the characterization of the geological processes. *Planetary and Space Science*, 128:30–51. doi: 10.1016/j.pss.2016.05.005.

Fernando, J., Schmidt, F., Pilorget, C., Pinet, P., Ceamanos, X., Douté, S., Daydou, Y., and Costard, F. (2015). Characterization and mapping of surface physical properties of Mars from CRISM multi-angular data: Application to Gusev Crater and Meridiani Planum. *Icarus*, 253:271–295. doi: 10.1016/j.icarus.2015.03.012.

Filacchione, G., Ciarniello, M., D'Aversa, E., Capaccioni, F., Clark, R. N., Buratti, B. J., Helfenstein, P., Stephan, K., and Plainaki, C. (2022). Saturn's icy satellites investigated by Cassini - VIMS. V. Spectrophotometry. *Icarus*, 375:114803. doi: 10.1016/j.icarus.2021.114803.

Foote, E. J., Paige, D. A., Shepard, M. K., Johnson, J. R., and Biggar, S. (2020). The bidirectional and directional hemispheric reflectance of Apollo 11 and 16 soils: Laboratory and Diviner measurements. *Icarus*, 336:113456. doi: 10.1016/j.icarus.2019.113456.

Fornasier, S., Hasselmann, P. H., Barucci, M. A., Feller, C., Besse, S., Leyrat, C., Lara, L., Gutierrez, P. J., Oklay, N., Tubiana, C., Scholten, F., Sierks, H., Barbieri, C., Lamy, P. L., Rodrigo, R., Koschny, D., Rickman, H., Keller, H. U., Agarwal, J., A'Hearn, M. F., Bertaux, J.-L., Bertini, I., Cremonese, G., Da Deppo, V., Davidsson, B., Debei, S., De Cecco, M., Fulle, M., Groussin, O., Güttler, C., Hviid, S. F., Ip, W., Jorda, L., Knollenberg, J., Kovacs, G., Kramm, R., Kührt, E., Küppers, M., La Forgia, F., Lazzarin, M., Lopez Moreno, J. J., Marzari, F., Matz, K.-D., Michalik, H., Moreno, F., Mottola, S., Naletto, G., Pajola, M., Pommerol, A., Preusker, F., Shi, X., Snodgrass, C., Thomas, N., and Vincent, J.-B. (2015). Spectrophotometric properties of the nucleus of comet 67P/Churyumov-Gerasimenko from the OSIRIS instrument onboard the ROSETTA spacecraft. *A&A*, 583:A30. doi: 10.1051/0004-6361/201525901.

Fortezzo, C. M., Spudis, P. D., and Harrel, S. L. (2020). Release of the Digital Unified Global Geologic Map of the Moon at 1:5,000,000-Scale. In *51st Annual Lunar and Planetary Science Conference*, Lunar and Planetary Science Conference, page 2760. Link.

Fritsch, D., Wagner, J., Ceranski, B., Simon, S., Niklaus, M., Zhan, K., and Mammadov, G. (2020). Making historical gyroscopes alive – 2D and 3D preservations by sensor fusion and open data access. doi: 10.20944/preprints202012.0205.v1.

Ganesh, I., Carter, L. M., and Henz, T. N. (2022). Radar backscatter and emissivity models of proposed pyroclastic density current deposits on Venus. *Journal of Geophysical Research: Planets*, 127(10):e2022JE007318. doi: 10.1029/2022JE007318.

Gao, C., Xu, M., Xu, H., and Zhou, W. (2021). Retrieving photometric properties and soil moisture content of tidal flats using bidirectional spectral reflectance. *Remote Sensing*, 13(7). doi: 10.3390/rs13071402.

García Moreno, R., Saa Requejo, A., Tarquis Alonso, A., Barrington, S., and Díaz, M. (2008). Shadow analysis: A method for measuring soil surface roughness. *Geoderma*, 146(1):201–208. doi: 10.1016/j.geoderma.2008.05.026.

Gastellu-Etchegorry, J., Demarez, V., Pinel, V., and Zagolski, F. (1996). Modeling radiative transfer in heterogeneous 3-D vegetation canopies. *Remote Sensing of Environment*, 58(2):131–156. doi: 10.1051/agro:19990302.

Gastellu-Etchegorry, J.-P., Lauret, N., Yin, T., Landier, L., Kallel, A., Malenovský, Z., Al Bitar, A., Aval, J., Benhmida, S., Qi, J., Medjdoub, G., Guilleux, J., Chavanon, E., Cook, B., Morton, D., Chrysoulakis, N.,

and Mitraka, Z. (2017). DART: Recent advances in remote sensing data modeling with atmosphere, polarization, and chlorophyll fluorescence. *IEEE Journal of Selected Topics in Applied Earth Observations and Remote Sensing*, PP:1–10. doi: 10.1109/JSTARS.2017.2685528.

Gastellu-Etchegorry, J.-P., Yin, T., Lauret, N., Cajgfinger, T., Gregoire, T., Grau, E., Feret, J.-B., Lopes, M., Guilleux, J., Dedieu, G., Malenovský, Z., Cook, B. D., Morton, D., Rubio, J., Durrieu, S., Cazanave, G., Martin, E., and Ristorcelli, T. (2015). Discrete Anisotropic Radiative Transfer (DART 5) for modeling airborne and satellite spectroradiometer and LiDAR acquisitions of natural and urban landscapes. *Remote Sensing*, 7(2):1667–1701. doi: 10.3390/rs70201667.

Georgiev, G. T. and Butler, J. J. (2007). Long-term calibration monitoring of Spectralon diffusers BRDF in the air-ultraviolet. *Appl. Opt.*, 46(32):7892–7899. doi: 10.1364/AO.46.007892.

Gerekos, C., Grima, C., Steinbrügge, G., Thakur, S., Scanlan, K. M., Young, D. A., Bruzzone, L., and Blankenship, D. D. (2021). Martian roughness analogues of Europan terrains for radar sounder investigations. *Icarus*, 358:114197. doi: 10.1016/j.icarus.2020.114197.

Gibbs, J. (1899). Fourier's series. *Nature*, 59(1539):606–606. doi: 10.1038/059606a0.

Gimar, C. J., Raut, U., Poston, M. J., Stevanovic, A., Protopapa, S., Greathouse, T. K., Retherford, K. D., Friday, J. M., and Grimes, J. T. (2022). Far-Ultraviolet photometric characteristics of JSC-1A and LMS-1 lunar regolith simulants: Comparative investigations with Apollo 10084. *Journal of Geophysical Research: Planets*, 127(11):e2022JE007508. doi: 10.1029/2022JE007508.

Giuranna, M., Hansen, G., Formisano, V., Zasova, L., Maturilli, A., Grassi, D., and Ignatiev, N. (2007). Spatial variability, composition and thickness of the seasonal north polar cap of Mars in mid-spring. *Planetary and Space Science*, 55(10):1328–1345. doi: 10.1016/j.pss.2007.03.006.

Gleyzes, M. A., Perret, L., and Kubik, P. (2012). Pleiades system architecture and main performances. *The International Archives of the Photogrammetry, Remote Sensing and Spatial Information Sciences*, XXXIX-B1:537–542. doi: 10.5194/isprsarchives-XXXIX-B1-537-2012.

Goel, N. S. (1988). Models of vegetation canopy reflectance and their use in estimation of biophysical parameters from reflectance data. *Remote Sensing Reviews*, 4(1):1–212. doi: 10.1080/02757258809532105.

Golish, D. R., Li, J.-Y., Clark, B. E., DellaGiustina, D. N., Zou, X.-D., Rizos, J. L., Hasselmann, P. H., Bennett, C. A., Fornasier, S., d'Aubigny, C. D., Rizk, B., Daly, M. G., Barnouin, O. S., Seabrook, J. A., Philpott, L., Asad, M. M. A., Johnson, C. L., Rozitis, B., Ryan, A. J., Emery, J. P., and Lauretta, D. S. (2021). Regional photometric modeling of asteroid (101955) Bennu. *The Planetary Science Journal*, 2(4):124. doi: 10.3847/PSJ/abfd3c.

Gou, S., Yue, Z., Di, K., Wan, W., Liu, Z., Liu, B., Peng, M., Wang, Y., He, Z., and Xu, R. (2020). In situ spectral measurements of space weathering by Chang'E-4 rover. *Earth and Planetary Science Letters*, 535:116117. doi: 10.1016/j.epsl.2020.116117.

Govaerts, Y. M. (1996). *A model of light scattering in three-dimensional plant canopies: A Monte Carlo ray tracing approach*. PhD thesis, European Commission, Joint Research Centre, European Union Publications. Link.

Grima, C., Putzig, N. E., Campbell, B. A., Perry, M., Gulick, S. P. S., Miller, R. C., Russell, A. T., Scanlan, K. M., Steinbrügge, G., Young, D. A., Kempf, S. D., Ng, G., Buhl, D., and Blankenship, D. D. (2022). Investigating the martian surface at decametric scale: Population, distribution, and dimension of heterogeneity from radar statistics. *The Planetary Science Journal*, 3(10):236. doi: 10.3847/PSJ/ac9277.

Grizonnet, M., Michel, J., Poughon, V., et al. (2017). Orfeo toolbox: open source processing of remote sensing images. *Open Geospatial Data, Software and Standards*, 2(15). doi: 10.1186/s40965-017-0031-6.

Grohmann, C. H., Smith, M. J., and Riccomini, C. (2011). Multiscale analysis of topographic surface roughness in the Midland Valley, Scotland. *IEEE Transactions on Geoscience and Remote Sensing*, 49(4):1200–1213. doi: 10.1109/TGRS.2010.2053546.

Grumpe, A., Belkhir, F., and Wöhler, C. (2014). Construction of lunar DEMs based on reflectance modelling. *Advances in Space Research*, 53(12):1735–1767. Image Processing and Analysis in Space Science. doi: 10.1016/j.asr.2013.09.036.

Gunderson, K., Lüthi, B., Russell, P., and Thomas, N. (2007). Visible/NIR photometric signatures of liquid water in martian regolith simulant. *Planetary and Space Science*, 55(10):1272–1282. doi: 10.1016/j.pss.2007.03.004.

Guo, D., Fa, W., Wu, B., Li, Y., and Liu, Y. (2021). Millimeter- to decimeter-scale surface roughness of the Moon at the Chang'e-4 exploration region. *Geophysical Research Letters*, 48(19):e2021GL094931. doi: 10.1029/2021GL094931.

Haase, I., Wählisch, M., Gläser, P., Oberst, J., and Robinson, M. S. (2019). Coordinates and maps of the Apollo 17 landing site. *Earth and Space Science*, 6(1):59–95. doi: 10.1029/2018EA000408.

Hagolle, O., Huc, M., Villa Pascual, D., and Dedieu, G. (2015). A multi-temporal and multi-spectral method to estimate aerosol optical thickness over land, for the atmospheric correction of FormoSat-2, Landsat, VENμS and Sentinel-2 images. *Remote Sensing*, 7(3):2668–2691. doi: 10.3390/rs70302668.

Hapke, B. (1984). Bidirectional reflectance spectroscopy: 3. Correction for macroscopic roughness. *Icarus*, 59(1):41–59. doi: 10.1016/0019-1035(84)90054-X.

Hapke, B. (1986). Bidirectional reflectance spectroscopy: 4. The extinction coefficient and the opposition effect. *Icarus*, 67(2):264–280. doi: 10.1016/0019-1035(86)90108-9.

Hapke, B. (2002). Bidirectional reflectance spectroscopy: 5. The coherent backscatter opposition effect and anisotropic scattering. *Icarus*, 157(2):523–534. doi: 10.1006/icar.2002.6853.

Hapke, B. (2008). Bidirectional reflectance spectroscopy: 6. Effects of porosity. *Icarus*, 195(2):918–926. doi: 10.1016/j.icarus.2008.01.003.

Hapke, B. (2012). *Theory of Reflectance and Emittance Spectroscopy*. Cambridge University Press, 2 edition. doi: 10.1017/CBO9781139025683.

Hapke, B., Nelson, R., and Smythe, W. (1998). The opposition effect of the Moon: Coherent backscatter and shadow hiding. *Icarus*, 133(1):89–97. doi: 10.1006/icar.1998.5907.

Hapke, B. and Sato, H. (2016). The porosity of the upper lunar regolith. *Icarus*, 273:75–83. doi: 10.1016/j.icarus.2015.10.031.

Hapke, B. and van Hoen, H. (1963). Photometric studies of complex surfaces, with applications to the Moon. *Journal of Geophysical Research (1896-1977)*, 68(15):4545–4570. doi: 10.1029/JZ068i015p04545.

Hartman, B. and Domingue, D. (1998). Scattering of light by individual particles and the implications for models of planetary surfaces. *Icarus*, 131(2):421–448. doi: 10.1006/icar.1997.5861.

Haruyama, J., Hara, S., Hioki, K., Iwasaki, A., Morota, T., Ohtake, M., Matsunaga, T., Araki, H., Matsumoto, K., Ishihara, Y., Noda, H., Sasaki, S., Goossens, S., and Iwata, T. (2012). Lunar Global Digital Terrain Model Dataset Produced from SELENE (Kaguya) Terrain Camera Stereo Observations. In *43rd Annual Lunar and Planetary Science Conference*, Lunar and Planetary Science Conference, page 1200. doi: Link.

Hasselmann, P., Barucci, M., Fornasier, S., Leyrat, C., Carvano, J., Lazzaro, D., and Sierks, H. (2016). Asteroid (21) Lutetia: Disk-resolved photometric analysis of Baetica region. *Icarus*, 267:135–153. doi: 10.1016/j.icarus.2015.11.023.

Heipke, C. (1997). Automation of interior, relative, and absolute orientation. *ISPRS Journal of Photogrammetry and Remote Sensing*, 52(1):1–19. doi: 10.1016/S0924-2716(96)00029-9.

Helfenstein, P. and Shepard, M. K. (1999). Submillimeter-scale topography of the lunar regolith. *Icarus*, 141(1):107–131. doi: 10.1006/icar.1999.6160.

Helfenstein, P. and Shepard, M. K. (2011). Testing the Hapke photometric model: Improved inversion and the porosity correction. *Icarus*, 215(1):83–100. doi: 10.1016/j.icarus.2011.07.002.

Helfenstein, P. and Veverka, J. (1989). Physical characterization of asteroid surfaces from photometric analysis. Link.

Helfenstein, P., Veverka, J., and Hillier, J. (1997). The lunar opposition effect: A test of alternative models. *Icarus*, 128(1):2–14. doi: 10.1006/icar.1997.5726.

Henyey, L. C. and Greenstein, J. L. (1940). Diffuse radiation in the galaxy. *The Astrophysical Journal*, 93:70–83. Link.

Hess, M., Tenthoff, M., Wohlfarth, K., and Wöhler, C. (2022). Atmospheric correction for high-resolution Shape from Shading on Mars. *Journal of Imaging*, 8(6). doi: 10.3390/jimaging8060158.

Hess, M., Wilhelm, T., Wöhler, C., and Wohlfarth, K. (2021). Uncertainty introduced by darkening agents in the lunar regolith: An unmixing perspective. *Remote Sensing*, 13(22). doi: 10.3390/rs13224702.

Hoffman, M. D. and Gelman, A. (2011). The No-U-Turn sampler: Adaptively setting path lengths in Hamiltonian Monte Carlo. Link.

Holschneider, M., Kronland-Martinet, R., Morlet, J., and Tchamitchian, P. (1989). A real-time algorithm for signal analysis with the help of the wavelet transform. *Wavelets, Time-Frequency Methods and Phase Space*, -1:286. doi: 10.1007/978-3-642-75988-8_28.

Horn, B. (1981). Hill shading and the reflectance map. *Proceedings of the IEEE*, 69(1):14–47. doi: 10.1109/PROC.1981.11918.

Humes, O., Thomas, C., Emery, J., and Grundy, W. (2022). Ultraviolet spectroscopy of Lucy mission targets with the Hubble Space Telescope. *Planetary Science Journal*, 3(8). Publisher Copyright: © 2022. The Author(s). Published by the American Astronomical Society. doi: 10.3847/PSJ/ac8059.

Jacquemoud, S., Baret, F., and Hanocq, J. (1992). Modeling spectral and bidirectional soil reflectance. *Remote Sensing of Environment*, 41(2):123–132. doi: 10.1016/0034-4257(92)90072-R.

Jiao, Z., Ding, A., Kokhanovsky, A., Schaaf, C., Bréon, F.-M., Dong, Y., Wang, Z., Liu, Y., Zhang, X., Yin, S., Cui, L., Mei, L., and Chang, Y. (2019). Development of a snow kernel to better model the anisotropic reflectance of pure snow in a kernel-driven brdf model framework. *Remote Sensing of Environment*, 221:198–209. doi: 10.1016/j.rse.2018.11.001.

Jiao, Z., Schaaf, C. B., Dong, Y., Román, M., Hill, M. J., Chen, J. M., Wang, Z., Zhang, H., Saenz, E., Poudyal, R., Gatebe, C., Bréon, F.-M., Li, X., and Strahler, A. (2016). A method for improving hotspot directional signatures in BRDF models used for MODIS. *Remote Sensing of Environment*, 186:135–151. doi: 10.1016/j.rse.2016.08.007.

Jin, W., Zhang, H., Yuan, Y., Yang, Y., Shkuratov, Y. G., Lucey, P. G., Kaydash, V. G., Zhu, M.-H., Xue, B., Di, K., Xu, B., Wan, W., Xiao, L., and Wang, Z. (2015). In situ optical measurements of Chang'E-3 landing site in Mare Imbrium: 2. Photometric properties of the regolith. *Geophysical Research Letters*, 42(20):8312–8319. doi: 10.1002/2015GL065789.

Johnson, J. R., Grundy, W. M., Lemmon, M. T., Liang, W., Bell, J. F., Hayes, A., and Deen, R. (2022). Spectrophotometric properties of materials from the Mars Science Laboratory at Gale crater: 1. Bradbury Landing to Cooperstown. *Planetary and Space Science*, 222:105563. doi: 10.1016/j.pss.2022.105563.

Johnson, J. R., Shepard, M. K., Grundy, W. M., Paige, D. A., and Foote, E. J. (2013). Spectrogoniometry and modeling of martian and lunar analog samples and Apollo soils. *Icarus*, 223(1):383–406. doi: 10.1016/j.icarus.2012.12.004.

Jost, B., Gundlach, B., Pommerol, A., Oesert, J., Gorb, S. N., Blum, J., and Thomas, N. (2013). Micrometer-sized ice particles for planetary-science experiments – ii. Bidirectional reflectance. *Icarus*, 225(1):352–366. doi: 10.1016/j.icarus.2013.04.007.

Kaasalainen, M. and Torppa, J. (2001). Optimization methods for asteroid lightcurve inversion: I. Shape determination. *Icarus*, 153(1):24–36. doi: 10.1006/icar.2001.6673.

Kar, A., Sen, A., and Gupta, R. (2016). Laboratory photometry of regolith analogues: Effect of porosity. *Icarus*, 277:300–310. doi: 10.1016/j.icarus.2016.05.024.

Kar, A., Sen, A., and Gupta, R. (2021). Laboratory photometry of regolith analogues: Effect of porosity-ii. *Icarus*, 358:114211. doi: 10.1016/j.icarus.2020.114211.

Kennelly, E. J., Price, S. D., Kraemer, K. E., and Aschbrenner, R. (2010). Calibration against the Moon i: A disk-resolved lunar model for absolute reflectance calibration. *Icarus*, 210(1):14–36. doi: 10.1016/j.icarus.2010.05.024.

Koukal, T., Atzberger, C., and Schneider, W. (2014). Evaluation of semi-empirical BRDF models inverted against multi-angle data from a digital airborne frame camera for enhancing forest type classification. *Remote Sensing of Environment*, 151:27–43. Special Issue on 2012 ForestSAT. doi: 10.1016/j.rse.2013.12.014.

Kreslavsky, M. A., Head, J. W., Neumann, G. A., Rosenburg, M. A., Aharonson, O., Smith, D. E., and Zuber, M. T. (2013). Lunar topographic roughness maps from Lunar Orbiter Laser Altimeter (LOLA) data: Scale dependence and correlation with geologic features and units. *Icarus*, 226(1):52–66. doi: 10.1016/j.icarus.2013.04.027.

Kreslavsky, M. A. and Head III, J. W. (2000). Kilometer-scale roughness of Mars: Results from MOLA data analysis. *Journal of Geophysical Research: Planets*, 105(E11):26695–26711. doi: 10.1029/2000JE001259.

Kugler, B. (2021). *Analyse massive d'images multi-angulaires hyperspectrales de la planète Mars par régression inverse de modèles physiques*. Theses, Université Grenoble Alpes. Link.

Kugler, B., Forbes, F., and Douté, S. (2022). Fast Bayesian inversion for high dimensional inverse problems. *Statistics and Computing*, 32(31). doi: 10.1007/s11222-021-10019-5.

La Forgia, F., Giacomini, L., Lazzarin, M., Massironi, M., Oklay, N., Scholten, F., Pajola, M., Bertini, I., Cremonese, G., Barbieri, C., Naletto, G., Simioni, E., Preusker, F., Thomas, N., Sierks, H., Lamy, P., Rodrigo, R., Koschny, D., Rickman, H., Keller, H. U., Agarwal, J., Auger, A. T., A'Hearn, M. F., Barucci, M. A., Bertaux, J. L., Besse, S., Bodewits, D., Da Deppo, V., Davidsson, B., Debei, S., De Cecco, M., El-Maarry, M. R., Ferri, F., Fornasier, S., Fulle, M., Groussin, O., Gutiérrez, P. J., Güttler, C., Hall, I., Hviid, S. F., Ip, W. H., Jorda, L., Knollenberg, J., Kramm, J. R., Kührt, E., Küppers, M., Lara, L. M., Lopez Moreno, J. J., Magrin, S., Marzari, F., Michalik, H., Mottola, S., Pommerol, A., Tubiana, C., and Vincent, J. B. (2015). Geomorphology and spectrophotometry of Philae's landing site on comet 67P/Churyumov-Gerasimenko. *Astronomy & Astrophysics*, 583:A41. doi: 10.1051/0004-6361/201525983.

Labarre, S. (2017). *Caractérisation et modélisation de la rugosité multi-échelle des surfaces naturelles par télédétection dans le domaine solaire*. PhD thesis. Thèse de doctorat dirigée par Ferrari, Cécile et Jacquemoud, Stéphane Physique. Physique de l'Univers Sorbonne Paris Cité 2017. Link.

Labarre, S., Ferrari, C., and Jacquemoud, S. (2017). Surface roughness retrieval by inversion of the Hapke model: A multiscale approach. *Icarus*, 290:63–80. doi: 10.1016/j.icarus.2017.02.030.

Labarre, S., Jacquemoud, S., Ferrari, C., Delorme, A., Derrien, A., Grandin, R., Jalludin, M., Lemaître, F., Métois, M., Pierrot-Deseilligny, M., Rupnik, E., and Tanguy, B. (2019). Retrieving soil surface roughness with the Hapke photometric model: Confrontation with the ground truth. *Remote Sensing of Environment*, 225:1–15. doi: 10.1016/j.rse.2019.02.014.

Lacherade, S., Aznay, O., Fougnie, B., and Lebègue, L. (2014). POLO: A unique dataset to derive the phase angle dependence of the Moon irradiance. volume 9241. doi: 10.1117/12.2067283.

Lachérade, S., Fourest, S., Gamet, P., and Lebègue, L. (2012). Pleiades absolute calibration : Inflight calibration sites and methodology. *The International Archives of the Photogrammetry, Remote Sensing and Spatial Information Sciences*, XXXIX-B1:549–554. doi: 10.5194/isprsarchives-XXXIX-B1-549-2012.

Lapotre, M. G. A., Ehlmann, B. L., and Minson, S. E. (2017). A probabilistic approach to remote compositional analysis of planetary surfaces. *Journal of Geophysical Research: Planets*, 122(5):983–1009. doi: 10.1002/2016JE005248.

Le Bris, A. and Paparoditis, N. (2010). Matching terrestrial images captured by a nomad system to images of a reference database for pose estimation purpose. Link.

Legendre-Champion, J. (2021). Simulations of surface BRF maps with DART. Technical report, Planetary and Space Sciences - Institut de Physique du Globe de Paris.

Lemelin, M., Morisset, C.-E., Germain, M., Hipkin, V., Goïta, K., and Lucey, P. G. (2013). Ilmenite mapping of the lunar regolith over Mare Australe and Mare Ingenii regions: An optimized multisource approach based on Hapke radiative transfer theory. *Journal of Geophysical Research: Planets*, 118(12):2582–2593. doi: 10.1002/2013JE004392.

Lewis, P. (1999). Three-dimensional plant modelling for remote sensing simulation studies using the Botanical Plant Modelling System. *http://dx.doi.org/10.1051/agro:19990302*, 19:185–210. doi: 10.1051/agro:19990302.

Leyrat, C., Fornasier, S., Barucci, A., Magrin, S., Lazzarin, M., Fulchignoni, M., Jorda, L., Belskaya, I., Marchi, S., Barbieri, C., Keller, U., Sierks, H., and Hviid, S. (2010). Search for Steins' surface inhomogeneities from OSIRIS Rosetta images. *Planetary and Space Science*, 58(9):1097–1106. Special Issue: Rosetta Fly-by at Asteroid (2867) Steins. doi: 10.1016/j.pss.2010.04.003.

Li, B., Wang, X., Zhang, J., Chen, J., and Ling, Z. (2016). Lunar textural analysis based on wac-derived kilometer-scale roughness and entropy maps. *Planetary and Space Science*, 125:62–71. doi: 10.1016/j.pss.2016.03.004.

Li, J.-Y., Le Corre, L., Schröder, S. E., Reddy, V., Denevi, B. W., Buratti, B. J., Mottola, S., Hoffmann, M., Gutierrez-Marques, P., Nathues, A., Russell, C. T., and Raymond, C. A. (2013). Global photometric properties of asteroid (4) Vesta observed with Dawn Framing Camera. *Icarus*, 226(2):1252–1274. doi: 10.1016/j.icarus.2013.08.011.

Li, J.-Y., Schröder, S. E., Mottola, S., Nathues, A., Castillo-Rogez, J. C., Schorghofer, N., Williams, D. A., Ciarniello, M., Longobardo, A., Raymond, C. A., and Russell, C. T. (2019). Spectrophotometric modeling and mapping of Ceres. *Icarus*, 322:144–167. doi: 10.1016/j.icarus.2018.12.038.

Li, J.-Y., Zou, X.-D., Golish, D. R., Clark, B. E., Ferrone, S., Fornasier, S., Hasselmann, P. H., Ryan, A. J., Rozitis, B., Emery, J. P., Siegler, M. A., Simon, A. A., DellaGiustina, D. N., Reuter, D. C., Hamilton, V. E., and Lauretta, D. S. (2021). Spectrophotometric modeling and mapping of (101955) Bennu. *The Planetary Science Journal*, 2(3):117. doi: 10.3847/PSJ/abfd2d.

Li, M., Huang, B., and Tian, G. (2022). A comprehensive survey on 3D face recognition methods. *Engineering Applications of Artificial Intelligence*, 110:104669. doi: 10.1016/j.engappai.2022.104669.

Li, Z., Zhu, Q., and Gold, C. (2005). *Digital Terrain Modeling: Principles and Methodology*. CRC Press, 1st edition. doi: 10.1201/9780203357132.

Liang, W., Johnson, J. R., Hayes, A. G., Lemmon, M. T., Bell, J. F., Grundy, W. M., and Deen, R. (2020). Spectrophotometry from Mars Hand Lens Imager goniometer measurements: Kimberley region, Gale crater. *Icarus*, 335:113361. doi: 10.1016/j.icarus.2019.06.022.

Lin, H., Mustard, J. F., and Zhang, X. (2019). A methodology for quantitative analysis of hydrated minerals on mars with large endmember library using CRISM near-infrared data. *Planetary and Space Science*, 165:124–136. doi: 10.1016/j.pss.2018.11.005.

Linder, W. (2009). *Digital Photogrammetry: A Practical Course*. Springer. Link.

Lisein, J., Bonnet, S., Lejeune, P., and Pierrot-Deseilligny, M. (2014). Modélisation de la canopée forestière par photogrammétrie depuis des images acquises par drone. *Revue Française de Photogrammétrie et de Télédétection*, (206):45–54. doi: 10.52638/rfpt.2014.7.

Lowe, D. (1999). Object recognition from local scale-invariant features. In *Proceedings of the Seventh IEEE International Conference on Computer Vision*, volume 2, pages 1150–1157 vol.2. doi: 10.1109/ICCV.1999.790410.

Lowe, D. G. (2004). Distinctive image features from scale-invariant keypoints. *International Journal of Computer Vision*, 60:91–110. doi: 10.1023/B:VISI.0000029664.99615.94.

Lowry, V. C., Hanna, K. L. D., Ito, G., Kelley, M. S. P., Campins, H., and Lindsay, S. (2022). T-matrix and Hapke modeling of the thermal infrared spectra of Trojan asteroids and (944) Hidalgo: Implications for their regolith particle size and porosity. *The Planetary Science Journal*, 3(7):181. doi: 10.3847/PSJ/ac7a30.

Lucas, S., Pacanowski, R., and Barla, P. (2022). Analyse numérique de modèles de matériaux poreux. In *JFIG 2022 - Journées Françaises de l'Informatique Graphique*, Bordeaux, France. Link.

Lucas, S., Ribardiere, M., Pacanowski, R., and Barla, P. (2023). A micrograin BSDF model for the rendering of porous layers. In *SIGGRAPH Asia 2023 Conference Papers*, SA '23, New York, NY, USA. Association for Computing Machinery. doi: 10.1145/3610548.3618241.

Lucey, P. G. (1998). Model near-infrared optical constants of olivine and pyroxene as a function of iron content. *Journal of Geophysical Research: Planets*, 103(E1):1703–1713. doi: 10.1029/97JE03145.

Lucht, W., Schaaf, C., and Strahler, A. (2000). An algorithm for the retrieval of albedo from space using semiempirical BRDF models. *Geoscience and Remote Sensing, IEEE Transactions on*, 38:977 – 998. doi: 10.1109/36.841980.

Lyapustin, A., Gatebe, C. K., Kahn, R., Brandt, R., Redemann, J., Russell, P., King, M. D., Pedersen, C. A., Gerland, S., Poudyal, R., Marshak, A., Wang, Y., Schaaf, C., Hall, D., and Kokhanovsky, A. (2010). Analysis of snow bidirectional reflectance from ARCTAS Spring-2008 Campaign. *Atmospheric Chemistry and Physics*, 10(9):4359–4375. doi: 10.5194/acp-10-4359-2010.

Lyapustin, A. I. and Privette, J. L. (1999). A new method of retrieving surface bidirectional reflectance from ground measurements: Atmospheric sensitivity study. *Journal of Geophysical Research: Atmospheres*, 104(D6):6257–6268. doi: 10.1029/1998JD200123.

Lyons, A. P., Fox, W. L. J., Hasiotis, T., and Pouliquen, E. (2002). Characterization of the two-dimensional roughness of wave-rippled sea floors using digital photogrammetry. *IEEE Journal of Oceanic Engineering*, 27:515–524. Link.

Macdonald, R., Griffiths, R., and Hall, D. (1998). An improved method for the estimation of surface roughness of obstacle arrays. *Atmospheric Environment*, 32(11):1857–1864. doi: 10.1016/S1352-2310(97)00403-2.

Malenovsky, Z., Lamsal, K., Janoutova, R., Devereux, T., Woodgate, W., Hambrecht, L., Cimoli, E., Lucieer, A., Homolova, L., Reagieg, O., Wang, Y., and Gastellu-Etchegorry, J. (2023). 3D radiative transfer modelling of forest canopies reconstructed from terrestrial laser scanning: A case of tall Australian Eucalypts. volume 2023-July, page 2683 – 2686. doi: 10.1109/IGARSS52108.2023.10281746.

Malinverno, A. (1990). A simple method to estimate the fractal dimension of a self-affine series. *Geophysical Research Letters*, 17(11):1953–1956. doi: 10.1029/GL017i011p01953.

Manighetti, I., Tapponnier, P., Gillot, P. Y., Jacques, E., Courtillot, V., Armijo, R., Ruegg, J. C., and King, G. (1998). Propagation of rifting along the Arabia-Somalia plate boundary: Into Afar. *Journal of Geophysical Research: Solid Earth*, 103(B3):4947–4974. doi: 10.1029/97JB02758.

Marquardt, D. W. (1963). An algorithm for least-squares estimation of nonlinear parameters. *Journal of the Society for Industrial and Applied Mathematics*, 11(2):431–441. doi: 10.1137/0111030.

Marshal, R. M., Rüsch, O., Wöhler, C., Wohlfarth, K., and Velichko, S. (2023). Photometry of LROC NAC resolved rock-rich regions on the Moon. *Icarus*, 394:115419. doi: 10.1016/j.icarus.2022.115419.

Marshall, D., Groussin, O., Vincent, J.-B., Brouet, Y., Kappel, D., Arnold, G., Capria, M., Filacchione, G., Hartogh, P., Hofstadter, M., Ip, W.-H., Jorda, L., Kührt, E., Lellouch, E., Mottola, S., Rezac, L., Rodrigo, R., Rodionov, S., Schloerb, P., and Thomas, N. (2018). Thermal inertia and roughness of the nucleus of comet 67P/Churyumov-Gerasimenko from MIRO and VIRTIS observations. *Astronomy and Astrophysics*, 616. doi: 10.1051/0004-6361/201833104.

Martonchik, J., Diner, D., Pinty, B., Verstraete, M., Myneni, R., Knyazikhin, Y., and Gordon, H. (1998). Determination of land and ocean reflective, radiative, and biophysical properties using multiangle imaging. *IEEE Transactions on Geoscience and Remote Sensing*, 36(4):1266–1281. doi: 10.1109/36.701077.

Martonchik, J. V. (1994). Retrieval of surface directional reflectance properties using ground level multiangle measurements. *Remote Sensing of Environment*, 50(3):303–316. doi: 10.1016/0034-4257(94)90080-9.

Martonchik, J. V., Bruegge, C. J., and Strahler, A. H. (2000). A review of reflectance nomenclature used in remote sensing. *Remote Sensing Reviews*, 19(1-4):9–20. doi: 10.1080/02757250009532407.

Masoumzadeh, N., Boehnhardt, H., Li, J.-Y., and Vincent, J.-B. (2015). Photometric analysis of asteroid (21) Lutetia from Rosetta-OSIRIS images. *Icarus*, 257:239–250. doi: 10.1016/j.icarus.2015.05.013.

McGuire, A. F. and Hapke, B. W. (1995). An experimental study of light scattering by large, irregular particles. *Icarus*, 113(1):134–155. doi: 10.1006/icar.1995.1012.

Merlin, F., Deshapriya, J. D. P., Fornasier, S., Barucci, M. A., Praet, A., Hasselmann, P. H., Clark, B. E., Hamilton, V. E., Simon, A. A., Reuter, D. C., Zou, X.-D., Li, J.-Y., Schrader, D. L., and Lauretta, D. S. (2021). In search of Bennu analogs: Hapke modeling of meteorite mixtures. *Astronomy & Astrophysics*, 648:A88. doi: 10.1051/0004-6361/202140343.

Miller, C., Verbiscer, A., Chanover, N., Holtzman, J., and Helfenstein, P. (2011). Comparing Phoebe's 2005 opposition surge in four visible light filters. *Icarus*, 212(2):819–834. doi: 10.1016/j.icarus.2010.12.024.

Minnaert, M. G. J. (1941). The reciprocity principle in lunar photometry. *The Astrophysical Journal*, 93:403–410. Link.

Mishra, I., Lewis, N., Lunine, J., Hand, K., Helfenstein, P., Carlson, R., and MacDonald, R. (2021a). A comprehensive revisit of select Galileo/NIMS observations of Europa. *The Planetary Science Journal*, 2:183. doi: 10.3847/PSJ/ac1acb.

Mishra, I., Lewis, N., Lunine, J., Helfenstein, P., MacDonald, R. J., Filacchione, G., and Ciarniello, M. (2021b). Bayesian analysis of Juno/JIRAM's NIR observations of Europa. *Icarus*, 357:114215. doi: 10.1016/j.icarus.2020.114215.

Moore, D. C. and Singer, M. J. (1990). Crust formation effects on soil erosion processes. *Soil Science Society of America Journal*, 54(4):1117–1123. doi: 10.2136/sssaj1990.03615995005400040033x.

Mouget, A. and Lucet, G. (2014). Photogrammetric archaeological survey with UAV. *ISPRS Annals of the Photogrammetry, Remote Sensing and Spatial Information Sciences*, II-5:251–258. doi: 10.5194/isprsannals-II-5-251-2014.

Munaretto, G., Lucchetti, A., Pajola, M., Cremonese, G., and Massironi, M. (2023). Assessing the spectrophotometric properties of Mercury's hollows through multiangular MESSENGER/MDIS observations. *Icarus*, 389:115284. doi: 10.1016/j.icarus.2022.115284.

Myneni, R. B., Ross, J., and Asrar, G. (1989). A review on the theory of photon transport in leaf canopies. *Agricultural and Forest Meteorology*, 45(1):1–153. doi: 10.1016/0168-1923(89)90002-6.

Nagori, R., Dagar, A. K., and Arya, A. (2023). Comparative analysis of photometric parameters over Apollo landing sites from Terrain Mapping Camera (Chandrayaan-1/2) and lab measured data. *Planetary and Space Science*, 226:105635. doi: 10.1016/j.pss.2023.105635.

Nelder, J. A. and Mead, R. (1965). A Simplex Method for Function Minimization. *The Computer Journal*, 7(4):308–313. doi: 10.1093/comjnl/7.4.308.

Nguyen, D. (2019). Study of the lunar surface roughness at the Apollo 17 landing site. 3rd semester project report.

Nguyen, M. (2021). Internship report. Technical report, Institut de Physique du Globe de Paris, Institut d'Optique Graduate School. 2nd year.

Nicodemus, F. E. (1965). Directional reflectance and emissivity of an opaque surface. *Appl. Opt.*, 4(7):767–775. doi: 10.1364/AO.4.000767.

Nicodemus, F. E., Richmond, J. C., Hsia, J. J., Ginsberg, I. W., Limperis, T., Harman, S., and Baruch, J. J. (1977). Geometrical considerations and nomenclature for reflectance. doi: 10.6028/NBS.MONO.160.

North, P. (1996). Three-dimensional forest light interaction model using a Monte Carlo method. *Geoscience and Remote Sensing, IEEE Transactions on*, 34:946 – 956. doi: 10.1109/36.508411.

Ohno, Y. (2000). *Radiometry and Photometry: Review for Vision Optics*. Number Chap. 14. OSA Handbook of Optics Book Chapter (14), OSA Handbook of Optics, Volume III Visual Optics and Vision,.

Pachepsky, Y. A., Ritchie, J. C., and Gimenez, D. (1997). Fractal modeling of airborne laser altimetry data. *Remote Sensing of Environment*, 61(1):150–161. doi: 10.1016/S0034-4257(96)00249-0.

Paparoditis, N., Thom, C., and Jibrini, H. (2000). Surface reconstruction in urban areas from multiple views of aerial digital frame cameras. *IAPRS*, XXXIII. Link.

Papike, J., Taylor, L., , and Simon, S. (1991). Lunar rocks. In *Lunar Sourcebook - A User's Guide to the Moon*, chapter 5. Cambridge University Press, 1 edition. Link.

Pardo-Igúzquiza, E. and Dowd, P. (2022). Fractal analysis of the martian landscape: A study of kilometre-scale topographic roughness. *Icarus*, 372:114727. doi: 10.1016/j.icarus.2021.114727.

Parviainen, H. and Muinonen, K. (2009). Bidirectional reflectance of rough particulate media: Ray-tracing solution. *Journal of Quantitative Spectroscopy and Radiative Transfer*, 110(14):1418–1440. XI Conference on Electromagnetic and Light Scattering by Non-Spherical Particles: 2008. doi: 10.1016/j.jqsrt.2009.02.030.

Pascuzzo, A. C., Condus, T., Li, S., and Mustard, J. F. (2022). Sensitivity analysis of ice/dust aerosol and phase function assumptions on Hapke spectral unmixing and band depth parameters of martian water ice. *Icarus*, 374:114804. doi: 10.1016/j.icarus.2021.114804.

Pierrot-Deseilligny, M. and Clery, I. (2011). APERO, an open source bundle adjusment software for automatic calibration and orientation of set of images. *ISPRS - International Archives of the Photogrammetry, Remote Sensing and Spatial Information Sciences*, XXXVIII-5/W16. doi: 10.5194/isprsarchives-XXXVIII-5-W16-269-2011.

Pierrot-Deseilligny, M. and Paparoditis, N. (2012). A multiresolution and optimization-based image matching approach: An application to surface reconstruction from SPOT5-HRS stereo imagery. *International Archives of Photogrammetry, Remote Sensing and Spatial Information Sciences*, 36-1. Link.

Pilorget, C. and Fernando, J. (2021). Quantifying the minerals abundances on planetary surfaces using VIS–NIR spectroscopy, what uncertainties should we expect? General results and application to the case of phyllosilicates and carbonates on Mars. *Icarus*, 365:114498. doi: 10.1016/j.icarus.2021.114498.

Pilorget, C., Fernando, J., Ehlmann, B., and Douté, S. (2015). Photometry of particulate mixtures: What controls the phase curve? *Icarus*, 250:188–203. doi: 10.1016/j.icarus.2014.11.036.

Pilorget, C., Fernando, J., Ehlmann, B., Schmidt, F., and Hiroi, T. (2016). Wavelength dependence of scattering properties in the VIS–NIR and links with grain-scale physical and compositional properties. *Icarus*, 267:296–314. doi: 10.1016/j.icarus.2015.12.029.

Pinte, A., Héno, R., Pierrot-Deseilligny, M., Brunetaud, X., Janvier-Badosa, S., and Janvier, R. (2015). Orthoimages of the outer walls and towers of the château de Chambord. *ISPRS Annals of the Photogrammetry, Remote Sensing and Spatial Information Sciences*, II-5/W3:243–250. doi: 10.5194/isprsannals-II-5-W3-243-2015.

Pinty, B., Verstraete, M. M., and Dickinson, R. E. (1989). A physical model for predicting bidirectional reflectances over bare soil. *Remote Sensing of Environment*, 27(3):273–288. doi: 10.1016/0034-4257(89)90088-6.

Pinzuti, P., Humler, E., Manighetti, I., and Gaudemer, Y. (2013). Petrological constraints on melt generation beneath the Asal rift (Djibouti) using quaternary basalts. *Geochemistry, Geophysics, Geosystems*, 14(8):2932–2953. doi: 10.1002/ggge.20187.

Pommerol, A., Thomas, N., Jost, B., Beck, P., Okubo, C., and McEwen, A. S. (2013). Photometric properties of Mars soils analogs. *Journal of Geophysical Research: Planets*, 118(10):2045–2072. doi: 10.1002/jgre.20158.

Protopapa, S., Grundy, W., Reuter, D., Hamilton, D., Dalle Ore, C., Cook, J., Cruikshank, D., Schmitt, B., Philippe, S., Quirico, E., Binzel, R., Earle, A., Ennico, K., Howett, C., Lunsford, A., Olkin, C., Parker, A., Singer, K., Stern, A., Verbiscer, A., Weaver, H., and Young, L. (2017). Pluto's global surface composition through pixel-by-pixel hapke modeling of New Horizons Ralph/LEISA data. *Icarus*, 287:218–228. Special Issue: The Pluto System. doi: 10.1016/j.icarus.2016.11.028.

Protopapa, S., Olkin, C. B., Grundy, W. M., Li, J.-Y., Verbiscer, A., Cruikshank, D. P., Gautier, T., Quirico, E., Cook, J. C., Reuter, D., Howett, C. J. A., Stern, A., Beyer, R. A., Porter, S., Young, L. A., Weaver, H. A., Ennico, K., Ore, C. M. D., Scipioni, F., and Singer, K. (2020). Disk-resolved photometric properties of Pluto and the coloring materials across its surface. *The Astronomical Journal*, 159(2):74. doi: 10.3847/1538-3881/ab5e82.

Pénard, L., Paparoditis, N., and Pierrot-Deseilligny, M. (2006). Reconstruction 3D automatique de façades de bâtiments en multi-vues automatic 3D building facade reconstruction from multiple views. In *Actes de la Conférence Reconnaissance des Formes et Intelligence Artificielle*, Tours, France. Link.

Qi, J. (2019). *Modélisation 3D du transfert radiatif dans les couverts végétaux et reconstruction de forêts à partir de mesures LiDAR*. PhD thesis. Thèse de doctorat dirigée par Gastellu-Etchegorry, Jean-Philippe et Yan, Guangjian Surfaces et interfaces continentales, hydrologie Toulouse 3 2019. Link.

Rahman, H., Pinty, B., and Verstraete, M. M. (1993). Coupled surface-atmosphere reflectance (CSAR) model: 2. Semiempirical surface model usable with NOAA advanced very high resolution radiometer data. *Journal of Geophysical Research: Atmospheres*, 98(D11):20791–20801. doi: 10.1029/93JD02072.

Raut, U., Karnes, P. L., Retherford, K. D., Davis, M. W., Liu, Y., Gladstone, G. R., Patrick, E. L., Greathouse, T. K., Hendrix, A. R., and Mokashi, P. (2018). Far-ultraviolet photometric response of Apollo soil 10084. *Journal of Geophysical Research: Planets*, 123(5):1221–1229. doi: 10.1029/2018JE005567.

Reddy, V., Li, J.-Y., Gary, B. L., Sanchez, J. A., Stephens, R. D., Megna, R., Coley, D., Nathues, A., Le Corre, L., and Hoffmann, M. (2015). Photometric properties of ceres from telescopic observations using Dawn Framing Camera color filters. *Icarus*, 260:332–345. doi: 10.1016/j.icarus.2015.06.039.

Reid, A. M., Meyer, C., Harmon, R. S., and Brett, R. (1970). Metal grains in Apollo 12 igneous rocks. *Earth and Planetary Science Letters*, 9(1):1–5. doi: 10.1016/0012-821X(70)90015-4.

Richter, R. and Schläpfer, D. (2002). Geo-atmospheric processing of airborne imaging spectrometry data. Part 2: Atmospheric/topographic correction. *International Journal of Remote Sensing*, 23:2631–2649. doi: 10.1080/01431160110115834.

Roosjen, P., Bartholomeus, H., and Clevers, J. (2015). Effects of soil moisture content on reflectance anisotropy — laboratory goniometer measurements and RPV model inversions. *Remote Sensing of Environment*, 170:229–238. doi: 10.1016/j.rse.2015.09.022.

Rosenburg, M. A., Aharonson, O., Head, J. W., Kreslavsky, M. A., Mazarico, E., Neumann, G. A., Smith, D. E., Torrence, M. H., and Zuber, M. T. (2011). Global surface slopes and roughness of the Moon from the Lunar Orbiter Laser Altimeter. *Journal of Geophysical Research: Planets*, 116(E2). doi: 10.1029/2010JE003716.

Ross, J. (2012). *The radiation regime and architecture of plant stands*, volume 3. Springer Science & Business Media. Link.

Rosu, A.-M., Pierrot-Deseilligny, M., Delorme, A., Binet, R., and Klinger, Y. (2015). Measurement of ground displacement from optical satellite image correlation using the free open-source software MicMac. *ISPRS Journal of Photogrammetry and Remote Sensing*, 100:48–59. High-Resolution Earth Imaging for Geospatial Information. doi: 10.1016/j.isprsjprs.2014.03.002.

Roujean, J.-L., Tanré, D., Bréon, F.-M., and Deuzé, J.-L. (1997). Retrieval of land surface parameters from airborne POLDER bidirectional reflectance distribution function during HAPEX-Sahel. *Journal of Geophysical Research: Atmospheres*, 102(D10):11201–11218. doi: 10.1029/97JD00341.

Rouquié, B., Hagolle, O., Bréon, F.-M., Boucher, O., Desjardins, C., and Rémy, S. (2017). Using Copernicus atmosphere monitoring service products to constrain the aerosol type in the atmospheric correction processor MAJA. *Remote Sensing*, 9(12). doi: 10.3390/rs9121230.

Roy, S. and Cox, I. (1998). A maximum-flow formulation of the N-camera stereo correspondence problem. In *Sixth International Conference on Computer Vision (IEEE Cat. No.98CH36271)*, pages 492–499. doi: 10.1109/ICCV.1998.710763.

Rucks, M. J., Ye, C., Sklute, E. C., Arnold, J. A., DiFrancesco, N. J., and Glotch, T. D. (2022). Visible to Mid-Infrared optical constants of Orthopyroxenes. *Earth and Space Science*, 9(4):e2021EA002104. doi: /10.1029/2021EA002104.

Rupnik, E., Pierrot-Deseilligny, M., and Delorme, A. (2018). 3D reconstruction from multi-view VHR-satellite images in MicMac. *ISPRS Journal of Photogrammetry and Remote Sensing*, 139:201–211. doi: 10.1016/j.isprsjprs.2018.03.016.

Sadeghi, M., Babaeian, E., Tuller, M., and Jones, S. B. (2018). Particle size effects on soil reflectance explained by an analytical radiative transfer model. *Remote Sensing of Environment*, 210:375–386. doi: 10.1016/j.rse.2018.03.028.

Sadrian, M. R., Calvin, W. M., and McCormack, J. (2022). Contrasting mineral dust abundances from X-ray diffraction and reflectance spectroscopy. *Atmospheric Measurement Techniques*, 15(9):3053–3074. doi: 10.5194/amt-15-3053-2022.

Sato, H., Robinson, M. S., Hapke, B., Denevi, B. W., and Boyd, A. K. (2014). Resolved Hapke parameter maps of the Moon. *Journal of Geophysical Research: Planets*, 119(8):1775–1805. doi: 10.1002/2013JE004580.

Schaaf, C. B., Gao, F., Strahler, A. H., Lucht, W., Li, X., Tsang, T., Strugnell, N. C., Zhang, X., Jin, Y., Muller, J.-P., Lewis, P., Barnsley, M., Hobson, P., Disney, M., Roberts, G., Dunderdale, M., Doll, C.,

d'Entremont, R. P., Hu, B., Liang, S., Privette, J. L., and Roy, D. (2002). First operational BRDF, albedo nadir reflectance products from MODIS. *Remote Sensing of Environment*, 83(1):135–148. The Moderate Resolution Imaging Spectroradiometer (MODIS): a new generation of Land Surface Monitoring. doi: 10.1016/S0034-4257(02)00091-3.

Schaepman-Strub, G., Schaepman, M., Painter, T., Dangel, S., and Martonchik, J. (2006). Reflectance quantities in optical remote sensing—definitions and case studies. *Remote Sensing of Environment*, 103(1):27–42. doi: 10.1016/j.rse.2006.03.002.

Schmidt, F. and Bourguignon, S. (2019). Efficiency of BRDF sampling and bias on the average photometric behavior. *Icarus*, 317:10–26. doi: 10.1016/j.icarus.2018.06.025.

Schmidt, F. and Fernando, J. (2015). Realistic uncertainties on Hapke model parameters from photometric measurement. *Icarus*, 260:73–93. doi: 10.1016/j.icarus.2015.07.002.

Scholten, F., Oberst, J., Matz, K.-D., Roatsch, T., Wählisch, M., Speyerer, E. J., and Robinson, M. S. (2012). GLD100: The near-global lunar 100 m raster DTM from LROC WAC stereo image data. *Journal of Geophysical Research: Planets*, 117(E12). doi: 10.1029/2011JE003926.

Schr oder, S., Mottola, S., Keller, H., Raymond, C., and Russell, C. (2013). Resolved photometry of Vesta reveals physical properties of crater regolith. *Planetary and Space Science*, 85:198–213. doi: 10.1016/j.pss.2013.06.009.

Schröder, S. E. and Keller, H. U. (2009). The unusual phase curve of Titan's surface observed by Huygens' Descent Imager/Spectral Radiometer. *Planetary and Space Science*, 57(14-15):1963–1974. doi: 10.1016/j.pss.2009.03.012.

Schröder, Stefan E., Li, Jian-Yang, Rayman, Marc D., Joy, Steven P., Polanskey, Carol A., Carsenty, Uri, Castillo-Rogez, Julie C., Ciarniello, Mauro, Jaumann, Ralf, Longobardo, Andrea, McFadden, Lucy A., Mottola, Stefano, Sykes, Mark, Raymond, Carol A., and Russell, Christopher T. (2018). Ceres' opposition effect observed by the Dawn framing camera. *Astronomy & Astrophysics*, 620:A201. doi: 10.1051/0004-6361/201833596.

Schröder, S., Mottola, S., Carsenty, U., Ciarniello, M., Jaumann, R., Li, J.-Y., Longobardo, A., Palmer, E., Pieters, C., Preusker, F., Raymond, C., and Russell, C. (2017). Resolved spectrophotometric properties of the Ceres surface from Dawn Framing Camera images. *Icarus*, 288:201–225. doi: 10.1016/j.icarus.2017.01.026.

Scott, D. H., Lucchitta, B. K., and Carr, M. H. (1972). Geologic maps of the Taurus-Littrow region of the Moon Apollo 17 pre-mission maps. 2 maps, Mare Serenitatis, Mare Tranquillitatis, Moon. doi: 10.3133/i800.

Sharma, S. K. (2015). *A review of approximate analytic light-scattering phase functions*. Springer Berlin Heidelberg, Berlin, Heidelberg. doi: 10.1007/978-3-642-37985-7_2.

Sheng, Y., Sun, Z., Lu, S., and Omasa, K. (2024). Ratio of physical model parameters can retrieve aggregate size from different types of soil in cultivated regions. *Soil and Tillage Research*, 244:106262. doi: 10.1016/j.still.2024.106262.

Shensa, M. (1992). The discrete wavelet transform: Wedding the a trous and Mallat algorithms. *IEEE Transactions on Signal Processing*, 40(10):2464–2482. doi: 10.1109/78.157290.

Shepard, M. K., Campbell, B. A., Bulmer, M. H., Farr, T. G., Gaddis, L. R., and Plaut, J. J. (2001). The roughness of natural terrain: A planetary and remote sensing perspective. *Journal of Geophysical Research: Planets*, 106(E12):32777–32795. doi: 10.1029/2000JE001429.

Shepard, M. K. and Helfenstein, P. (2007). A test of the Hapke photometric model. *Journal of Geophysical Research: Planets*, 112(E3). doi: 10.1029/2005JE002625.

Shiltz, D. J. and Bachmann, C. M. (2023). An alternative to Hapke's macroscopic roughness correction. *Icarus*, 390:115240. doi: 10.1016/j.icarus.2022.115240.

Shkuratov, I. G. (1988). Diffractional model of the brightness surge of complex structure surfaces. *Kinematika i Fizika Nebesnykh Tel*, 4:33–39. Link.

Shkuratov, Y., Bondarenko, S., Kaydash, V., Videen, G., Muñoz, O., and Volten, H. (2007). Photometry and polarimetry of particulate surfaces and aerosol particles over a wide range of phase angles. *Journal of Quantitative Spectroscopy and Radiative Transfer*, 106(1):487–508. IX Conference on Electromagnetic and Light Scattering by Non-Spherical Particles, doi: 10.1016/j.jqsrt.2007.01.031.

Shkuratov, Y., Kaydash, V., Korokhin, V., Velikodsky, Y., Opanasenko, N., and Videen, G. (2011). Optical measurements of the Moon as a tool to study its surface. *Planetary and Space Science*, 59(13):1326–1371. Exploring Phobos. doi: 10.1016/j.pss.2011.06.011.

Shkuratov, Y., Petrov, D., and Videen, G. (2003). Classical photometry of prefractal surfaces. *J. Opt. Soc. Am. A*, 20(11):2081–2092. doi: 10.1364/JOSAA.20.002081.

Shkuratov, Y. G. (1983). A model of the opposition effect in the brightness of airless cosmic bodies. 60:1005. Link.

Shkuratov, Y. G. and Helfenstein, P. (2001). The opposition effect and the quasi-fractal structure of regolith: I. Theory. *Icarus*, 152(1):96–116. doi: 10.1006/icar.2001.6630.

Shkuratov, Y. G., Muinonen, K., Bowell, E., Lumme, K., Peltoniemi, J., Kreslavsky, M., Stankevich, D., Tishkovetz, V., Opanasenko, N., and Melkumova, L. (1994). A critical review of theoretical models of negatively polarized light scattered by atmosphereless solar system bodies. *Earth Moon and Planets*, 65(3):201–246. doi: 10.1007/BF00579535.

Shoshany, M. (1991). The equifinality of bidirectional reflectance distribution functions of various microstructures. *International Journal of Remote Sensing*, 12(11):2267–2281. doi: 10.1080/01431169108955257.

Simonelli, D. P., Kay, J., Adinolfi, D., Veverka, J., Thomas, P. C., and Helfenstein, P. (1999). Phoebe: Albedo map and photometric properties. *Icarus*, 138(2):249–258. doi: 10.1006/icar.1999.6077.

Smith, M. W. (2014). Roughness in the Earth sciences. *Earth-Science Reviews*, 136:202–225. doi: 10.1016/j.earscirev.2014.05.016.

Smittarello, D., Grandin, R., De Chabalier, J.-B., Doubre, C., Deprez, A., Masson, F., Socquet, A., and Saad, I. A. (2016). Transient deformation in the Asal-Ghoubbet rift (Djibouti) since the 1978 diking event: Is deformation controlled by magma supply rates? *Journal of Geophysical Research: Solid Earth*, 121(8):6030–6052. doi: 10.1002/2016JB013069.

Sobel, I. and Feldman, G. (1973). A 3x3 isotropic gradient operator for image processing. *Pattern Classification and Scene Analysis*, pages 271–272.

Soderblom, J. M., Bell, J. F., Hubbard, M. Y., and Wolff, M. J. (2006). Martian phase function: Modeling the visible to near-infrared surface photometric function using HST-WFPC2 data. *Icarus*, 184(2):401–423. doi: 10.1016/j.icarus.2006.05.006.

Souchon, A., Besse, S., Pinet, P., Chevrel, S., Daydou, Y., Josset, J.-L., D'Uston, L., and Haruyama, J. (2013). Local spectrophotometric properties of pyroclastic deposits at the Lavoisier lunar crater. *Icarus*, 225(1):1–14. doi: 10.1016/j.icarus.2013.03.004.

Souchon, A., Pinet, P., Chevrel, S., Daydou, Y., Baratoux, D., Kurita, K., Shepard, M., and Helfenstein, P. (2011). An experimental study of Hapke's modeling of natural granular surface samples. *Icarus*, 215(1):313–331. doi: 10.1016/j.icarus.2011.06.023.

Speagle, J. S. (2020). dynesty: a dynamic nested sampling package for estimating Bayesian posteriors and evidences. *Monthly Notices of the Royal Astronomical Society*, 493(3):3132–3158. doi: 10.1093/mnras/staa278.

Spjuth, S., Jorda, L., Lamy, P., Keller, H., and Li, J.-Y. (2012). Disk-resolved photometry of asteroid (2867) Steins. *Icarus*, 221(2):1101–1118. doi: 10.1016/j.icarus.2012.06.021.

Starck, J. and Murtagh, F. (2006). *Astronomical Image and Data Analysis*. Springer-Verlag. doi: 10.1007/978-3-540-33025-7.

Starck, J.-L., Fadili, J., and Murtagh, F. (2007). The undecimated wavelet decomposition and its reconstruction. *IEEE transactions on image processing : a publication of the IEEE Signal Processing Society*, 16:297–309. doi: 10.1109/TIP.2006.887733.

Stein, R. S., Briole, P., Ruegg, J. C., Tapponnier, P. E., and Gasse, F. (1991). Contemporary, Holocene, and Quaternary deformation of the Asal rift, Djibouti: Implications for the mechanics of slow spreading ridges. *Journal of Geophysical Research*, 96:21789–21806. Link.

Stieltjes, L. (1973). *L'axe tectono-volcanique d'Asal (Afar Central-Territoire Français des Afars et des Issas)*. PhD thesis, Université Paris Sud. Thèse de 3e cycle, 196 pp.

Stieltjes, L. (1980). Carte géologique du rift d'asal (dépression afar, est-africain). BRGM (Orléans), CNRS (Paris). 1/50 000, 88 × 114 cm.

Sun, C., Xing, F., Liu, D., Han, J., and Yang, B. (2022). Nonlinear spectral unmixing of hyperspectral imagery based on Hapke model and relevance vector regression algorithm. *Journal of Physics: Conference Series*, 2219:012044. doi: 10.1088/1742-6596/2219/1/012044.

Sun, L. and Lucey, P. G. (2021). Unmixing mineral abundance and Mg# with radiative transfer theory: Modeling and applications. *Journal of Geophysical Research: Planets*, 126(2):e2020JE006691. doi: 10.1029/2020JE006691.

Sun, L. and Lucey, P. G. (2022). Near-infrared spectroscopy of boulders with dust or patina coatings on the Moon: A two-layer radiative transfer model. *Icarus*, 387:115204. doi: 10.1016/j.icarus.2022.115204.

Sun, Z., Lv, Y., and Lu, S. (2015). An assessment of the bidirectional reflectance models basing on laboratory experiment of natural particulate surfaces. *Journal of Quantitative Spectroscopy and Radiative Transfer*, 163:102–119. doi: 10.1016/j.jqsrt.2015.05.005.

Sun, Z., Lv, Y., and Tong, Z. (2016). Effects of particle size on bidirectional reflectance factor measurements from particulate surfaces. *Opt. Express*, 24(6):A612–A634. doi: 10.1364/OE.24.00A612.

Tatsumi, E., Domingue, D., Hirata, N., Kitazato, K., Vilas, F., Lederer, S., Weissman, P. R., Lowry, S. C., and Sugita, S. (2018). VIS-NIR disk-integrated photometry of asteroid 25143 Itokawa around opposition by AMICA/hayabusa. *Icarus*, 311:175–196. doi: 10.1016/j.icarus.2018.04.001.

Taylor, G. J., Warren, P., Ryder, G., Delano, J., Pieters, C., and Lofgren, G. (1991). Lunar rocks. In *Lunar Sourcebook - A User's Guide to the Moon*, chapter 6. Cambridge University Press, 1 edition. Link.

Tenthoff, M., Wohlfarth, K., and Wöhler, C. (2020). High resolution Digital Terrain Models of Mercury. *Remote Sensing*, 12(23). doi: 10.3390/rs12233989.

Trevisani, S., Teza, G., and Guth, P. (2023). A simplified geostatistical approach for characterizing key aspects of short-range roughness. *CATENA*, 223:106927. doi: 10.1016/j.catena.2023.106927.

Triggs, B., McLauchlan, P. F., Hartley, R. I., and Fitzgibbon, A. W. (2000). Bundle adjustment - a modern synthesis. In Triggs, B., Zisserman, A., and Szeliski, R., editors, *Vision Algorithms: Theory and Practice*, pages 298–372, Berlin, Heidelberg. Springer Berlin Heidelberg. Link.

Trowbridge, T. S. (1984). Rough-surface retroreflection by focusing and shadowing below a randomly undulating interface. *J. Opt. Soc. Am. A*, 1(10):1019–1027. doi: 10.1364/JOSAA.1.001019.

Twomey, S. A., Bohren, C. F., and Mergenthaler, J. L. (1986). Reflectance and albedo differences between wet and dry surfaces. *Appl. Opt.*, 25(3):431–437. doi: 10.1364/AO.25.000431.

Valantinas, A., Becerra, P., Pommerol, A., Tornabene, L., Affolter, L., Cremonese, G., Hauber, E., McEwen, A., Munaretto, G., Pajola, M., Bowen, A. P., Patel, M., Rangarajan, V., Schorghofer, N., and Thomas, N. (2021). CaSSIS color and multi-angular observations of martian slope streaks. *Planetary and Space Science*, 209:105373. doi: 10.1016/j.pss.2021.105373.

Van Den Eeckhaut, M., Kerle, N., Poesen, J., and Hervás, J. (2012). Object-oriented identification of forested landslides with derivatives of single pulse LiDAR data. *Geomorphology*, 173-174:30–42. doi: 10.1016/j.geomorph.2012.05.024.

Vedaldi, A. (2007). An open implementation of the SIFT detector and descriptor. Link.

Velikodsky, Y., Opanasenko, N., Akimov, L., Korokhin, V., Shkuratov, Y., Kaydash, V., Videen, G., Ehgamberdiev, S., and Berdalieva, N. (2011). New Earth-based absolute photometry of the Moon. *Icarus*, 214(1):30–45. doi: 10.1016/j.icarus.2011.04.021.

Verbiscer, A. J., Helfenstein, P., Porter, S. B., Benecchi, S. D., Kavelaars, J. J., Lauer, T. R., Peng, J., Protopapa, S., Spencer, J. R., Stern, S. A., Weaver, H. A., Buie, M. W., Buratti, B. J., Olkin, C. B., Parker, J., Singer, K. N., Young, L. A., and Team, T. N. H. S. (2022). The diverse shapes of dwarf planet and large KBO phase curves observed from New Horizons. *The Planetary Science Journal*, 3(4):95. doi: 10.3847/PSJ/ac63a6.

Vidal Vázquez, E., Vivas Miranda, J., and Paz González, A. (2005). Characterizing anisotropy and heterogeneity of soil surface microtopography using fractal models. *Ecological Modelling*, 182(3):337–353. Scaling, fractals and diversity in soils and ecohydrology. doi: 10.1016/j.ecolmodel.2004.04.012.

Vo, L. N. (2023). Millimeter-scale surface roughness of lunar landing sites. 3rd semester project report.

Wang, Y. (2022). *Modélisation 3D du transfert radiatif avec polarisation pour l'étude des surfaces terrestres par télédétection*. PhD thesis. Thèse de doctorat dirigée par Gastellu-Etchegorry, Jean-Philippe et Deschamps, Adrien Surfaces et interfaces continentales, hydrologie Toulouse 3 2022. Link.

Wang, Z., Wu, Y., Blewett, D. T., Cloutis, E. A., Zheng, Y., and Chen, J. (2017). Submicroscopic metallic iron in lunar soils estimated from the in situ spectra of the Chang'E-3 mission. *Geophysical Research Letters*, 44(8):3485–3492. doi: 10.1002/2017GL072652.

Wanner, W., Li, X., and Strahler, A. H. (1995). On the derivation of kernels for kernel-driven models of bidirectional reflectance. *Journal of Geophysical Research: Atmospheres*, 100(D10):21077–21089. doi: 10.1029/95JD02371.

Wanner, W., Strahler, A. H., Hu, B., Lewis, P., Muller, J.-P., Li, X., Schaaf, C. L. B., and Barnsley, M. J. (1997). Global retrieval of bidirectional reflectance and albedo over land from EOS MODIS and MISR data: Theory and algorithm. *Journal of Geophysical Research: Atmospheres*, 102(D14):17143–17161. doi: 10.1029/96JD03295.

Warell, J. and Davidsson, B. (2010). A Hapke model implementation for compositional analysis of VNIR spectra of Mercury. *Icarus*, 209(1):164–178. Mercury after Two MESSENGER Flybys. doi: 10.1016/j.icarus.2009.11.037.

Wilhelms, D., McCauley, J., and Trask, N. (1987). *The Geologic History of the Moon*, volume 1348 of *U.S. Geological Survey Professional Paper*. U.S. Government Printing Office. doi: 10.3133/pp1348.

Wilm, J. (2024). Iterative closest point. MATLAB Central File Exchange, Retrieved August 19, 2024. Link.

Wise, J. and Mars, J. (2022). Field reflectance measurements at night of beach and desert sands within a particulate BRDF model. *Remote Sensing*, 14:5020. doi: 10.3390/rs14195020.

Wohlfarth, K. and Wöhler, C. (2022). Wavelength-dependent seeing systematically changes the normalized slope of telescopic reflectance spectra of Mercury. *Remote Sensing*, 14(2). doi: 10.3390/rs14020405.

Wong, U.-H., Wu, Y., Wong, H.-C., Liang, Y., and Tang, Z. (2014). Modeling the reflectance of the lunar regolith by a new method combining Monte Carlo ray tracing and Hapke's model with application to Chang'E-1 IIM data. *The Scientific World Journal*, 2014(1):457138. doi: 10.1155/2014/457138.

Wu, J., Yang, Q., and Li, Y. (2018). Partitioning of terrain features based on roughness. *Remote Sensing*, 10(12). doi: 10.3390/rs10121985.

Wu, Y., Gong, P., Liu, Q., and Chappell, A. (2009). Retrieving photometric properties of desert surfaces in China using the hapke model and MISR data. *Remote Sensing of Environment*, 113(1):213–223. doi: 10.1016/j.rse.2008.09.006.

Wöhler, C. (2011). Remote determination of small-scale three-dimensional surface properties based on imaging photometry and polarimetry: An introduction. *3D Research*, 1(4):3. doi: 10.1007/3DRes.04(2010)03.

Wöhler, C., Grumpe, A., Berezhnoy, A., Bhatt, M. U., and Mall, U. (2014). Integrated topographic, photometric and spectral analysis of the lunar surface: Application to impact melt flows and ponds. *Icarus*, 235:86–122. doi: 10.1016/j.icarus.2014.03.010.

Xu, F., West, R., and Davis, A. (2013). A hybrid method for modeling polarized radiative transfer in a spherical-shell planetary atmosphere. *Journal of Quantitative Spectroscopy and Radiative Transfer*, 117:59–70. doi: 10.1016/j.jqsrt.2012.10.013.

Xu, X., Liu, J., Liu, D., Liu, B., and Shu, R. (2020). Photometric correction of Chang'E-1 Interference Imaging Spectrometer's (IIM) limited observing geometries data with Hapke model. *Remote Sensing*, 12(22). doi: 10.3390/rs12223676.

Xu, T. Y., Hapke, B., Zhang, X. P., Wu, Y. Z., and Lu, X. P. (2022). Spectrophotometry of the lunar regolith using the Chang'E-3 Panoramic Camera (PCAM). *Astronomy & Astrophysics*, 665:A15. doi: /10.1051/0004-6361/202143012.

Yang, G.-J., Zhao, C.-J., Huang, W.-J., and Wang, J.-H. (2011). Extension of the Hapke bidirectional reflectance model to retrieve soil water content. *Hydrology and Earth System Sciences*, 15(7):2317–2326. doi: 10.5194/hess-15-2317-2011.

Ye, C., Sklute, E. C., and Glotch, T. D. (2021). Orientation averaged Visible/Near-infrared and Mid-Infrared optical constants of hydrous Ca-Sulfates: Gypsum and Bassanite. *Earth and Space Science*, 8(10):e2021EA001834. doi: 10.1029/2021EA001834.

Yin, T., Gastellu-Etchegorry, J.-P., Lauret, N., Grau, E., and Rubio, J. (2013). A new approach of direction discretization and oversampling for 3D anisotropic radiative transfer modeling. *Remote Sensing of Environment*, 135:213–223. doi: 10.1016/j.rse.2013.03.030.

Zeeshan, M. and Sayyad, S. (2020). *Implementation of the Bidirectional Reflectance Function for Modeling the Spectra Derived from Hyperspectral Images*, pages 483–498. doi: 10.1007/978-981-15-2475-2_45.

Zevenbergen, L. W. and Thorne, C. R. (1987). Quantitative analysis of land surface topography. *Earth Surface Processes and Landforms*, 12(1):47–56. doi: 10.1002/esp.3290120107.

Zhang, Y., Tan, K., Wang, X., and Chen, Y. (2020). Retrieval of soil moisture content based on a modified Hapke photometric model: A novel method applied to laboratory hyperspectral and Sentinel-2 MSI data. *Remote Sensing*, 12(14). doi: 10.3390/rs12142239.

Zhou, P., Zhao, Z., Huo, H.-Y., and Liu, Z. (2021). Retrieval of photometric parameters of minerals using a self-made multi-angle spectrometer based on the Hapke radiative transfer model. *Remote Sensing*, 13(15). doi: 10.3390/rs13153022.

Zhou, P., Zhao, Z., Wei, G., and Huo, H.-Y. (2022). Two simulated spectral databases of lunar regolith: Method, validation, and application. *Remote Sensing*, 14(2). doi: 10.3390/rs14020277.

Zhuang, Y., Zhang, H., Ma, P., Jiang, T., Yang, Y., Milliken, R. E., and Hsu, W. (2023). Visible and near-infrared reflectance spectra of igneous rocks and their powders. *Icarus*, 391:115346. doi: 10.1016/j.icarus.2022.115346.

Zribi, M. (1995). *Développement de nouvelles méthodes de modélisation de la rugosité pour la rétrodiffusion hyperfréquence de la surface du sol*. PhD thesis. Thèse de doctorat dirigée par Paillgé, Jean Tgélgédgétection. Traitement du signal Toulouse 3 1995. url: http://www.theses.fr/1995TOU30297.

Zribi, M. (2003). A new empirical model to retrieve soil moisture and roughness from C-band radar data. *Remote Sensing of Environment*, 84(1):42–52. doi: 10.1016/S0034-4257(02)00069-X.

Žižka, J. and Vokrouhlický, D. (2011). Solar radiation pressure on (99942) Apophis. *Icarus*, 211(1):511–518. doi: 10.1016/j.icarus.2010.08.011.